TECHNISCHE UNIVERSITÄT MÜNCHEN
TUM School of Engineering and Design

Measuring Earth Surface Strain Components at different Spatial Scales using SAR Interferometry and its Application in Glaciology and Plate Tectonics

Alessandro Parizzi

Vollständiger Abdruck der TUM School of Engineering and Design
der Technischen Universität München zur Erlangung eines

Doktors der Ingenieurwissenschaften (Dr.-Ing.)

genehmigten Dissertation.

Vorsitz:
Prof. Dr. rer. nat. habil. Marco Körner

Prüfende der Dissertation:
1. Hon.-Prof. Dr. rer. nat. Michael Eineder
2. Prof. Dr.-Ing. habil. Richard Hans Georg Bamler

Die Dissertation wurde am 04.02.2025 bei der Technischen Universität München eingereicht und durch die TUM School of Engineering and Design am 10.06.2025 angenommen.

Abstract

The advent of remote sensing satellites has significantly transformed geoscientific approaches to investigating geophysical phenomena on Earth's surface, enabling more systematic and comprehensive mapping of regions that would otherwise be challenging or costly to survey. Over the past few decades, radar interferometry has emerged as a valuable tool for measuring surface deformation, aiding research across various scientific fields such as geology and glaciology. The inherently relative nature of Synthetic Aperture Radar (SAR) interferometry makes it particularly effective for measuring motion gradients. However, certain limitations related to accuracy and sensitivity must be taken into account. This work aims to explore methodologies for deriving strain measurements from SAR interferometry and to assess their accuracy within specific applications.

In scenarios where deformation patterns exhibit displacements several times the radar wavelength over localized areas (e.g., earthquakes, ice movement), a local linear approximation of the deformation phase can be utilized. This approach enables the modeling of the gradient tensor without the need for phase unwrapping. By leveraging different radar Line of Sight (LoS) measurements, it is possible to resolve the various components of the tensor, thus distinguishing between different types of motion (compression/extension, shear, rotation, and tilting). This methodology is applied to glacier flow, separating the strain-related components of the gradient tensor from those associated with rotation. Additionally, supported by appropriate geophysical models, this estimation of the local gradient tensor can be applied to determine the slip distribution of an earthquake using SAR interferometry. Although derivative analysis can be hindered by a low signal-to-noise ratio, this technique offers the advantage of avoiding the spatial phase unwrapping issues that can lead to erroneous interpretations. The method is tested on a real case study, with results discussed and compared to traditional approaches. Another model-based application examined in this study is the characterization of glacier grounding zones. These areas are characterized by a narrow band of dense interferometric fringes generated by the uplift motion of sea tides, which displace the floating portion of the glacier, thus identifying where the ice is no longer grounded. By applying a mechanical model, this motion is directly modeled in the wrapped phase, allowing for the retrieval of the parameters of interest.

Furthermore, the study of strain accumulation over large areas (e.g., inter- or post-seismic motions) is another critical task supported by SAR interferometry. To accurately identify and understand tectonic processes occurring beneath the Earth's surface, precise relative displacement measurements (1-2 mm/year) over large distances (100-300 km) are necessary. Meeting these requirements poses significant challenges, as systematic errors—such as those related to acquisition geometry and atmospheric delays—become more pronounced over greater distances. Although the new generation of SAR satellites offers centimeter-level accuracy in satellite position knowledge, atmospheric delays must be mitigated to meet these stringent requirements. If mitigation is not feasible, integration with Global Navigation Satellite System (GNSS) measurements is required. This work investigates an approach that begins with an error analysis of the measurements and, based on this analysis, defines an optimal merging strategy using error covariance. Moreover, this framework enables cross-validation between GNSS and interferometric deformation rates, verifying the computed error margins of InSAR and providing a performance evaluation of the InSAR/GNSS integrated product.

Zusammenfassung

DAs Aufkommen von Fernerkundungssatelliten hat geowissenschaftliche Ansätze zur Untersuchung geophysikalischer Phänomene an der Erdoberfläche erheblich verändert und eine systematischere und umfassendere Kartierung von Regionen ermöglicht, die sonst schwer oder kostspielig zu vermessen wären. In den letzten Jahrzehnten hat sich die Radarinterferometrie als wertvolles Werkzeug zur Messung von Oberflächendeformationen etabliert und unterstützt die Forschung in verschiedenen wissenschaftlichen Bereichen wie Geologie und Glaziologie. Die grundsätzlich relative Natur der synthetischen Apertur-Radar-Interferometrie (SAR) macht sie besonders geeignet zur Messung von Bewegungsgradienten. Allerdings müssen bestimmte Einschränkungen hinsichtlich der Genauigkeit und Empfindlichkeit berücksichtigt werden. Diese Arbeit zielt darauf ab, Methoden zur Ableitung von Dehnungsmessungen aus der SAR-Interferometrie zu untersuchen und deren Genauigkeit in spezifischen Anwendungen zu bewerten.

In Szenarien, in denen Deformationsmuster Verschiebungen aufweisen, die mehrere Radarwellenlängen über lokalisierte Gebiete hinweg betragen (z. B. Erdbeben, Eisbewegungen), kann eine lokale lineare Approximation der Deformationsphase genutzt werden. Dieser Ansatz ermöglicht die Modellierung des Gradiententensors, ohne dass eine Phasenentfaltung erforderlich ist. Durch die Nutzung unterschiedlicher Radar-Sichtlinienmessungen (Line of Sight, LoS) ist es möglich, die verschiedenen Komponenten des Tensors aufzulösen und so zwischen unterschiedlichen Bewegungsarten (Kompression/Extension, Scherung, Rotation und Neigung) zu unterscheiden. Diese Methodik wird auf Gletscherbewegungen angewendet, um die dehnungsbezogenen Komponenten des Gradiententensors von denen zu trennen, die mit der Rotation assoziiert sind. Unterstützt durch geeignete geophysikalische Modelle kann diese Schätzung des lokalen Gradiententensors zudem auf die Bestimmung der Schlupfverteilung eines Erdbebens mittels SAR-Interferometrie angewendet werden. Obwohl die Analyse von Ableitungen durch ein niedriges Signal-Rausch-Verhältnis beeinträchtigt werden kann, bietet diese Technik den Vorteil, die räumliche Phasenentfaltung zu vermeiden, die zu fehlerhaften Interpretationen führen kann. Die Methode wird an einer realen Fallstudie getestet, deren Ergebnisse diskutiert und mit traditionellen Ansätzen verglichen werden. Eine weitere modellbasierte Anwendung, die in dieser Arbeit untersucht wird, ist die Charakterisierung der Gletscher-Grundungszonen. Diese Bereiche zeichnen sich durch ein schmales Band dichter interferometrischer Streifen aus, die durch die Hebungsbewegung von Gezeiten entstehen und die schwimmende Gletscherfront verschieben, wodurch festgestellt wird, wo das Eis nicht mehr verankert ist. Durch die Anwendung eines mechanischen Modells wird diese Bewegung direkt in der gewickelten Phase modelliert, was die Bestimmung der interessierenden Parameter ermöglicht.

Darüber hinaus ist die Untersuchung der Dehnungsakkumulation über große Gebiete (z. B. inter- oder postseismische Bewegungen) eine weitere wichtige Aufgabe, die durch SAR-Interferometrie unterstützt wird. Um tektonische Prozesse, die unter der Erdoberfläche ablaufen, präzise zu erkennen und zu verstehen, sind genaue relative Verschiebungsmessungen (1-2 mm/Jahr) über große Distanzen (100-300 km) erforderlich. Die Erfüllung dieser Anforderungen stellt große Herausforderungen dar, da systematische Fehler – wie solche, die mit der Aufnahmekonstellation und atmosphärischen

Verzögerungen zusammenhängen – über größere Entfernungen stärker ins Gewicht fallen. Obwohl die neue Generation von SAR-Satelliten eine Zentimeter-genaue Kenntnis der Satellitenposition bietet, müssen atmosphärische Verzögerungen minimiert werden, um diese strengen Anforderungen zu erfüllen. Ist eine Minderung nicht möglich, ist eine Integration mit Global Navigation Satellite System (GNSS)-Messungen erforderlich. Diese Arbeit untersucht einen Ansatz, der mit einer Fehleranalyse der Messungen beginnt und basierend auf dieser Analyse eine optimale Fusionsstrategie unter Verwendung der Fehlerkovarianz definiert. Zudem ermöglicht dieser Rahmen die Kreuzvalidierung zwischen GNSS- und interferometrischen Deformationsraten, um die berechneten Fehlermargen von InSAR zu überprüfen und eine Leistungsbewertung des integrierten InSAR/GNSS-Produkts vorzunehmen.

Contents

1 Introduction

1.1 Motivation

Spaceborne Synthetic Aperture Radar interferometry allows a synoptic mapping of Earth deformation phenomena without the deployment of any in-situ instrumentation. This opens the doors to a global view of the Earth dynamics including areas typically difficult to survey due to their remote location as well as large extension. This work investigates the capabilities of InSAR in surveying ground deformation from the point of view of the scales of the deformation pattern to be measured. The performance of InSAR in measuring deformations is limited by error sources that reduce both precision and accuracy of the interferometric phase, hence limiting its application in different contexts. The point of view of this work is to model the two cases in spatially correlated errors and spatially uncorrelated errors. The first, such like atmospheric distortions or systematic orbit errors increase their effect with the distance, while the latter are independent from the scale. Figure 1.1 shows how the different applications are differently influenced by the two groups depending on their spatial extension.

The larger the observation pattern to be observed are the more the spatially correlated distortions will play a role in the final accuracy of the measurements. Error sources like atmospheric distortions increase their power with the distance degrading the sensitivity of one order of magnitude from the scale of some kilometers to hundreds of kilometers. Unfortunately some applications, such like the study of tectonic motions, have very challenging requirements in order to be able to detect very slow secular deformations. The investigation of the achievable accuracies and the potential synergies with other techniques is therefore an important topic in order to support the scientific work aimed to study the earth dynamics.

1.2 Scope

This thesis investigates the capabilities and performance of Synthetic Aperture Radar (SAR) in measuring strain, with a specific focus on tectonic deformation, seismic events, and glacier dynamics.

1.3 Thesis structure

This is a cumulative dissertation. It gathers the findings of the author in measuring strain using SAR interferometry presented in four peer-reviewed papers and one conference papers (see the Appendix). The thesis is structured as follows.

Fundamentals and state of the art

This chapter provides a general description of Synthetic Aperture Radar Interferometry from the point of view of this study. An overview of the different error sources is given distinguishing between

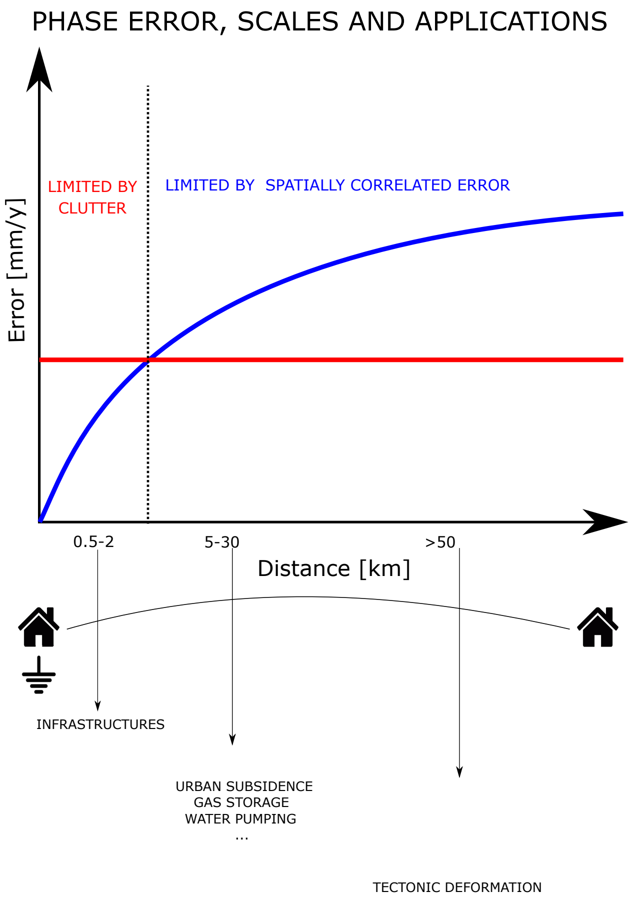

Figure 1.1: InSAR scales, applications and limitations

different characteristics in space and time domain. Finally the state of the art is discussed in the light of the different limitations of the technique.

Modeling local deformation using the wrapped interferometric phase

The use of InSAR in the analysis of strong local Earth surface deformations such like glaciers flow or earthquakes is often limited by the technical difficulty of resolving phase ambiguities. The presence of a very high fringe frequency and the possibility of losing spatial continuity, due to lack of coherence could in fact seriously limit the capabilities of the phase unwrapping algorithms. Chapter 3 investigates the possibility of avoiding phase unwrapping for a set of very specific applications. In particular, the possibility of modeling the physics of the motion in terms of wrapped phase is studied. Practical case studies are shown measuring glaciers strain/rotation, grounding line positioning and earthquakes source modeling.

This part refers to the journal papers in Appendixes A and B : *A. Parizzi and W. Abdel Jaber, "Estimating Strain and Rotation From Wrapped SAR Interferograms," in IEEE Geoscience and Remote Sensing Letters, vol. 15, no. 9, pp. 1367-1371, Sept. 2018*, *A. Parizzi, "Inversion of the Slip Distribution of an Earthquake From InSAR Phase Gradients: Examples Using Izmit Case Study," in IEEE Geoscience and Remote Sensing Letters, vol. 16, no. 11, pp. 1726-1730, Nov. 2019* and the Conference paper in Appendix E *A. Parizzi, "Potential of an Automatic Grounding Zone Characterization Using Wrapped InSAR Phase," IGARSS 2020 - 2020 IEEE International Geoscience and Remote Sensing Symposium, 2020, pp. 802-805*

Accuracy of the large-scale deformation measurements using InSAR

Chapter 4 discusses the performance of InSAR in measuring large scale deformation patterns. Particular emphasis is given to the impact of tropospheric corrections applied on the data. A general error model is provided and used for validation using GNSS data in different test sites around the world. A description of the improved performance using tropospheric models is given considering a variety of different test sites.

This part refers to the journal paper in Appendix D : *Parizzi, A., Brcic R. and De Zan F. (2021). InSAR Performance for Large-Scale Deformation Measurement. IEEE Transactions on Geoscience and Remote Sensing, 59(10):8510-8520.*

Calibration of the InSAR deformation measurements using GNSS

Exploiting the error model studied in Chapter 4, Chapter 5 describes the development of an algorithm aimed to provide an optimal combination of InSAR and GNSS measurements. The basic idea is to exploit the error spectral characteristic of the the two techniques in order to merge them in the best way. The principle of the algorithm is described also providing some verification using numerical simulations. Then practical examples are presented using real data in different applications context.

This part refers to the journal paper in Appendix C : *Alessandro Parizzi , Fernando Rodriguez Gonzalez and Ramon Brcic (2021). A Covariance-Based Approach to Merging InSAR and GNSS Displacement Rate Measurements. Remote Sensing.*

Conclusion

This thesis has investigated the capability of InSAR in detecting ground deformation from the point of view of the motion spatial scale. Due to the inherent relativity of interferometry, this is a very significant point of view since the performance are strongly related to the distance of the relative measurement. Therefore when for local deformations atmospheric effects are almost negligible on the other side for large deformation patterns they can be considered as the main limiting factor. In order to tackle this aspect the impact of tropospheric corrections has been evaluated as well as the integration with GNSS. The general validation approach shows the achievable performance in the different scenarios also supporting the evaluations for future missions

2 Fundamentals and state of the art

This chapter provides the reader with fundamentals about the use of SAR interferometry for the measurements of ground displacement.

Moreover, the main error sources that limit the precision of the InSAR measurements are presented and discussed.

2.1 Synthetic Aperture Radar Interferometry InSAR

The digital processing of SAR images includes a large number of steps before being able to form a so called SAR interferogram. The data, after the acquisition needs to be focused algorithmically compensating the phase effect of the synthetic aperture and integrating along the aperture. This improves the resolution along the moving direction of the sensor (19) providing the equivalent of having a large antenna along the flight direction. As output, the focusing procedure provides a full resolution SAR image (single look complex, SLC) sampled on a raster in general different from acquisition to acquisition. However in order to guarantee the generation of an interference figure, the two raster must be precisely aligned. This operation is done estimating, in a space varying fashion, the difference between the two point grids using the state vectors information as well as the shifts estimated by cross-correlating patches of images. Defined mapping between the two raster one image (secondary) is then re-sampled on the raster of the other (reference). After this operation two equally sampled complex matrices are available to form a SAR interferogram. A generic pixel $p_{s,l}$ located in the sample line position (l,s) can be written a as a complex phasor:

$$p_{s,l} = Ae^{j\phi} \tag{2.1}$$

where A is the amplitude of the backscattered signal that depends typically on the type of target and ϕ its phase that depends on the travelled path r and from the electromagnetic properties of the reflecting target.

$$\phi_{s,l} = -\frac{4\pi}{\lambda} r + \phi_{scat} \tag{2.2}$$

being λ the carrier wavelength and ϕ_{scat} the phase related to the electromagnetic properties of the target.

The radar signal is characterized by a certain bandwidth B_w modulated on a carrier frequency $f_0 >> B_w$. By demodulating the received signal using two carriers at $\pi/2$ phase difference it is possible to reconstruct the phase in modulo 2π. Since the bandwidth is much smaller than the carrier the corresponding resolution of the sensor does not allow to spatially follow the phase variation which will "'turn"' several cycles between one resolution cell to the others.

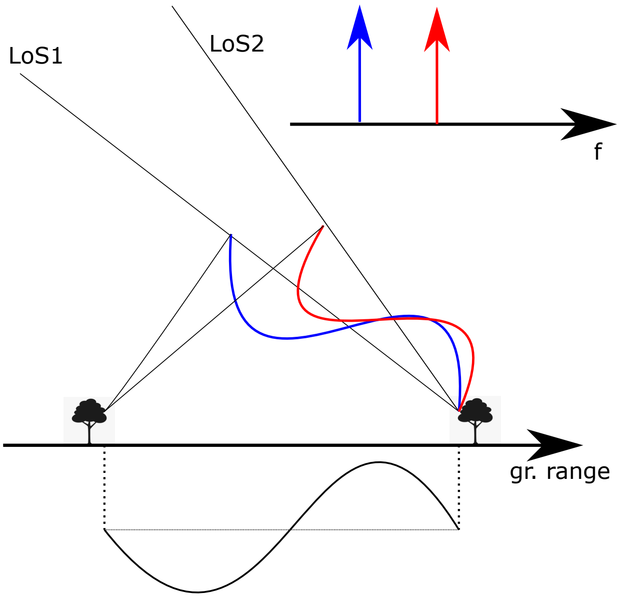

Figure 2.1: Geometric intepretation of the wavenumber shift effect

SAR interferometry allows to exploit this phase information by observing its relative spatial variation between two SAR acquisitions. Supposing to have two images presenting some delays variations in the order of the wavelength it will be possible to observe the spatial patterns of such variations by forming a complex interferogram i at the position s, l by multiplying an image (secondary) for the complex conjugate of a reference acquisition.

$$i_{s,l} = r_{s,l}s^*_{s,l} = A_r A_s e^{\phi_s - \phi_r} \tag{2.3}$$

The resulting interferometric phase $\phi_i = \phi_s - \phi_r$ is still ambiguous, however its smoother variation allows a reconstruction, through spatial integration, of the original phase w.r.t. a reference point. Therefore it is possible to observe that the information retrieved by interferometric phase is inherently relative since it needs a referencing both w.r.t. the temporal and spatial domains. For the temporal domain the reference is an entire acquisition, for the spatial is a point that can be located everywhere in the image.

2.1.1 Interferometric phase: wavenumber shift and fringe frequency

In view of the next chapter it is worth to spend some words in discussing SAR interferometry from the point of view of the signal spectrum. As said in the previous section interferometric phase is able to track a spatial variation of the propagation delay between the two images. In frequency domain this corresponds to a different projection of the reflectivity spectrum onto the radar line of sight direction. In order to give a more intuitive explanation Figure 2.1 recalls the description in (**?**). Figure 2.1 shows how a given harmonic in ground range direction is de facto differently mapped in two different geometries (LoSs).

This change on the geometry can be generated from different reasons, different view angles as in Figure 2.1 or for a change in the geometry of the surface itself related to ground deformation occurring between the two acquisitions. Nonetheless in practice is the illumination of a different portion of the ground reflectivity spectrum by the radar pulse. That means that even if the two SAR acquisitions share the same carrier frequency f_0 and bandwidth B_w the information contained in the two frequencies band is slightly misaligned. Due to this shift there will be part of the acquired spectrum not common to both acquisitions that will only generate noise since it will not interfere. Knowing the amount of occurred shift it is possible to perform a spectral filtering aimed to maximize

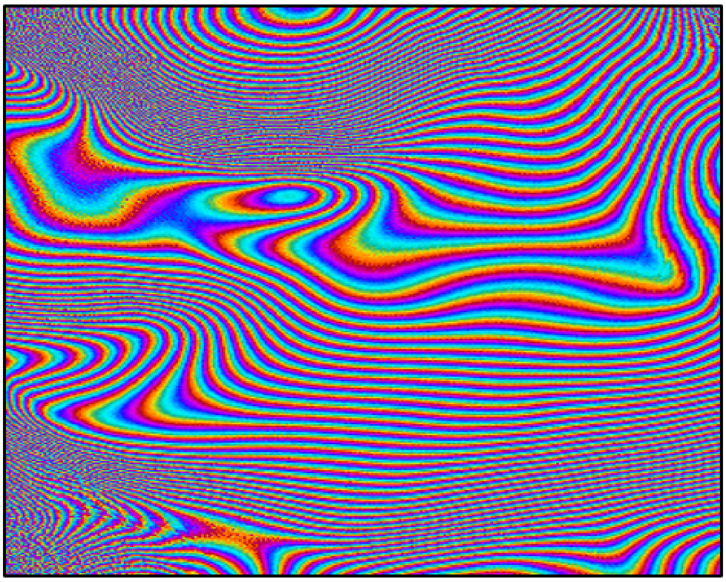

Figure 2.2: Fringe pattern from a glacier deformation. The decorrelation effect is observable where the variation is stronger

the coherence of the interferogram (38). Since the bandwidth of the signals is limited, the extreme consequence of such effect is the shift of the whole bandwidth, that leads to total de-correlation. In space domain this corresponds to a spatial phase variation that cannot be followed by the given resolution.

The relevant aspect for this dissertation is to have an idea of how the fringe patterns are generated. Fringe patterns are in fact generated when the scene is observed by slightly different geometries, but also when the observed scene is deformed between the two acquisitions. In general we can state that the wave-number shift occurring between the two SAR acquisition is exactly described by the fringe patterns that we see since they are its direct consequence. Therefore having the local fringe frequency defined as:

$$f_\phi = \frac{1}{2\pi}\frac{\partial\phi}{\partial r} = \frac{2}{\lambda}\frac{\Delta\theta}{tan(\theta)} \tag{2.4}$$

In case of topography the variation $\Delta\theta$ is approximated by the ratio between normal baseline B_n and range distance r_i leading to the well known expression:

$$f_\phi = \frac{2}{\lambda}\frac{B_n}{r_i tan(\theta)} \tag{2.5}$$

After these considerations is again evident the inherent relative nature of the interferometric measurements that do not observe directly the motion or the topography profile itself but only their spatial variation. In practice, given a certain patch of pixels, its absolute motion is not directly measured by the inteferometric phase. Nonetheless it is possible to carry out a very precise measurement of its "“internal"” motion gradient independently whether it is due to a deformation or a rigid rotation. The decomposition of the motion in this sense is formally discussed in the next Chapter.

2.1.2 Interferometric phase: models and parameters estimation

As seen in the previous sections the interferometric phase is able to map changes in the delay between two different SAR acquisitions. Such changes can be related to different causes and are observed all integrated into the measured interferometric phase. Therefore an important issue in exploiting the interferometric measurements is the capability of separating the different components of the delay. Moreover, depending on the application, some of them could be object of interest and others are undesired and thus considered as noise.

Then in order to be able to estimate parameters it is necessary to formulate analytical models that can be use to estimate unknowns and separating them from other undesired effects. A typical example is the separation between topography and deformation. As seen previously these two observables are related to two different changes between reference and secondary acquisition. The first is visible if a difference in the acquisition geometry is present the second if the scene is changing. The models used to parametrize this case is the following:

$$\Delta\phi = \frac{4\pi}{\lambda}\Big(d(\underline{\xi},t) + \frac{B_n}{r_0 sin\theta}H\Big) + n \tag{2.6}$$

where $d(\underline{\xi},t)$ is the deformation model function of a set of parameters $\underline{\xi}$ depending on its complexity, H is the topography projected onto phase according to the normal baseline B_n which accounts for the difference in geometry and n is the phase noise. Now having available a set of interferograms having different time and B_n differences it is possible to separate the topography H from the of parameters $\underline{\xi}$. The accuracy of this estimate is related to the domain sampling if we consider the variance of the estimator but also to the degree of orthogonality of the domains if we estimate multiple parameters using different domains. In the case of the pair topography and deformation this will result in having well sampled measurements on $\underline{t}$ and $\underline{B_n}$ but also having $\left\langle \underline{t}\underline{B_n} \right\rangle$ minimized.

This case is of course a simplification, since many other effects typically are over imposed and not all of them can be separated exploiting their projection on different domains. This means that the only way to get rid of some additional delays is to compensate them using external information, applying educated filtering procedures or simply being able to account for their effects in terms of performance degradation. In the next Section an overview is proposed briefly discussing some undesired effects and their impact on the interferometric measurements.

2.2 Limitations in interferometric phase precision

The application of SAR interferometry to perform displacement measurements can be affected by a large number of limitations. As already mentioned before it is worth to notice that such noise sources have different nature and can affect differently depending on the application. In particular for the purpose of this dissertation it is necessary to divide them in two macro-groups, the spatially uncorrelated errors and the spatially correlated errors.

The first can be mitigated through some spatial average basically trading precision with a spatial resolution reduction. The latter are characterized by spatially varying patterns often spectral overlapped to the deformation patterns to be measured. Their spatial correlation makes them not too critical for application aimed to measure deformation patterns on a small spatial scale, however increasing the scale, or to say it in other words, increasing the distance from the reference point, such errors increase drastically their power hence limiting the observability of the deformation signal.

Since also temporal stacks of interferograms are discussed it is worth to spend some words about the temporal characteristics of these noise sources. In general, it is possible to state that almost all of them are uncorrelated in time nonetheless some exceptions are present. In case of tropospheric delays we can in fact have some seasonality due to the periodical changes in the physical quantities that determine the refraction index, therefore especially in case of stratification with the topography such delays can repeat themselves with a certain correlation through the different years. Another example is given by the frequency drift of the radar oscillator: this can happen slowly in time (as in the case of Envisat-ASAR) hence generating spatial phase ramps that increase their slope with the time. The table 2.1 is aimed to give a general overview of the noise sources, more details will be discussed in the following sections.

Error Sources Characteristics		
ERROR SOURCE	**SPACE**	**TIME**
System SNR	*uncorrelated*	*uncorrelated*
Temporal Decorrelation	*uncorrelated*	*uncorrelated*
Troposphere Turbulence	*correlated*	*uncorrelated*
Troposphere Stratification	*correlated*	*seasonal*
Ionosphere	*correlated*	*uncorrelated*
Solid Earth Tides	*correlated*	*uncorrelated*
Clock Drifts	*correlated*	*uncorrelated/drifts*
Soil/Vegetation Effects	*correlated*	*seasonal/drifts*

Table 2.1: Errors Resume

2.2.1 Temporal decorrelation

The reflectivity of the ground is changing gradually in time. This leads to a loss of correlation between the radar echoes and a consequent increasing of the noise. A valid physical model that can encompass all the characteristics of the decorrelating interferometric phase is still missing. However a simple way to describe at least its temporal behavior is to model it as a stationary process described by three parameters: a starting coherence γ_0, a long-term coherence γ_∞ and a time constant τ to describe the transition (80):

$$\gamma(t) = (\gamma_0 - \gamma_\infty)e^{-\frac{t}{\tau}} + \gamma_\infty (t > 0) \tag{2.7}$$

This model catches also the long term coherence component that is able to strongly improve the performance since it contains information of the deformation signal also at large time spans. This contribution is in C and X band typically present only on urbanized areas. However in lower frequencies InSAR residual coherence of $0.2 - 0.3$ have been observed also on bare soils.

2.2.2 Atmospheric effects

The velocity of radar pulses can vary with the variability of refractive index of the medium. Since SAR missions are typically located between 500 and 800 km, in spaceborne SAR the transmitted pulse crosses almost the whole Earth atmosphere hence accumulating space variant phase screen generated by this variability. Such patterns are generally low-pass in space but can affect interferometric measurements with relative errors that can reach tens of centimeters at large distance. At the moment the additive atmospheric delay can be considered the main source of error in measuring large scale deformation using InSAR. Since its spatial spectrum is very much overlapped to the deformation signal spectrum it is difficult to find a clean way to remove it without affecting also the signal to be measured. However the term "‘atmospheric delay"’ is rather generic and some more precise specifications have to be done discussing this topic.

2.2.2.1 Ionospheric distortions

Ionosphere is located in a band between 50 and 1000 km above the sea level, even thought its maximum concentration extends from 150 to 500 km. Since it acts pretty far away from the ground during the synthetic aperture the sensor collects pulses that travels through different ionospheric states hence forming phase screens inside the raw data. This can be problematic also for SAR processing triggering de-focusing or pixel-shifts (71). In extreme conditions such distortions can generate coherence losses that can be avoided only through a precise co-registration. In particular the impact of ionosphere on SAR interferometric phase, apart from some constants like the speed of light and $K = 40.28\ m^3/s^2$, depends strongly on the carrier frequency f_0 and the electron concentration (TEC) that the radar pulses travel into (71).

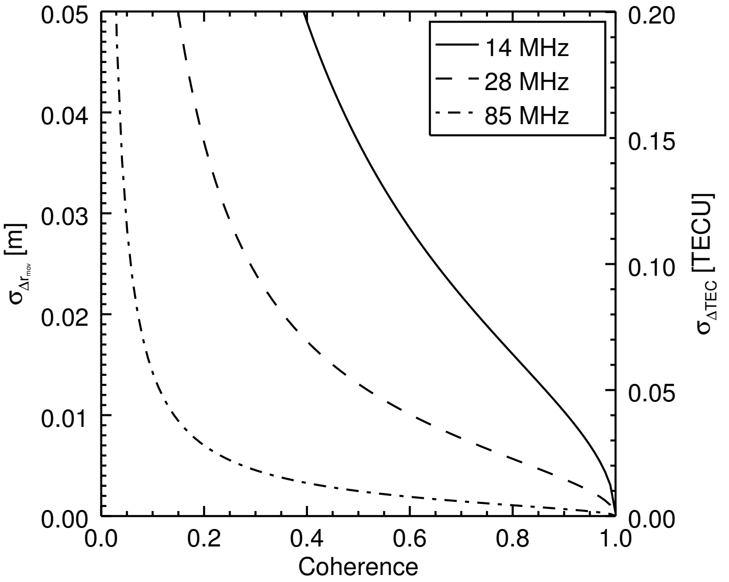

Figure 2.3: Split-Spectrum performance graphics from (42). The picture shows the performance in different bandwidth scenarios. The assumed multi-look corresponds to the number of pixels necessary to cover an area of 1 km^2

$$\Delta_{\phi} \approx -\frac{2K}{cf_0^2} TEC \tag{2.8}$$

The carrier frequency is determined by the mission design, making L-band sensors strongly more affected than C or X-band. The electron concentration can vary with the latitude the time of the day and with the years according to the solar cycle. Based on these basic remarks it is possible to state that the mission design can be carried out in order to minimize such impact, for example preferring short wavelengths, adjusting mission start with solar minimums and avoiding the acquisitions in hours having maximum TEC concentration. Nonetheless, this could not be enough if the target is the measurement of very large scale motions such like tectonic deformations. Major effects have been shown for instance, also in C-band mission like Sentinel (43). Therefore, compensation approaches have been developed in order to further reduce the ionosphere-induced phase error. At the moment the more common approach is the so called Split-Spectrum. This method exploits exactly the strong dependence with the frequency of the ionospheric delay to separate its contribution from the other signal components (42). Such diversity is obtained by using the range bandwidth forming two interferograms at "‘lower’" and "‘higher’" frequencies. Subtracting them all the other components but the ionospheric one are deleted hence obtaining an estimation of the ionospheric phase screen. The improvement in performance has been derived in (42) showing the residual error in meters of such compensation.

$$\sigma_{defo} = \frac{3c}{16\pi Bw} \sqrt{\frac{3}{N}} \frac{\sqrt{1-\gamma^2}}{\gamma} \tag{2.9}$$

Where Bw is the bandwidth N is the number of independent samples and γ is the coherence. Equation 2.9 shows that the capability of mitigating the ionospheric delays in deformation measurements depends basically on the bandwidth and the number of looks only. Therefore fixing a performance target in terms of accuracy and resolution (N of looks) it is possible to derive in first approximation how much bandwidth is necessary (see Figure 2.3) to keep this disturbance at the same level as the other error sources.

2.2.2.2 *Troposheric distortions*

Even though they can be both considered as atmospheric effects, tropospheric related distortions differ radically from the ionospheric ones at least from the point of view of the geoscientist that want to perform deformation measurements using InSAR. The first big difference is related to their independence from the carrier frequency. In fact, in the range of radio-frequencies where the SAR instruments are operated, the delay triggered by the troposphere is the same. Hence the additive delay measured in meters for a given tropospheric situation is the same independently from the sensor carrier frequency. The second difference is related to the position of the troposphere with respect to the platform and the ground. The great majority of the delay is generated in the lower 2 km of the pulse path. This means that its effect does not vary too much along the synthetic aperture as it happens for ionosphere, hence avoiding the related co-registration problems. Therefore it is possible to state that the tropospheric delay is almost perfectly imaged by the SAR processing hence generating full resolution phase screen over imposed to the deformation pattern to be observed. The effect on the phase is generated only by the change in the refraction index of the troposphere according to its state in terms of temperature, pressure and humidity. The so-called scaled up refractivity N is modeled as:

$$N = k_1\frac{P_d}{T} + k_2\frac{e}{T} + k_2\frac{e}{T^2} \tag{2.10}$$

where $k_1 = 0.776KPa^{-1}$, $k_2 = 0.716KPa^{-1}$ and $k_3 = 3.75 \times 10^3K^2Pa^{-1}$ are constants derived from laboratory measurements, T is the absolute temperature in Kelvin (K), P_d is the partial pressure of dry air in Pascal (Pa) and e the partial pressure of water vapor in Pascal. The spatial variability of these parameters is related to different factors such like the weather conditions but also the topography since the troposphere tend to be less dense increasing the altitude. As mentioned before, SAR interferometry provides maps of this variation at a resolution not available for other specific instruments, therefore a full compensation through external data is not possible. Moreover, its independence from the wavelength does not allow techniques such like the Split-Spectrum for the ionosphere. Therefore its mitigation is possible only using low-res meteorological model or through tailored spatio-temporal filters. The latter is general not well suited if the objective is the large scale motion measurements since they could remove part of the deformation signal, the first will be discussed in more details in Chapter 4.

2.2.2.3 *Topography related distortions*

The tropospheric distortion stems from the delay accumulated by the radar pulse in traveling through the troposphere. This implies a dependency on the acquisition geometry. Let us assume a simple model where the troposphere is a constant layer enveloping the first few kilometers from the earth surface and no further variation related to physical parameters variation is present. Given that it is easy to notice that the LoS variation along the swath can already generate path variations and consequently differential delay variations referring to Equation 2.10. The eventual presence of topography triggers further changes in the traveled path further distorting the differential delay pattern. Therefore even in this oversimplified scenario a complex differential phase pattern is present. Such pattern is not necessarily to be considered low-pass but it is strongly correlated with topography profile and the acquisition geometry. The mitigation of this delay component can exploit this correlation. In application scenario a data-driven approach, that estimates this component through a phase-height correlation, has provided good performance nonetheless, as previously mentioned, if the target is the observation of large scale tectonic signals as well as volcanic deformation such an approach could lead to biased estimations and consequent misdetection between motion and tropospheric delay. Therefore it should be limited to the measurement of local deformation: for large scale motion detection the use of external models is preferable (15).

Another important feature of of topography related tropospheric distortions is its behavior in time. Troposphere physical parameters are subject to seasonal variations along the year. Since the spatial

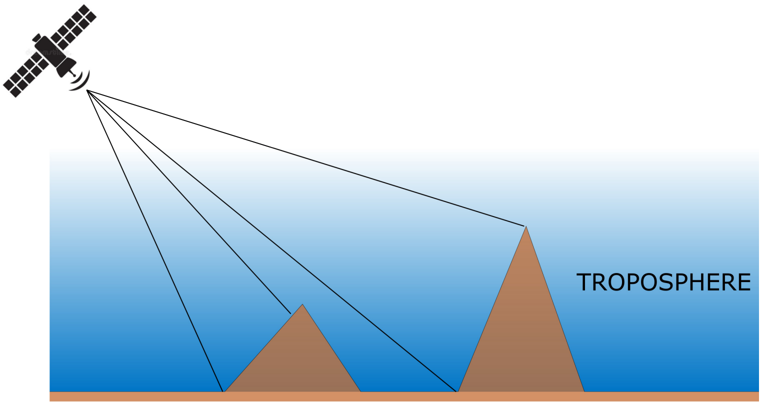

Figure 2.4: Schematic showing the dependence with topography and acquisition geometry

variation pattern of the phase is mainly geometry driven, it is easy to imagine that the generated phase patterns could appear pretty similar in shape although variable in intensity due to such seasonality. From a multi-interferogram perspective this could generate seasonal biases correlated with the geometry such like ramps as well as more high pass topography related patterns. The pre-compensation of the delay using models could help at least to detangle this temporal correlation allowing to keep the hypothesis of temporal whiteness of the tropospheric delay.

2.2.2.4 Turbulence related distortions

The model used for explanation reasons in Section 2.2.2.3 is handy to use but in some way over-simplified. In fact it is well known that troposphere can have local variation due to clouds or variable temperature/pressure. Therefore we have also to consider such variations if we want to list an error budget for the interferometric phase. The spatial scale of such variation can vary a lot being also completely overlapped to the deformation signal to be observed. The use of external models, in these cases, can help only up to the resolution of the meteorological data typically in the range of the tens of kilometers as it will be discussed in more details in Chapter 4.

Having available a set of interferograms it is possible to exploit the statistical properties in space and time domain of deformation and tropospheric signal. The first presents a correlation in both domains nonetheless the latter is completely uncorrelated in time. Therefore it possible to design spatio-temporal filters capable to provide some separation between the two components. However this capability is limited in accuracy since it introduces a temporal correlated error that can bias the estimation of secular trends especially at large scales where the power of the tropospheric noise is higher. Hence, when possible, an apriori mitigation of the noise using weather model is preferable for such cases.

2.2.3 Solid Earth Tides

The deformation of the Earth surface related to the interaction with the gravitational forces of both the Sun and the Moon is known as Solid Earth Tides (SET). Such deformation can reach reach more than 40 cm. This is a quite remarkable number if compared to the radar wavelength nonetheless, it has to be taken in account that SET related deformation patterns develop on scale of hundreds of kilometers. The dimension of spaceborne radar swaths and the relative nature of interferometry reduces its impact on the measurements since only its projection on the variable LoS is visible. This effects in case of big swaths can anyway reach the centimeter level and necessitates a compensation in order not to be mixed with tectonic movements. However geodesists are able to precisely model the SET displacements, therefore a model-based correction of the interferometric phase is possible in order to meet the accuracy requirements (95), (15), (44) and (106).

2.2.4 Orbit accuracy

The precise knowledge of the platform position during the acquisition is of key importance in SAR interferometry. This information is in fact used to geometrically simulate a synthetic phase used to compensate flat earth and topography in SAR interferograms. Therefore errors in the state vectors knowledge leads to an inaccurate flattening of the interferograms and consequently to the generation of residual spurious ramps in the observed interferometric phase. Such ramps are of course particularly dangerous in measuring large-scale deformation patterns reducing the accuracy of the measurements.

Given the errors in horizontal and vertical direction in the plane perpendicular to the flight direction ϵ_H and ϵ_V, the measured spurious ramp between near and far range will be:

$$\phi_{ramp} = \frac{4\pi}{\lambda}\left(\epsilon_H(sin\theta_{far} - sin\theta_{near}) - \epsilon_V(cos\theta_{far} - cos\theta_{near})\right) \tag{2.11}$$

in the past generation of SAR missions (ERS, Radarsat-1 ,JERS) such error source was pretty important and it could be a showstopper for the measurement of the the large-scale deformation. Nowadays missions like Sentinel-1 are characterized by a very precise state vector knowledge (83) therefore the related phase errors can be considered negligible in comparison with other sources like troposphere or ionosphere.

2.2.5 Clock drift

The accurate measurements of large scale phase patterns indeed depends on the stability of the on-board clock. Small fluctuations of the central frequency of the oscillator between reference and secondary acquisitions may in fact drive to residual phase ramps in range direction. Such fluctuations can be random in time leading to a degradation in the phase accuracy. Nonetheless when the clock central frequency is characterized by a drift in time the consequences for the performance, especially of time series, can be pretty serious (70).In general we can write that the clock-related phase error is:

$$\phi_{ramp} = \frac{4\pi}{c}\delta f \Delta R \tag{2.12}$$

where δf is the frequency difference between the two SAR acquisitions and ΔR is the range difference between two points. Also in this case the new generation of SAR missions are equipped with hardware able to avoid this to be the performance bottleneck (65).

2.2.6 Soil and vegetation effects

It has been observed that when InSAR bases its measurements on distributed targets a further and considerable noise source can occur (5). Distributed targets are not characterized by man-made features like PSs but they are obtained by averaging a conjunct of radar resolution cells each of them containing more than one phase center. This operation can lead to phase inconsistencies (22) (109) (23) due to presence of different phase centers evolving independently. The mixing of the different mechanisms results in biased time series. In (5) is shown how the possibility to rely on long-term stable areas mitigates this effects since the phase estimation, "‘guided"’ by the stable targets is able to dump the other seasonal effects like soil moisture or vegetation growth that trigger the drift. The effect on the final velocity estimation for the time series can be of several mm/y in C band or bigger if we increase the wavelength. Such orders of magnitude can not be considered negligible in the final error-budget. Therefore nowadays the scholars are particularly pushed to find solutions in this direction. At the moment there is no well defined solution, being carefully in phase estimation is for sure a good norm, however in many cases this is not enough and unwanted biased spots shall be masked. Model based de-biasing using physical models are still in study (21).

2.3 State of the art of spaceborne InSAR for deformation measurements

As discussed in the previous sections spaceborne SAR interferometry is a powerful instrument to measure earth surface deformation. Several scientific and commercial applications benefit of such measurements. Nonetheless the accuracy performance can be an issue in some cases. Therefore a deep knowledge of the measurements performance is needed in order to fully exploit the capabilities of the technique. In the Section 2.2 a brief introduction to the limiting factors have been given observing that not all of them can be easily overcome. Therefore in the last 30 years a lot of research work has been carried out in order to find technical solutions to improving the applicability of the technique. The main problems can be coarsely resumed in three bullets:

- limited temporal coherence of the radar targets
- 2D and 3D phase unwrapping
- atmosphere or other low pass effects

The first two points were tackled since the beginning, the latter became more evident as soon as the accuracy requirements were pushed to the millimeter level. Nowadays having missions with wide swath capabilities, the issue is even more important, since clocks accuracy and orbit knowledge has been improved to a point that cannot be considered limiting factors anymore.

The limitations derived from the vanishing correlation of the radar targets were studied since the early nineties in particular in (108) temporal and geometrical decorrelation were studied and quantified providing physical models. In (38) a filter to mitigate geometric decorrelation was proposed reducing the amount of non-interfering bandwidth. Deformation measurements require to be able to retrieve valuable interferometric information for long time spans, in order to form phase time series. Therefore the temporal decorrelation in particular plays a major limiting role. A the end of the nineties a first solution was proposed to overcome this problem (35). The PSInSAR technique limits the interferometric analysis on stable targets that are able to guarantee phase stability on long time spans. The identification of such targets is not trivial and involves several steps that exploits all the SLC information including backscatter amplitude in order to progressively identify the targets that can be safely unwrapped. The main idea of this approach is that once a stable target is identified its capability to interfere is guaranteed in all the interferometric pairs in the time series. Such targets are often man-made features (roofs,buildings corners,...) (82) that provides an ideal backscatter mechanism also allowing to use the information in a single look fashion. However these man-made features are limited to urban areas and very difficult to find in vegetated areas. Therefore the so called Small Baseline (SBAS) approach was introduced (9). Complementary to the PSInSAR approach, SBAS focus the attention on decorrelating targets generating all the possible coherent interferogram combinations and estimating the interferometric phase integrating through the generated interferograms network. The idea is to be able to "'follow"' the vanishing coherence until is present hence providing a stacking approach that is no longer based on a single reference image like in PSInSAR but on several coherent interferometric pairs. This includes a spatial multilooking that reduces the resolution but allows to cover areas where no man-made features are present. After these achievements the InSAR community started to move towards a more systematic and operational use of the InSAR measurements, therefore several others processing approaches were developed on this line (75),(101), (1), (52). The need of unification between persistent targets interferometry and decorrelating targets interferometry found its theoretical basis in studies that tried to exploit the information of all the the possible combinations of images of a given stack (47) (20) (48) (33) (79). This more comprehensive approach to InSAR phase estimation become quickly the state of the art of the processing chains (33) (2) (81). The new generation of SAR satellite constellations are able to provide fast revisit time and very long time series due to the mission continuity. This technological breakthrough posed new issues in the InSAR phase estimation in particular regarding the possibility of generating huge time series (4) and their accuracy (5). The handling of the moisture/vegetation (22) (109) (23) phase biases is at the moment not completely solved and represents the cutting edge of the research in this field.

The second bullet is about the phase unwrapping. The difficulty in solving this problem is already well known from other fields (39). Nonetheless the problem is of crucial importance for the exploitation of the InSAR data since it allows to solve the ambiguities of the phase in order to properly integrate phase gradients and reconstruct the unwrapped phase w.r.t. a reference point and image. Therefore a lot of literature was produced on the topic since the beginning of the development of InSAR technology (41). During the nineties the focus was on the 2D phase unwrapping since the main driver was the generation of DEMs using a single interferometric pair. Many different approaches were developed following also the experience in other fields like MRI. In specific, InSAR has particular requirements in order to cope with its particular data characteristics, such like space varying SNR or variable ground resolution. Some techniques were specifically developed for InSAR data like the Minimum Cost Flow (MCF) (18) or SNAPHU (14) and they are still some of the most used approaches. The increasing importance of the interferometric time series pushed the research to find solutions that consider also the information from different inteferograms in order to unwrap them jointly rather than separately (34). For deformation time series the solution of the problem in 3D is necessary in order to provide meaningful measurements. A formalization of the problem in three dimension was provided in (53). Phase unwrapping, due to its high non-linearity, remains open in general hence forcing the researchers to find tailored solutions depending on the problem.

New missions like Sentinel-1 are able to provide very large swaths (250 km). Future SAR missions are aimed to further enlarge the radar swaths (92)(76). The measurement of large-scale deformation is the DInSAR application that takes much advantage from this new generations of sensors since they are able to capture tectonic deformation on regional scale. Nevertheless, since the magnitude of the relative error increases with distance (91)(45)(50), the performance of relative deformation measurements between very distant points may not achieve the required accuracy (104). It is well known that interferometry works well for applications such as infrastructure monitoring or urban subsidence since they involve relatively short scales (0.1–20 km). The removal of the lowpass spatial frequencies of the estimated deformation signal by filtering or detrending, often applied in these cases, is for the measurements of the large scale deformation patterns not applicable. However, the rising scientific interest in using InSAR to measure this kind of deformation (54) pushes in the direction of the preservation of all the spatial wavelengths of the deformation and a proper treatment and knowledge of the error bars at such distances.

Since the firsts spaceborne radar experiments, atmosphere has been recognized as one of the main error sources (91). The main problem stems from its spatial characteristic that prevents complete separation from the deformation signal. Temporal filtering, even if it improves the time series quality is also not a general solution since the temporal high-pass signal derived from earthquakes or slow-slip events could be lost. Therefore, the use of external information to reconstruct and compensate the unwanted delay in the interferograms (24) has been taken in consideration. Considering the available information it was clear that it was not possible to have corrections at the same metric resolution of the InSAR data, nonetheless it has been shown that even kilometer resolutions are already able to strongly mitigate the noise. At the beginning GNSS stations or other remote sensing instruments such as MODIS or MERIS were typically used (68)(72)(67). The correction of tropospheric stratification was successful using both model-based and data-driven approaches (26)(66)(15). Then, in the past decade, the use of Numerical Weather Prediction (NWP) became a valuable tool for systematic correction of both SAR group and phase delays, hence improving the performance and capabilities of the techniques (56)(28)(55)(16)(8).

The ionosphere can also generate huge errors at low frequency (L-band, P-band) SAR (71). In C-band its effect is less severe even though exceptions have been reported (43). In such cases, compensation using the split spectrum technique can reduce the error to the level of the troposphere so that it is no longer the limiting factor (42). The effect of Solid Earth Tides (SETs) involves scales much larger than the SAR swath, however, their projection onto the SAR Line of Sight (LoS) along the swath can generate centimeter-level phase ramps. Therefore, SETs can be compensated using the IERS 2010 convention (27)(44). Finally, SAR missions are characterized by very stable oscillators (65) and very good orbit knowledge (107)(83). Hence it is possible to conclude that as long as the tropospheric correction accuracy will remain in the order of centimeters the troposphere will be the limiting factor for the measurement of the large scale deformation patterns. Therefore the knowledge of its impact as well as the capability to mitigate it is of primary importance for these applications.

3 Modeling local deformation using the wrapped interferometric phase

This chapter aims to discuss a general framework that allows the direct interpretation of the wrapped DInSAR phase in terms of surface strain S and rotation R components. The methodology should allow to address applications that shows very concentrated patterns of interferometric fringes and therefore very likely to be prone to spatial unwrapping errors.

The idea is to allow a geophysical interpretation of the interferometric fringe patterns in order to support geoscientists in modeling particular deformation phenomena.

This chapter summarizes the journal papers in Appendixes A and B : *A. Parizzi and W. Abdel Jaber, "Estimating Strain and Rotation From Wrapped SAR Interferograms," in IEEE Geoscience and Remote Sensing Letters, vol. 15, no. 9, pp. 1367-1371, Sept. 2018, A. Parizzi, "Inversion of the Slip Distribution of an Earthquake From InSAR Phase Gradients: Examples Using Izmit Case Study," in IEEE Geoscience and Remote Sensing Letters, vol. 16, no. 11, pp. 1726-1730, Nov. 2019* and the Conference paper in Appendix E *A. Parizzi, "Potential of an Automatic Grounding Zone Characterization Using Wrapped InSAR Phase," IGARSS 2020 - 2020 IEEE International Geoscience and Remote Sensing Symposium, 2020, pp. 802-805*

3.1 Phase gradients interpretation in terms of strain and rotation

Interferometric measurements can be directly related to the spatial gradients of the motion (30) (94) (97) (37). In this Chapter this property is exploited for the reconstruction of strain and rotation tensor as well as its interpretation into physically relevant observables, in order to tackle some particular DInSAR applications.

Considering a SAR interferogram, where all the topographic components have been compensated and neglecting the atmospheric delay, the expression of the absolute interferometric phase will be:

$$\phi = \frac{4\pi}{\lambda}\boldsymbol{\delta} \cdot \boldsymbol{s} \tag{3.1}$$

where λ is the wavelength. Being (e, n, v) the reference system oriented in accordance with the local east, the local north and the geodetic vertical, the change in radar range can be written as the projection of the displacement vector $\boldsymbol{\delta} = [\delta_e, \delta_n, \delta_v]$ on the sensing direction of the radar $\boldsymbol{s}$. Deriving with respect to the two horizontal dimensions, the displacement gradients observed in the sensing direction of the radar can be written as:

$$\vec{\nabla}(\boldsymbol{\delta} \cdot \boldsymbol{s}) = \boldsymbol{\Psi}^T \cdot \mathbf{s} = \frac{\lambda}{4\pi}\vec{\nabla}\phi \tag{3.2}$$

Equation (3.2) is a vector providing the derivatives of $\boldsymbol{\delta} \cdot \boldsymbol{s}$ w.r.t. the north and the east directions. $\boldsymbol{\Psi}$ is defined as the gradient tensor [1] and represents the derivatives of $\boldsymbol{\delta}$.

$$\boldsymbol{\Psi} = \left[\begin{array}{cc|c} u_{ee} & u_{en} & u_{ev} \\ u_{ne} & u_{nn} & u_{nv} \\ u_{ve} & u_{vn} & u_{vv} \end{array} \right] \tag{3.3}$$

Since a single SAR interferometric pair is not able to provide resolution/sampling in the third dimension (7), it is not possible to perform derivative measurements along the v axis. Therefore the third column of the gradient tensor can not be observed. Now in order to retrieve the six observable components of $\boldsymbol{\Psi}$ at least three diverse interferometric measurements are needed. The inversion results then to be completely analogous to the inversion of the 3D displacement vector (105) (46) and (6) from a geometric point of view. Therefore all the considerations regarding the performance with diverse acquisition geometries are valid also for the inversion of Equation (3.2).

$\boldsymbol{\Psi}$ represents the first order Taylor approximation of the displacement field and it contains the information about all the relative movements of the portion of surface which it represents. The gradient tensor can be then decomposed in its symmetrical and anti-symmetrical parts. Those are respectively the strain $\boldsymbol{S}$ and rotation $\boldsymbol{R}$ components (25).

$$\begin{aligned} \boldsymbol{S} &= \frac{1}{2}(\boldsymbol{\Psi} + \boldsymbol{\Psi}^T) = \left[\begin{array}{cc|c} u_{ee} & \frac{u_{en}+u_{ne}}{2} & \frac{u_{ve}}{2} \\ \frac{u_{ne}+u_{en}}{2} & u_{nn} & \frac{u_{vn}}{2} \\ \hline \frac{u_{ve}}{2} & \frac{u_{vn}}{2} & 0 \end{array} \right] \\ \boldsymbol{R} &= \frac{1}{2}(\boldsymbol{\Psi} - \boldsymbol{\Psi}^T) = \left[\begin{array}{cc|c} 0 & \frac{u_{en}-u_{ne}}{2} & -\frac{u_{ve}}{2} \\ \frac{u_{ne}-u_{en}}{2} & 0 & -\frac{u_{vn}}{2} \\ \hline \frac{u_{ve}}{2} & \frac{u_{vn}}{2} & 0 \end{array} \right] \end{aligned} \tag{3.4}$$

Since the derivatives w.r.t. the v direction (u_{ev}, u_{nv}, u_{vv}) are missing (see Equation (3.3)), only the 2×2 upper part of $\boldsymbol{S}$ and $\boldsymbol{R}$ tensors can be properly characterized. Consequently the third line and the third column of $\boldsymbol{S}$ and $\boldsymbol{R}$ end up being the same. This in practice means that even if the sensor is sensitive to the gradients of the vertical motion, it is not possible to distinguish weather it is generated by a rotation or a deformation. In other words to resolve between a vertical tilt (rotation) and a vertical extension/compression (strain). It is worth mentioning that according to the theory (25) some assumptions could be made allowing the observation of more components of $\boldsymbol{\Psi}$ or reducing the set of equations needed and also improving the estimation accuracy. For instance, in the specific case of ice flows, assuming ice to be incompressible allows us to impose the first invariant of the strain tensor $I_S \equiv Tr(\boldsymbol{S}) \equiv 0$ deriving consequently also u_{vv} (Michel and Rignot) and (25). In other cases it is possible to set $S \equiv 0$, then the problem reduces to a rotation only estimation (69).

3.1.1 Phase Gradients estimation

It is now necessary to discuss how the gradient measurements $\vec{\nabla}\phi$ can be estimated from the complex interferograms. The interferogram is a complex number $z(r,a) = A(r,a)\exp\left(j\phi(r,a)\right)$ where A is the product of master and slave reflectivity, (r,a) are the range and azimuth coordinates in radar geometry and ϕ is the interferometric phase as in Equation (3.1). Since in the application discussed here, the interferometric phase varies by several wavelengths within the scale of the deformation pattern, it is possible to perform a local linear approximation of the deformation phase. Hence at a given point (r_0, a_0) the phase of the interferogram z can be substituted by its first order Taylor approximation:

---

[1] For the sake of simplicity, the notation $u_{ij} = \partial \delta_i / \partial j$ will be used to identify the derivatives from now on.

$$z \approx Aexp\Big(j\frac{4\pi}{\lambda}\Big(\frac{\partial \delta_s}{\partial r}(r-r_0)+\frac{\partial \delta_s}{\partial a}(a-a_0)\Big)+\phi_0\Big) \tag{3.5}$$

where $\delta_s = \boldsymbol{\delta} \cdot \boldsymbol{s}$ is the projection of the displacement vector along the line of sight. Equation (3.5) shows how the problem is basically the estimation of the main local fringe frequency of the interferogram. The problem can be solved in different ways with varying performance. Typically the periodogram estimator is used (60), however this estimator assumes flat spectrum which is not the case for the interferograms. Moreover in the case of very strong fringe patterns, such an estimator does not take into account the spectral shift effect (38), hence reducing the estimation performance. In such a case the ML approach proposed in (49) would be more suitable.

3.1.2 Variance and covariance of the gradient measurements

In order to fully exploit the gradients in parameters inversion a description of the measurements accuracy is also necessary. As a consequence of the problem statement in Equations 3.2 and 3.5, the gradients' accuracy is hence seen as a scaling of the accuracy of the local fringe frequency estimation. This in the case of SAR interferograms can be in general a difficult task. The movement-induced wavenumber shift (38) triggers a degradation of the accuracy reducing the common band between the two acquisitions. In this case a ML approach for the fringe frequency estimation is indicated (49). The general case expression of the accuracy can be computed only numerically. However if the fringe rate is not too high, as mentioned before, it is possible to approximate the interferogram as a complex sinusoid using the periodogam estimator. Then the performance can be computed in close form properly rescaling the expression in (60).

$$\sigma_\Delta^2 = \frac{6(1-\gamma)}{\gamma N(N^2-1)}\frac{\lambda^2}{16\pi^2\rho^2} \tag{3.6}$$

Where γ is the interferometric coherence N the number of samples in the derivative direction and ρ the resolution in the derivative direction.

Another important topic are the effects of additive delays α generated by the propagation of the signal trough the atmosphere. Such delays generate spatially correlated patterns in the interferometric phase strongly varying according to the season, the time of the day and the atmospheric conditions. However their behavior can be statistically described by a covariance function C_α^ϕ if we assume at least the local stationarity of the process (50). Supposing known the covariance function of the atmospheric related delays C_α^ϕ it is possible to derive the description of gradient errors. The variance can be calculated supposing to perform a linear regression of the phase subjected to a spatially correlated noise.

$$\sigma_\Delta^2 = \frac{\sum\sum_{i,j}\rho^2 ij C_\alpha^\phi(\rho\,|i-j|)}{(\sum_i \rho^2 i^2)^2} \tag{3.7}$$

The covariance function of delay gradient C_α^Δ w.r.t. a given direction l can be computed considering Fourier transform properties:

$$C_\alpha^\Delta = \frac{\partial^2 C_\alpha^\phi}{\partial l^2} \tag{3.8}$$

It is worth to notice that the high-pass effect of the derivative operator drops the spatial correlation forcing the covariance function to be almost impulsive in the direction where the derivative is applied. This means that an eventual isotropic behavior of $C_\alpha^\phi(r,a)$ (62) will not be preserved in $C_\alpha^\Delta(r,a)$.

3.2 Application: strain and rotation of a glacier flow

As first application of the proposed framework, the estimation of the surface strain and rotation of the Darwin Glacier has been investigated. Darwin Glacier ($79°53'S$ $159°00'E$) is an outlet glacier of the Transantarctic Mountains draining ice from the East Antarctic Ice Sheet into the Ross Ice Shelf.

SAR interferomgrams from different acquisition geometries have been formed and the phase gradients estimated. The results have been geocoded in order to be able to merge them on a common grid. A local transformation based on orbital information must hence be established between the geographic reference system used in the previous section and the radar coordinates. Let $\boldsymbol{T}$ be the rotation matrix representing such a transformation. $\widetilde{\vec{\nabla}\phi}$ and $\widetilde{C_d}$, the phase gradients and their covariance matrix calculated in radar geometry, can be recomputed in the local reference system as:

$$\begin{aligned} \vec{\nabla}\phi &= \boldsymbol{T}^T \widetilde{\vec{\nabla}\phi} \\ C_d &= \boldsymbol{T}^T \widetilde{C_d} \boldsymbol{T} \end{aligned} \tag{3.9}$$

In Equation (3.2) the direct problem that links the phase gradients measurements with the gradient tensor $\boldsymbol{\Psi}$ has been defined. Let us now suppose that in a general case we have N gradient measurements in N different geometries. $C_{d,k}$ is the covariance matrix relative to the k^{th} acquisition geometry, $\boldsymbol{\Psi}$ can be inverted in the Least Square sense by minimizing the figure of merit M w.r.t. each u_{ij}:

$$\begin{aligned} M = \sum_{k=0}^{N-1} \Big(\frac{\lambda_k}{4\pi} \vec{\nabla}\phi_k - \boldsymbol{\Psi}(u_{ij})^T \cdot \mathbf{s}_k \Big)^T C_{d,k}^{-1} \\ \Big(\frac{\lambda_k}{4\pi} \vec{\nabla}\phi_k - \boldsymbol{\Psi}(u_{ij})^T \cdot \mathbf{s}_k \Big) \end{aligned} \tag{3.10}$$

The strain $\boldsymbol{S}$ and rotation $\boldsymbol{R}$ components have been firstly estimated using all three available geometries. The same inversion has been subsequently performed with two geometries only assuming the ice is flowing parallel to the glacier surface. A comparison of the two approaches is then shown in Figure 3.1 (c).

3.2.1 Inversion using three acquisition geometries

The framework proposed in the previous sections can support glaciological studies aimed at measuring and resolving the strain and rotation components of an ice flow. As previously mentioned, three different acquisition geometries are needed in order to be able to retrieve the six elements of $\boldsymbol{\Psi}$. Currently SAR missions observe a given area on the Earth with ascending and descending geometries only. In cases where SAR footprints from different tracks overlap, a third and a fourth geometries may be available for the inversion. Nevertheless such a configuration has proved to be ill conditioned (6). Hence left looking or squinted acquisitions have to be used in order to achieve a sufficient inversion accuracy (105) (6). For this experiment three TerraSAR-X stripmap interferometric pairs have been acquired in ascending right-looking and descending right/left-looking. The temporal distribution of the acquisitions used is optimal since they have the minimal temporal baseline between the interferometric acquisitions, 11 days between the pairs and 1 day between the different geometries. Therefore the observed motion can be assumed to be the same.

The components of the gradient tensor $\boldsymbol{\Psi}$ have then been inverted w.r.t. the geographic directions N/S and E/W and the tensors $\boldsymbol{S}$ and $\boldsymbol{R}$ have been computed as shown in Equation (3.4). In order to have a more intuitive measurement unit the strain is displayed in $[cm/km]$. Results are shown in Figure 3.1 (a).

The results in Figure 3.1 shows the deformation/rotation effects that can be related to the lateral drag of the ice flowing downhill.

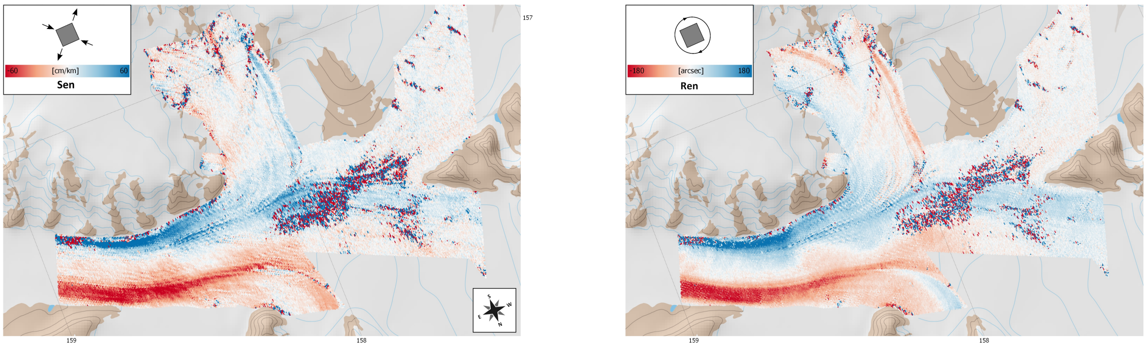

(a)

(b)

Figure 3.1: Separation of the estimated gradient tensor in strain and rotation components. (a) shear component ($\boldsymbol{S}_{1,2}$) estimated using three LoSs, (b) rotation component ($\boldsymbol{R}_{1,2}$) estimated using three LoSs.

3.2.2 Inversion using two acquisition geometries assuming surface parallel flow

Unfortunately no SAR mission currently performs observation campaigns in left or squinted geometry on a regular basis. It is hence worth discussing some assumptions that allow the removal of two of the six equations in (3.10). The idea is to exploit the information provided by an external DEM by assuming that ice flows parallel to the surface (58) (64). The topography profile is approximated with the plane tangent to the DEM and the displacement is imposed to lie on that plane. This can be done by fitting a plane to the DEM samples surrounding the area of interest. The plane can be fully characterized by its normal $\boldsymbol{n}_D$. It is then possible to set $\boldsymbol{\delta} \cdot \boldsymbol{n}_D = 0$ and differentiate w.r.t. e, n :

$$\vec{\nabla}(\boldsymbol{\delta} \cdot \boldsymbol{n}_D) = \boldsymbol{\Psi}^T \cdot \boldsymbol{n}_D = \boldsymbol{0} \tag{3.11}$$

Since the topography slope is assumed constant in the estimation window it is possible to extract two more equations to retrieve the six parameters. For the sake of completeness it has to be noted that now the equation system depends also on the quality of external data. This means that a covariance matrix $C_{d,DEM}$ has to be derived from the DEM error map to characterize the error of the two equations coming from (3.11). The ascending/descending right-looking TerraSAR-X have been used for this experiment. The TanDEM-X DEM used for the interferometric processing has also been used to determine the local perpendicular to the topography. A comparison of the 3 and 2 LoSs inversions is given in Figure 3.2 (a) (b) and (c). The results look spatially smooth except for an area that is decorrelated ,probably due to the lack of backscatter intensity. The results obtained with the two approaches agree very well as can be seen from the difference plot (Figure 3.1-c). Moreover this can be taken, at least for this specific case, as an evidence of the correctness of the surface parallel flow assumption also used in other studies (64).

3.3 Application: earthquake source modeling using wrapped InSAR phase

This problem of phase unwrapping errors has a particular negative impact in applications working with the geophysical modeling of a single interferometric pair. A possible solution, where a modeling of tectonic fault is carried out using directly the wrapped interferometric phase, has been proposed in (32) and (36). This avoid of course the phase unwrapping but it has the drawback of having non-gaussian distributed misfits (32). Therefore the inversion of the system implies the choice of

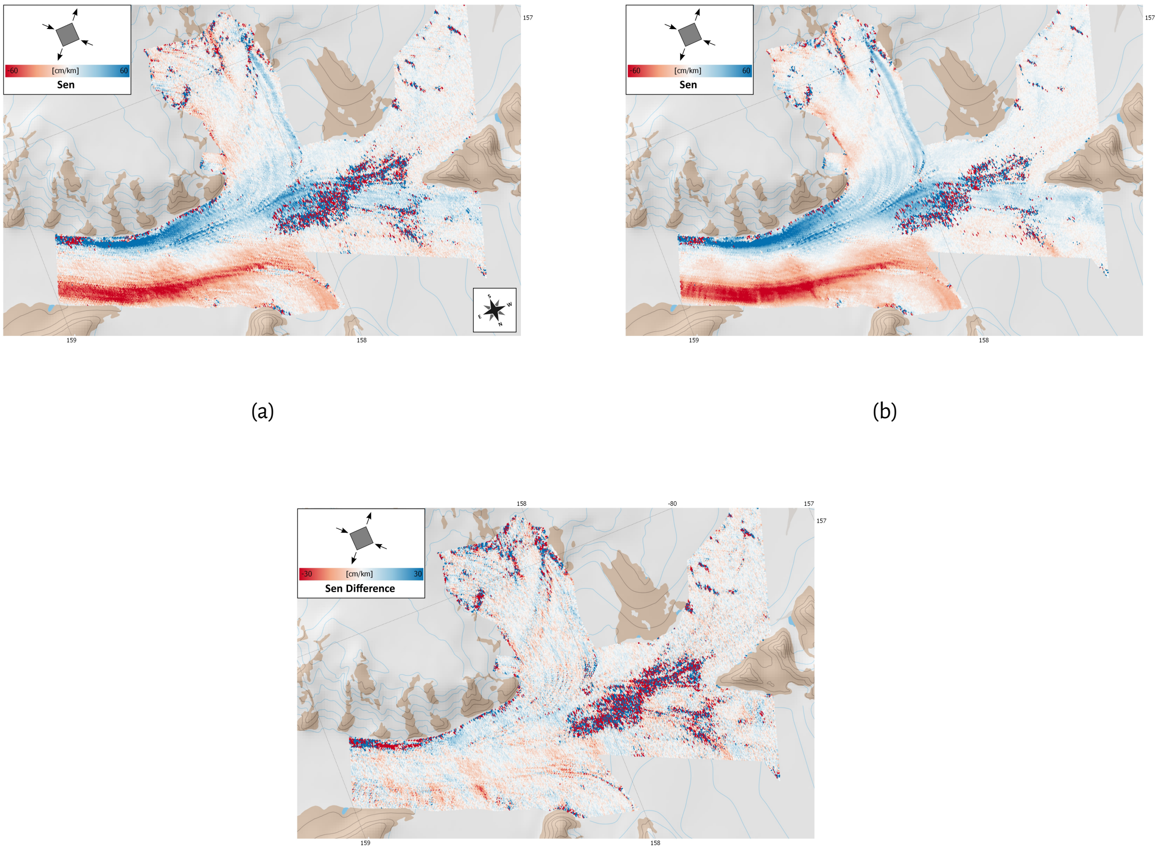

(a)

(b)

(c)

Figure 3.2: Shear estimation using 3 geometries and 2 geometries assuming surface parallel flow using TanDEM-X DEM. (a) shear component ($\boldsymbol{S}_{1,2}$) estimated using three LoSs, (b) shear component ($\boldsymbol{S}_{1,2}$) estimated using two LoSs and DEM. (c) difference between the two estimations.

the proper ambiguity band that fits the model making anyway the problem similar to a phase unwrapping. The idea of using phase gradients to interpret geophysical phenomena was hence often considered (94) (97). This should extend the spatial range of exploitation of the SAR interferograms since it permits to include also isolated spots of coherent phase. However, the interpretation of a phenomena using its derivatives has the drawback of filtering its high-pass component only (94) (3) . This results in a significant reduction of the SNR since small scales of natural phenomena contain in general less signal. Nonetheless in case of strong motions compared to the radar wavelength, the gradients SNR is acceptable and such information can be important especially in areas that can not be reached due to the unwrapping errors.

The model proposed by Okada in (78) describes the earth surface motion generated by a seismic event both in terms of displacement and displacement gradients (gradient tensor). Fixed the geometry of the fault the gradient tensor $\boldsymbol{\Psi}$ derived from Okada model can be linearized w.r.t. the vector of slips ξ occurring on the fault plane. Inverting an equation system it should be possible to estimate ξ from the estimated gradients. Knowing the local SAR geometry from the state vectors information, it is possible to locally rotate the tensor provided by the model into radar geometry using a proper rotation matrix $\boldsymbol{T}$.

$$\boldsymbol{\Theta}(\xi) = \boldsymbol{T}^T \boldsymbol{\Psi}(\xi) \boldsymbol{T} \tag{3.12}$$

In the measurements reference system it is possible to write a system of equation that equates model and measurements to be inverted retrieving the vector of parameters ξ minimizing the figure of merit M:

$$\begin{aligned} M = \sum_{k=0}^{N-1} \Big(\frac{\lambda_k}{4\pi} \vec{\nabla}\phi - \boldsymbol{\Theta}_k(\xi)^T \mathbf{s}_k \Big)^T C_{d,k}^{-1} \\ \Big(\frac{\lambda_k}{4\pi} \vec{\nabla}\phi - \boldsymbol{\Theta}_k(\xi)^T \mathbf{s}_k \Big) \end{aligned} \tag{3.13}$$

The equation system is written in general for N measurement's geometries and $\boldsymbol{C}_{d,k}$ is the covariance matrix of the gradients of the k^{th} geometry.

3.3.1 Izmit test case

The Mw 7.6 Izmit earthquake occurred on the 17th August 1999 and it was the product of the right lateral strike-slip movement of a part the North Anatolian fault (12). Because of the E/W orientation of the fault the co-seismic displacement was very well captured by ERS 1-2 SAR interferogram that shows a dense pattern of azimuth oriented interferometric fringes. The high fringe density and the temporal decorrelation (35 days interferograms) make the phase unwrapping procedure particularly prone to errors. Therefore this case study fits very well for the investigation of a phase unwrapping-free approach. Although previous works showed the complexity of the fault (103) (12), a simplified source geometry (single fault segment) has been used as in (36). As a reference result for the inverted slip and its residual phase the reader can refer to the study in (12).

The modeled fault has been divided in patches of 5×4 km along the strike and dip direction respectively. The inversion imposes also a laplacian as regularization ($\nabla^2 \xi = \mathbf{0}$) to control the smoothness of the estimated slips on the fault plane (57). In order to better discuss the feature of the gradient based inversion of the slip distribution the same inversion has been carried out also using the unwrapped phase.

3.3.1.1 Gradient Solution

The computation of the interferometric phase gradients has been performed starting from the SLCs In order to preserve the information no multi-looking was applied in forming the interferogram. The LoS projected component of the gradient tensor has been carried out estimating the local fringe frequency using a periodogram. The estimation window used was about 5 × 5 km sampled at a finer grid. The estimated range and azimuth fringe frequencies are scaled to range and azimuth LoS deformation gradients as in Equation(3.5). The direct problem is calculated using Okada model and locally rotating the derived tensor $\boldsymbol{\Psi}(\boldsymbol{\xi})$ into radar geometry, as described in Section 3.3. The inversion has been performed in Least Square sense forcing the vector $\boldsymbol{\xi} \geq \mathbf{0}$.

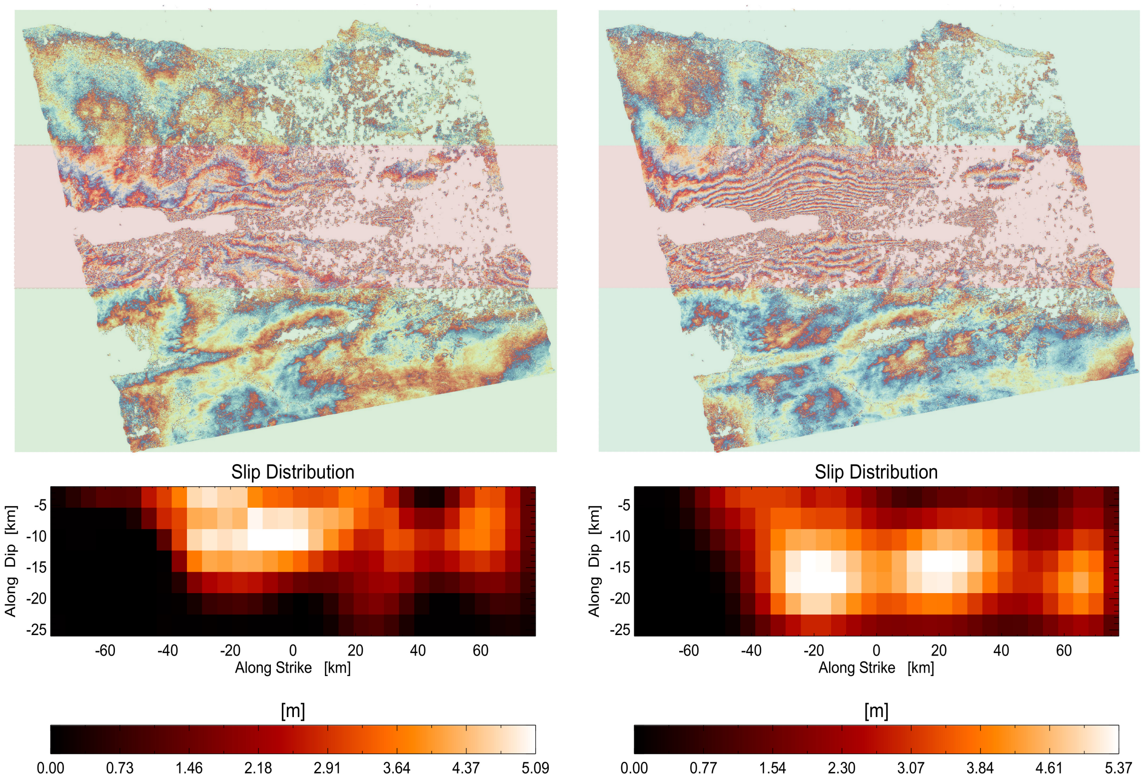

(a) (b)

Figure 3.3: Results comparison. In (a) wrapped residual interferogram and slip distribution over the fault plane for the gradient solution. In (b) wrapped residual interferogram and slip distribution over the fault plane for the unwrapped phase solution. The re-shaded area is aimed to highlight the area closer to the fault where the unwrapping errors are more likely to occur.

3.3.1.2 Unwrapped Phase Solution

In order to compare the previously derived results the inversion has been also carried out using the unwrapped interferometric phase. A coherence mask having threshold 0.18 has been over imposed in order to keep the phase error in a reasonable range. The extracted points have been unwrapped using a sparse grid Minimum Cost Flow (MCF) (18). Due to the fact that the whole scene is crossed by the tectonic fault, critical unwrapping errors have been avoided unwrapping the scene in two separate "tiles": one covering the area north to the fault the other covering the south area. Two reference points have set close to the north-west corner of the interferogram and the south-west corner respectively. In this case the direct problem is designed describing the projection of the displacement generated by the Okada model in LoS calibrated to the displacement generated by the Okada model in LoS in the reference point. The absolute phases of the two tiles have been jointly inverted obtaining a parameter vector ξ_ϕ comparable to the one obtained using the gradients (ξ_Δ).

3.3.1.3 Discussion of the results

In order to fairly compare the results obtained the residuals displayed in wrapped interferometric phase have been used. The modeled phase corresponding to the inverted results has been computed, wrapped and used to compensate the original interferogram. In this way it is possible to visually evaluate the capability of the inverted models to explain the interferometric measurement. Unwrapped phase provides a higher sensitivity to deformation, as expected from the theory. This is visible far away from the fault (highlighted in green in Figure 3.3) where the interferometric phase is better compensated by the model derived from unwrapped phase. However, close to the fault (highlighted in red in Figure 3.3), the solution obtained using gradients is considerably better. Here the deformation pattern generates strong phase gradients that compromise the success of the phase unwrapping. However, the gradients measurements are able to provide an ambiguity-free information that can be more easily inverted in a least square sense despite their noisy nature.

Both inversions have been almost identically regularized so that the two inverted slip distribution ξ_{ϕ} and $\xi_{\triangle}$present the same spatial smoothness (57). The two slip distributions ξ_{ϕ} $\xi_{\triangle}$ present a similar spatial pattern although shifted on the fault plane along the dip direction. This can be interpreted considering the relation between the depth of the slip and the scale of the corresponding surface deformation (the deeper is the motion the more low-pass is the surface deformation) (96). Therefore since the gradients measurements are limited in observing the high-pass part of the motion the maximum observable depth results also to be limited accordingly.

3.4 Application: grounding line position retrieval using wrapped InSAR phase

The characterization of the transition from floating to grounded ice is a very important information for glaciologists. Its behavior and evolution supports the understanding of the dynamic processes of the ice sheets. A systematic monitoring is therefore necessary to support scientists working in this field.

Since many years researchers deploy instrumentation to derive measurements to locating and understanding the temporal evolution of the ice-sea boundary(99) (98) . The use of Synthetic Aperture Radar Interferometry (90) has been proved since its beginning to be a powerful instrument to monitor of these areas (40). Its strong sensitivity to vertical displacements allows a clear identification of the transition highlighting the ice deformation due to the tidal cycle. In (86) and (87) the potential of interferometry for the study of grounding areas has been shown identifying their position and measuring their movements. Over many years the coverage and the systematic of the interferometric measurements has been increased reaching a global maps of the Grounding Lines (89) of Antarctica and Greenland.

However, the interferometric data, are typically used to identify the grounding area manually marking the position of the Grounding Line (GL) directly on the computed interferograms. In this Section an approach that shall be able to identify and measure the Grounding Zone (GZ) in a more automatic fashion is proposed, relying, as for the previous applications, on the wrapped interferometric phase as measure of the deformation gradient. InSAR data can be then used analogously to the tiltmeter measurement also avoiding to unwrap the phase. The study exploits the physical model proposed in (51) and used in (86) and (87) but using the phase gradients instead of the absolute phase. The gradient information is used both to identify and follow the geometry of the GZ and to estimate the model parameters, hence addressing two big issues of this application: the robustness of the unwrapping in presence of intense motion that could be rather difficult the identification of the coastline path that allows to identify where to perform the model fitting.

The methodology is first briefly described in Section 3.4.1, then two test cases using ERS Tandem pairs and Sentinel-1 A/B are examined.

3.4.1 Methodology

The model proposed in (51) describes the displacement due to the tide cycle of the floating ice w.r.t the grounded ice.

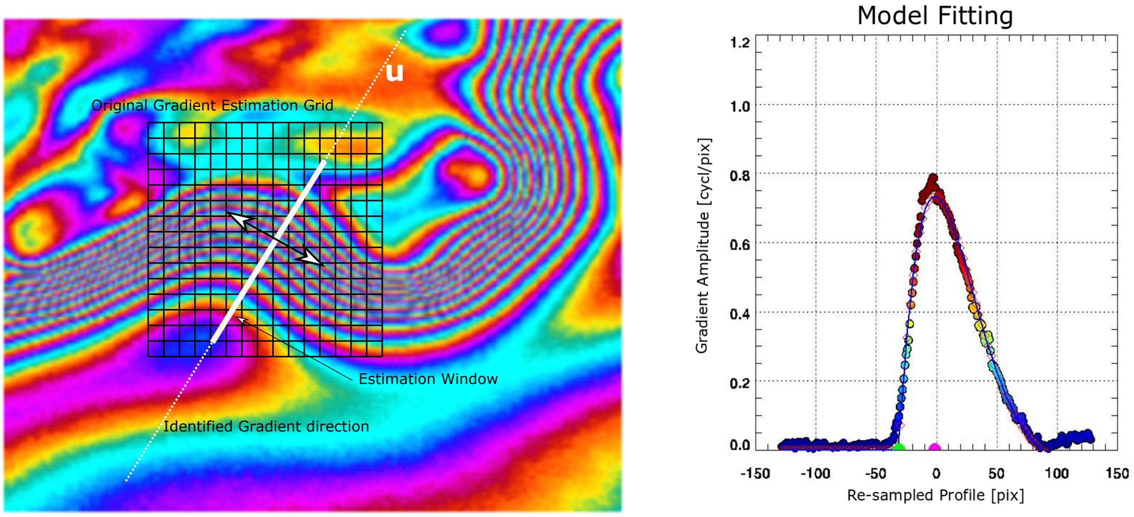

(a) (b)

Figure 3.4: Schematic of the proposed method. In (a) the identification of the maximum gradient is shown, in (b) an example of the model fitting.

$$\delta(u) = \frac{\Delta}{1+e^{-\pi}}(1-e^{-\beta(u-H)})(cos(\beta(u-H))+ \\ sin(\beta(u-H))) \quad \forall u \geq H \tag{3.14}$$

where Δ is the tide displacement[2], β is a shape factor describing the width of the bending area, H is the Hinge Line (HL) position along the axis u. The idea of the proposed algorithm is to be able to spatially follow the direction of the grounding zone on the wrapped SAR interferogram and characterize it fitting the physical model in Equation 3.14. As previously mentioned in Section 3.4 the approach is based on the spatial gradients of the interferometric phase $\vec{\nabla}\phi$ that are computed estimating the main fringe frequency window-wise on the complex SAR interferogram. Being (x, y) the range and azimuth coordinates in radar geometry, the interferogram is a complex number $z(x, y)$. Considering the interferometric phase varying by several wavelengths within the scale of the deformation pattern, it is possible to perform a local linear approximation of the deformation phase as shown in Equation 3.5.

The deformation gradient provides basically two information: the amplitude $\Gamma = \left\|\vec{\nabla}\delta_s(u)\right\|$ and the angle $\eta = \angle\vec{\nabla}\delta_s$. η, represents the direction of maximum slope and $\frac{\pi}{2} + \eta$ identifies the local direction of the GZ path. Given then the coordinates $\underline{p} = [x_0, y_0]$ of a point lying in the Grounding Zone it is possible to identify the positions of the direction u having $\eta(\underline{p})$. This is basically the line having slope $tan(\eta(\underline{p}))$ and passing through $\underline{p}$.

$$u_p \rightarrow \{x, y\} : \big(y - y_0\big) - tan\big(\eta(x_0, y_0)\big)\big(x - x_0\big) = 0 \tag{3.15}$$

The gradient data can be then re-sampled along the the direction u knowing $\eta(\underline{p})$ as shown in Figure 3.4 (a) and the gradient amplitude Γ can be fitted using the model Figure 3.4 (b). The model expression to fit Γ can be computed deriving Equation 3.14 w.r.t. direction u as in Equation 3.16. The inversion of the GZ parameters can be hence performed using Equation 3.16 and the estimated gradients bypassing the 2D phase unwrapping (18)

---

[2] For the sake of simplicity we can suppose to have it alreadz projected onto the radar LoS

$$\Gamma = \frac{\partial \delta_v(u)}{\partial u} = \frac{2\beta\Delta}{1+e^{-\pi}} sin(\beta(u-H))e^{-\beta(u-H)} \quad \forall u \geq H \tag{3.16}$$

Indeed the procedure move the unwrapping problem into a single dimension and implicitly solve the phase ambiguities along the rotated geometry with the support of a model. The inversion derives first the position of the Hinge Line (H in Equations 3.14 and 3.16) and β that provide a characterization of the GZ. β is a shape factor that describes the curve determining the width of the GZ. This is visible from the analytic expression of the distance W_{peak} between the HL and the maximum of the deformation gradient that identify the peak of the GZ see Figure 3.4 (b).

$$W_{peak} = \frac{\pi}{4\beta} \tag{3.17}$$

Based on the previous analysis the proposed approach starts computing the phase gradients maps from the complex interferogram. Then a small set of points,roughly lying inside the GZ, have to be selected as start. From each point the maximum gradient direction is computed and the input gradient data re-sampled onto such direction. Finally the model is fitted in the gradient amplitude data retrieving HL positions and shape factors of the GZ.

3.4.2 Results

Real data experiments have been carried out in order to assess in practice the capabilities of the proposed methodology. The technique has been tested first on 'single' interferograms relying on the ERS-Tandem data (1 day temporal baseline only) to removing the effects of the horizontal motion related to the ice flow. Using such data the results have been also quantitatively compared with results available from the MEaSURES data-sets deriving some statistics. In order to avoid a loss of generality, also the use of 'double-difference' interferograms (89) has been tested verifying the potential use of the technique with the Sentinel-1 A/B mission. The same test site has been selected for the Sentinel-1 and ERS-Tandem data. This allowed a comparison between results with more than 23 years difference, see Table 3.1.

Finally using more than two months of Sentinel-1 acquisitions the systematic generation of Grounding Zones measurements has been tested. A time series of the hinge line position has been computed using 4 independent double difference interferograms in Queen Maud Land test area.

3.4.2.1 Princess Raghild Coast test-site: inter-comparison with MEaSURES data set

A quantitative comparison of the derived measurements with existing products is necessary in order to verify the trustworthiness of the estimated positions. The selected area is part of the Princess Raghild Coast in Antarctica. The same ERS Tandem data used to generate the MEaSUREs product have been then processed. The HL positions have been calculated using the proposed approach. As already visible from the overview Figure 3.5 (a) the positions are very similar nonetheless the result has been compared with MEaSUREs computing the local distance of each extracted point from the reference product. The local distance between the two product has been calculated computing for each point of the distance from the slope that fits the three closest points of the other product. Proceeding in this way it was possible to collect a vector of local distances to be used to derive some statistics.

The histogram and the statistics of the differences are plotted in Figure 3.5 (b) and resumed in Table 3.2. The deviation of the position is about 115 m but drops to 82 m if robustly computed using MAD. Such numbers are compatible with accuracies measured in (89). A not negligible bias (> 150 m) is however detectable between the different position. Looking more in detail to Figure 3.5 (a) is visible that the proposed method positions are located systematically more in the inland. This could be related to a different definition of the position between the MEaSUREs product and the model used in this study (that identifies the HL).

Test Site	Mission	Acquisitions Date
A) Princess Raghild Coast		
	ERS	2 APR 1996
	ERS	3 APR 1996
B) Queen Maud Land		
	ERS	5 APR 1996
	ERS	6 APR 1996
	Sentinel-1	23 OCT 2019
	Sentinel-1	29 OCT 2019
	Sentinel-1	04 NOV 2019
	Sentinel-1	10 NOV 2019
	Sentinel-1	16 NOV 2019
	Sentinel-1	22 NOV 2019
	Sentinel-1	28 NOV 2019
	Sentinel-1	04 DEC 2019
	Sentinel-1	10 DEC 2019
	Sentinel-1	16 DEC 2019
	Sentinel-1	22 DEC 2019
	Sentinel-1	28 DEC 2019

Table 3.1: Test Data-Sets

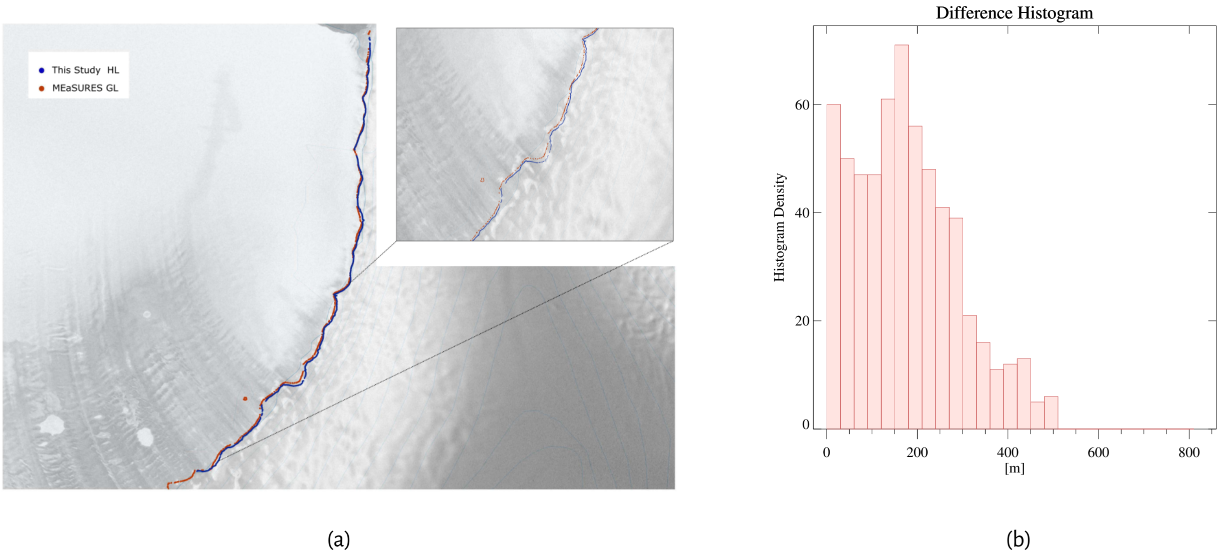

(a)

(b)

Figure 3.5: Result of the comparison on the second test site, extracted products (MEaSUREs in red , this study in blue) (a) and the histogram and the statistics of the local distances (b).

	Distance from MEaSURES [m]
Mean	177.7
Median	165.9
Std. Dev.	114.9
MAD	82.4
5 %	16.0
95 %	402.9

Table 3.2: Comparison with MEaSURES Statistics

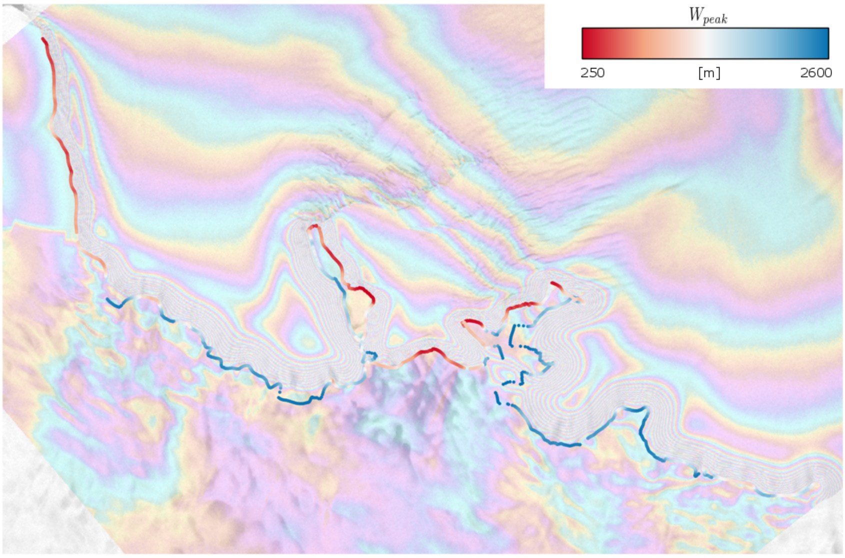

Figure 3.6: The overview of the whole processed area showing both the HL positions and the W_{peak} distance color-coded. The map is derived from the 5-6 April 1996 ERS-Tandem interferogram.

3.4.2.2 *Queen Maud Land test site: results using ERS-Tandem and Sentinel-1 A/B Double Differences time series*

The analysis of the second test site is interesting due to the complex geometry of the grounding zone that follows the coastline in narrow gulfs and peninsulas. The method has been first applied on a ERS Tandem pair acquired in April 1996. Figure 3.6 shows a the result of the estimation displaying the retrieved positions of the HL and the distance between HL and maximum gradient point color-coded. This information can compactly show a model-based characterization of the GZ since it displays position and dimension of the GZ.

However nowadays the Sentinel-1 mission is able to provide interferometric data on regular basis with a global coverage. This is therefore the most suitable sensor to address the problem of Grounding Zones monitoring using InSAR. The 6 days revisit time does not allow to neglect the ice motion in particular in proximity of glaciers. Therefore, the use of interferometric double differences has to be considered as the baseline approach to study the border between grounded and floating ice with InSAR (89). The double difference technique subtracts two interferograms of the same area with the aim of deleting the horizontal motion due to the glacier flow that is assumed to be stable in time. The approach can be extended to gradients having two interferograms w.r.t a master image temporally located in the middle of the three acquisitions. Given that it would be possible to delete

	Distance [m]	**1996-GZ Width [m]**	**2019-GZ Width [m]**
Mean	196.3	980.4	1048.3
Median	133.2	821.3	972.5

Table 3.3: 1996-2019 Comparison Statistics

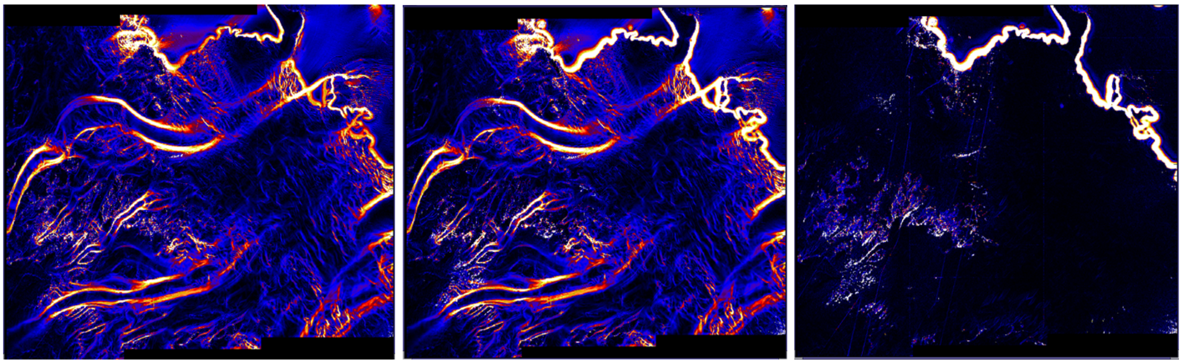
(a) (b) (c)

Figure 3.7: Gradient Amplitude maps for the Sentinel-1 data set (a) the first interferogram (b) the second interferogram (c) the double difference.

the constant horizontal motion component simply adding the gradients vector retrieved from the two interferograms.

$$\vec{\nabla}\phi_{dd} = \vec{\nabla}\phi_{-1} + \vec{\nabla}\phi_1 \tag{3.18}$$

where ϕ_{-1} and ϕ_1 represent the two interferograms. For the sake of clarity it is worth to specify that the model in Equation 3.16 could not properly describe the double difference data. The estimation can be performed assuming H and β to be the same between the two interferogram, and measuring in Δ the 'double difference' of the tides. This could be considered reasonable at least for β in Sentinel since the acquisitions are separated only by 6 days. In any case also more complex scenarios can be encompassed by Equation 3.16 simply modeling the double difference gradient as the sum of two different gradients, of course the number of estimated parameters increases and the over-fitting shall be avoided performing an appropriate model selection.

It is now interesting to compare the results from ERS and Sentinel missions since they have been acquired with more than 23 years time difference. For this comparison the acquisitions of 10-16 and 22 November 2019 has been considered. Using the same method as in Section 3.4.2.1 the distance between the two estimated HL has been computed and analyzed. The results show that he measured distances are rather small close to the sensitivity of the technique. However looking closer an average advance of the hinge line associated with an enlargement of the GZ, see Table 3.3.

Moreover the six-days coverage performed by Sentinel-1 mission over the Antarctica allowed to build up relatively easily an acquisitions time series over the selected test site. In total 12 acquisitions have been interferometrically processed allowing the computation of 4 independent double difference interferograms. The results show, as expected (88)(74), a wide spatial variability of the HL position due to the different tide conditions. Notwithstanding the position measured in 1996 by ERS data seems to be systematically located more inland showing a slow advancing of the ice sheet. Even thought this work is only aimed to the development of an efficient algorithm for grounding zone measurement it is worth to mention that these test measurement are in agreement with the re-

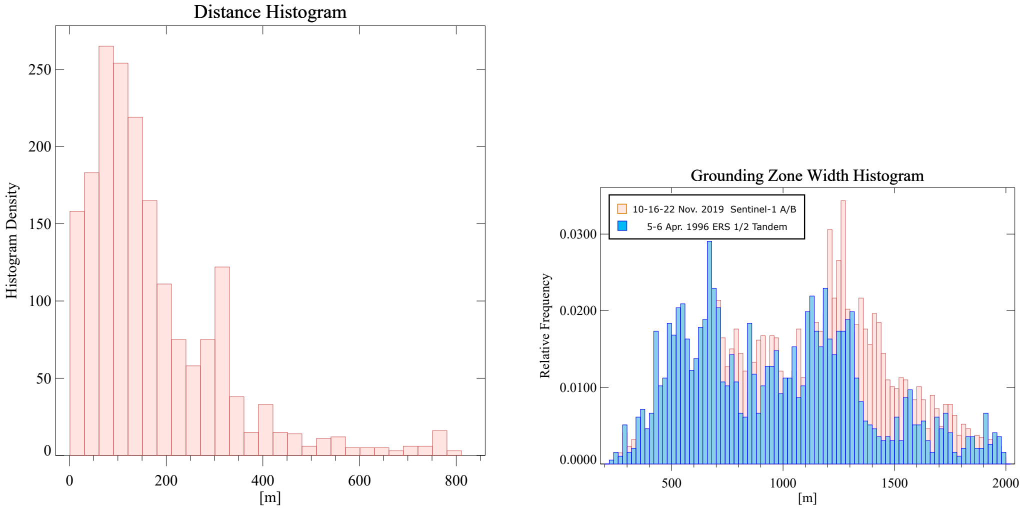

(a) (b)

Figure 3.8: Results of the ERS Tandem Sentinel-1 comparison. (a) Distance histogram (b) W_{peak} histogram.

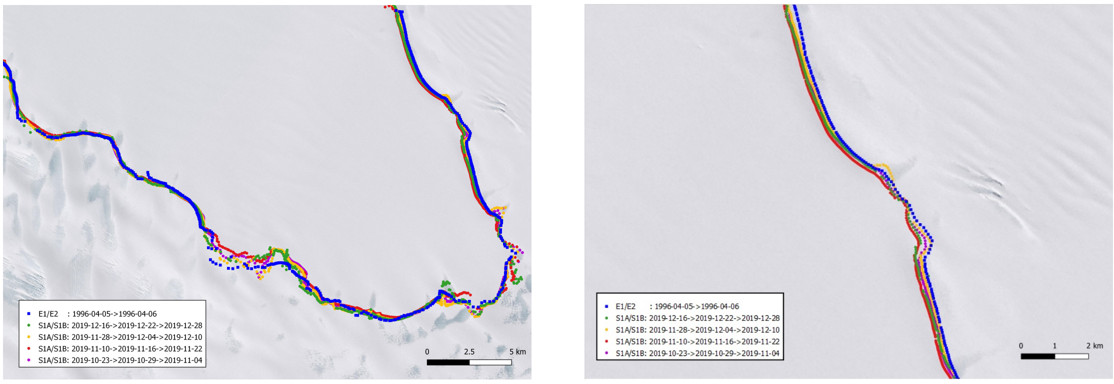

(a) (b)

Figure 3.9: Extracted Hinge Lines profiles time series. (a) Overview and (b) zoom.

sults published in (63) which reported an average advance of 6.3 m/yr for the area of Queen Maud Land.

3.5 Conclusions

In this chapter, an approach to interpret wrapped SAR interferograms has been discussed. A general rationale for modeling the wrapped InSAR phase has been provided, followed by three possible applications. Although the application to earthquake source modeling may have limited utility, it could be valuable for handling measurements particularly prone to unwrapping errors. This is especially relevant when dense and isolated fringe patterns are present, causing difficulties for unwrapping algorithms in spatially integrating the phase. Conversely, for the other two applications, direct interpretation of the wrapped phase is more advantageous than using the unwrapped phase. In the case of strain-rotation resolution, this is because these observables are inherently differential and do not require the integration operation performed by phase unwrapping. For grounding zone characterization, the proposed approach significantly reduces the complexity of phase unwrapping by reducing its dimensionality to 1D and using a supporting physical model for the operation.

4 Accuracy of the large-scale deformation measurements using InSAR

The atmosphere has always been recognized as one of the main error sources in interferometric measurements. The main problem stems from its spatial characteristic that prevents complete separation from the deformation signal by spatial filtering. Temporal filtering, even if it improves the time series quality is also not a general solution. This is due to nonlinear deformation, uncompensated seasonal effects and irregular sampling due to snow cover. The performance of the estimated deformation rates are still limited by the atmospheric delay.

Starting from this basis, this chapter first investigates the interferometric performance at large distances as well as the impact of the ECMWF ERA-5 NWP when used to correct the InSAR phase.

This chapter summarizes the journal paper in Appendix D : *Parizzi, A., Brcic R. and De Zan F. (2021). InSAR Performance for Large-Scale Deformation Measurement. IEEE Transactions on Geoscience and Remote Sensing, 59(10):8510-8520.*

4.1 InSAR phase tropospheric correction using external data

In order to preserve all the information contained in the interferometric phase, external data are necessary to reconstruct and compensate the unwanted delay in the interferograms (24). GNSS stations or other remote sensing instruments such as MODIS or MERIS are typically used despite the different resolutions (68)(72)(67). The correction of topography-related delays was successful using both model-based and data-driven approaches (26)(66)(15). In the past decade, the use of Numerical Weather Prediction (NWP) became a valuable tool for systematic correction of both SAR group and phase delays, hence improving the performance and capabilities of the techniques (56)(28)(55)(16)(8). The approach used exploits such information to compute the refraction indexes in the volume crossed by the radar pulses. It is worth to recall Equation 2.10 that models the refractive index N in dependence of meteorological parameters.

$$N = k_1 \frac{P_d}{T} + k_2 \frac{e}{T} + k_2 \frac{e}{T^2} \tag{4.1}$$

where $k_1 = 0.776KPa^{-1}$, $k_2 = 0.716KPa^{-1}$ and $k_3 = 3.75 \times 10^3 K^2 Pa^{-1}$ are constants derived from laboratory measurements, T is the absolute temperature in Kelvin (K), P_d is the partial pressure of dry air in Pascal (Pa) and e the partial pressure of water vapor in Pascal. Such physical quantities are provided by the NWP via simulation at a certain spatial and temporal resolution and can be used to compute the delay difference due to the change in the refraction index. In this study the ECMWF ERA-5 data are used. The data are sampled on a 31 km grid in space and distributed on 137 heights levels with a temporal sampling of 1 hour. The data are properly interpolated in the 4

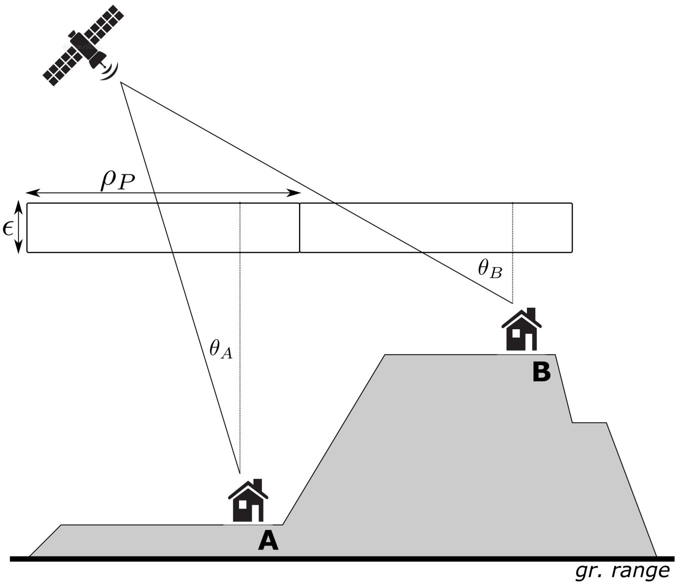

Figure 4.1: Representation of Equation 4.2. Where $\epsilon = z_t - \hat{z}_t$ is the NWP error in zenith direction and ρ_p is the posting of the NWP data

dimensions, the refractive index computed and the additional delay derived taking in account the acquisition geometry and the path of the radar pulse through the tropospheric layer. For more details the work of (15) is suggested, in this work the attention is focused on the study of the performance improvements in measuring large scale deformation signals.

4.2 A mathematical model for the errors in InSAR large scale measurements after tropospheric corrections

The use of NWP for mitigating the tropospheric signal in the interferometric phase is limited both in accuracy, due to the limitations of the model itself, and in resolution. The best sampling available is 9 km in the case of ECMWF products (31 km for the data used in this work), several orders of magnitude larger than the SAR resolution, even after interferometric multi-looking. The accuracy of NWP can be strongly site dependent since it depends on data availability and the fit of the model to actual tropospheric conditions. The quantity $\epsilon = z_t - \hat{z}_t$ can be defined as the error between the real zenith delay z_t and the modeled delay $\hat{z}_t$. This is assumed to be a Gaussian process in time and space with mean μ_ϵ, variance σ^2_ϵ and spatial correlation function Λ. The interferometric error between two points A and B for reference acquisition r and secondary acquisition s is

$$\phi_\epsilon = \left(\epsilon_{r,A} - \epsilon_{s,A}\right)\frac{e^{-\frac{h_A}{H}}}{\cos\theta_A} - \left(\epsilon_{r,B} - \epsilon_{s,B}\right)\frac{e^{-\frac{h_B}{H}}}{\cos\theta_B} \tag{4.2}$$

where θ is the local incidence angle. The effect of the altered path delay due to topography is taken in to account using the exponential mapping function as in (11) with h_A and h_B the height of the points w.r.t to the ellipsoid and H, the so called height of the atmosphere, typically fixed to 7 km. Assuming the error is first-order stationary, the mean interferometric phase error is $\mathbb{E}[\phi_\epsilon] = 0$ even if the residual error has non-zero mean, $\mu_\epsilon \neq 0$ as visible from Equation 4.2. This is a consequence of the inherent differential nature of the interferometric measurements and allows to neglect the absolute error of the NWP focusing the attention only on its variance. Assuming the atmosphere and the error are temporally uncorrelated, the interferometric phase error power is

$$\begin{aligned}\mathbb{E}\Big[\phi_\epsilon^2\Big] = 2\sigma_\epsilon^2 \frac{e^{-\frac{2h_B}{H}}\cos^2\theta_A + e^{-\frac{2h_A}{H}}\cos^2\theta_B}{\cos^2\theta_A\cos^2\theta_B} - \\ - \frac{4\Lambda(A,B)}{\cos\theta_A\cos\theta_B} e^{-\frac{h_B+h_A}{H}}\end{aligned} \tag{4.3}$$

Where Λ is a correlation function that $\Lambda(A \equiv B) = \sigma_\epsilon^2$ and $\Lambda(A,B) \to 0$ at large distance. The residual error in the interferometric phase between points A and B described in Equation 4.3 is a parametrization of the sample variograms that can be calculated from data. Equation 4.3 approaches 0 as the distance $d \to 0$ and is $\propto \sigma_\epsilon^2$ as $d \to \infty$. That means that at large distances ($\geq$ 40-50 km) the interferometric measurements become limited by the accuracy of the models used for the correction, as verified in Section 4.3.1.

In order to study the troposphere induced error and its mitigation through the use of NWP, short time interferograms are generated from every acquisition with the next one. This approach should prevent bias due to a common reference as well as eventual seasonality present in the tropospheric delay [1] and the impact of deformation. The latter point requires clarification. The fast revisit time of the Sentinel-1 mission allows temporal baselines of 6,12 or in worse case, 24 days. Since the residual error, including effects such as tropospheric turbulence, are assessed to be on the order of centimeters, deformation rates of several tens of cm/y would be necessary in order to produce effects comparable to those from the troposphere. Such rates occur due to landslides or in mining areas that are typically restricted in time and space. It follows that variograms computed by averaging over the scene should not be strongly impacted by such rapid deformation types. The projection of tectonic plate motion onto the range varying LoS is a large-scale effect that could seriously bias variogram estimation. Such movements are mainly horizontal and can reach 6-7 cm/y. Projection onto the LoS (30° to 45° at near and far range respectively for Sentinel-1), combined with the previously mentioned revisit times, shows its impact to be negligible. The eventual presence of seismic events in the time series should be assessed and co-seismic interferometric pairs avoided when estimating the variograms. After this brief clarification the temporal characteristic of the troposphere-related phase shall be discussed. In this study the tropospheric error is considered temporally uncorrelated. This hypothesis should hold at least for the troposphere-corrected phase since all seasonal effects are included in the NWP and are hence compensated. The interferometric phase variogram between acquisitions n and m, $\Gamma_{n,m}$, is then the sum of the two variograms of the errors in acquisition n and m, Γ_n and Γ_m

$$\begin{aligned}\Gamma_{n,m}(d) &= \mathbb{E}\Big[\big((\phi_n(A) - \phi_n(B)) - (\phi_m(A) - \phi_m(B))\big)^2\Big] \\ &= \Gamma_n + \Gamma_m\end{aligned} \tag{4.4}$$

where ϕ is the phase at points A and B and d is the distance between the points.

By averaging the set of short time baseline variograms $\bar{\Gamma} = \mathbb{E}\big[\Gamma\big]$, it is possible to derive the average behavior of the residual interferometric phase error.

Assuming the troposphere is the main source of error at large distances ($\geq$ 40-50 km), one can now derive its impact on deformation rate measurements. The variogram of the linear deformation rate estimates is obtained by scaling $\bar{\Gamma}$ by the linear regression formula (29),

$$\Gamma_v(d) = \frac{1}{2}\frac{\lambda^2}{16\pi^2}\frac{\bar{\Gamma}(d)}{M\sigma_t^2} \tag{4.5}$$

where the factor 1/2 accounts for the common reference acquisition, M is the number of acquisitions and σ_t^2 is the spread of the temporal sampling $\sigma_t^2 = \sum_i t_i^2/M - (\sum_i t_i/M)^2$

---

[1] Seasonality should be removed by the tropospheric models but could be still present in the non-corrected interferograms used to compute the performance gain

4.3 Impact NWP Tropospheric Correction

Section 4.2 proposed a model to evaluate the effects related with the spatially correlated noise. Variograms are a convenient way to characterize this component. By comparing the interferometric phase variograms before and after the correction, it should be possible to observe the performance gain at different scales. Since the data used for compensation are not provided at the same resolution of the interferograms, a significant reduction of the tropospheric contribution can only be expected at scales larger than the NWP model resolution. Here, ECMWF ERA-5 data are used with a spatial gridding of 30 km. Figure 4.2 shows an example of variogram behavior before and after correction using a long stripe of mosaicked Sentinel-1 interferograms, see also Section 4.3.1 and (44). Although the spread of the gain is large at all scales, the temporal average of the variograms clearly shows the considerable gain due to the NWP correction that increases at large scales ($\geq$ 40-50 km). This is particularly important in tectonic strain applications where high relative accuracy is required at such distances.

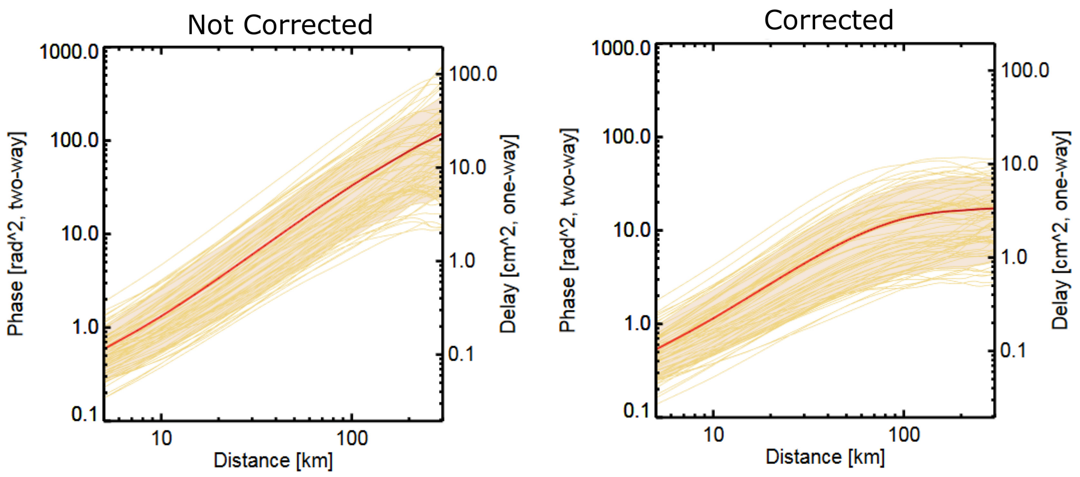

(a) (b)

Figure 4.2: Single variograms, $\Gamma_i + \Gamma_{i+1}$ (thin orange lines), and their mean, $\bar{\Gamma}$ (bold red line) (a) without and (b) with NWP corrections.

Figure 4.3 shows an example of the impact of NWP corrections on the deformation rate estimates at different scales when varying the length of the time series. It is interesting to note how the typical 1 mm/y accuracy requirement is achieved after 4 years with the corrected dataset, while almost 8 years are required if no correction is applied.

4.3.1 Cross-Validation GNSS/ERA-5 tropospheric corrections using InSAR data

In Section 4.2 was pointed out that increasing the distance between two points the accuracy ends up to be limited by the accuracy of the external models use to correct the interferometric phases. In this Section is presented an experiment aimed to validate this hypothesis.

Equation 4.2 models the residual tropospheric error in NWP corrected interferograms. The variance of the error is obtained by expanding

$$\mathbb{E}\left[\phi_\epsilon^2\right] = \mathbb{E}\left[\left((\epsilon_{r,A}-\epsilon_{s,A})\frac{e^{-\frac{h_A}{H}}}{\cos\theta_A} - (\epsilon_{r,B}-\epsilon_{s,B})\frac{e^{-\frac{h_B}{H}}}{\cos\theta_B}\right)^2\right] \tag{4.6}$$

The temporal correlation of the reference and secondary acquisitions errors can be considered 0 everywhere since they are separated by at least 6 days $\mathbb{E}\left[\epsilon_r \epsilon_s\right] \equiv 0$. On the other hand a spatial cor-

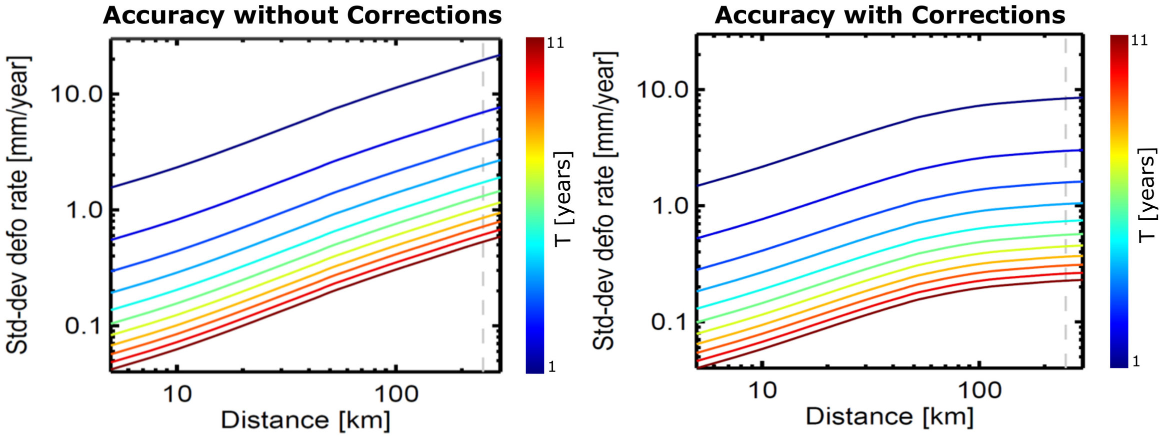

(a)

(b)

Figure 4.3: Variograms of the deformation rate estimates with the length of the time series color-coded and assuming a 12 day revisit time, (a) without tropospheric corrections and (b) with tropospheric corrections.

relation $\mathbb{E}\left[\epsilon_A \epsilon_B\right] = \Lambda(A, B)$ exists for both reference and secondary acquisitions, leading to Equation 4.3.

According to this model, the spatial correlation function at large distances should tend to 0 $\Lambda(\infty) = 0$ therefore the error variance in such a regime should only depend on the accuracy of the tropospheric corrections used. Moreover, since this verification experiment is performed on a large area characterized by flat or slightly varying topography, the exponential term can be considered constant and hence absorbed by the measurement error.

$$\mathbb{E}\left[\phi_\epsilon^2\right] = \frac{2\sigma_\epsilon^2}{\cos^2\theta_A} + \frac{2\sigma_\epsilon^2}{\cos^2\theta_B} \tag{4.7}$$

In order to verify this, a study was carried out using Sentinel-1 interferograms with very long azimuth extension over Germany. The unwrapped phases from multiple slices were mosaicked allowing variograms at scales of up to 300 km. The variogram samples were chosen along (almost) iso-range lines in order that the incidence angle not vary and the measurements projected onto the zenith direction. In this way, the effects of incidence angle could be factored out.

Analogously to (17), the zenith path delay predicted by ERA-5 was compared to GNSS based estimates. Since the NWP model accuracy varies with geographic location, a subset of 9 GNSS stations in Germany were used. The difference between the GNSS and ERA-5 ZPDs should approximate the NWP error, given the GNSS values represent the true delay. This comparison was performed for ascending and descending geometries at local solar times of 18:00 and 06:00 respectively. Statistics were calculated over one year of data for each geometry.

In an ERA-5 corrected interferogram the error between two points separated by a distance d should approach the saturation value $\sigma_Z^2 = 4\widehat{\sigma_\epsilon^2}$ in Equation 4.7 since $\Lambda(d) \rightarrow 0$ for large d and $\theta_A = \theta_B = 0$ at zenith. Hence, it is sufficient to confirm that the variograms saturate on average at the value $4\widehat{\sigma_\epsilon^2}$. The results in Figure 4.4 show an estimate of $4\widehat{\sigma_\epsilon^2}$ along with the variograms for ascending and descending geometries. It is interesting to note that the performance for these two geometries are comparable at 300 km. One would expect better performance for the descending pass, made in the morning when the atmosphere contains less energy. This is partially true considering mid-scales from 50-80 km where stronger turbulence due to more atmospheric power for the ascending pass leads to a larger average power and spread around the average. However, once the distance reaches the scale of the NWP model, one is limited by the error of the NWP model independently of the time

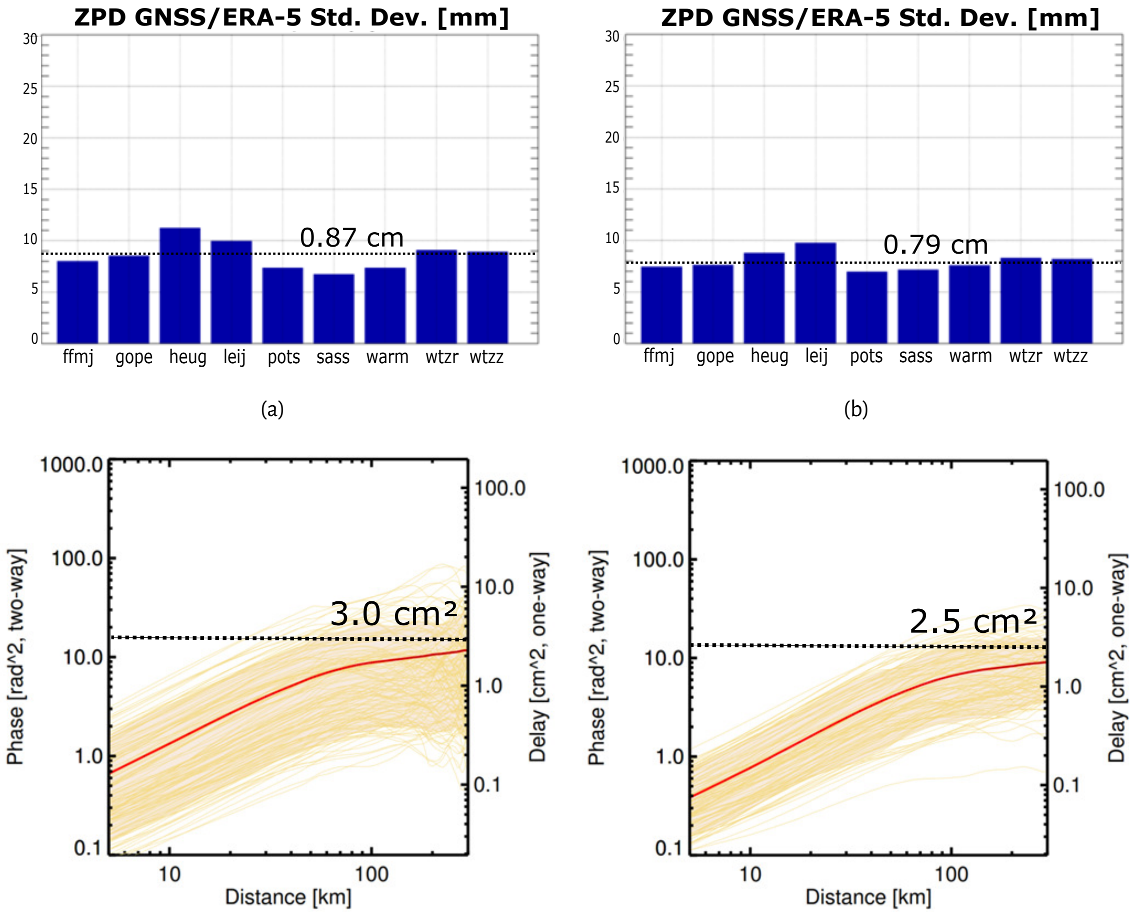

(a) (b)

(c) (d)

Figure 4.4: In (a) and (b) the standard deviation of the ECMWF ERA5 and GNSS ZPD differences are shown for each station for ascending (18:00) and descending (06:00) passes respectively. The estimated variograms saturate at the values expected due to NWP model error for both (c) ascending and (d) descending passes(this corresponds to the variogram in Figure 4.2 computed in zenith direction).

of day.

An important implication of this is that a global analysis of ERA-5/GNSS deviations could provide a lower bound for the achievable accuracy in measuring large scale displacement using NWP corrected InSAR phase.

4.3.2 A more global view for the predicted performance

It should be noted that the accuracy of the correction has been demonstrated to vary considerably worldwide (17)(15) therefore, in order to comprehensively evaluate correction performance, 146 Sentinel-1 stacks have been processed over various regions of the world. Each of these stacks spans at least 4 years and contains up to 200 acquisitions. As described in Section 4.2, only short time baseline interferograms were used to ensure the troposphere signal dominates. The average variogram $\bar{\Gamma}$ was also calculated at different scales. A measure of the gain provided by the correction is provided by the metric:

$$G_{\text{dB}}(d) = 10\log_{10}\left(\frac{\bar{\Gamma}_{\text{corr}}(d)}{\bar{\Gamma}_{\text{raw}}(d)}\right) \tag{4.8}$$

the ratio, in decibels, of the average variograms with and without the correction.

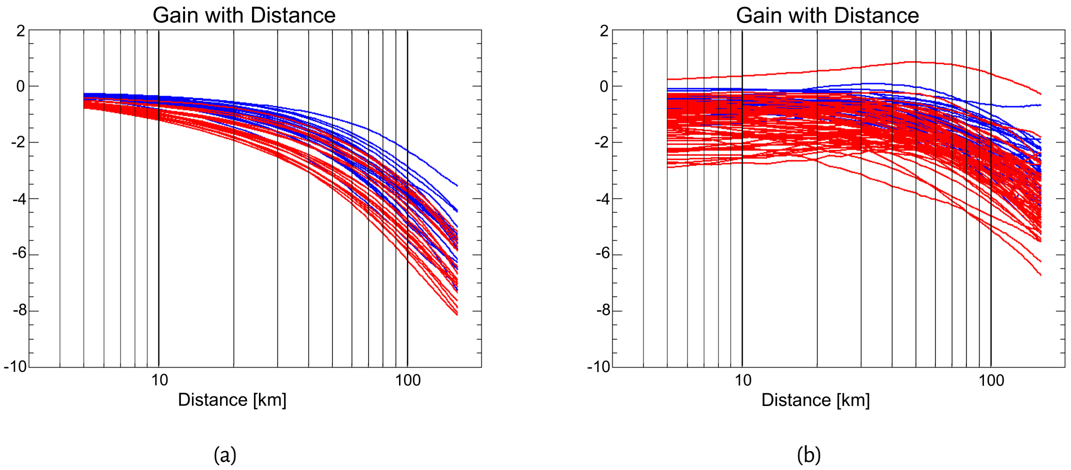

Figure 4.5: Variogram ratios, $G_{\text{dB}}(d)$, for (a) the German Ground Motion Service and (b) all other stacks. Every line corresponds to $G_{\text{dB}}(d)$ for a single stack. The ascending stacks are depicted in blue and the descending in red.

Figure 4.5 shows $G_{dB}(d)$ for stacks from the German Ground Motion Service separately from all others.

An evaluation of the performance at large distances was also performed. The average variograms before and after corrections were fitted using typical variogram models (exponential, gaussian and spherical) hence reducing the variance of the variogram estimate. Using this information together with temporal sampling information and Equation 4.5, the performance in measuring the deformation rates at 150 km was estimated with and without the tropospheric corrections. Figure 4.6 shows the histograms of the accuracies in mm/y with the German Ground Motion Service shown separately from all others.

Figures 4.5, 4.6 and 4.7 show a significant gain is attained when the tropospheric delay is corrected. As already pointed out in (17) the gain is region dependent. A very high gain is achieved where the model accuracy is also very good such as in Europe or the U.S. In only one of the 146 stacks, located in Indonesia, were the corrections found to slightly worsen the performance at medium scale and is clearly visible in Figure 4.6.

In Figure 4.5, a smaller but non-negligible gain is also observable at short scales ($\leq$ 10 km). This value can vary from 0 up to 3-4 dB depending on the test site. The tropospheric models can correct stratification effects at scales smaller that he models resolution since the topography, available at the reference DEM resolution, can be used to project the models to phase errors (15). Therefore such a gain can only be attributed to the compensation of tropospheric stratification since the resolution of the correction model is much coarser than the topographic variation. For the sake of completeness what discussed in Section 4.2 shall be recalled. In case of tropospheric corrected phase can be considered more or less uncorrelated in time due to the corrections that should remove a good part of the seasonal effects that trigger correlation. On the other side for the uncorrected phases some correlation could be present making the evaluation of the phase error optimistic. Therefore the performance computed in terms of gain between corrected and non corrected interferograms shall be more precisely considered as a lower bound of the achievable improvement.

To conclude the Section it is worth to notice that the mitigation of tropospheric effects and the evaluation of their performance on a global scale is a very important aspect in developing error models for missions that allow (100) or will allow (92) (76) systematic interferometric processing on a global scale, in order to be able to provide an assessment of the high level products performance.

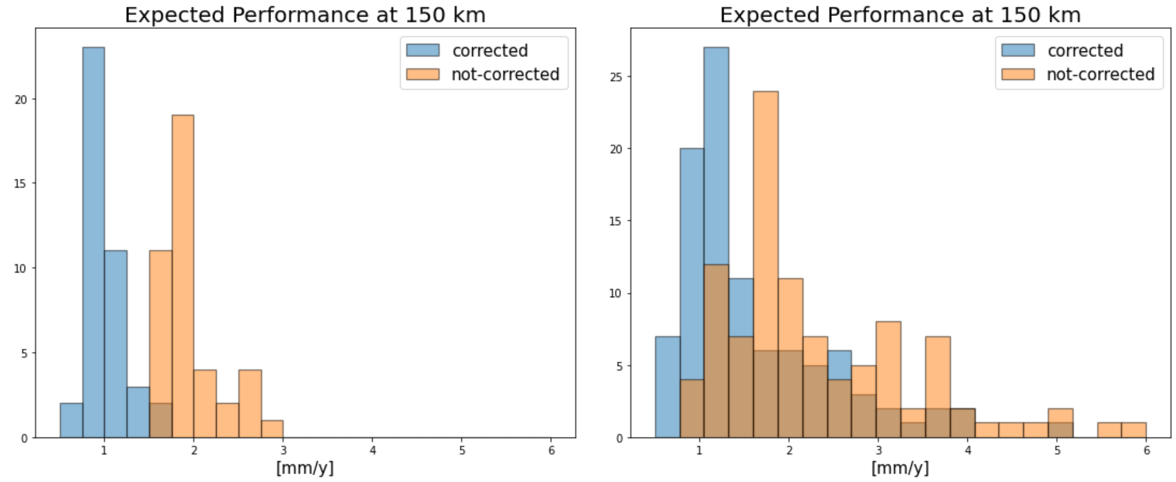

(a) (b)

Figure 4.6: Expected performance at 150 km before (red) and after (blue) the tropospheric corrections. The German Ground Motion Service only (a) and all other available datasets (b).

4.4 Measurements accuracy model validation using GNSS

Knowledge of displacement rate precision is of central importance in geophysical studies of large-scale tectonic movements where the precision requirements are often very high (104). In Section 4.2 it has been shown how the residual tropospheric noise can be characterized from short time baseline interferograms and how this can be translated into displacement rate accuracy. This approach involves assumptions about the residual error, i.e. that short time baseline interferograms characterize the error, that could be questioned. For the sake of completeness, the behavior of the displacement rate as described in Equation 4.5 must be verified in practice.

Consider N locations where two displacement rates v_D (in LoS) and $\underline{v}_G$ (in x, y, z) are obtained from InSAR and GNSS respectively. With $\underline{s}$ as the LoS vector, the difference between the two velocities at position i, Δ_i, is

$$\Delta_i = v_{D,i} - \underline{v}_{G,i}^T \underline{s} = \delta_i + v_{ref} + n_i \tag{4.9}$$

where v_{ref} is the velocity of the reference point used in InSAR processing, δ_i represents spatially varying residual atmospheric zero-mean error from InSAR processing and n_i is random error. The quantity Δ_i is obtained in practice by selecting a set of InSAR measurements located within a radius of a few hundred meters around the GNSS stations. In order to reduce the influence of clutter, the interferometric measurements are averaged. In this way the random noise component n_i can be considered almost completely due to GNSS.

To use Equation (4.9), a statistical description of the vector $\underline{\Delta}$ is required, i.e. the covariance matrix $\mathbf{R}$ of the difference measurements. Three terms can be distinguished: 1) random noise from the GNSS measurements $\sigma_{G,i}^2$ obtained by projecting the variance of the (x, y, z) components of the velocities onto the LoS, 2) random noise from the InSAR measurements $\sigma_{D,i}^2$, and 3) spatially correlated noise due to residual atmospheric effects. The full covariance matrix is:

$$\mathbf{R} = \text{diag}(\sigma_{G,0}^2, \dots \sigma_{G,N-1}^2) + \text{diag}(\sigma_{D,0}^2, \dots \sigma_{D,N-1}^2) + \mathbf{C}_\delta \tag{4.10}$$

The first two terms are diagonal matrices since they represent the spatially uncorrelated errors of the independent GNSS and InSAR measurements, respectively. The last term, $\mathbf{C}_\delta$, representing residual atmospheric error, still has to be found (31). It can be determined from the average variogram $\bar{\Gamma}_{\text{corr}}(d)$ according to Equation 4.5.

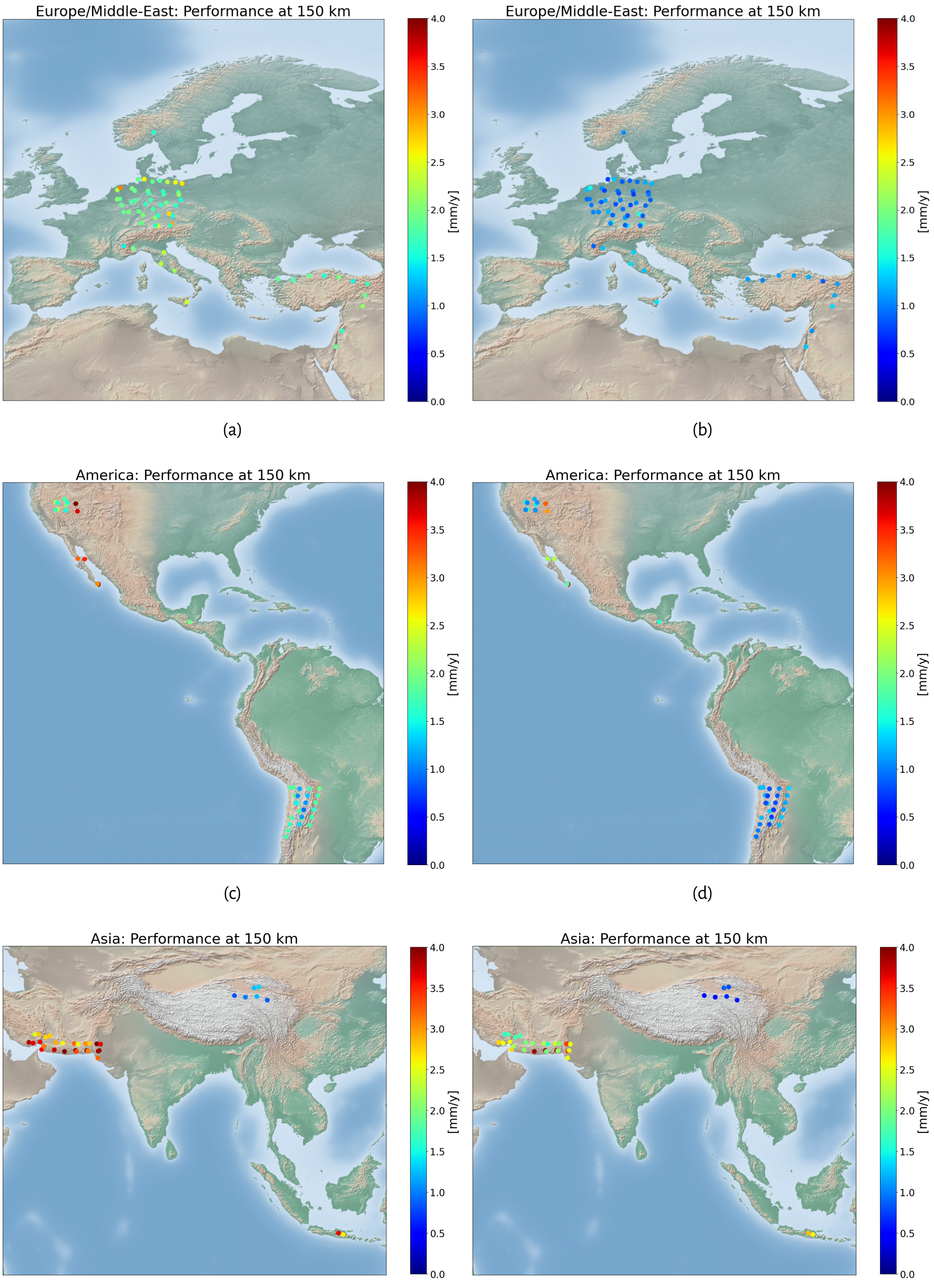

(a) (b)

(c) (d)

(e) (f)

Figure 4.7: The performance at 150 km before (left column) and after (right column) the corrections. Europe and the Middle East (top row), North and South America (middle row), and Asia (bottom row).

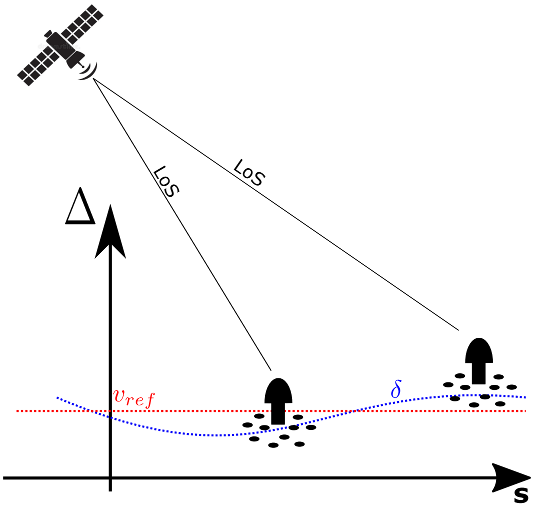

Figure 4.8: Graphical visualization of Equation 4.9.

Given a full statistical characterization of the GNSS/InSAR differences, and assuming the GNSS accuracies to be correct, we can now verify if Γ_v actually represents the variogram of the velocity error. First, from the vector $\underline{\Delta}$ of N differences between GNSS and InSAR velocities, we compute all $(N^2 - N)/2$ unique pairwise differences between the elements. Their mean is expected to be zero according to Equation 4.9 and their variance is

$$\sigma_\Delta^2(i,j) = \mathbb{E}[(\Delta_i - \Delta_j)^2] = \sigma_{G,i}^2 + \sigma_{G,j}^2 + \Gamma_v(d_{i,j}) \tag{4.11}$$

The scales at which Γ_v can be verified by this method clearly depend on the spatial distribution of GNSS stations, with the range of scales being set by the smallest and largest distances between stations. It is worth to notice that for this study the GNSS measurements are assumed to be spatially uncorrelated. This could not be true in general (84), however known the spatial behaviour of the GNSS measurements Equation 4.10 could be corrected adding an appropriate covariance matrix in order to take it in account.

A statistic defined as the standardized difference

$$T_{i,j} = \frac{\Delta_i - \Delta_j}{\sigma_\Delta(i,j)} \tag{4.12}$$

should follow a standard normal distribution if the error description is correct. To test the validity of the variance model in Equation 4.11, a χ^2-test can be performed on $\underline{T}$. The confidence region at significance level α for the true σ_T^2 is

$$\sqrt{\frac{(N-1)\hat{\sigma}_T^2}{\chi^2_{1-\alpha/2,N-1}}} < \sigma_T < \sqrt{\frac{(N-1)\hat{\sigma}_T^2}{\chi^2_{\alpha/2,N-1}}} \tag{4.13}$$

where the number of degrees of freedom is $N-1$ and $\hat{\sigma}_T^2$ is the sample variance of T. The validation approach will focus on analyzing the distribution of $\underline{T}$ and the confidence interval for σ_T.

4.4.1 Cross-Validation of the German Ground Deformation Service Dataset using GNSS Stations

The cross-validation scheme was performed on the German deformation map. The dataset includes 41 stacks acquired in both ascending and descending geometry. This region was chosen due to easy and open access to a very dense GNSS network from Nevada Geodetic Laboratories (77; 10) with all stacks containing sufficient GNSS stations.

The confidence intervals for σ_T at 5% significance level are shown in Figure 4.9(a). Of course, the dependence on the number of GNSS stations, shown in Figure 4.9(b), is strong. However, for almost all stacks the confidence intervals include $\sigma_T = 1$ indicating acceptance of the null hypothesis $H_0 : \sigma_T = 1$ versus the alternative $H_1 : \sigma_T \neq 1$.

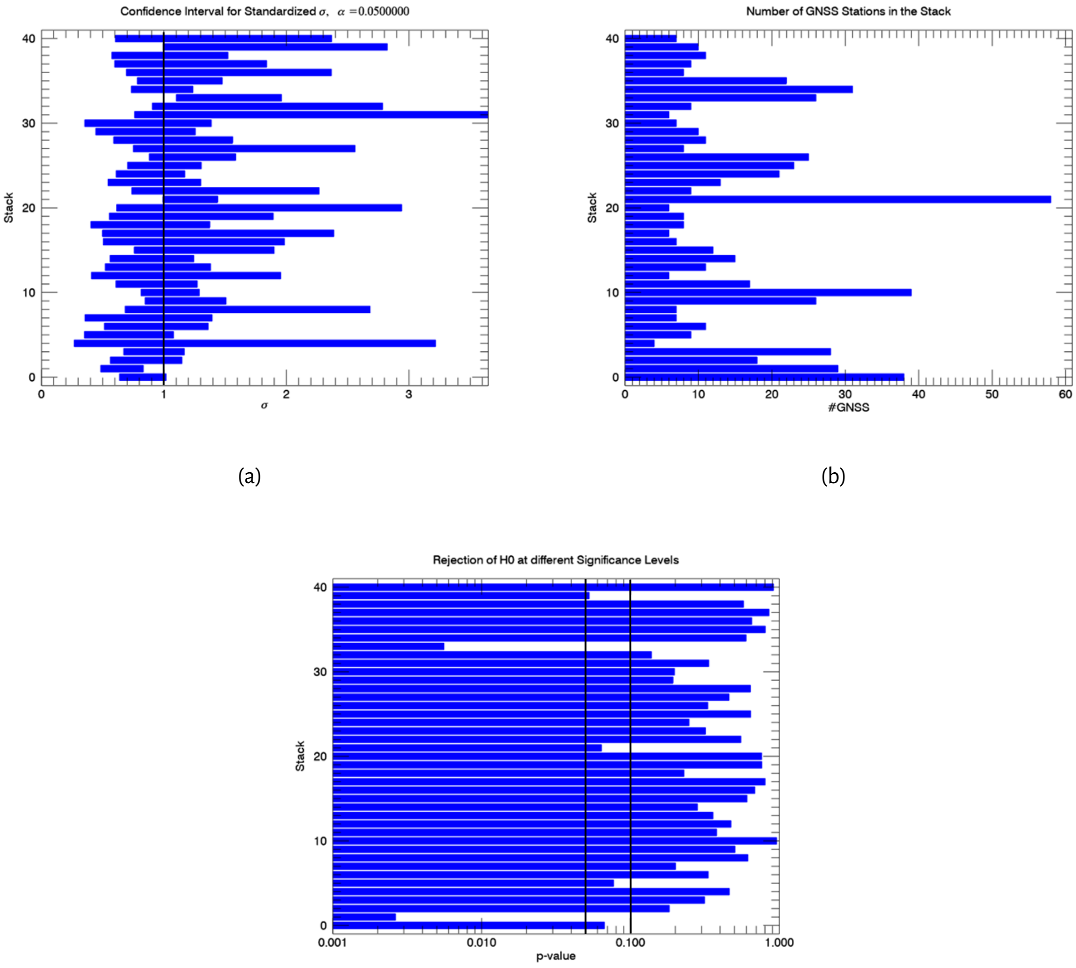

(a)

(b)

(c)

Figure 4.9: Results of the InSAR/GNSS velocities cross-validation: (a) the number of GNSS stations present in each stack, (b) the confidence intervals where the black line denotes $\sigma_T = 1$.(c) p-values for each stack where the black lines denote significance levels of 5% and 10%.

The p-values are shown in Figure 4.9(c), the null hypothesis is rejected for only 2 stacks at 5% significance. Figure 4.10 shows the distribution of $\underline{T}$ pooled over all stacks, along with the nominal standard normal distribution under the null. The pooled value of $\hat{\sigma}_T$ is 1.03, showing very good agreement between the model and GNSS data 4.10(b).

Figure 4.10(a) displays the error variogram from InSAR data compared to all possible pairwise differences $(\Delta_i - \Delta_j)^2$ in order to show the fit of the variogram model at various scales. Since the accuracy of GNSS measurements also play a role, the GNSS error contribution is included as per Equation 4.11.

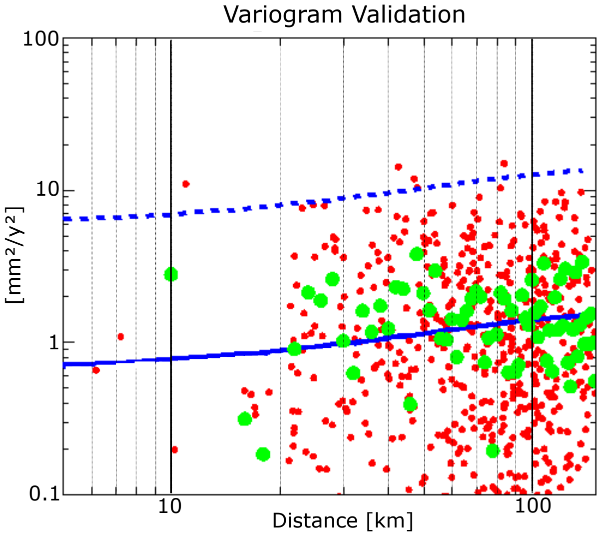

(a)

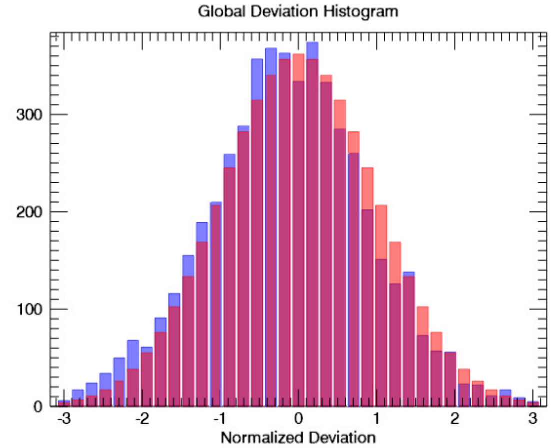

(b)

Figure 4.10: In (a) comparison between variograms (blue line) and all pairwise differences $(\Delta_i - \Delta_j)^2$ (red dots) for an ascending stack of the German Ground Motion Service. In order to highlight the plausible area for the measurements the dashed blue lines correspond to $(3\sigma)^2$ variograms and the bold one to σ^2. The green dots correspond to the pairwise differences after averaging over 2 km bins, as in Equation 4.11. In (b) histogram of the pooled vectors $\underline{T}$ using NGL GNSS results (blue) compared to the nominal $N(0,1)$ distribution (red).

4.5 Conclusions

This chapter discussed the potential and the limitations of InSAR for large-scale displacement measurements. In general we can conclude that the measurement of large-scale displacement signals precludes spatial filtering since all displacement components must be preserved in the final product. Therefore, in order to provide sufficient accuracy at large scales, tropospheric corrections are recommended. In Section 4.3.1 a lower bound on the interferometric phase accuracy at large distance was outlined and related to the accuracy of the models used for the corrections. This gives some further prospective on the potentiality of the techniques in measuring tectonic movements, since as NWP models are continuously being improved, follow-on effects for InSAR can be expected. It has been observed that the performance may be site dependent but the target of 1 mm/y at 100 km is achievable in 5 years given good weather models (in Europe or the US) or in general where the errors are small due to reduced atmospheric delay, i.e. over the Tibetan Plateau. In order to evaluate them short time baseline variograms have been proved to allow a reasonable evaluation of displacement rate performance providing valuable error estimates to users. Such information shall be included in the product since residual tropospheric noise is the main limiting factor at large distances.

5

Calibration of the InSAR deformation measurements using GNSS

Based on the derivations of the Chapter 4 an optimal combination of InSAR and GNSS techniques is designed taking in account the spectral properties of their errors. Only the InSAR/GNSS differences, which can be statistically characterized, are estimated and used to compensate the original InSAR measurements. The error is then propagated from the data to the results, allowing full description of the output uncertainty.

This chapter summarizes the journal paper in Appendix C : *Alessandro Parizzi , Fernando Rodriguez Gonzalez and Ramon Brcic (2021). A Covariance-Based Approach to Merging InSAR and GNSS Displacement Rate Measurements. Remote Sensing.*

5.1 Algorithm description

In Section 4.4 the statistical properties of the GNSS/InSAR offsets have been estimated in order to be able to perform a cross-validation between the two measurements. Now starting from what has been previously assessed, the developed framework is used to establish an algorithm that is able to optimally combine the InSAR and GNSS measurements. In order to do that the statistical characterization of the two set of measurements is considered. Analogously as in Section 4.4 let us then consider N locations in the processed area of interest, where two deformation rate measurements v_D and $\underline{v}_G$ are performed using InSAR and GNSS, respectively. Recalling Equation 4.9 the InSAR/GNSS difference is defined as:

$$\Delta_i = v_{D,i} - \underline{v}_{G,i}^T \underline{s} = \delta(r_i, a_i) + v_{ref} + n(r_i, a_i), \tag{5.1}$$

The implicit hypothesis behind this definition is that the spatially correlated noise, basically related to the residual atmospheric delay, is present in the interferometric measurement only. As previously pointed out this cannot be considered in general true, but it has to be considered as an assumption of this framework. Nonetheless known the statistic characterization of the spatially correlated error in GNSS measurements, it could be easily integrated in the problem statement of Equation 5.1. The proposed algorithm is aimed to extract, through the subtraction of the two velocities, the parameters $\delta(r, a)$ and v_{ref}, which have to be estimated in order to properly merge the data. Figure 5.1 displays an overview of the steps of the proposed approach. In the first step, the error statistics are derived and the covariance matrix $\mathbf{R}$ is computed, see Sections 4.1 and 4.4. The reference point velocity v_{ref} is then estimated and subtracted from the offset vector $\underline{\Delta}$ in order to obtain a 0-mean error screen. Finally, the residual error screen is interpolated at each InSAR measurement point, exploiting knowledge of the error statistics (102).

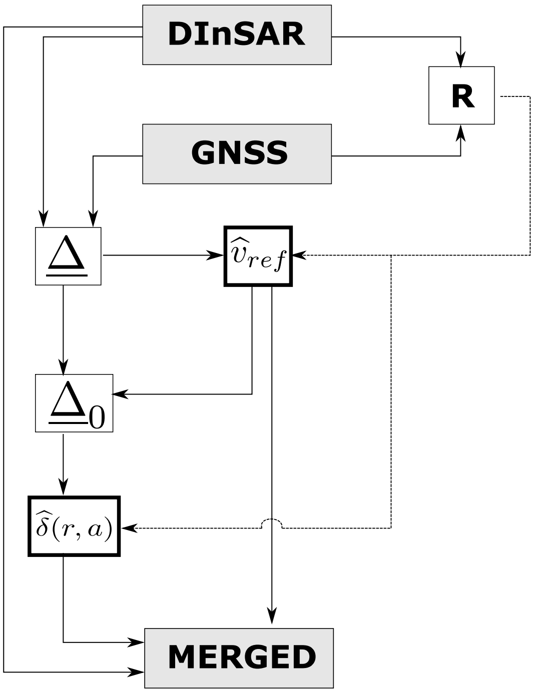

Figure 5.1: Flow chart of the proposed method.

5.1.1 Estimation of the Reference Point Motion

Equation (5.1) shows how $\underline{\Delta}$ can be seen as an observation of v_{ref} with superimposed random and colored noise. Since the noise statistics of $\underline{\Delta}$ exhibit stationary behavior, the derivation of the reference point velocity can be carried out by averaging the observed $\underline{\Delta}$. Therefore, according to the considerations in Section 4.1 and 4.4, $\widehat{v}_{ref}$ can be found by taking into account the computed covariance matrix **R** in Equation 4.10:

$$\widehat{v}_{ref} = (\underline{u}\mathbf{R}^{-1}\underline{u}^T)^{-1}\underline{u}^T\mathbf{R}^{-1}\underline{\Delta}, \tag{5.2}$$

where $\underline{u}$ is a vector of ones that maps, one to one, the measurements $\underline{\Delta}$ with the unknown scalar v_{ref}. The estimated $\widehat{v}_{ref}$ represents the motion of the reference point in its local LoS and has to be added to the InSAR velocities in order to make them absolute.

5.1.2 Estimation of the 0-Mean Calibration Screen

In the previous Section 5.1.1, the overall offset between InSAR and GNSS deformation rates was estimated while accounting for the covariance matrix. Now, the space-variant error screen between the GNSS and InSAR velocities can be estimated by performing a covariance-based interpolation (Kriging) of the residual offsets $\underline{\Delta}_0 = \underline{\Delta} - \widehat{v}_{ref}$. A set of coefficients $\underline{c}$ that, combined with the vector $\underline{\Delta}_0$, allows the reconstruction of $\delta(r,a)$ everywhere must be estimated.

$$\widehat{\delta}(r,a) = \underline{c}^T\underline{\Delta}_0 \tag{5.3}$$

According to theory, this can be obtained by imposing the condition that the interpolation/prediction error be uncorrelated:

$$\epsilon_n = \widehat{\delta}(r_n,a_n) - \delta(r_n,a_n) \tag{5.4}$$

with the data $\underline{\Delta}_0$ (85). Substituting Equation (5.3) into Equation (5.4) and imposing the uncorrelatedness condition with $\underline{\Delta}_0$ gives:

$$\underline{c} = \mathbf{R}^{-1}\underline{\rho}, \tag{5.5}$$

where $\underline{\rho} = \mathbb{E}[\delta(r,a)\underline{\Delta}_0]$ is the vector representing the correlation between the data vector $\underline{\Delta}_0$ and the error screen δ at the current position.

5.1.3 Accuracy of the calibrated product

In order to allow a complete usability of the calibrated/merged product, its performance in terms of accuracy shall also be described. The final result is obtained by compensating the InSAR velocities for the estimated $\widehat{v}_{ref}$ and $\widehat{\delta}(r,a)$. The reference point deformation rate is a bias added to all points. Its error is therefore a constant value in the final product. Its contribution can be derived by computing the variance of the linear system inversion:

$$\sigma^2_{\widehat{v}_{ref}} = (\underline{u}\mathbf{R}^{-1}\underline{u}^T)^{-1}. \tag{5.6}$$

The error of the estimated $\widehat{\delta}$ will be space variant. The variance and covariance of the estimated error screen $\widehat{\delta}(r,a)$ can be derived as in (85).

$$\mathbb{E}[\epsilon_n^2] = \mathbb{E}[(\delta(r_n,a_n) - \underline{c}^T\underline{\Delta}_0)^2] = \Gamma(0) - \underline{\rho_n}^T\mathbf{R}^{-1}\underline{\rho_n} \tag{5.7}$$

where $\Gamma(0)$ represents the original error due to the spatially correlated signal, and the second part of the equation represents a "mitigation factor" that reduces such variance according to the distance from the GNSS data. Analogously, the covariance is:

$$\mathbb{E}[\epsilon_n\epsilon_m] = \Gamma(d_{m,n}) - \underline{\rho_m}^T\mathbf{R}^{-1}\underline{\rho_n}. \tag{5.8}$$

Some conclusions concerning the final product can now be drawn. The result provides absolute measurements that can be characterized by a variance directly derived from the applied methodology. It still contains a residual spatial correlation, though mitigated by the removal of $\widehat{\delta}(r,a)$. However, this residual error is no longer stationary. Its covariance depends on the two considered points, as highlighted by Equation (5.8). A variogram or covariance representation of the error as for the input InSAR velocities is hence no longer possible, but must must to be computed locally, accounting for the position (r,a) with respect to the GNSS stations. This is anyway not particularly demanding from an implementation point of view, since the amount of information that have to be saved, in order to reconstruct the error covariance, is relatively small. The covariance matrix $\mathbf{R}$ is in general not too big since it is $N \times N$, the rest can be easily computed on the fly.

5.2 Simulations

Simulations were performed to understand and quantify the effects of the spatial distribution (density) and the quality of the GNSS measurements in different processing scenarios.

A set of randomly distributed points with zero deformation was simulated over a surface of 175×250 km^2 (Sentinel-1 slice size) in order to represent the InSAR measurements. Random noise (clutter) and spatially correlated noise (atmospheric residuals) were added to the points. For the generation of spatially correlated noise, an exponential covariance $\Gamma(d) = \sigma_\alpha^2 exp(-d/L_c)$ was used. A reduced set of GNSS zero-deformation data were also simulated at random positions within the scene. According to the model only random noise was added to the simulated GNSS velocities. For the sake of simplicity, positions were uniformly distributed within the scene. Of course, a regular sampling is desirable, but it cannot be considered as a realistic requirement.

The simulations were performed while varying the two main parameters, the number of reference GNSS measurements, and their accuracy. Two different scenarios were tested with low and high atmospheric residual power σ_α^2. In the first scenario, $\sigma_\alpha^2 = 2$ mm^2/y^2; for the Sentinel-1 mission, this is comparable to having a long time series of $T_{obs} \approx 3$ y in the case of applied atmospheric corrections (44). In the second scenario, $\sigma_\alpha^2 = 9$ mm^2/y^2, representing the case of a short time series of

$T_{obs} \approx 1$ y (44). A realistic correlation length, according to real data, was used for the simulations—$L_{corr} = 60$ km in both cases. This comes from direct experience with the data. We observed that the average variograms after tropospheric corrections exhibited values of 40–100 km when fitted with an exponential model. An example of the simulation framework is shown in Figure 5.2.

Observing the simulation results in Figure 5.3 and 5.4 it can be concluded that, due to the spatial correlation of the error, higher densities of GNSS measurements improves the estimation of δ since it provides a better sampling of the error field, but does not help much in retrieving the absolute velocity v_{ref}, due to the "data redundancy" introduced by the spatial covariance.

5.2.1 Performance in Retrieving $\widehat{v}_{ref}$

The accuracy of $\widehat{v}_{ref}$ is that of the mean computed from a set of correlated samples. The level of dependence of the given dataset is controlled by the spatial density of the latter and the correlation length L_{corr} of the superimposed noise. We observed that it is logical to expect that, given a L_{corr}, increasing the number of data improves estimation of $\widehat{v}_{ref}$ up to a certain level, since as the density of measurements increases, so to does the amount of correlation between measurement, hence limiting its impact on final performance. In a typical scenario ($T_{obs} \approx 3$ y , σ^2_α =2 mm^2/y^2), the accuracy can easily be brought below 1 mm/y, even with a limited set of GNSS stations (Figure 5.3).

5.2.2 Performance in Retrieving $\widehat{\delta}$

Evaluating the performance of $\widehat{\delta}$ is not a simple task. The most natural way would be to compare the variograms of the results before and after application of the technique. This approach would deliver a deeper insight into the achieved gain, since it would be possible to show this as a function of the scale. However, as mentioned in Section 5.1.3, the error of the merged results is no longer stationary making a variogram representation questionable. In order to avoid this issue, a simpler but more robust approach was followed. The performances were evaluated in terms of mean square error (MSE) in dB, over the whole scene. In practice, the mean power of the residual deformation signal after removal of the estimated error screen $\widehat{\delta}$ from the measured rates v_{meas} is:

$$MSE_{dB} = 10Log_{10}\Big(\mathbb{E}[(v_{meas} - \widehat{\delta})^2]\Big). \tag{5.9}$$

The results displayed in Figure 5.4a,b show that, in both cases, the performance cannot improve beyond a certain level by improving the quality of the GNSS measurements only. An improvement in GNSS coverage is also necessary in order to better compensate the higher wave-numbers of the error screen.

5.3 Real data results

For the study, two Sentinel-1A/B datasets covering the northern part of the Netherlands (two stacks, ascending and descending) and the junction between the North Anatolian Fault and East Anatolian Fault (three stacks, descending) were used. The interferograms were computed, corrected for tropospheric delays using ECMWF ERA-5 (ECMWF Re-Analysis) data (44) and processed using the PSInSAR technique (35). In order to preserve all wave-numbers of the deformation signal, no spatial high-pass filtering or polynomial detrending was performed on the final data. The technique described above was applied to the estimated deformation rates.

For the reference measurements, the GNSS data processed by Nevada Geodetic Laboratories (77; 10) were used. The correspondence GNSS/PSs for the calculation of vector $\underline{\Delta}$ was implemented by averaging all of the PS rates within a radius of 250 m from the GNSS station.

A further elucidation needs to be made. The reference system that describes SAR geometry (state vectors) does not account for continental drift making plate movement visible in the interferometric measurements, projected along the LoS. The GNSS data used for the calibration must therefore

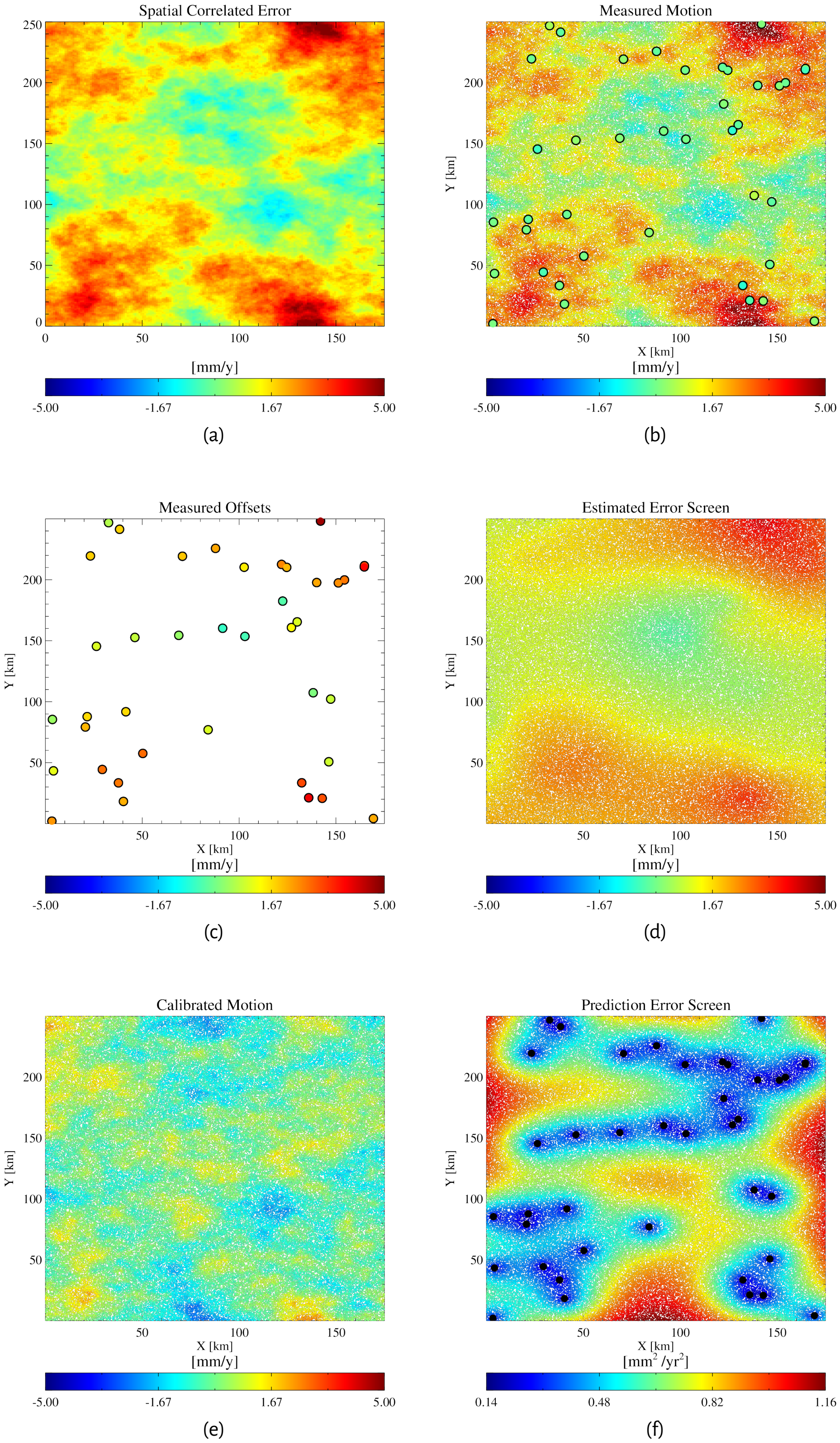

(a) (b)

(c) (d)

(e) (f)

Figure 5.2: The Figure shows an example of the framework used for the simulations. The simulated motion is 0 over the entire scene. In (**a**), the simulated spatially correlated noise is depicted. In (**b**), the dense Synthetic Aperture Radar Interferometry (InSAR) measurements and the coarse Global Navigation Satellite System (GNSS; large dots, atmosphere-free) are depicted. In (**c**), the measured offsets InSAR/GNSS ($\underline{\Delta}_0$) are depicted. In (**d**), the estimated error screen to be removed from (**b**) is depicted. In (**e**), the final results obtained by calibrating (**b**) with (**d**) are depicted. In (**f**), the estimated error for the merged product is depicted.

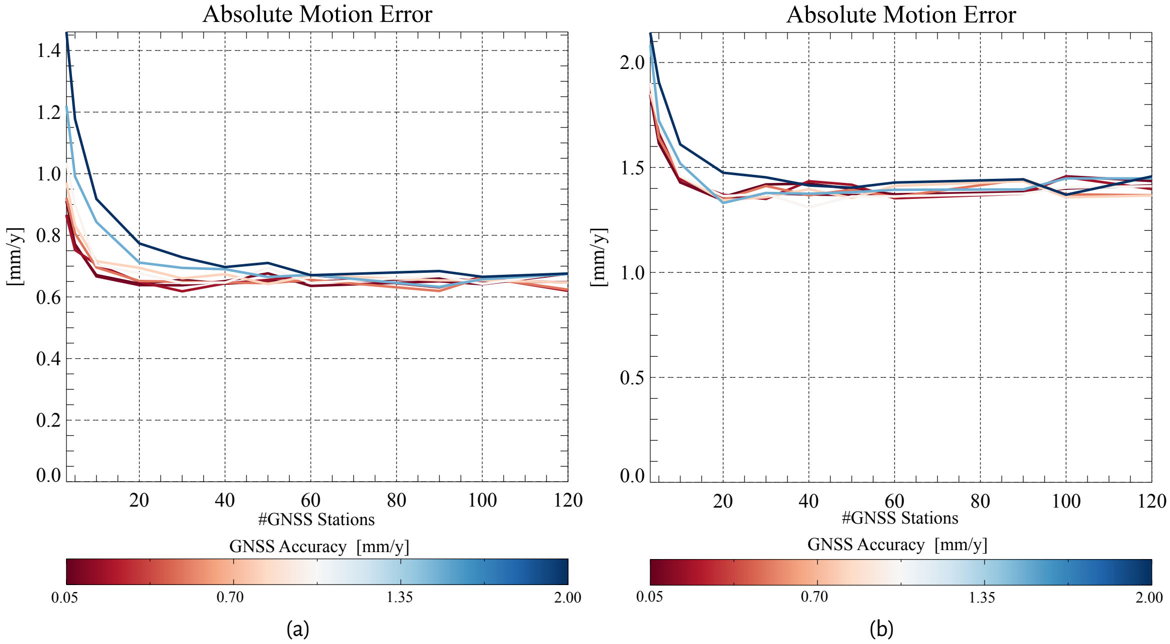

Figure 5.3: Performance simulations in retrieving $\widehat{v}_{ref}$ carried out with different atmospheric noise sills: (**a**) σ_α^2 =2 mm^2/y^2 and (**b**) σ_α^2 =9 mm^2/y^2.

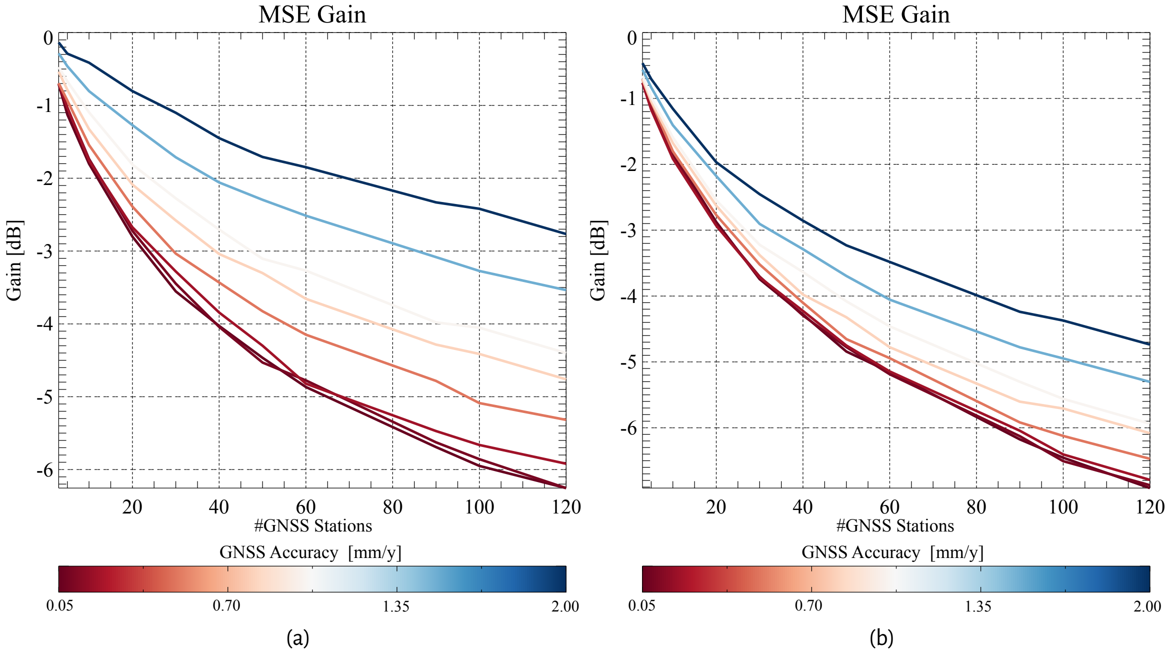

Figure 5.4: Performance simulations in retrieving $\widehat{\delta}$ carried out with different atmospheric noise sills: (**a**) σ_α^2 =2 mm^2/y^2 and (**b**) σ_α^2 =9 mm^2/y^2.

Track	Orbit	Acquisitions	Time [years]	GNSS Stations
088	ASCE	140	3.4	47
037	DESCE	122	3.0	37

Table 5.1: Netherlands Dataset.

also not being continental drift compensated in order to make the two data-sets “compatible”. After merging (also adding v_{ref}), the data contains continental drift that could dominant the visualization. Therefore, plate movement was compensated using the model in (93) to show movement relative to a specific plate (Eurasian). The removed motion is basically an overall offset of several mm/y, plus a light ramp due to the LoS projection of the horizontal motion. This is generally not necessary since it is only a representation issue, but it facilitates the interpretation of the results.

5.3.1 Netherlands Datasets

The systematic generation of deformation maps on a national scale using SAR interferometry has become more feasible, as missions like Sentinel-1 provide global coverage on a regular basis. Often, these kinds of services must be combined with existing geodetic measurements in order to make them integrated and comparable (59). In this work, a typical example is provided where InSAR velocities covering a large area—acquired in descending and ascending passes—are combined with a consistent number of GNSS-derived velocities. The considered datasets are two Sentinel-1A/B stacks covering the northern part of the Netherlands. The area includes many examples of man-induced subsidences, such as in Groeningen (61). The details of the dataset are described by Table 5.1. Observing the raw result of the PSI-processing, some spatially correlated deformation signals are visible when observing between ±4 mm/y. Since no large-scale deformation phenomena are expected in this area, such patterns must therefore be related to the residual atmospheric signal. In the area of interest, a considerably high number of GNSS data are available (see Table 5.1). The previously described methodology was applied to the data using the available GNSS measurements (77). The results in Figures 5.5 and 5.6 show how the technique permits the further reduction of the residual atmospheric error and the relation of every single PS measurement to the Eurasian plate only.

5.3.2 North Anatolian Fault Dataset

Applications related to the measurement of tectonic movements are the most challenging for InSAR. The requirement of an accuracy of 1 mm/y at more that 100 km (< 10 nstrain) pushes the technique to its limits (104). Notwithstanding, it has been demonstrated that, since actual SAR missions have very strict requirements about oscillators stability (**?**) and very good orbit knowledge (107; 83), such numbers can be considered achievable. The major limitation is atmospheric effects. If the interferometric time series is not long enough, integration with other data would be necessary in order to fulfill the requirements at very large distances. Moreover, the possibility of referencing the measurements to standard reference systems (e.g. Eurasian Plate, etc.) would extend the usability of the final results.

The technique must then also be demonstrated on an appropriate example for tectonics. The North Anatolian Fault was chosen, as it is a typical case study investigated by many geo-scientists using SAR interferometry (13; 54). The area of interest is covered by a Sentinel-1A/B stripe extending for more than 600 km in the along-track direction, see Table 5.2. In order to make the processing feasible, the stripe was divided into three frames. The three frames were processed independently using the PSInSAR technique. The area is tectonically very active, hence in order to be able to catch the deformation signal it is very important to preserve all tspatial frequencies of the meaasured pattern. Figure 5.7 displays the results together with a mapping of the main path of the North and East Anatolian Fault (dashed white line).

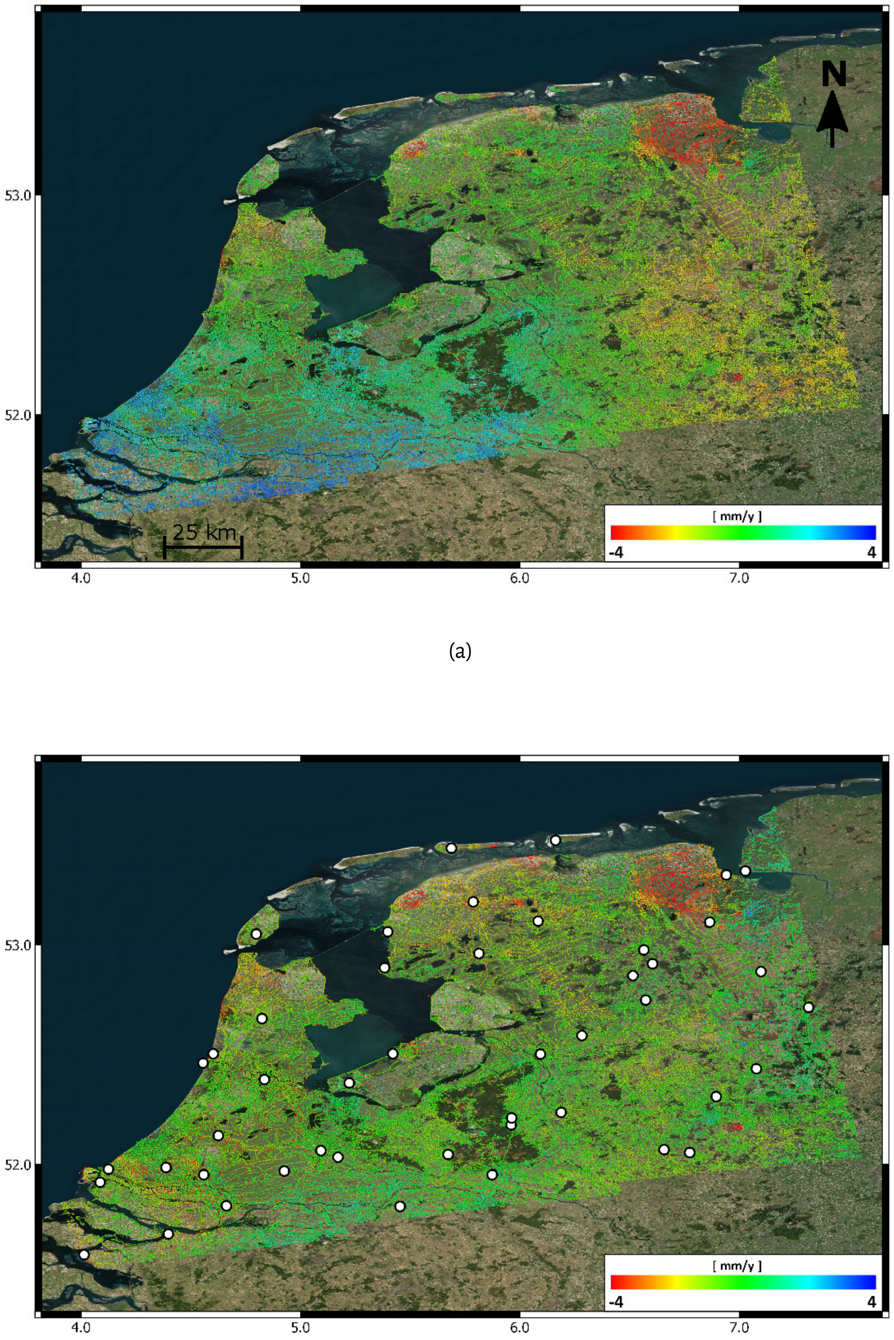

(a)

(b)

Figure 5.5: Results for the ascending Netherlands stack (**a**) before and (**b**) after performing merging with GNSS data. In (**b**), the GNSS stations used are displayed with black–white circles.

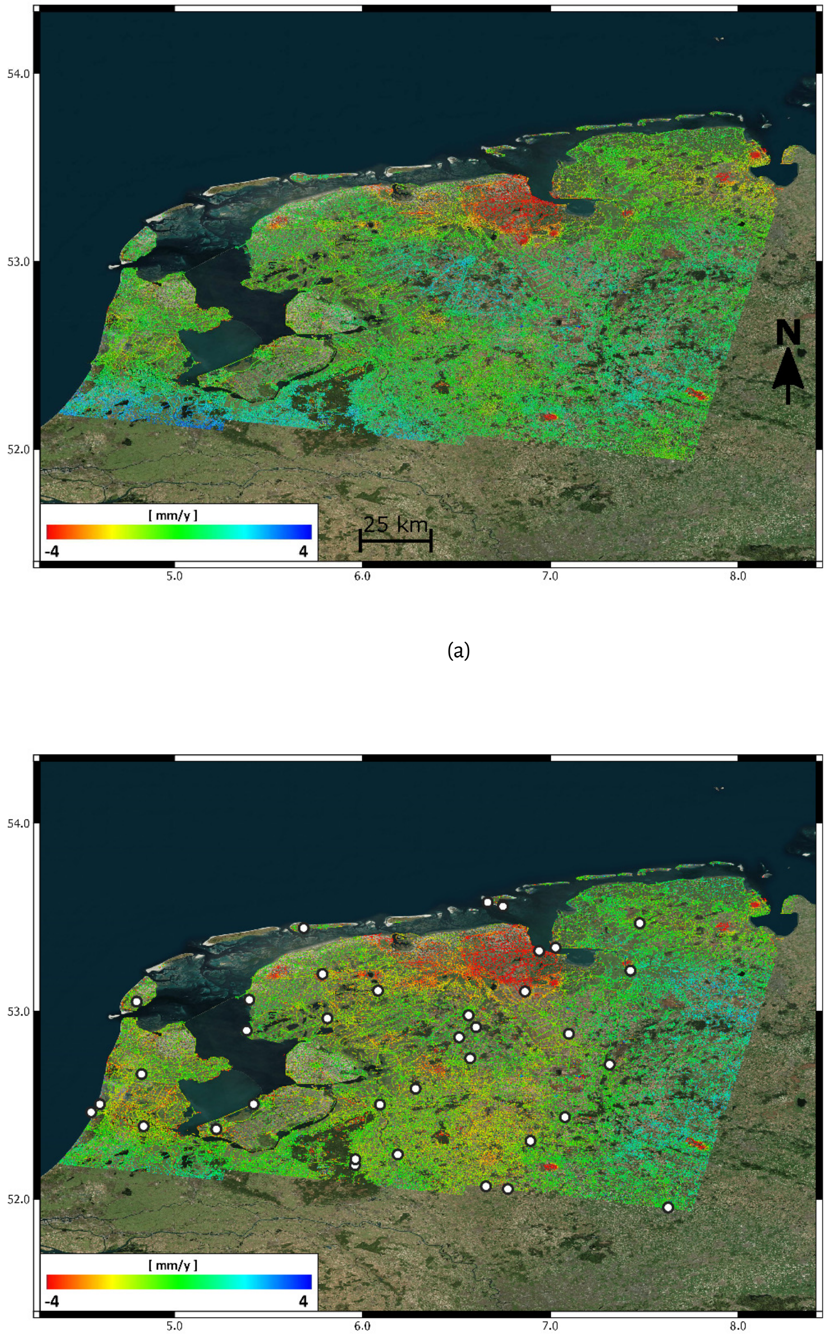

(a)

(b)

Figure 5.6: Results for the descending Netherlands stack, showing (**a**) before and (**b**) after performing merging with GNSS data. In (**b**), the GNSS stations used are displayed with black–white circles.

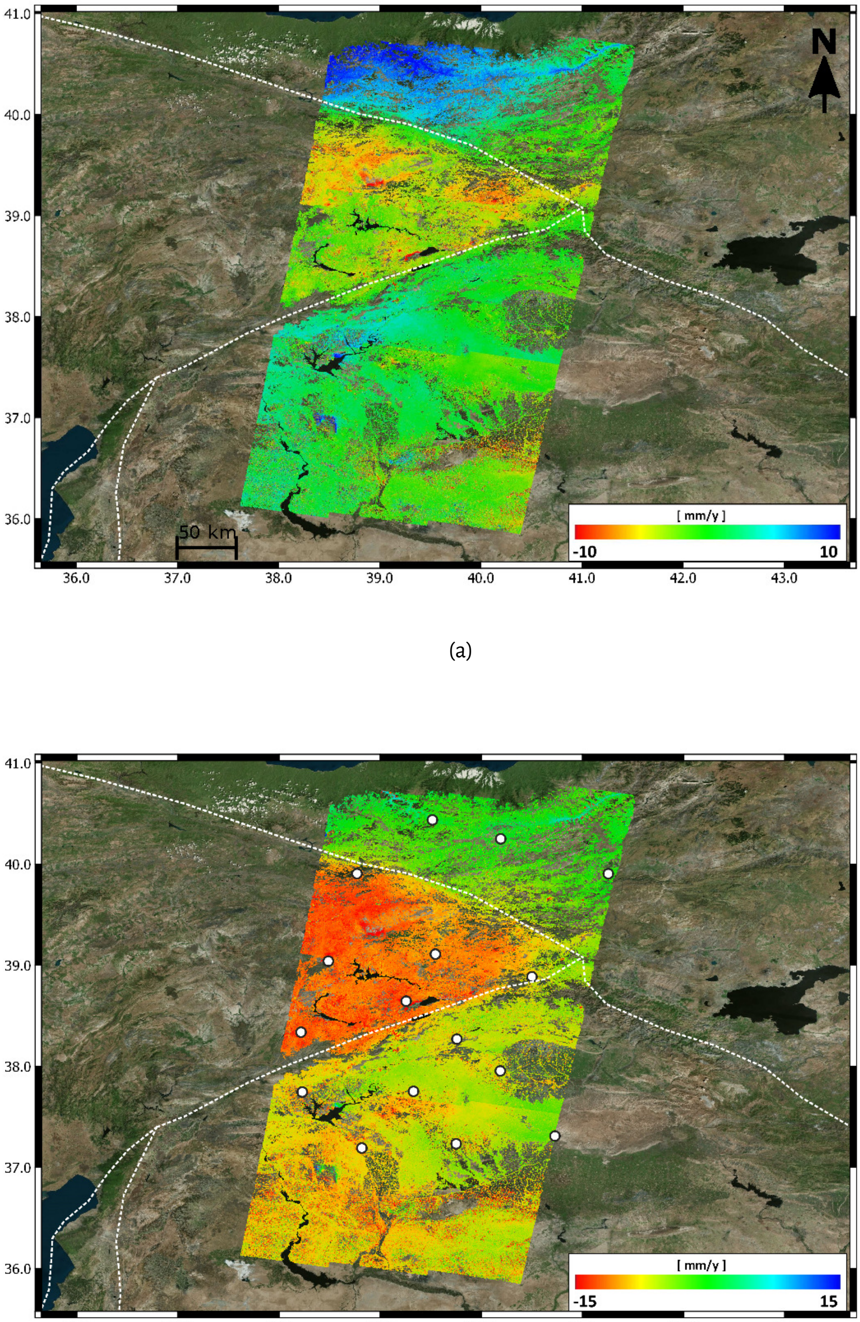

(a)

(b)

Figure 5.7: Results for the North Anatolian Fault (**a**) before and (**b**) after performing merging with GNSS data. In (**b**), the GNSS stations used are displayed with black–white circles and the fault lines are displayed using a white dashed line.

Track	Orbit	Acquisitions	Time [years]	GNSS Stations
123/2	DESCE	134	3.3	5
123/3	DESCE	134	3.3	9
123/4	DESCE	134	3.3	4

Table 5.2: North Anatolian Fault Dataset.

5.4 Conclusions

The results show how the technique is able to both remove dependence on the reference point and mitigate residual atmospheric errors present in the final InSAR results under a set of relatively straightforward assumptions.

The method was studied on both simulated and real data. Simulations show that even with a reduced set of GNSS stations it is possible to retrieve the absolute motion with good accuracy. On the other hand, the capability of the approach to mitigate residual atmospheric errors depends both on the GNSS station density and the spatial correlation of the errors. In order to provide some numbers, the error was modeled as an $AR(1)$ process with a correlation length of 60 km and variable overall variance. Two real test cases were then processed to demonstrate the approach by trying to address applications that should benefit from the technique. The extension of the approach to time series would also be interesting, merging InSAR phases with continuous GNSS measurements. The approach could be conceptually equivalent, since the deformation rates are just a scaling of the single-phase measurements, but the spatial covariance of each interferogram would be needed.

In general, it is possible to conclude that the developed method helps to increase, when necessary, the accuracy of InSAR over large distances (44). The final product has the spatial coverage of InSAR, and is an optimal combination of InSAR and GNSS information based on the knowledge of the error statistics. All the spatial frequencies of the deformation signal are preserved moreover a characterization of the final product error is allowed.

6 Conclusion and future developments

Observing surface strain on Earth is a crucial topic in various branches of geoscience. Its behavior can be in fact related, inverting mathematical models, to processes happening below the surface that cannot be directly observed and measured. Therefore, measuring strain and understanding its precision are fundamental for developing and solving inverse problems that model internal processes.

The relative nature of interferometry makes InSAR measurements particularly suitable for this task. However, depending on the scale and intensity of surface deformation, the technique can face inherent limitations. Thus, a thorough understanding of measurement performance is essential, and in extreme cases, exploring approaches to mitigate these limitations is necessary.

This dissertation is aimed to explore these issues using the scale of the observed phenomena as the independent variable. Referring to Figure 1.1 it can be concluded that various deformation phenomena have been considered based on their spatial scale, with a focus on InSAR's ability to detect them. Additionally, several ad-hoc solutions have been proposed to address limitations that could impede the accurate detection of deformation patterns.

In Chapter 3 the case of very strong deformation patterns on a relatively small spatial scales has been presented. In this situation the difficulty in the phase unwrapping procedure can be a show-stopper in retrieving information from the radar data. For this case a framework that allows the interpretation of the wrapped SAR interferograms directly has been presented together with three different examples of potential applications. In particular:

- for earthquake source modeling, the direct interpretation of phase gradients in terms of strain tensor projection has been investigated. Although this approach is sub-optimal, as it disregards information in the low-pass component of the deformation phase, it can be useful in certain areas to avoid artifacts related to unwrapping errors..

- for resolving strain and rotation in glacier flow, the proposed interpretation is highly effective, as these observables are inherently differential and do not require the integration process involved in phase unwrapping

- for grounding zone characterization, gradient interpretation significantly simplifies the unwrapping process by reducing its dimensionality to 1D and exploiting a physical model to support the operation.

In Chapters 4 and 5, a dual situation has been investigated. In case of mild deformations spanned over large areas primary challenge is the technique's ability to detect the deformation. Atmospheric effects (troposphere and/or ionosphere) and other systematic biases (orbit accuracies, clocks, dielectric effects...) can significantly reduce the accuracy of InSAR measurements, thereby limiting their applicability. Specifically, the measurement of tectonic strain requires extremely high precision, typically on the order of centimeters over hundreds of kilometers on a single interferogram. Achieving this level of accuracy often necessitates external corrections for some of these systematic biases.

In Chapter 4 the performance of InSAR, following the correction of certain systematic biases, has been investigated. This study includes a modeling phase and tests conducted across numerous test sites worldwide, as well as a validation exercise. The modeling provides the tools to define confidence interval for the InSAR results based on the scale of the observed motion. The testing and validation phases aid in predicting the expected InSAR performance for future missions, taking into account the accuracy of the applied corrections.

In Chapter 5,an approach has been proposed for integrating InSAR and GNSS measurements. This integration is frequently employed in geophysical studies as it combines the high spatial resolution of InSAR measurements with the accuracy of GNSS data. In alignment with the objectives of this study, an algorithm has been developed to optimize this fusion by leveraging the error characterization of the measurements.

Further investigations and developments are recommended. Additional efforts should focus on improving the semi-automatic detection of the grounding line and its operationalization. Utilizing previous results as a-priori information, the algorithm could enable a fully automatic approach, facilitating the systematic application to the extensive Sentinel data acquired in polar regions.

A better understanding of performance degradation due to topography-troposphere interaction (stratification) is also desirable. Although several studies have shown that ECMWF corrections significantly reduce this effect, a physical model that accurately describes InSAR phase precision in these cases is still needed.

Finally, extending the GNSS-InSAR integration to interferogram time series appears feasible, provided that GNSS time series with error descriptions are available.

A

Parizzi, A., Abdel Jaber W. (2018). Estimating Strain and Rotation From Wrapped SAR Interferograms. IEEE Geoscience and Remote Sensing Letters, 15(9):1367-1371

Summary This letter aims to discuss a general framework that allows the direct interpretation of the wrapped differential synthetic aperture radar interferometry phase in terms of surface strain S and rotation R components. The methodology is demonstrated showing the estimation of strain and rotation components of a glacier flow using three TerraSAR-X interferometric geometries (ascending right-looking, descending right-looking, and descending left-looking). Finally, since the leftlooking geometry can be difficult to obtain on a regular basis, the surface parallel flow assumption is extended to the phase gradients inversion in order to reduce the amount of necessary geometries from three to two.

Contributions of the candidate Initiator of this work, including the development of the method. Practical implementation and testing with the data sets. Writing the paper.

Estimating Strain and Rotation From Wrapped SAR Interferograms

Alessandro Parizzi and Wael Abdel Jaber

***Abstract*—This letter aims to discuss a general framework that allows the direct interpretation of the wrapped differential synthetic aperture radar interferometry phase in terms of surface strain *S* and rotation *R* components. The methodology is demonstrated showing the estimation of strain and rotation components of a glacier flow using three TerraSAR-X interferometric geometries (ascending right-looking, descending right-looking, and descending left-looking). Finally, since the left-looking geometry can be difficult to obtain on a regular basis, the surface parallel flow assumption is extended to the phase gradients inversion in order to reduce the amount of necessary geometries from three to two.**

***Index Terms*—Differential synthetic aperture radar interferometry (DInSAR), frequency estimation, glaciers flow, gradient tensor, rotation, strain.**

I. INTRODUCTION AND MOTIVATION

INTERFEROMETRIC measurements can be directly related to the spatial gradients of the motion [1]–[4]. The idea is to exploit this property to resolve between strains and rotation components without the need to unwrap the interferometric phase. This letter deals first with the theoretical framework: the direct problem is described showing the link between the gradient tensor and the interferometric phase gradients. The inversion is then discussed in the general case of N available geometries. In Section III, it is shown how the interferometric measurements, necessary for the problem inversion, can be obtained by estimating the local fringe frequency, avoiding therefore phase unwrapping [5]. Finally, the method is tested on Darwin Glacier (Antarctica). Strain and rotation components are inverted in two scenarios: first using three interferometric lines of sight (LoSs), then using two LoSs and assuming surface parallel flow. The study of a glacier flow has been used as test case for the methodology since the measurement of strains is a relevant topic for glaciology [6]. However, the use of the interferometric phase in glaciological applications is limited by the large amount of motion that makes phase unwrapping very challenging. Therefore, such measurements are presently computed mainly using correlation techniques [7]. This letter proposes a methodology that, by relying on more than one acquisition geometry, exploits directly interferometric phase avoiding the phase unwrapping. Furthermore, improving also significantly the estimation accuracy. This is due to the inherent frequency-bandwidth gain. Such gain can be computed from cross correlation and interferometric phase accuracy expressions (σ^2_{corr} and σ^2_{ϕ}). Being f_0 the central frequency of the sensor and B the signal bandwidth, such ratio is $(\sigma^2_{\text{corr}}/\sigma^2_{\phi}) = (12\ f_0^2/B^2)$ [8] assuming the measurements resolution the same. The aforementioned accuracy ratio is considerable, 50 dB for Sentinel IW mode. For PALSAR-2 Stripmap mode between 34 and 43 dB and about 47 dB in the specific case of the TerraSAR-X Stripmap used for this letter.

II. GRADIENT TENSOR FROM INTERFEROMETRIC SYNTHETIC APERTURE RADAR MEASUREMENTS

Considering a synthetic aperture radar (SAR) interferogram, where all the topographic components have been compensated, and neglecting the atmospheric delay, the expression of the absolute interferometric phase will be

$$\phi = \frac{4\pi}{\lambda}\boldsymbol{\delta} \cdot \boldsymbol{s} \tag{1}$$

where λ is the wavelength and (e, n, υ) is the reference system oriented in accordance with the local east, the local north, and the geodetic vertical. The change in radar range can be written as the projection of the displacement vector $\boldsymbol{\delta} = [\delta_e, \delta_n, \delta_\upsilon]$ on the sensing direction of the radar $\boldsymbol{s}$. In order to be able to separate the strain and rotation components, the gradient tensor $\boldsymbol{\Psi}$ has to be estimated [9]. The gradient tensor $\boldsymbol{\Psi}$[1] represents the derivatives of $\boldsymbol{\delta}$

$$\boldsymbol{\Psi} = \left[\begin{array}{cc|c} u_{ee} & u_{en} & u_{e\upsilon} \\ u_{ne} & u_{nn} & u_{n\upsilon} \\ u_{\upsilon e} & u_{\upsilon n} & u_{\upsilon\upsilon} \end{array}\right]. \tag{2}$$

Since a single SAR interferometric pair is not able to provide resolution/sampling in the third dimension [10], it is not possible to perform derivative measurements along the υ-axis. Therefore, the third column of the gradient tensor cannot be observed. Hence, the displacement gradients observed in the sensing direction of the radar can be written as

$$\vec{\nabla}(\boldsymbol{\delta} \cdot \boldsymbol{s}) = \boldsymbol{\Psi}^T \cdot \mathbf{s} = \frac{\lambda}{4\pi}\vec{\nabla}\phi. \tag{3}$$

Manuscript received November 2, 2017; revised February 16, 2018 and May 3, 2018; accepted May 16, 2018. Date of publication June 20, 2018; date of current version August 27, 2018. This work was supported by Helmoltz Alliance Remote Sensing and Earth System Dynamics. *(Corresponding author: Alessandro Parizzi.)*

The authors are with the Remote Sensing Technology Institute, German Aerospace Center, 82230 Wessling, Germany (e-mail: Alessandro.Parizzi@dlr.de).

Digital Object Identifier 10.1109/LGRS.2018.2838763

[1] For the sake of simplicity, the notation $u_{ij} = \partial\delta_i/\partial j$ will be used to identify the derivatives from now on.

Equation (3) is a vector providing the derivatives of $\boldsymbol{\delta}\cdot\boldsymbol{s}$ with respect to the north and the east directions. Hence, to retrieve the six components of $\boldsymbol{\Psi}$, at least three diverse interferometric measurements are needed.

A. Problem Inversion

In (3), the direct problem that links the phase gradients measurements with the gradient tensor $\boldsymbol{\Psi}$ has been defined. Let us now suppose that in a general case we have N gradient measurements in N different geometries. $C_{d,k}$ is the covariance matrix relative to the kth acquisition geometry, $\boldsymbol{\Psi}$ can be inverted in the least square sense by minimizing the figure of merit M with respect to each u_{ij}

$$M = \sum_{k=0}^{N-1} \left(\frac{\lambda_k}{4\pi} \vec{\nabla}\phi_k - \boldsymbol{\Psi}(u_{ij})^T \cdot \mathbf{s}_k \right)^T C_{d,k}^{-1} \times \left(\frac{\lambda_k}{4\pi} \vec{\nabla}\phi_k - \boldsymbol{\Psi}(u_{ij})^T \cdot \mathbf{s}_k \right). \quad (4)$$

The inversion is completely analogous to the inversion of the 3-D displacement vector [11]–[13]. Therefore, all the considerations regarding the performance with diverse acquisition geometries are valid also for the inversion of (3).

B. Separation Between Strain and Rotation Components

$\boldsymbol{\Psi}$ represents the first-order Taylor approximation of the displacement field and it contains the information about all the relative movements of the portion of surface which it represents. The gradient tensor can be then decomposed in its symmetrical and antisymmetrical parts. Those are, respectively, the strain $\boldsymbol{S}$ and rotation $\boldsymbol{R}$ components [9]

$$\boldsymbol{S} = \frac{1}{2}(\boldsymbol{\Psi} + \boldsymbol{\Psi}^T) = \left[\begin{array}{cc|c} u_{ee} & \frac{u_{en}+u_{ne}}{2} & \frac{u_{ve}}{2} \\ \frac{u_{ne}+u_{en}}{2} & u_{nn} & \frac{u_{vn}}{2} \\ \hline \frac{u_{ve}}{2} & \frac{u_{vn}}{2} & 0 \end{array} \right]$$

$$\boldsymbol{R} = \frac{1}{2}(\boldsymbol{\Psi} - \boldsymbol{\Psi}^T) = \left[\begin{array}{cc|c} 0 & \frac{u_{en}-u_{ne}}{2} & -\frac{u_{ve}}{2} \\ \frac{u_{ne}-u_{en}}{2} & 0 & -\frac{u_{vn}}{2} \\ \hline \frac{u_{ve}}{2} & \frac{u_{vn}}{2} & 0 \end{array} \right]. \quad (5)$$

Since the derivatives with respect to v-direction (u_{ev}, u_{nv}, u_{vv}) are missing [see (2)], only the 2×2 upper part of $\boldsymbol{S}$ and $\boldsymbol{R}$ tensors can be properly characterized. Consequently, the third line and the third column of $\boldsymbol{S}$ and $\boldsymbol{R}$ end up being basically the same. This in practice means that even if the sensor is sensitive to the gradients of the vertical motion, it is not possible to resolve between a vertical tilt and a vertical extension/compression. It is worth mentioning that according to the theory [9], some assumptions could be made allowing the observation of more components of $\boldsymbol{\Psi}$ or reducing the set of equations needed and also improving the estimation accuracy. For instance, assuming that the ice is incompressible allows us to impose the first invariant of the strain tensor $I_S \equiv Tr(\boldsymbol{S}) \equiv 0$ deriving consequently also u_{vv} [7], [9]. Setting $S \equiv 0$, the problem reduces to a rotation only estimation [14]. However, this letter is mainly methodological; therefore, the aim is to present the problem in a general fashion. Case-specific considerations are left for application studies.

III. PHASE GRADIENTS ESTIMATION AVOIDING PHASE UNWRAPPING

In Section II, the general framework of the estimation of the strain and rotation components was outlined. It is now necessary to discuss how the gradient measurements $\vec{\nabla}\phi_k$ can be estimated from the complex interferograms. The interferogram is a complex number $z(r,a) = A(r,a)\exp(j\phi(r,a))$, where A is the product of master and slave reflectivity, (r,a) are the range and azimuth coordinates in radar geometry, and ϕ is the interferometric phase as in (1). Since in the case of glacier flow the interferometric phase varies by several wavelengths within the scale of the deformation pattern, it is possible to perform a local linear approximation of the deformation phase. Hence, at a given point (r_0, a_0), the interferogram z can be substituted by its first-order Taylor approximation

$$z \approx A \exp\left(j\frac{4\pi}{\lambda} \left(\frac{\partial \delta_s}{\partial r}(r - r_0) + \frac{\partial \delta_s}{\partial a}(a - a_0) \right) + \phi_0 \right) \quad (6)$$

where $\delta_s = \boldsymbol{\delta} \cdot \boldsymbol{s}$ is the projection of the displacement vector along the LoS. Equation (6) shows how the problem is basically the estimation of the main local fringe frequency of the interferogram. The problem can be solved in different ways with varying performance. Typically, the periodogram estimator is used [15]; however, this estimator assumes flat spectrum which is not the case for the interferograms. Moreover, in the case of very strong fringe patterns, such an estimator does not take into account the spectral shift effect [16], hence reducing the estimation performance. In such a case, the maximum likelihood approach proposed in [17] would be more suitable. In order to preserve the original interferometric information, the estimation of the main fringe frequency has to be performed directly from the single-look interferogram in radar geometry. This does not match with the direct problem stated in (3). A local transformation based on orbital information must hence be established between the geographic reference system used in Section II and the radar coordinates. Let $\boldsymbol{T}$ be the rotation matrix representing such a transformation. $\widetilde{\vec{\nabla}\phi}$ and $\widetilde{C_d}$, the phase gradients and their covariance matrix calculated in radar geometry, can be recomputed in the local reference system as

$$\begin{aligned} \vec{\nabla}\phi &= \boldsymbol{T}^T \widetilde{\vec{\nabla}\phi} \\ C_d &= \boldsymbol{T}^T \widetilde{C_d} \boldsymbol{T}. \end{aligned} \quad (7)$$

Fig. 1 shows an example of gradient estimation from a single-look interferogram for Darwin Glacier in Antarctica. Fig. 1(a) and (b) basically represents two of the six equations in (4) measured with respect to the radar coordinates ($\widetilde{\vec{\nabla}\phi}$ in (7)).

IV. STRAIN AND ROTATION OF ICE FLOW: EXAMPLE OF DARWIN GLACIER

As an illustration of the application of the proposed method, the estimation of the surface strain and rotation of

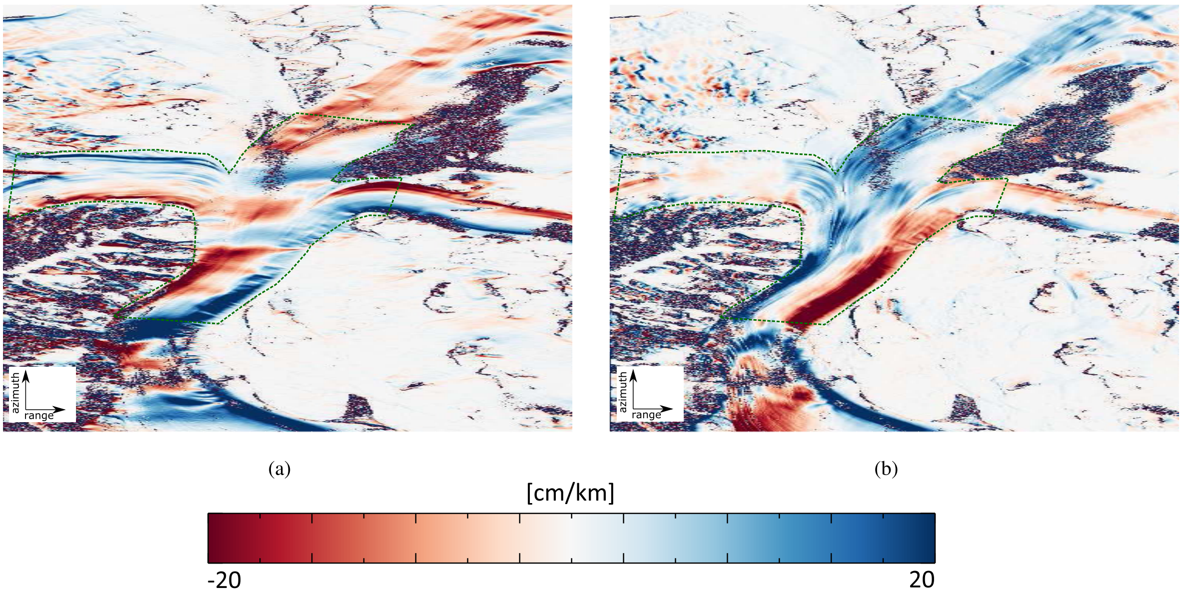

(a)

(b)

Fig. 1. Estimated gradients in radar geometry for the descending right-looking data set. The area of interest is highlighted by the dashed line. (a) Azimuth gradients. (b) Range gradients.

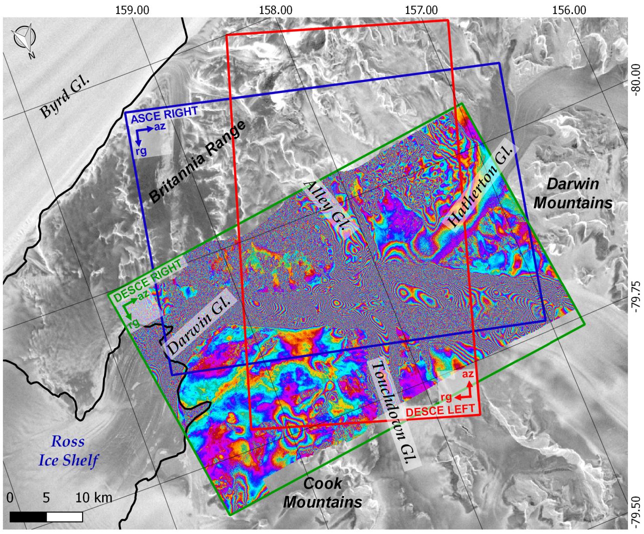

Fig. 2. Overview of the study area. The descending right-looking interferogram (April 20, 2017–May 01, 2017), the footprints of the three geometries, and the grounding line [18].

the Darwin Glacier has been investigated. Darwin Glacier (79°53′S 159°00′E) is an outlet glacier of the Transantarctic Mountains draining ice from the East Antarctic Ice Sheet into the Ross Ice Shelf. It flows in the east direction with a velocity of several tens of meters per year [11] between the Britannia Range and the Darwin Mountains to the south and the Cook Mountains to the north (see Fig. 2). The analysis focuses on the overlapping area of the three acquisition geometries covering the midsection of the glacier, including the junction with its tributaries Hatherton and Touchdown Glacier. Both tributaries feature a slower ice flow as can be seen from the descending right-looking interferogram in Fig. 2. The strain $\boldsymbol{S}$ and rotation $\boldsymbol{R}$ components have been first estimated using all three available geometries. The same inversion has been subsequently performed with two geometries only assuming the ice is flowing parallel to the glacier surface. A comparison of the two approaches follows at the end of this Section.

A. Inversion Using Three Acquisition Geometries

The framework proposed in Section II can support glaciological studies aimed at measuring and resolving the strain and rotation components of an ice flow. As previously mentioned, three different acquisition geometries are needed in order to be able to retrieve the six elements of $\boldsymbol{\Psi}$. Currently, SAR missions observe a given area on the Earth with ascending and descending geometries only. In cases where SAR footprints from different tracks strongly overlap, a third geometry is available for the inversion, nevertheless such a configuration has proved to be ill conditioned [13]. Hence, left-looking or squinted acquisitions have to be used in order to achieve a sufficient inversion accuracy [11], [13]. For this experiment, three TerraSAR-X Stripmap interferometric pairs have been acquired in ascending right-looking and descending right/left-looking (coverage is shown in Fig. 2). Acquisitions dates and geometries are summarized in Table I. The temporal distribution of the acquisitions is optimal since they have the minimal temporal baseline between the interferometric acquisitions, 11 days between the pairs and 1 day between the different geometries. Therefore, the observed motion can be assumed to be the same. Given the high latitude, the acquisitions result in high geometrical diversity providing good conditioning for the inverse problem. The TanDEM-X digital elevation model (DEM) [19] with posting of 0.8 arcsec in latitude and 0.4 arcsec in longitude was also available and has been used for coregistration and topographic phase removal. After the interferometric processing, the LoS gradients were

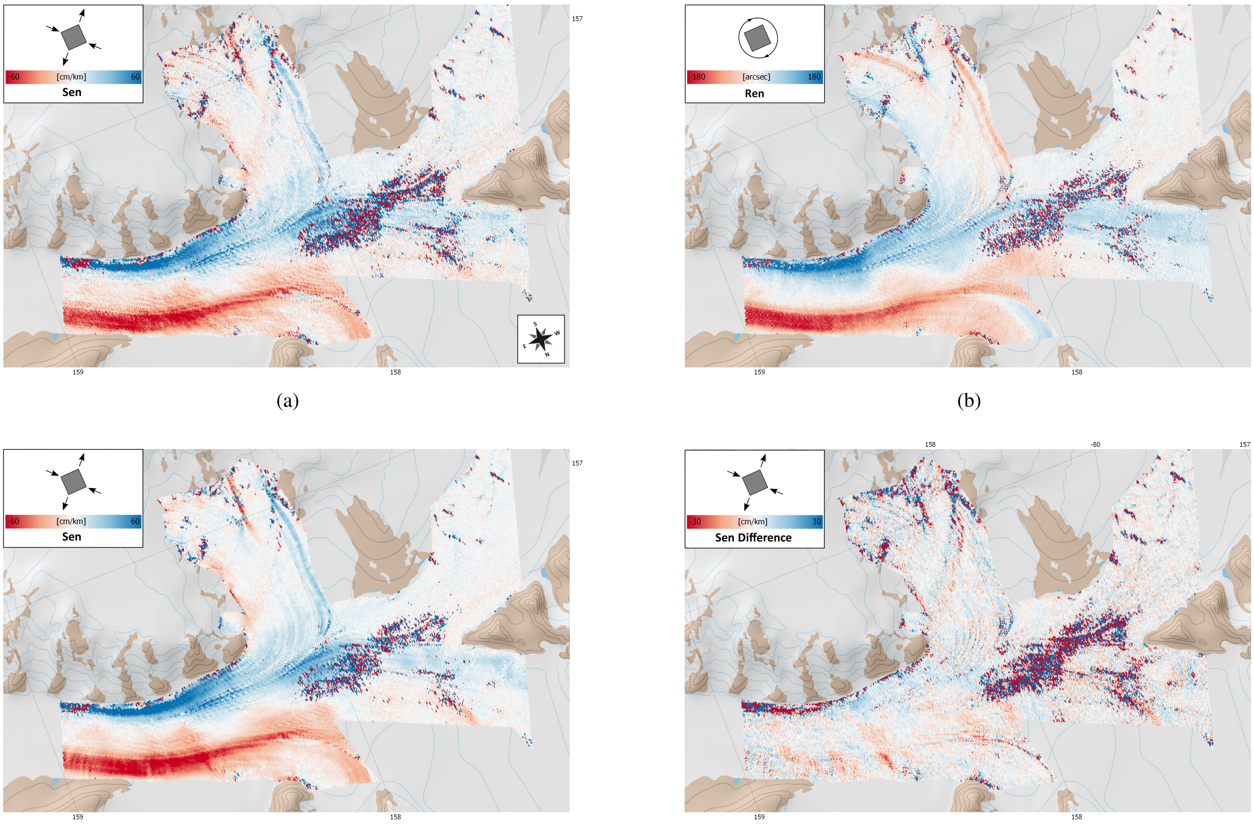

(a) (b) (c) (d)

Fig. 3. Separation of the estimated gradient tensor in strain and rotation components. (a) Shear component ($\boldsymbol{S}_{1,2}$) estimated using three LoSs. (b) Rotation component ($\boldsymbol{R}_{1,2}$) estimated using three LoSs. (c) Shear component ($\boldsymbol{S}_{1,2}$) estimated using two LoSs and assuming surface parallel flow. (d) Difference map between (a) and (c) ($\boldsymbol{S}^{3\text{LoS}}_{1,2} - \boldsymbol{S}^{2\text{LoS}}_{1,2}$).

TABLE I

DARWIN GLACIER TERRASAR-X ACQUISITIONS

Orbit	Look Dir.	θ_{inc}	Date
ASCE	right	28°	19-APR-2017
DESCE	right	31°	20-APR-2017
DESCE	left	46°	21-APR-2017
ASCE	right	28°	30-APR-2017
DESCE	right	31°	01-MAY-2017
DESCE	left	46°	02-MAY-2017

computed using estimation windows of about 180 m × 180 m sampled on a 90 m × 90 m raster (half a window overlap). As previously discussed, three LoSs are sufficient for a constraint-free inversion of the problem in (3). The components of the gradient tensor $\boldsymbol{\Psi}$ have then been inverted with respect to the geographic directions N/S and E/W, and the tensors $\boldsymbol{S}$ and $\boldsymbol{R}$ have been computed as shown in (5). In order to have a more intuitive measurement unit, the strain is displayed in [cm/km] and the rotation in [arcsec] (1 arcsec ≈ 0.0002°). Results are shown in Fig. 3.

B. Inversion Using Two Acquisition Geometries Assuming Surface Parallel Flow

Unfortunately, no SAR mission currently performs observation campaigns in left or squinted geometry on a regular basis. It is hence worth discussing some assumptions that allow the removal of two of the six equations in (4). The idea is to exploit the information provided by an external DEM by assuming that ice flows parallel to the surface [20], [21]. The topography profile is approximated with the plane tangent to the DEM and the displacement is imposed to lie on that plane. This can be done by fitting a plane to the DEM samples surrounding the area of interest. The plane can be fully characterized by its normal $\boldsymbol{n}_D$. It is then possible to set $\boldsymbol{\delta} \cdot \boldsymbol{n}_D = 0$ and differentiate with respect to e, n

$$\vec{\nabla}(\boldsymbol{\delta} \cdot \boldsymbol{n}_D) = \boldsymbol{\Psi}^T \cdot \boldsymbol{n}_D = \boldsymbol{0}. \tag{8}$$

Since the topography slope is assumed constant in the estimation window, it is possible to extract two more equations to retrieve the six parameters. For the sake of completeness, it has to be noted that now the equation system depends also on the quality of external data. This means that a covariance matrix $C_{d,\text{DEM}}$ has to be derived from the DEM error map to characterize the error of the two equations coming from (8). The ascending/descending right-looking TerraSAR-X data described in Table I have been used for this experiment. The TanDEM-X DEM used for the interferometric processing has also been used to determine the local perpendicular to the topography. A comparison of the three and two LoSs inversions is given in Fig. 3(a), (c), and (d). The results look spatially smooth except for an area that is decorrelated, probably due to the lack of backscatter intensity. The results obtained with the two approaches agree very well as can be seen from the difference plot [see Fig. 3(d)].

V. CONCLUSION

The presented methodology extracts LoS-projected gradients information from wrapped SAR interferograms and inverts the observable part of the gradient tensor. From this description of the motion, it is then possible to resolve between the gradient related to the surface deformation (strain) and the gradient representing a change in the orientation only (rotation). Since the measurements have no resolution along the vertical direction, no information about the gradients of the vertical motion is directly available. Hence, even if the vertical motion is very well captured by SAR interferometry, it will never be possible (without models/assumptions) to determine whether such movement is triggered by tilting or vertical deformation (compressions/extensions) of the observed surface. The framework has been tested using three interferometric geometries estimating the deformation of glacier flow. Moreover, the surface parallel flow assumption used in previous publications [20], [21] has been extended to the case of gradients tensor estimation. The results show good agreement between the two inversions; however, more glaciology-related assumptions should be discussed and tested in a more applicative context. Future work should also consider a validation campaign using *in situ* measurements.

ACKNOWLEDGMENT

The authors would like to thank Dr. D. Floricioiu for providing the TerraSAR-X data, Dr. R. Brcic for revising this letter, and Prof. A. Humbert and Dr. F. De Zan for the fruitful discussions.

REFERENCES

[1] M. Facchini and P. Zanetta, “Derivatives of displacement obtained by direct manipulation of phase-shifted interferograms,” *Appl. Opt.*, vol. 34, no. 31, pp. 7202–7206, Nov. 1995. [Online]. Available: http://ao.osa.org/abstract.cfm?URI=ao-34-31-7202

[2] D. Sandwell and E. Price, “Phase gradient approach to stacking interferograms,” *J. Geophys. Res.*, vol. 103, pp. 30183–30204, Dec. 1998.

[3] A. Sharov, “Gradient Approach to InSAR modelling of glacial dynamics and morphology,” in *Proc. 22nd EARSeL Symp.* Rotterdam, The Netherlands: Millpress, 2003, pp. 373–381.

[4] R. R. Forster, K. C. Jezek, L. Koenig, and E. Deeb, “Measurement of glacier geophysical properties from InSAR wrapped phase,” *IEEE Trans. Geosci. Remote Sens.*, vol. 41, no. 11, pp. 2595–2604, Nov. 2003.

[5] A. Parizzi and M. Eineder, “InSAR fringe frequency and deformation gradient. Application for geophysical modelling,” presented at the EGU General Assembly, Vienna, Austria, 2015.

[6] J. Nye, “The mechanics of glacier flow,” *J. Glaciol.*, vol. 2, no. 12, pp. 82–93, 1952.

[7] R. Michel and E. Rignot, “Flow of Glaciar Moreno, Argentina, from repeat-pass Shuttle Imaging Radar images: Comparison of the phase correlation method with radar interferometry,” *J. Glaciol.*, vol. 45, no. 149, pp. 93–100, 1999.

[8] R. Bamler and M. Eineder, “Accuracy of differential shift estimation by correlation and split-bandwidth interferometry for wideband and delta-k SAR systems,” *IEEE Geosci. Remote Sens. Lett.*, vol. 2, no. 2, pp. 151–155, Apr. 2005.

[9] C. J. van der Veen, *Fundamentals of Glacier Dynamics*. Boca Raton, FL, USA: CRC Press, 2013.

[10] F. Banda, J. Dall, and S. Tebaldini, “Single and multipolarimetric P-band SAR tomography of subsurface ice structure,” *IEEE Trans. Geosci. Remote Sens.*, vol. 54, no. 5, pp. 2832–2845, May 2016.

[11] T. J. Wright, B. E. Parsons, and Z. Lu, “Toward mapping surface deformation in three dimensions using InSAR,” *Geophys. Res. Lett.*, vol. 31, no. 1, p. L01607, 2004.

[12] L. Gray, “Using multiple RADARSAT InSAR pairs to estimate a full three-dimensional solution for glacial ice movement,” *Geophys. Res. Lett.*, vol. 38, no. 5, p. l05502, Mar. 2011, doi: 10.1029/2010GL046484.

[13] H. Ansari, F. De Zan, A. Parizzi, M. Eineder, K. Goel, and N. Adam, “Measuring 3-D surface motion with future SAR systems based on reflector antennae,” *IEEE Geosci. Remote Sens. Lett.*, vol. 13, no. 2, pp. 272–276, Feb. 2016.

[14] P. López-Dekker, P. Prats, F. De Zan, D. Schulze, G. Krieger, and A. Moreira, “TanDEM-X first DEM acquisition: A crossing orbit experiment,” *IEEE Geosci. Remote Sens. Lett.*, vol. 8, no. 5, pp. 943–947, Sep. 2011.

[15] S. Kay and R. Nekovei, “An efficient two-dimensional frequency estimator,” *IEEE Trans. Acoust., Speech, Signal Process.*, vol. 38, no. 10, pp. 1807–1809, Oct. 1990.

[16] F. Gatelli, A. Monti Guamieri, F. Parizzi, P. Pasquali, C. Prati, and F. Rocca, “The wavenumber shift in SAR interferometry,” *IEEE Trans. Geosci. Remote Sens.*, vol. 32, no. 4, pp. 855–865, Jul. 1994.

[17] A. M. Guarnieri and S. Tebaldini, “ML-based fringe-frequency estimation for InSAR,” *IEEE Geosci. Remote Sens. Lett.*, vol. 7, no. 1, pp. 136–140, Jan. 2010.

[18] R. Bindschadler *et al.*, “Getting around Antarctica: New high-resolution mappings of the grounded and freely-floating boundaries of the Antarctic ice sheet created for the International Polar Year,” *Cryosphere*, vol. 5, no. 3, pp. 569–588, 2011. [Online]. Available: http://www.the-cryosphere.net/5/569/2011/

[19] G. Krieger *et al.*, “TanDEM-X: A satellite formation for high-resolution SAR interferometry,” *IEEE Trans. Geosci. Remote Sens.*, vol. 45, no. 11, pp. 3317–3341, Nov. 2007.

[20] I. R. Joughin, R. Kwok, and M. A. Fahnestock, “Interferometric estimation of three-dimensional ice-flow using ascending and descending passes,” *IEEE Trans. Geosci. Remote Sens.*, vol. 36, no. 1, pp. 25–37, Jan. 1998.

[21] O. Lang, B. T. Rabus, and S. W. Dech, “Velocity map of the Thwaites Glacier catchment, West Antarctica,” *J. Glaciol.*, vol. 50, no. 168, pp. 46–56, 2004.

B

Parizzi, A. (2019). Inversion of the Slip Distribution of an Earthquake From InSAR Phase Gradients: Examples Using Izmit Case Study. IEEE Geoscience and Remote Sensing Letters, 16(11):1726-1730

Summary This letter investigates the estimation of the slip distribution of a seismic event using the information provided by interferometric phase gradients. Even if the technique is expected to be suboptimal when compared with an estimation using the unwrapped interferometric phase, such an approach would permit to avoid the solution of phase ambiguities also including the parts of the interferogram that could not be reached by the phase unwrapping otherwise. This specifically addresses the cases where the motion gradients are so strong that particular areas have to be masked out due to unwrapping errors. Aim of this letter is to propose a possible way to include such areas modeling the motion with phase gradients. The rationale of this letter relies on the description of the coseismic motion given by the Okada model that provides both the 3-D surface displacement and the gradient tensor information. Based on the latter, this letter defines an inversion strategy that uses the information extracted by the phase gradients, hence avoiding phase unwrapping. This technique is tested on real test sites and compared with the results obtained using the absolute phase.

Contributions of the candidate Initiator of this work. Development and testing of the method. Writing the paper.

Inversion of the Slip Distribution of an Earthquake From InSAR Phase Gradients: Examples Using Izmit Case Study

Alessandro Parizzi

***Abstract*— This letter investigates the estimation of the slip distribution of a seismic event using the information provided by interferometric phase gradients. Even if the technique is expected to be suboptimal when compared with an estimation using the unwrapped interferometric phase, such an approach would permit to avoid the solution of phase ambiguities also including the parts of the interferogram that could not be reached by the phase unwrapping otherwise. This specifically addresses the cases where the motion gradients are so strong that particular areas have to be masked out due to unwrapping errors. Aim of this letter is to propose a possible way to include such areas modeling the motion with phase gradients. The rationale of this letter relies on the description of the coseismic motion given by the Okada model that provides both the 3-D surface displacement and the gradient tensor information. Based on the latter, this letter defines an inversion strategy that uses the information extracted by the phase gradients, hence avoiding phase unwrapping. This technique is tested on real test sites and compared with the results obtained using the absolute phase.**

***Index Terms*— Differential SAR interferometry, fault modeling, frequency estimation, gradient tensor.**

I. INTRODUCTION

THE phase unwrapping is the main limitation factor for the exploitation of the repeat-pass interferometry. The presence of noise and the strong deformation gradients can, in fact, lead to a wrong interpretation of the phase ambiguities and, consequently, the generation of errors that propagates in space. Such errors are particularly hard to handle since they cannot be reduced by spatial averaging. This problem is an issue in applications working with the geophysical modeling of a single interferometric pair. A possible solution, where a modeling of tectonic fault is carried out by directly using the wrapped interferometric phase, has been proposed in [1] and [2]. This avoids, of course, the phase unwrapping, but it has the drawback of having non-Gaussian distributed misfits [1]. Therefore, the inversion of the system implies the choice of the proper ambiguity band that fits the model, making the problem anyway similar to a phase unwrapping. The idea of using the phase gradients to interpret the geophysical phenomena was, hence, often considered [3], [4]. This should extend the spatial range of exploitation of the SAR interferograms since it permits to include also isolated spots of the coherent phase. However, the interpretation of a phenomena using its derivatives has the drawback of filtering its high-pass component only [3]. This results in a significant reduction of the SNR since small scales of natural phenomena contain, in general, less signal. Nonetheless, in case of strong motions compared to the radar wavelength, the gradients SNR is acceptable, and such information can be important, especially in areas that cannot be reached due to the unwrapping errors.

Ali and Feigl [5] modeled the displacement induced by volcanic activity using interferometric phase gradients. This letter investigates the use of phase gradients also for fault slip distribution inversion. The aim is to keep a methodological point of view, focusing the attention mainly on the remote sensing aspects. In Sections II and III, the problem is defined from the radar measurement point of view, and in Section IV, it is then applied to real data. In order to discuss the methodology, a particular example has been chosen. The ERS interferogram of the Izmit earthquake is a typical case, where the phase unwrapping can critically influence the results [2], and hence, it has been analyzed in this letter. The approach has been applied to the data, and the results are compared with the results obtained using the absolute phase, discussing them in the light of the theoretical expectations.

II. INSAR PHASE GRADIENTS' MEASUREMENTS

The key feature of the technique is the possibility of estimating phase gradients directly from the wrapped interferometric phase. The problem can be seen in different ways. The point of view of this letter is to see the deformation gradients as proportional to the main local fringe frequency since the frequency is, by definition, the derivative of the phase. The gradient measurements $\vec{\nabla}\phi_k$ can be, hence, estimated from the single-look complex data performing a frequency estimation. Multilooking and subsampling are anyhow implicit in the fringe frequency estimation since the computation is done windowwise. Nevertheless, this allows theoretically identifying the gradients that would not be any more visible at the multilooked interferogram level due to the resolution reduction. Being (r, a) the range and azimuth coordinates in radar geometry, the interferogram is a complex number $z(r, a)$. Considering the interferometric phase varying by several wavelengths within the scale of the

Manuscript received June 10, 2018; revised August 1, 2018, October 24, 2018, and March 7, 2019; accepted March 29, 2019. Date of publication May 15, 2019; date of current version October 30, 2019. This work was supported by Helmoltz Alliance Remote Sensing and Earth System Dynamics.

The author is with the Remote Sensing Technology Institute, German Aerospace Center (DLR), 82234 Weßling, Germany (e-mail: alessandro.parizzi@dlr.de).

Digital Object Identifier 10.1109/LGRS.2019.2909025

deformation pattern, it is possible to perform a local linear approximation of the deformation phase. Hence, in a given point (r_0, a_0), the phase of the interferogram $z = Ae^{j\phi}$ can be substituted by its first-order Taylor approximation

$$\phi \approx \frac{4\pi}{\lambda}\left(\frac{\partial \delta_s}{\partial r}(r - r_0) + \frac{\partial \delta_s}{\partial a}(a - a_0)\right) + \phi_0 \qquad (1)$$

where A is the product of master and slave reflectivity and $\delta_s = \boldsymbol{\delta}^T \boldsymbol{s}$ is the projection of the displacement vector $\boldsymbol{\delta}$ along the line of sight (LoS) $\boldsymbol{s}$. It is worth to point out that the complexity of the deformation patterns could require a local adapting of the dimension of the estimation window in order to make the first-order Taylor approximation reasonable [5]. The optimal estimation of the phase gradients is, in general, not trivial since the complex SAR interferograms cannot be considered simply as an ideal complex sinusoid. For very high gradients, the effect of the wavenumber shift has to be taken into account as in [6]. However, for moderate gradients, the approximation holds and periodogram can be used [7].

III. PROBLEM INVERSION USING GRADIENT TENSOR

Being (e, n, v) the reference system oriented in accordance with the local east, the local north, and the geodetic vertical, the change in radar range can be written as the projection of the displacement vector on the sensing direction of the radar $\boldsymbol{s}$. The gradient tensor $\boldsymbol{\Psi}$ represents the derivatives of $\boldsymbol{\delta}$

$$\boldsymbol{\Psi} = \begin{bmatrix} u_{\mathrm{ee}} & u_{\mathrm{en}} & 0 \\ u_{\mathrm{ne}} & u_{\mathrm{nn}} & 0 \\ u_{\mathrm{ve}} & u_{\mathrm{vn}} & 0 \end{bmatrix}. \qquad (2)$$

Radar echoes measure the projection of $\boldsymbol{\Psi}$ on the LoS at the earth's surface only; therefore, in order to satisfy the equilibrium equations, $\boldsymbol{\Psi}$ has no contributions in the column of the derivatives along the v-axis [8]. For the sake of simplicity, the notation has been shortened to $u_{ij} = \partial\delta_i/\partial j$. Hence, the displacement gradients observed in the sensing direction of the radar can be written as [9]

$$\vec{\nabla}(\boldsymbol{\delta}^T \boldsymbol{s}) = \boldsymbol{\Psi}^T \mathbf{s} = \frac{\lambda}{4\pi}\vec{\nabla}\phi. \qquad (3)$$

The model proposed by Okada [10] describes the earth's surface motion generated by a seismic event both in terms of displacement and deformation (gradient tensor). Fixed the geometry of the fault, the gradient tensor $\boldsymbol{\Psi}$ derived from the Okada model can be linearized with respect to the vector of slips $\boldsymbol{\xi}$ to be estimated. Knowing the local SAR geometry from the state vectors' information, it possible to locally rotate the tensor provided by the model into radar geometry using a proper rotation matrix $\boldsymbol{T}$

$$\boldsymbol{\Theta}(\boldsymbol{\xi}) = \boldsymbol{T}^T \boldsymbol{\Psi}(\boldsymbol{\xi}) \boldsymbol{T}. \qquad (4)$$

In the measurements' reference system, it is possible to write a system of equations that equate the model and measurements to be inverted, retrieving the vector of parameters $\boldsymbol{\xi}$ that are minimizing the figure of merit M

$$M = \sum_{k=0}^{N-1}\left(\frac{\lambda_k}{4\pi}\vec{\nabla}\phi - \boldsymbol{\Theta}_k(\boldsymbol{\xi})^T \mathbf{s}_k\right)^T C_{d,k}^{-1} \times \left(\frac{\lambda_k}{4\pi}\vec{\nabla}\phi - \boldsymbol{\Theta}_k(\boldsymbol{\xi})^T \mathbf{s}_k\right). \qquad (5)$$

The equation system is written in general for N measurement's geometries, and $\boldsymbol{C}_{d,k}$ is the covariance matrix of the gradients of the kth geometry. Supposing that we know the statistical properties of the interferometric phase uncertainties (noise, atmosphere, and so on), it is possible to derive the covariance as the covariance of the derivative. It is worth to notice that the high-pass effect of the derivative operator drops the spatial correlation forcing the covariance function to be almost impulsive in the direction in which the derivative is applied. This means that an eventual isotropic behavior of the interferometric phase covariance function [11] will not be preserved in the gradients' covariance.

IV. SLIP DISTRIBUTION INVERSION USING IZMIT EARTHQUAKE INTERFEROGRAM

The Mw 7.6 Izmit earthquake occurred on August 17, 1999, and it was the product of the right lateral strike-slip movement of a part the North Anatolian Fault [12]. Because of the E/W orientation of the fault, the coseismic displacement was very well captured by the ERS 1-2 SAR interferogram that shows a dense pattern of the azimuth-oriented interferometric fringes. The high fringe density and the temporal decorrelation (35-day interferograms) make the phase unwrapping procedure particularly prone to errors. Therefore, this case study fits very well for the investigation of a phase unwrapping-free approach. Although previous works showed the complexity of the fault [12], [13], a simplified source geometry (single fault segment) has been used, as in [2] (see Fig. 1). This is related to the scope of this letter that is aimed to focus more on methodological aspects. As a reference result for the inverted slip and its residual phase, the reader can refer to the study in [12].

The modeled fault has been divided in patches of 5 × 4 km along the strike and dip direction, respectively. The inversion imposes also a Laplacian as regularization ($\nabla^2\boldsymbol{\xi} = \mathbf{0}$) to control the smoothness of the estimated slips on the fault plane [14]. In order to better discuss the feature of the gradient-based inversion of the slip distribution, the same inversion has been carried out also using the unwrapped phase.

A. Gradient Solution

The computation of the interferometric phase gradients has been performed starting from the SLCs. In order to preserve the information, no multilooking was applied in forming the interferogram. The LoS-projected component of the gradient tensor has been carried out, estimating the local fringe frequency using a periodogram. The estimation windows used was about 5 × 5 km, sampled at a finer grid. The estimated range and azimuth fringe frequencies are scaled to the range and azimuth LoS deformation gradients, as in (1).

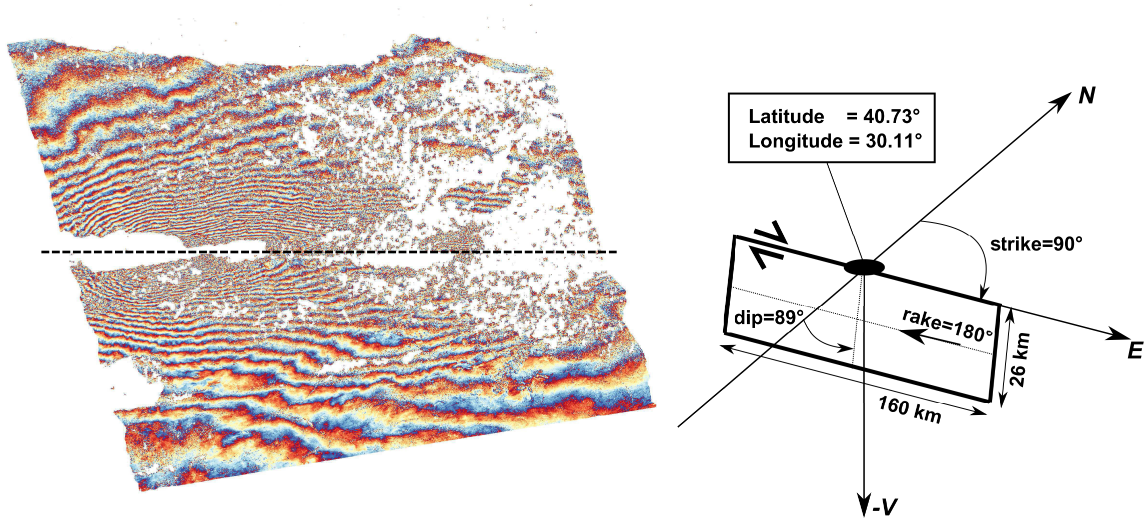

(a) (b)

Fig. 1. Izmit earthquake displacement and geometry of the problem. (a) 35-day ERS interferogram. Black dashed line: position of the fault used in the modeling. (b) Fault geometry used for the inversion (in detail).

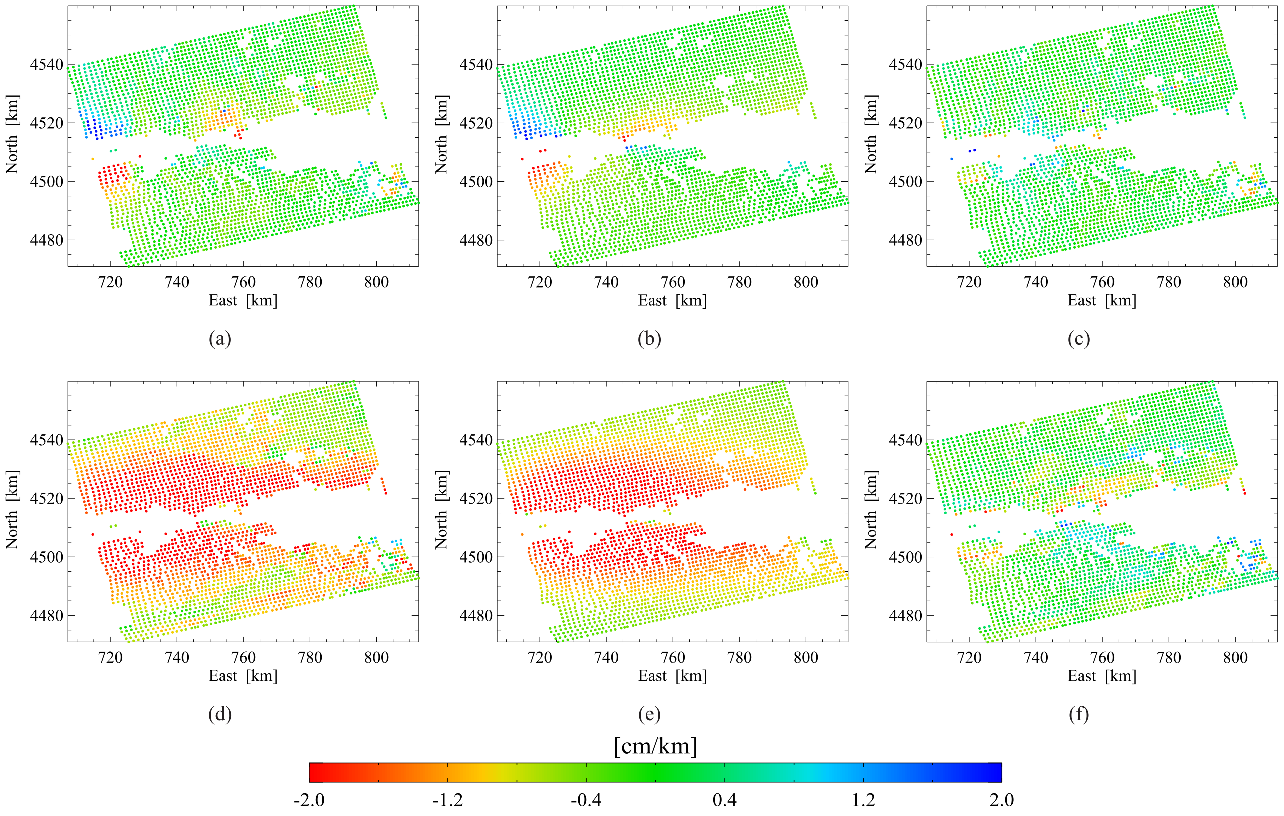

(a) (b) (c)

(d) (e) (f)

Fig. 2. Results of the gradient-based inversion. (a) and (d) Measured LoS gradients in range and azimuth, respectively. (b) and (e) Gradients modeled by the inverted slip distribution in range and azimuth, respectively. (c) and (f) Residual LoS gradients obtained, compensating the measurements with the derived model.

The direct problem is calculated using the Okada model and locally rotating the derived tensor $\boldsymbol{\Psi}(\boldsymbol{\xi})$ into radar geometry, as described in Section III. The inversion has been performed in the least square sense, forcing the vector $\boldsymbol{\xi} \geq \mathbf{0}$. The measured, modeled, and residual gradients in the range and azimuth direction are shown in Fig. 2.

B. Unwrapped Phase Solution

In order to compare the previously derived results, the inversion has been also carried out using the unwrapped interferometric phase. A coherence mask having 0.18 threshold has been over imposed in order to keep the phase error in a reasonable range. The extracted points have been unwrapped

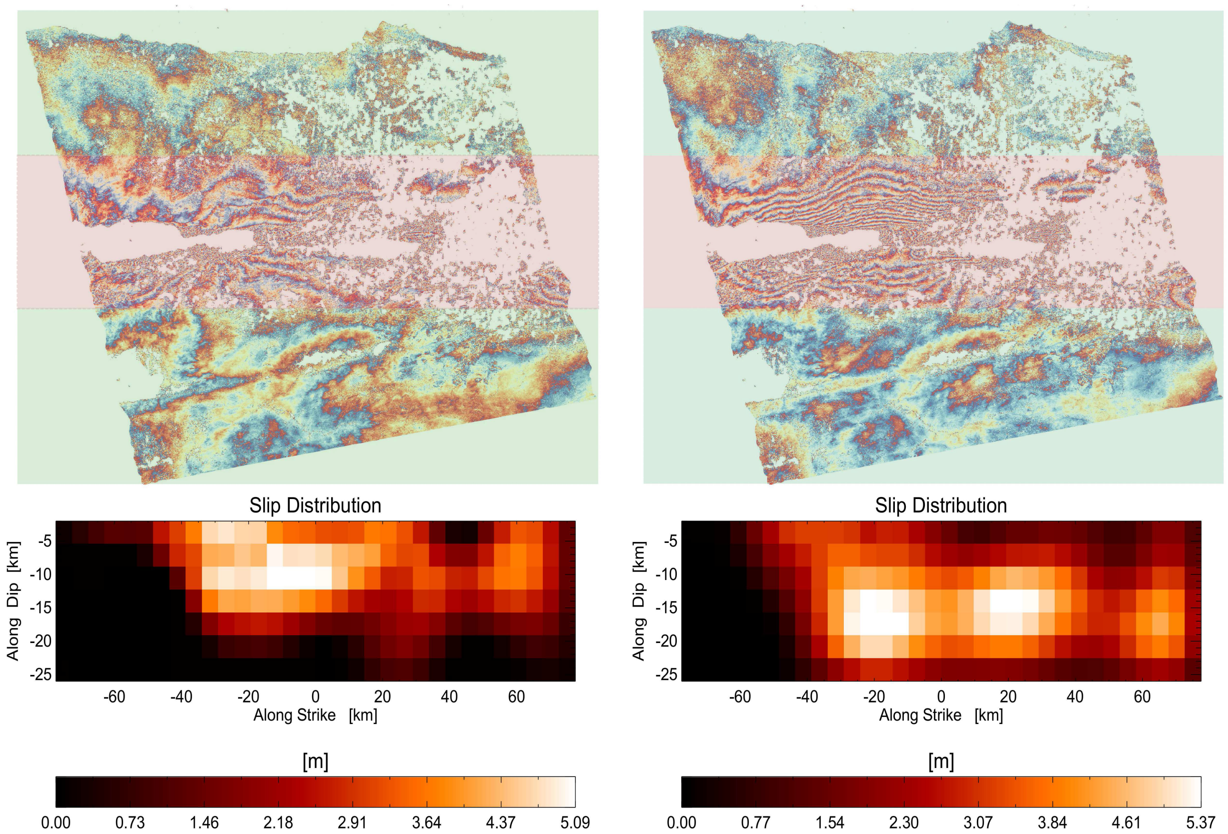

(a) (b)

Fig. 3. Results comparison. (a) Wrapped residual interferogram and slip distribution over the fault plane for the gradient solution. (b) Wrapped residual interferogram and slip distribution over the fault plane for the unwrapped phase solution. The reshaded area is aimed to highlight the area closer to the fault, where the unwrapping errors are more likely to occur.

using a sparse grid minimum cost flow (MCF) [15]. Due to the fact that the whole scene is crossed by the tectonic fault, critical unwrapping errors have been avoided unwrapping the scene in two separate "tiles": one covering the area north of the fault and the other covering the southern area. Two reference points have set close to the northwest corner of the interferogram and the southwest corner, respectively. In this case, the direct problem is designed, describing the projection of the displacement generated by the Okada model in LoS calibrated to the displacement generated by the Okada model in LoS in the reference point. The absolute phases of the two tiles have been jointly inverted, obtaining a parameter vector $\boldsymbol{\xi}_{\phi}$ comparable to the one obtained using the gradients ($\boldsymbol{\xi}_{\Delta}$).

C. Discussion

In order to fairly compare the obtained results, the residuals displayed in the wrapped interferometric phase have been used. The modeled phase corresponding to the inverted results has been computed, wrapped, and used to compensate for the original interferogram. In this way, it is possible to visually evaluate the capability of the inverted models to explain the interferometric measurement. Unwrapped phase provides higher sensitivity to deformation, as expected from the theory. This is visible far away from the fault (highlighted in green dots in Fig. 3), where the interferometric phase is better compensated by the model derived from the unwrapped phase. However, close to the fault (highlighted in red dots in Fig. 3), the solution obtained using gradients is considerably better. Here, the deformation pattern generates strong phase gradients that compromise the success of the phase unwrapping. However, the gradients' measurements are able to provide an ambiguity-free information that can be more easily inverted in a least square sense despite their noisy nature.

Both inversions have been almost identically regularized so that the two inverted slip distributions, $\boldsymbol{\xi}_{\phi}$ and $\boldsymbol{\xi}_{\Delta}$, present the same spatial smoothness [14]. The two slip distributions, $\boldsymbol{\xi}_{\phi}$ $\boldsymbol{\xi}_{\Delta}$, present a similar spatial pattern although shifted on the fault plane along the dip direction. This can be interpreted, considering the relation between the depth of the slip and the scale of the corresponding surface deformation (the deeper the motion is, the more low pass the surface deformation is) [8]. Therefore, since the gradients' measurements are limited in observing the high-pass part of the motion, the maximum observable depth results are also to be limited accordingly.

V. CONCLUSION

This letter has discussed and shown the possibility of using the interferometric phase gradients in slip distribution inversion. Although the use of such measurements is inherently suboptimum, their robustness to unwrapping error is an interesting feature that helps in fully exploiting the interferometric phase information. In line with the theory, the results discussed in this letter show how the absolute interferometric phase is performing, in general, better. However, this statement has been proven to be true only in the case of a correct solution of the phase ambiguities, as it happened far away from the fault, where the motion gradients are small (see Fig. 3). The unwrapping errors due to high fringe rate in the proximity of the fault lead to an underestimation of the motion in this area and, consequently, to a different interpretation of the motion in terms of the fault slip (see Fig. 3). The gradient-based solution, on the other side, proved to be more robust, being able to better compensate the interferometric phase close to the fault. Therefore, one could think of a synergistic use of phase gradients that can help mitigating the unwrapping-related problems. Some possible applications include the integration with cross correlation (the shifts catching the low pass part of the motion, the gradients the high pass one), the improvement of the data coverage (including areas where the phase unwrapping is bound to fail), or the estimation of an *a priori* solution that can be used to properly unwrap the interferogram.

REFERENCES

[1] K. L. Feigl and C. H. Thurber, "A method for modelling radar interferograms without phase unwrapping: Application to the M 5 Fawnskin, California earthquake of 1992 December 4," *Geophys. J. Int.*, vol. 176, no. 2, pp. 491–504, Feb. 2009.

[2] G. Fornaro, S. Atzori, F. Calo, D. Reale, and S. Salvi, "Inversion of wrapped differential interferometric SAR data for fault dislocation modeling," *IEEE Trans. Geosci. Remote Sens.*, vol. 50, no. 6, pp. 2175–2184, Jun. 2012.

[3] D. T. Sandwell and E. J. Price, "Phase gradient approach to stacking interferograms," *J. Geophys. Res.*, vol. 103, no. B12, pp. 30183–30204, Dec. 1998.

[4] A. Sharov, "Gradient approach to InSAR modelling of glacial dynamics and morphology," in *Proc. 22nd EARSeL Symp.* Rotterdam, The Netherlands: Mill Press, 2003, pp. 373–381.

[5] S. T. Ali and K. L. Feigl, "A new strategy for estimating geophysical parameters from InSAR data: Application to the Krafla central volcano in Iceland," *Geochem., Geophys. Geosyst.*, vol. 13, no. 6, Jun. 2012.

[6] A. M. Guarnieri and S. Tebaldini, "ML-based fringe-frequency estimation for InSAR," *IEEE Geosci. Remote Sens. Lett.*, vol. 7, no. 1, pp. 136–140, Jan. 2010.

[7] S. Kay and R. Nekovei, "An efficient two-dimensional frequency estimator," *IEEE Trans. Acoust., Speech Signal Process.*, vol. 38, no. 10, pp. 1807–1809, Oct. 1990.

[8] P. Segall, *Earthquake and Volcano Deformation*. Princeton, NJ, USA: Princeton Univ. Press, 2010.

[9] A. Parizzi and W. A. Jaber, "Estimating strain and rotation from wrapped SAR interferograms," *IEEE Geosci. Remote Sens. Lett.*, vol. 15, no. 9, pp. 1367–1371, Sep. 2018.

[10] Y. Okada, "Surface deformation due to shear and tensile faults in a half-space," *Bull. Seismol. Soc. Amer.*, vol. 75, no. 4, pp. 1135–1154, Aug. 1985.

[11] S. Knospe and S. Jonsson, "Covariance estimation for dInSAR surface deformation measurements in the presence of anisotropic atmospheric noise," *IEEE Trans. Geosci. Remote Sens.*, vol. 48, no. 4, pp. 2057–2065, Apr. 2010.

[12] Z. Çakir, J.-B. de Chabalier, R. Armijo, B. Meyer, A. Barka, and G. Peltzer, "Coseismic and early post-seismic slip associated with the 1999 Izmit earthquake (Turkey), from SAR interferometry and tectonic field observations," *Geophys. J. Int.*, vol. 155, no. 1, pp. 93–110, 2003. doi: 10.1046/j.1365-246X.2003.02001.x.

[13] T. Wright, E. Fielding, and B. Parsons, "Triggered slip: Observations of the 17 August 1999 Izmit (Turkey) Earthquake using radar interferometry," *Geophys. Res. Lett.*, vol. 28, no. 6, pp. 1079–1082, Mar. 2001.

[14] S. Jonsson, H. Zebker, P. Segall, and F. Amelung, "Fault slip distribution of the 1999 Mw 7.1 hector mine, california, earthquake, estimated from satellite radar and GPS measurements," *Bull. Seismological Soc. Amer.*, vol. 92, no. 4, pp. 1377–1389, May 2002.

[15] M. Costantini, "A novel phase unwrapping method based on network programming," *IEEE Trans. Geosci. Remote Sens.*, vol. 36, no. 3, pp. 813–821, May 1998.

C

Alessandro Parizzi , Fernando Rodriguez Gonzalez and Ramon Brcic (2021). A Covariance-Based Approach to Merging InSAR and GNSS Displacement Rate Measurements. Remote Sensing

Summary This paper deals with the integration of deformation rates derived from Synthetic Aperture Radar Interferometry (InSAR) and Global Navigation Satellite System (GNSS) data. The proposed approach relies on knowledge of the variance/covariance of both InSAR and GNSS measurements so that they may be combined accounting for the spectral properties of their errors, hence preserving all spatial frequencies of the deformation detected by the two techniques. The variance/covariance description of the output product is also provided. A performance analysis is carried out on realistic simulated scenarios in order to show the boundaries of the technique. The proposed approach is finally applied to real data. Five Sentinel-1A/B stacks acquired over two different areas of interest are processed and discussed. The first example is a merged deformation map of the northern part of the Netherlands for both ascending and descending geometries. The second example shows the deformation at the junction between the North and East Anatolian Fault using three consecutive descending stacks.

Contributions of the candidate Idea and development of the concept. Practical implementation and testing with the data sets. Writing the paper.

Article

A Covariance-Based Approach to Merging InSAR and GNSS Displacement Rate Measurements

Alessandro Parizzi *, Fernando Rodriguez Gonzalez and Ramon Brcic

Remote Sensing Technology Institute German Aerospace Center (DLR) Münchenerstraße 20,
82234 Weßling, Germany; fernando.rodriguezgonzalez@dlr.de (F.R.G.); ramon.brcic@dlr.de (R.B.)
* Correspondence: alessandro.parizzi@dlr.de

Received: 4 December 2019; Accepted: 2 January 2020; Published: 16 January 2020

Abstract: This paper deals with the integration of deformation rates derived from Synthetic Aperture Radar Interferometry (InSAR) and Global Navigation Satellite System (GNSS) data. The proposed approach relies on knowledge of the variance/covariance of both InSAR and GNSS measurements so that they may be combined accounting for the spectral properties of their errors, hence preserving all spatial frequencies of the deformation detected by the two techniques. The variance/covariance description of the output product is also provided. A performance analysis is carried out on realistic simulated scenarios in order to show the boundaries of the technique. The proposed approach is finally applied to real data. Five Sentinel-1A/B stacks acquired over two different areas of interest are processed and discussed. The first example is a merged deformation map of the northern part of the Netherlands for both ascending and descending geometries. The second example shows the deformation at the junction between the North and East Anatolian Fault using three consecutive descending stacks.

Keywords: InSAR; GNSS; deformation

1. Introduction and Motivation

Synthetic Aperture Radar Interferometry (InSAR) deformation rate measurements support a wide range of applications in the fields of geology, geophysics, and geohazards [1]. Since the nature of the interferometric measurements is inherently relative, the additive delays—like those of the troposphere and ionosphere—make the accuracy of such measurements strongly dependent on the distance [2–4]. Hence, InSAR performance varies according to the particular application. Typically, interferometry works well for applications such as infrastructure monitoring or urban subsidence, since they involve relatively short scales (10–20 km). However, there is also scientific interest in using InSAR to measure the strain accumulation of tectonic faults. This type of study requires very accurate measurements (1 mm/year at distances larger than 100 km) [5].

The new generation of Synthetic Aperture Radar (SAR) sensors—like Sentinel-1—provides systematically acquired data with a swath width of 250 km [6]; future missions plan to further extend this to 350 km [7]. Due to the atmospheric errors at such scales, the requirement of 1 mm/y could be a challenging goal for InSAR, especially if the available time series have a reduced observation time [8]. Therefore, in order to fully exploit the coverage capabilities of these missions, we are motivated to develop techniques that merge interferometric deformation rates with other geodetic measurements, not only to improve the performance of applications particularly affected by atmospheric effects (e.g., inter-seismic deformations), but also to remove the reference point, hence facilitating an easier integration with the other geometries or techniques.

The best candidate for this integration with SAR interferometry are the deformation rates estimated using a Global Navigation Satellite System (GNSS). This is due firstly to their well-known complementarity where InSAR coverage is combined with GNSS accuracy. Indeed, there is a long tradition of research in this area as evidenced by studies performed by geo-scientists; for example, in supporting interferometric phase unwrapping [9,10]. Combining InSAR and GNSS deformation rates has also been studied in order to calibrate the InSAR-estimated velocities [11–13], and to help the limited geometric sensitivity of the SAR system in measuring deformation [14–16]. The integration of InSAR with other instrumentation such as active transponders has been investigated in order to design optimal geodetic networks that enhance the spatial distribution of the deformation measurements [17–19].

However, it is important to highlight that the main argument of this work is not to claim the complementary InSAR/GNSS—which is well known, as previously mentioned—but rather to discuss the use of their error statistics in the combination, as well as its propagation through to the final product. In [8], the effect of the correction of the interferometric phase for tropospheric delays and solid earth tides using external models was shown. After such corrections, the mean variograms of the interferometric measurements error show a stationary behavior that can be well approximated by a covariance function. An optimal combination of the two measurement techniques is hence possible, since the spectral properties of their own errors can be taken into account. Moreover, no assumptions about the displacement pattern characteristics [19] and GNSS measurement density are necessary as in [11] and the data need not be filtered. Only the InSAR/GNSS differences, which can be statistically characterized, are estimated and used to compensate the original InSAR measurements. The error can then be propagated from the data to the results, allowing full characterization of the output uncertainty.

The measurement of strain accumulation along hundreds of kilometers is a potential application for this framework. The integration of InSAR and GNSS does not remove any deformation component, but performs a weighted merging of the different spatial frequencies of the deformation detected by the two techniques according to their reliability. Moreover, the mathematical modeling, often applied on final measurements, requires a proper weighting of the different input data [20]. Other possible applications include the InSAR-based National Ground Motion Services [21]. Such projects are often required to provide a product that merges the InSAR-derived results and the results derived by the GNSS networks already deployed on the territory. Since these products are part of a Service, a consistent description and traceability of the uncertainties is strictly required.

In Section 2 the proposed methodology is described, separating the capability of retrieving the absolute motion from the calibration of the residual atmospheric errors. An analytical description of the error of the merged product is also provided. In Section 3, simulations are performed in order to provide reference numbers in terms of coverage and quality versus performance. Finally, the results of using real data in significant test cases are presented and discussed. The first example covers the northern part of the Netherlands and demonstrates merging on a large scale in order to provide a consistent product like those in national ground motion services. The second example is aimed at addressing geophysical applications, and shows the calibration of interferometric measurements over North Anatolian Fault to the Eurasian plate.

2. Methodology

Let us consider N locations in the processed area of interest, where two deformation rate measurements v_D and $\underline{v}_G$ are performed using InSAR and GNSS, respectively. With $\underline{s}$ as the radar line of sight (LoS) it is possible to state the problem modeling the difference between the two velocities at the ith position Δ_i as follows:

$$\Delta_i = v_{D,i} - \underline{v}_{G,i}^T \underline{s} = \delta(r_i, a_i) + v_{ref} + n(r_i, a_i), \tag{1}$$

where v_{ref} is the velocity of the reference point used in InSAR processing, $\delta(r_i, a_i)$ is a space-variant error screen in the interferometric data, and $n(r_i, a_i)$ is the random error. The implicit hypothesis behind this definition is that the spatially correlated noise, basically related to the residual atmospheric delay, is present in the interferometric measurement only. This characteristic allows extraction, through the subtraction of the two velocities, of the parameters $\delta(r, a)$ and v_{ref}, which have to be estimated in order to properly merge the data. It is worth noticing that this operation can also be seen as a calibration of the InSAR data: it exploits GNSS reference rates so that the interferometric measurement is no longer relative to the reference point while also removing residual systematic effects. Figure 1 displays an overview of the steps of the proposed approach. In the first step, the error statistics are derived and the covariance matrix **R** is computed. The reference point velocity v_{ref} is then estimated and subtracted from the offset vector $\underline{\Delta}$. Finally, the residual error screen is interpolated at each InSAR measurement point, exploiting knowledge of the error statistics.

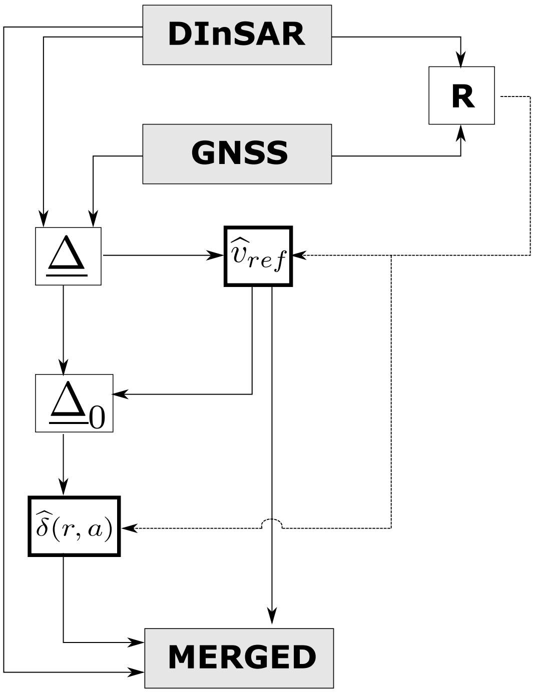

Figure 1. Flow chart of the proposed method.

2.1. Error Description of the Input Data

A proper handling of the relation defined in Equation (1) requires a statistical description of the vector $\underline{\Delta}$. Therefore, the covariance matrix **R** of the difference measurements has to be derived. It is possible to distinguish between three contributions: The random noise of the GNSS measurements $\sigma^2_{G,i}$ obtained by projecting the variance of the different components of the estimated rates onto the radar LoS, the random noise of the InSAR measurements $\sigma^2_{D,i}$, and spatially correlated noise due to residual atmospheric effects. The full covariance matrix can be defined as:

$$\begin{aligned}\mathbf{R} = \mathbb{E}[\underline{\Delta}\underline{\Delta}^T] &= \mathrm{diag}(\sigma^2_{G,0}, ...\sigma^2_{G,N-1})+ \\ &+ \mathrm{diag}(\sigma^2_{D,0}, ...\sigma^2_{D,N-1}) + \mathbf{C}_\alpha.\end{aligned} \tag{2}$$

The first two contributions are diagonal matrices, since they represent the spatially uncorrelated errors of the independent GNSS and InSAR measurement processes, respectively. On the other hand, the derivation of the covariance matrix $\mathbf{C}_\alpha$ that represents the residual atmospheric error is particularly interesting [22]. A covariance function $\Gamma(d)$ representing the residual error has to be robustly estimated and evaluated at the N positions where the Δ_i are located; with $d_{i,j}$ as the distance between the ith and the jth measurement, this is:

$$\mathbf{C}_\alpha(i, j) = \Gamma(d_{i,j}). \tag{3}$$

The first two components of Equation (2) can be estimated using the supplied accuracy of the GNSS data and the interferometric temporal coherences, respectively. However, estimation of $\mathbf{C}_\alpha$ requires a more detailed discussion.

2.2. Estimation of the Residual Atmospheric Error Covariance Matrix

The covariance of the residual atmospheric error can be estimated from interferograms where the residual atmospheric delay is the dominant measured delay. The fast revisit time of the Sentinel-1 mission allows the computation of short time interferograms with temporal baselines δt down to 6 days. Following the approach in [8], the short temporal baseline interferograms are used to compute variograms merely representing the residual atmospheric errors. Since such errors are expected to be on the order of magnitude of a centimeter, deformation rates of several tens of cm/y are necessary in order to bias the estimation of atmospheric errors. Such rates can be reached in landslides or mining areas that are typically restricted in coverage. Since the variograms are computed by averaging many different measurements over the whole scene, the effect of such areas should not strongly impact the estimation. It should be noted that since variogram estimation requires the unwrapped phase, this step must be performed at the end of the processing. At this stage, areas of very high deformation are apparent and can eventually be masked out. The effect of solid earth tides has been corrected in the interferometric phase using models [8]. However, the projection of tectonic plate motion onto the line of sight is a large-scale effect whose spatial characteristics cause a bias in variogram estimation. Such movements are mainly horizontal and can reach 6–7 cm/y. How large the horizontal motion must be in order to be comparable with the troposphere in a short temporal baseline interferogram can be easily estimated. For a 1 cm gradient along the radar swath, a horizontal motion of $1/(sin(\theta_{near}) - sin(\theta_{far}))$ is necessary where θ_{near} is the incidence angle at near range and θ_{far} the incidence angle at far range, leading to a horizontal motion of $\approx$ 5 cm or 152 cm/y for a revisit time of 12 days. Therefore, keeping the maximum $\delta t < 30$ days should result in negligible impact. It should be mentioned that the eventual presence of seismic events in the time series should also be assessed, and co-seismic interferometric pairs not be used to generate the variograms.

Given that such interferograms are almost deformation-free, it is possible to assume that the average of the variograms $\mathbb{E}[V]$ is a good estimator $\widehat{V}$ (the $\widehat{\ }$ symbol indicates an estimated parameter) of the covariance characteristics of the residual atmospheric delays. Since velocity estimation implies a linear regression on the phase, a scaling factor accounting for acquisitions' time span and number must be applied to convert the single-phase measurement accuracy into deformation rate accuracy:

$$\widehat{V}_{rate}(d) = \frac{\lambda^2}{16\pi^2} \frac{\widehat{V}(d)}{2} \frac{M}{M \sum_k t_k^2 - (\sum_k t_k)^2}, \tag{4}$$

where d is the distance, λ the radar wavelength, t_k the acquisition times, and M the number of interferograms used for the linear regression. The analysis in [8] showed that if atmospheric phase corrections based on European Centre for Medium-Range Weather Forecasts (ECMWF) models are performed [23,24], the residual atmospheric effects after processing are well-modeled as stationary.

$\widehat{V}_{rate}(d)$ can then be fitted using a covariance model in order to compute the model parameters, converted to $\widehat{\Gamma}(d)$, and to estimate the covariance matrix $\mathbf{C}_\alpha$ in Equation (3). In this study, the exponential covariance model was used, as seen in Figure 2.

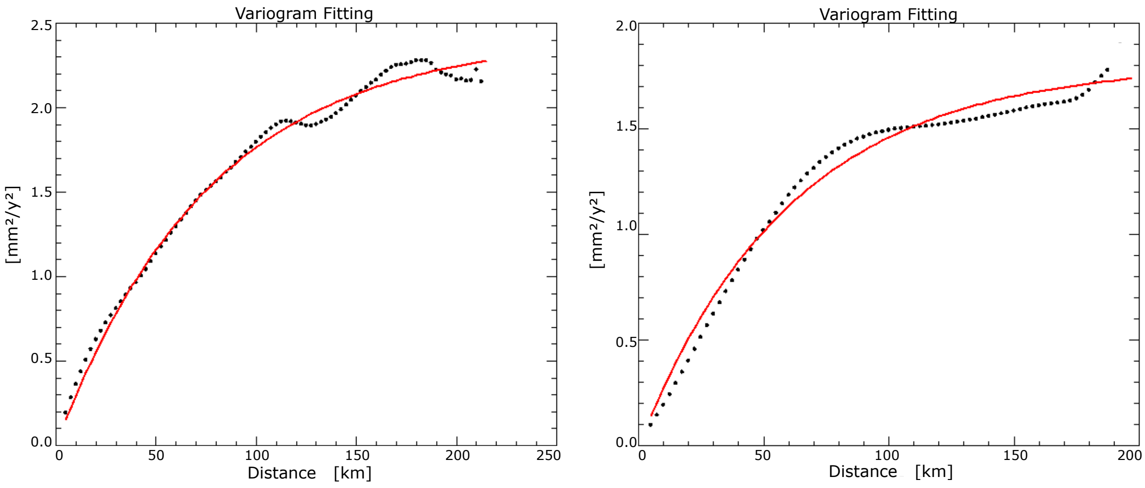

(**a**) (**b**)

Figure 2. Examples of an exponential fitting of the deformation rate variograms. The black dots represent the estimated variogram and the bold red line represents the estimated model. The variograms in (**a**) and (**b**) refer to the stacks 123/2 and 123/3 of the North Anatolian Fault data set respectively , see Section 4.2.

2.3. Estimation of the Reference Point Motion

Equation (1) shows how $\underline{\Delta}$ can be seen as an observation of v_{ref} with superimposed random and colored noise. Since the noise statistics of $\underline{\Delta}$ exhibit stationary behavior, the derivation of the reference point velocity can be carried out by averaging the observed $\underline{\Delta}$. Therefore, according to the considerations in the previous Section 2.1, $\widehat{v}_{ref}$ can be found by taking into account the computed covariance matrix $\mathbf{R}$:

$$\widehat{v}_{ref} = (\underline{u}\mathbf{R}^{-1}\underline{u}^T)^{-1}\underline{u}^T\mathbf{R}^{-1}\underline{\Delta}, \tag{5}$$

where $\underline{u}$ is a unitary vector that maps, one to one, the measurements $\underline{\Delta}$ with the unknown scalar v_{ref}. The estimated $\widehat{v}_{ref}$ represents the motion of the reference point in its local LoS and has to be added to the InSAR velocities in order to make them absolute.

2.4. Estimation of the 0-Mean Calibration Screen

In the previous Section 2.3, the overall offset between InSAR and GNSS deformation rates was estimated while accounting for the covariance matrix. Now, the space-variant error screen between the GNSS and InSAR velocities can be estimated by performing a covariance-based interpolation (Kriging) of the residual offsets $\underline{\Delta_0} = \underline{\Delta} - \widehat{v}_{ref}$. A set of coefficients $\underline{c}$ that, combined with the vector $\underline{\Delta_0}$, allows the reconstruction of $\delta(r,a)$ everywhere must be estimated.

$$\widehat{\delta}(r,a) = \underline{c}^T\underline{\Delta_0} \tag{6}$$

According to theory, this can be obtained by imposing the condition that the interpolation/prediction error be uncorrelated:

$$\epsilon_n = \widehat{\delta}(r_n,a_n) - \delta(r_n,a_n) \tag{7}$$

with the data $\underline{\Delta_0}$ [25]. Substituting Equation (6) into Equation (7) and imposing the uncorrelatedness condition with $\underline{\Delta_0}$ gives:

$$\underline{c} = \mathbf{R}^{-1}\underline{\rho}, \tag{8}$$

where $\underline{\rho} = \mathbb{E}[\delta(r,a)\underline{\Delta_0}]$ is the vector representing the correlation between the data vector $\underline{\Delta_0}$ and the error screen δ at the current position.

2.5. Variance and Covariance of the Results

To enhance usability, the error of the final product should be characterized. The final result is obtained by compensating the InSAR velocities for the estimated $\widehat{v}_{ref}$ and $\widehat{\delta}(r,a)$. The reference point deformation rate is a bias added to all points. Its error is therefore a constant value in the final product. Its contribution can be derived by computing the variance of the linear system inversion:

$$\sigma^2_{\widehat{v}_{ref}} = (\underline{u}\mathbf{R}^{-1}\underline{u}^T)^{-1}. \tag{9}$$

The error of the estimated $\widehat{\delta}$ will be space variant. The variance and covariance of the estimated error screen $\widehat{\delta}(r,a)$ can be derived as in [25].

$$\mathbb{E}[\epsilon_n^2] = \mathbb{E}[(\delta(r_n,a_n) - \underline{c}^T\underline{\Delta_0})^2] = \Gamma(0) - \underline{\rho_n}^T\mathbf{R}^{-1}\underline{\rho_n} \tag{10}$$

where $\Gamma(0)$ represents the original error due to the spatially correlated signal, and the second part of the equation represents a "mitigation factor" that reduces such variance according to the distance from the GNSS data. Analogously, the covariance is:

$$\mathbb{E}[\epsilon_n\epsilon_m] = \Gamma(d_{m,n}) - \underline{\rho_m}^T\mathbf{R}^{-1}\underline{\rho_n}. \tag{11}$$

Some conclusions concerning the final product can now be drawn. It provides absolute measurements that can be characterized by a variance directly derived from the applied methodology. It still contains a residual spatial correlation, though mitigated by the removal of $\widehat{\delta}(r,a)$. However, this residual error is no longer stationary. Its covariance depends on the two considered points, as highlighted by Equation (11). The variogram or covariance representation of the error—as for the input InSAR velocities—is hence no longer possible, but must must to be computed locally, accounting for the position (r,a) with respect to the GNSS stations.

3. Simulations

Simulations were performed in order to assess the validity of the method and evaluate its performance. The scope of these simulations is to understand and quantify the effects of the spatial distribution (density) and the quality of the GNSS measurements in different processing scenarios, and to provide some numbers that summarize the achievable accuracies in the retrieval of $\widehat{v}_{ref}$ and $\widehat{\delta}$.

A set of randomly distributed points with zero deformation was simulated over a surface of 175×250 km^2 (Sentinel-1 slice size) in order to represent the InSAR measurements. Random noise (clutter) and spatially correlated noise (atmospheric residuals) were added to the points. For the generation of spatially correlated noise, an exponential covariance $\Gamma(d) = \sigma_\alpha^2 exp(-d/L_c)$ was used. A reduced set of GNSS zero-deformation data were also simulated at random positions within the scene. According to the model only random noise was added to the simulated GNSS velocities. For the sake of simplicity, positions were uniformly distributed within the scene. The reconstruction depends on how well the available samples are able to represent the error spectrum. In practice, the more high-pass the error, the more samples will be needed. Of course, a regular sampling is desirable. If the data are concentrated in an area, the re-construction will be good in this area. When moving away from data points, the estimator will extrapolate.

The simulations were performed while varying the two main parameters, the number of reference GNSS measurements, and their accuracy. Two different scenarios were tested with low and high atmospheric residual power σ_α^2. In the first scenario, $\sigma_\alpha^2 = 2$ mm^2/y^2; for the Sentinel-1 mission, this is comparable to having a long time series of $T_{obs} \approx 3$ y in the case of applied atmospheric corrections [8]. In the second scenario, $\sigma_\alpha^2 = 9$ mm^2/y^2, representing the case of a short time series of $T_{obs} \approx 1$ y [8].

A realistic correlation length, according to real data, was used for the simulations—$L_{corr} = 60$ km in both cases. This comes from direct experience with the data. We observed that the average variograms after tropospheric corrections exhibited values of 40–100 km when fitted with an exponential model. An example of the simulation framework is shown in Figure 3.

Observing the simulation results in Figures 4 and 5 it can be concluded that, due to the spatial correlation of the error, higher densities of GNSS measurements improves the estimation of δ since it provides a better sampling of the error field, but does not help much in retrieving the absolute velocity v_{ref}, due to the "data redundancy" introduced by the spatial covariance.

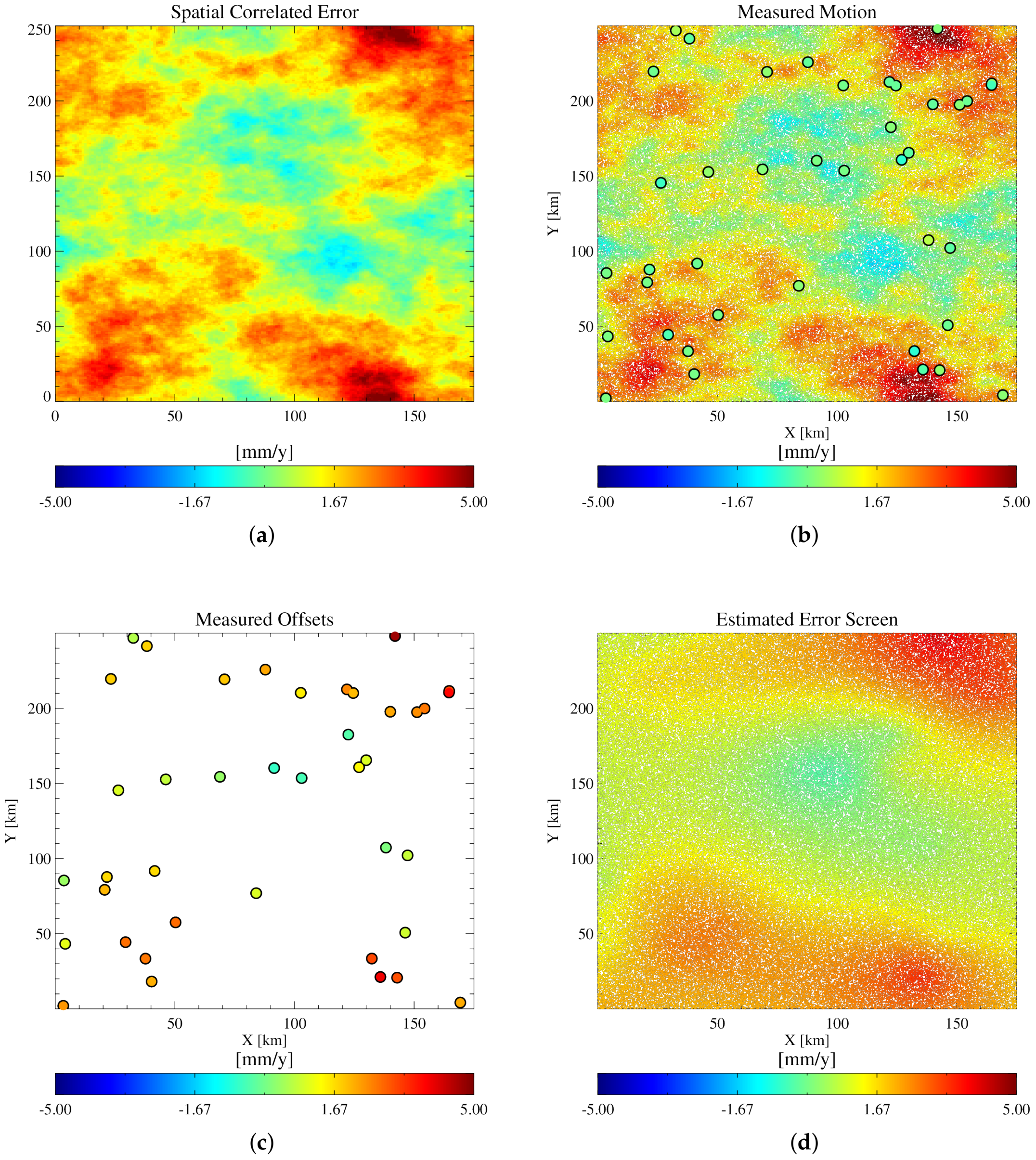

(a) (b) (c) (d)

Figure 3. *Cont.*

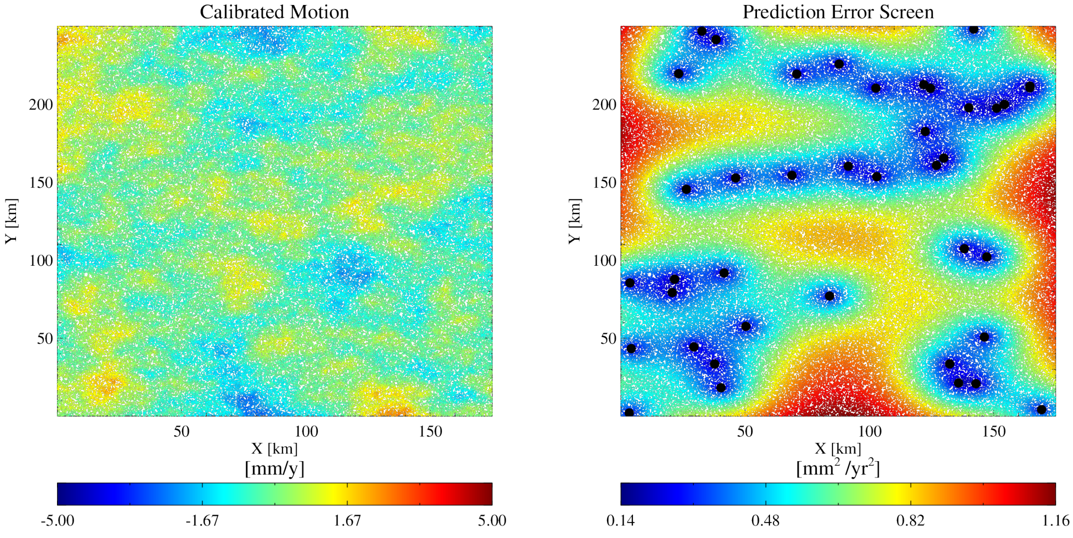

(**e**) (**f**)

Figure 3. The Figure shows an example of the framework used for the simulations. The simulated motion is 0 over the entire scene. In (**a**), the simulated spatially correlated noise is depicted. In (**b**), the dense Synthetic Aperture Radar Interferometry (InSAR) measurements and the coarse Global Navigation Satellite System (GNSS; large dots, atmosphere-free) are depicted. In (**c**), the measured offsets InSAR/GNSS (Δ_0) are depicted. In (**d**), the estimated error screen to be removed from (**b**) is depicted. In (**e**), the final results obtained by calibrating (**b**) with (**d**) are depicted. In (**f**), the estimated error for the merged product is depicted.

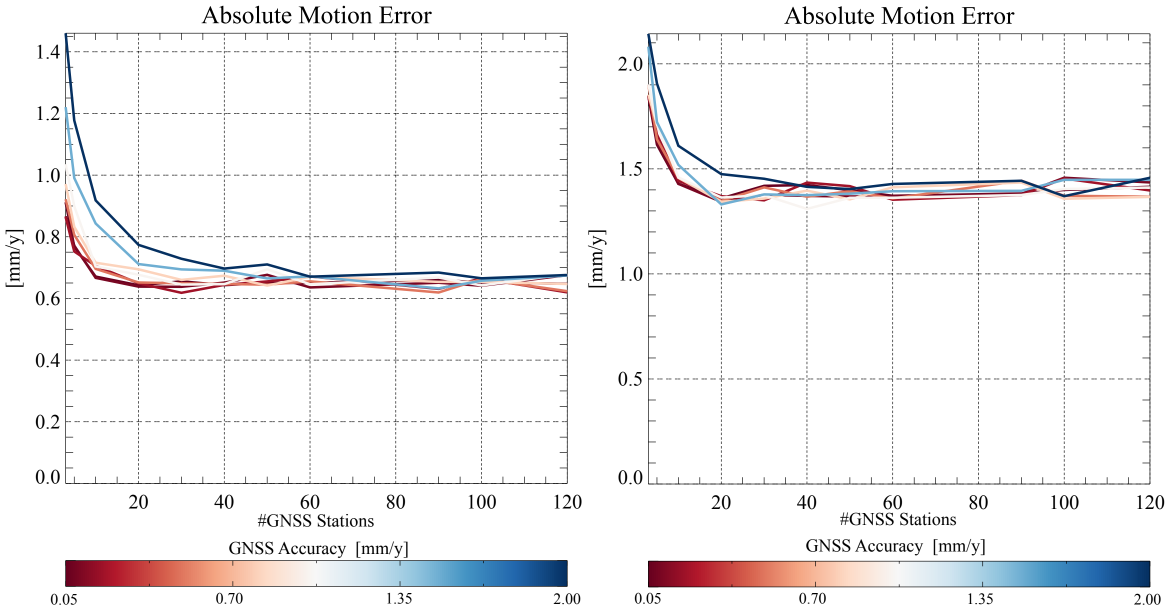

(**a**) (**b**)

Figure 4. Performance simulations in retrieving $\widehat{v}_{ref}$ carried out with different atmospheric noise sills: (**a**) $\sigma_\alpha^2 = 2\ \text{mm}^2/\text{y}^2$ and (**b**) $\sigma_\alpha^2 = 9\ \text{mm}^2/\text{y}^2$.

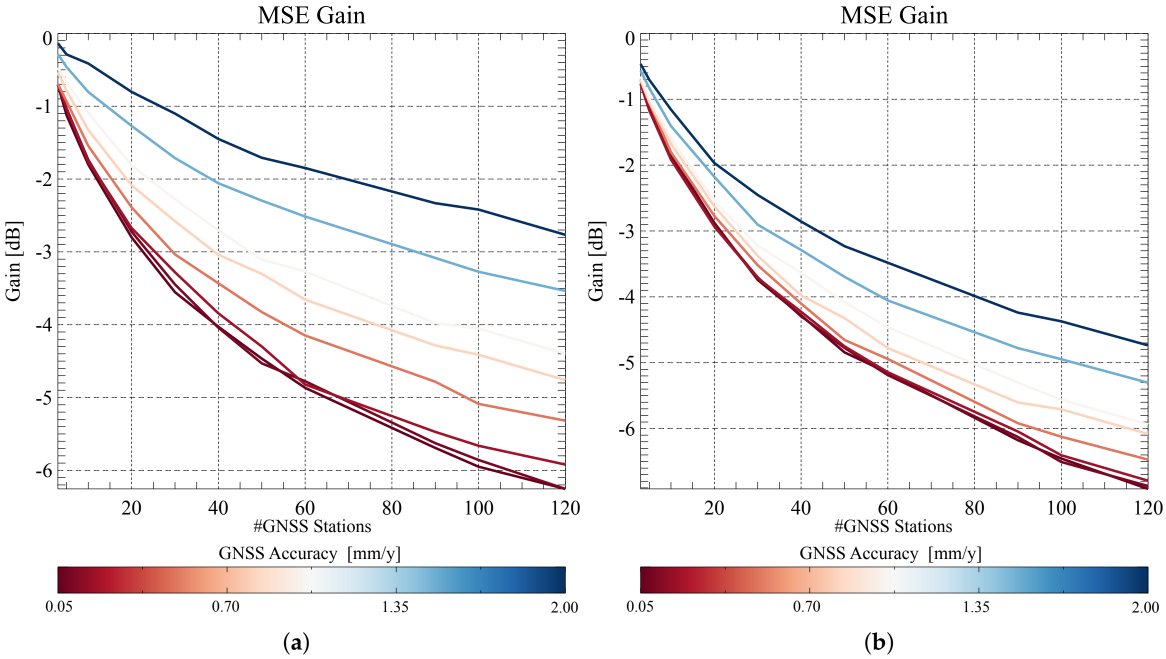

Figure 5. Performance simulations in retrieving $\widehat{\delta}$ carried out with different atmospheric noise sills: (**a**) $\sigma_\alpha^2 = 2\ \mathrm{mm}^2/\mathrm{y}^2$ and (**b**) $\sigma_\alpha^2 = 9\ \mathrm{mm}^2/\mathrm{y}^2$.

3.1. Performance in Retrieving $\widehat{v}_{ref}$

The accuracy of $\widehat{v}_{ref}$ is that of the mean computed from a set of correlated samples. The level of dependence of the given dataset is controlled by the spatial density of the latter and the correlation length L_{corr} of the superimposed noise. We observed that it is logical to expect that, given a L_{corr}, increasing the number of data improves estimation of $\widehat{v}_{ref}$ up to a certain level, since as the density of measurements increases, so to does the amount of correlation between measurement, hence limiting its impact on final performance. In a typical scenario ($T_{obs} \approx 3$ y , $\sigma_\alpha^2 = 2\ \mathrm{mm}^2/\mathrm{y}^2$), the accuracy can easily be brought below 1 mm/y, even with a limited set of GNSS stations (Figure 4).

3.2. Performance in Retrieving $\widehat{\delta}$

Evaluating the performance of $\widehat{\delta}$ is not a simple task. The most natural way would be to compare the variograms of the results before and after application of the technique. This approach would deliver a deeper insight into the achieved gain, since it would be possible to show this as a function of the scale. However, as mentioned in Section 2.5, the error of the merged results is no longer stationary making a variogram representation questionable. In order to avoid this issue, a simpler but more robust approach was followed. The performances were evaluated in terms of mean square error (MSE) in dB, over the whole scene. In practice, the mean power of the residual deformation signal after removal of the estimated error screen $\widehat{\delta}$ from the measured rates v_{meas} is:

$$MSE_{dB} = 10Log_{10}\Big(\mathbb{E}[(v_{meas} - \widehat{\delta})^2]\Big). \tag{12}$$

The results displayed in Figure 5a,b show that, in both cases, the performance cannot improve beyond a certain level by improving the quality of the GNSS measurements only. An improvement in GNSS coverage is also necessary in order to better compensate the higher wave-numbers of the error screen.

4. Results

For the study, two Sentinel-1A/B datasets covering the northern part of the Netherlands (two stacks, ascending and descending) and the junction between the North Anatolian Fault and East Anatolian Fault (three stacks, descending) were used. The interferograms were computed, corrected for tropospheric delays using ECMWF ERA-5 (ECMWF Re-Analysis) data [8] and processed using the PSInSAR technique [26]. In order to preserve all wave-numbers of the deformation signal, no spatial high-pass filtering or polynomial detrending was performed on the final data. The technique described above was applied to the estimated deformation rates. As visible in Figures 6–11, the method is able to retrieve the absolute motion while also mitigating the undesired residual atmospheric error, hence displaying all available spectral components in the deformation signal. Figures 7a, 9a, and 11a show that the residual zero-mean error Δ_0 is quite small, varying between ±2 mm/y. This can already be considered as a kind of validation of the InSAR data, whose accuracy is close to 1 mm/y.

For the reference measurements, the GNSS data processed by Nevada Geodetic Laboratories [27,28] were used. The correspondence GNSS/PSs for the calculation of vector $\underline{\Delta}$ was implemented by averaging all of the PS rates within a radius of 250 m from the GNSS station.

A further elucidation needs to be made. The reference system that describes SAR geometry (state vectors) does not account for continental drift making plate movement visible in the interferometric measurements, projected along the LoS. The GNSS data used for the calibration are also not continental drift compensated. Hence, the two data-sets can be considered "compatible". After merging (also adding v_{ref}), the data contains continental drift that could dominant the visualialization. Therefore, plate movement was compensated using the model in [29] to show movement relative to a specific plate (Eurasian). The removed motion is basically an overall offset of several mm/y, plus a light ramp due to the LoS projection of the horizontal motion. This is generally not necessary since it is only a representation issue, but it facilitates the interpretation of the results. For the sake of completeness, the removed model is also shown in Figures 7b, 9b, and 11b.

4.1. Netherlands Datasets

The systematic generation of deformation maps on a national scale using SAR interferometry has become more feasible, as missions like Sentinel-1 provide global coverage on a regular basis. Often, these kinds of services must be combined with existing geodetic measurements in order to make them integrated and comparable [21]. In this work, a typical example is provided where InSAR velocities covering a large area—acquired in descending and ascending passes—are combined with a consistent number of GNSS-derived velocities. The considered datasets are two Sentinel-1A/B stacks covering the northern part of the Netherlands. The area includes many examples of man-induced subsidences, such as in Groeningen [30]. The details of the dataset are described by Table 1. Observing the raw result of the PSI-processing, some spatially correlated deformation signals are visible when observing between ±4 mm/y. Since no large-scale deformation phenomena are expected in this area, such patterns must therefore be related to the residual atmospheric signal. In the area of interest, a considerably high number of GNSS data are available (see Table 1). The previously described methodology was applied to the data using the available GNSS measurements [27]. The results in Figures 6 and 8 show how the technique permits the further reduction of the residual atmospheric error and the relation of every single PS measurement to the Eurasian plate only. Further information about the measured Δ_0 and the removed continental drift model is also available in Figures 7 and 9. Since the ascending/descending data are now absolute, it would be possible to combine them directly using the error description provided in Equations (9)–(11).

Table 1. Netherlands Dataset.

Track	Orbit	Acquisitions	Time [years]	GNSS Stations
088	ASCE	140	3.4	47
037	DESCE	122	3.0	37

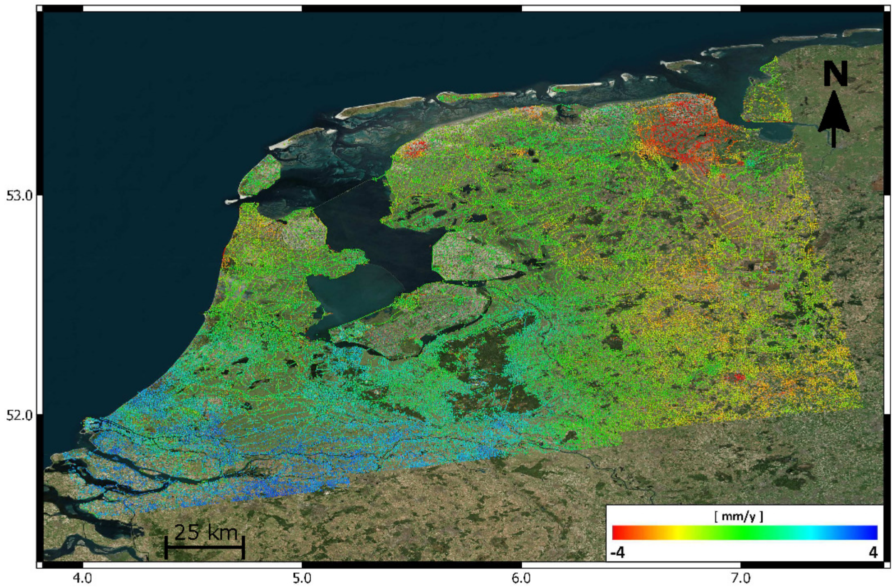

(**a**)

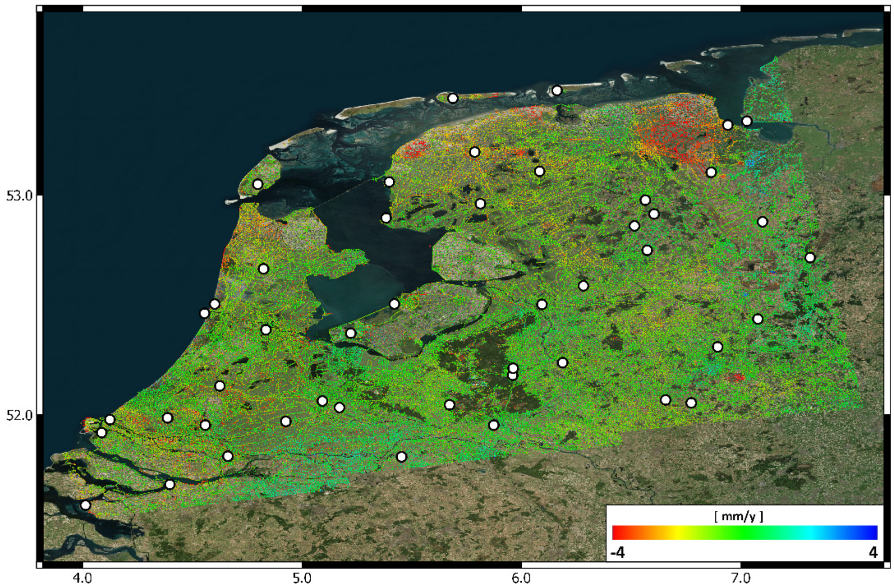

(**b**)

Figure 6. Results for the ascending Holland stack (**a**) before and (**b**) after performing merging with GNSS data. In (**b**), the GNSS stations used are displayed with black–white circles.

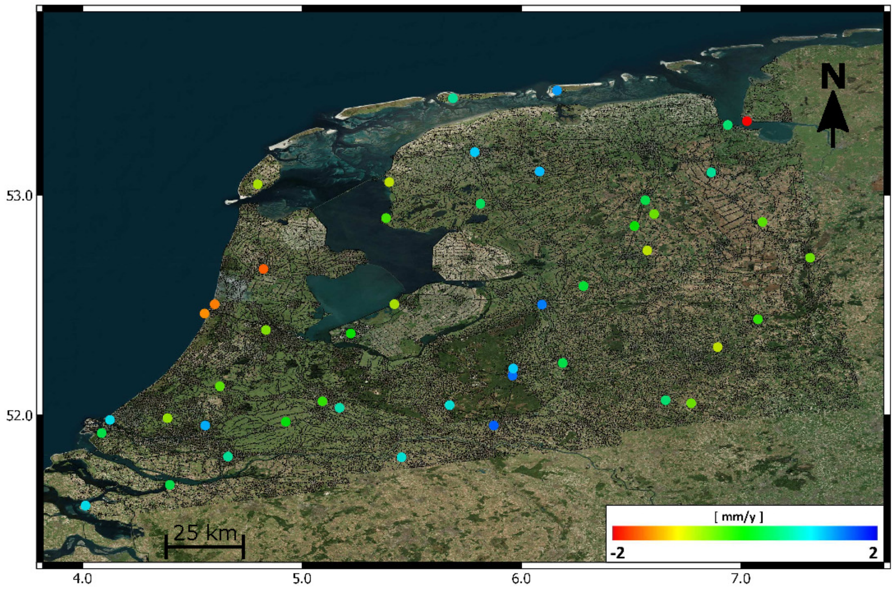

(**a**)

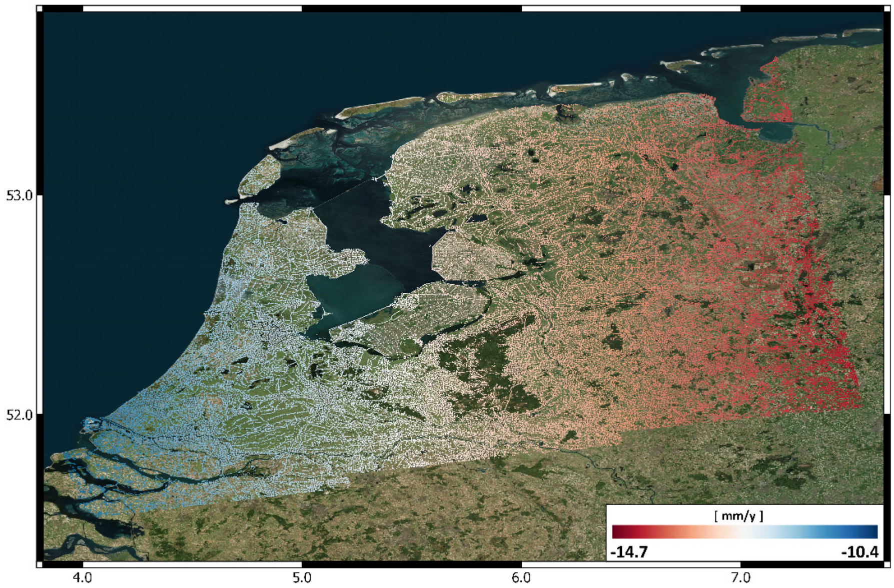

(**b**)

Figure 7. Results for the ascending Holland stack, showing the measured and color-coded Δ_0 in (**a**) and the removed continental drift screen in (**b**).

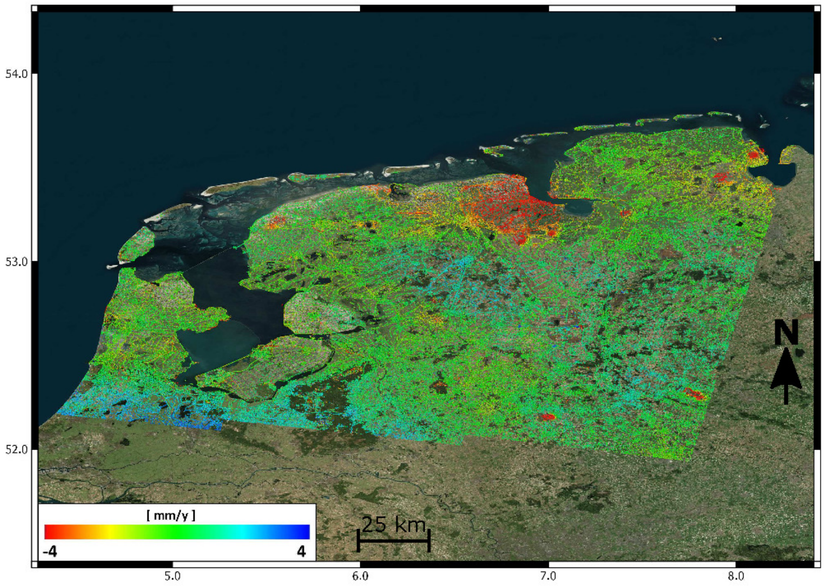

(**a**)

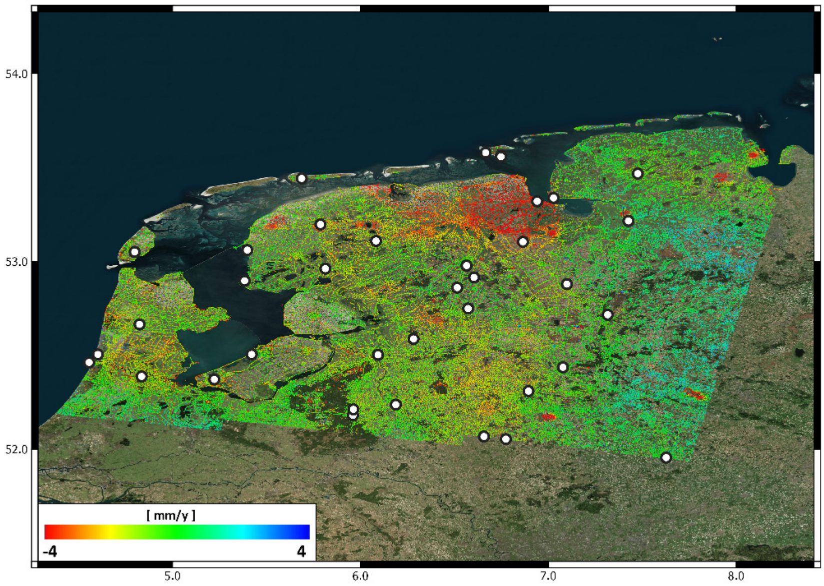

(**b**)

Figure 8. Results for the descending Holland stack, showing (**a**) before and (**b**) after performing merging with GNSS data. In (**b**), the GNSS stations used are displayed with black–white circles.

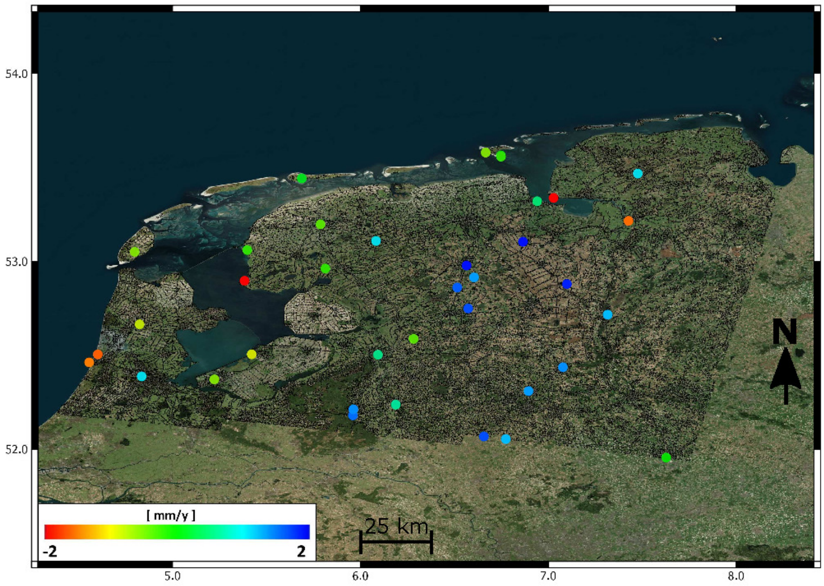

(**a**)

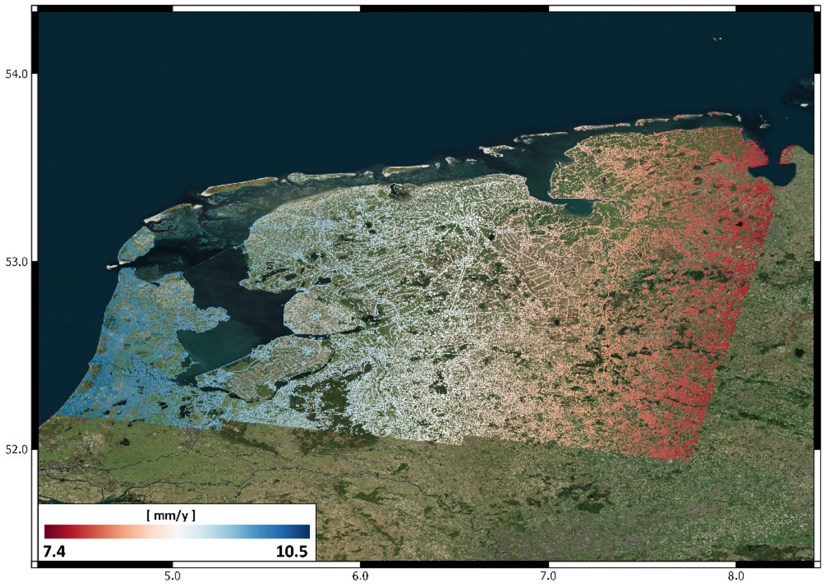

(**b**)

Figure 9. Results for the descending Holland stack, showing (**a**) the measured and color-coded Δ_0 and (**b**) the removed continental drift screen.

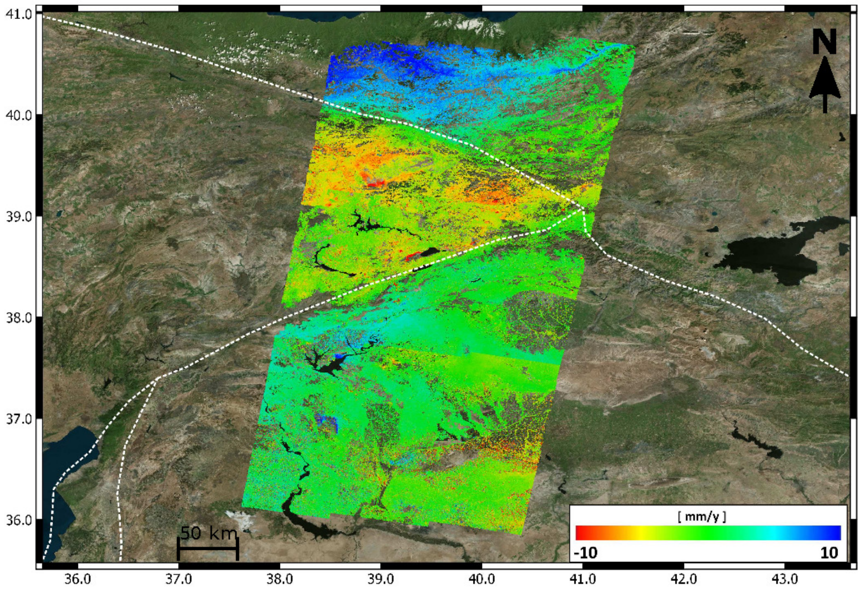

(a)

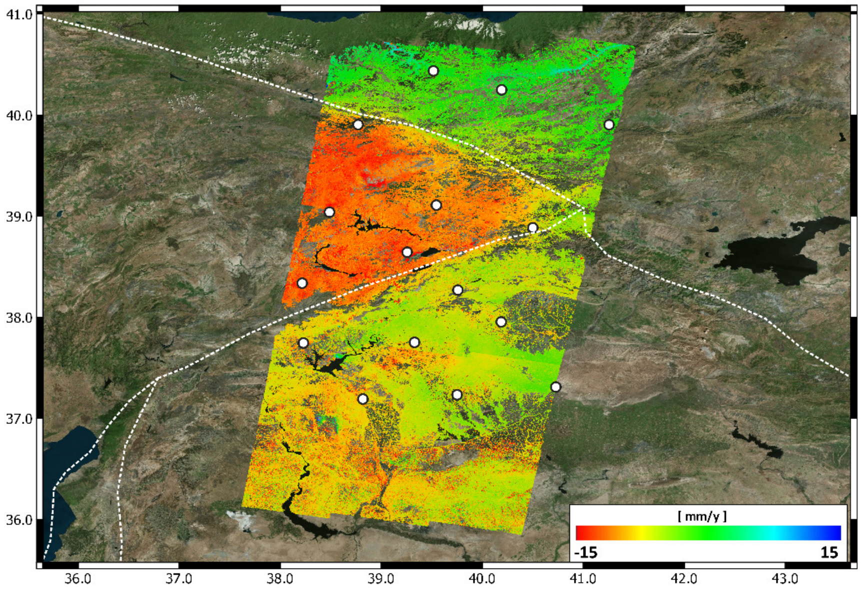

(b)

Figure 10. Results for the North Anatolian Fault (**a**) before and (**b**) after performing merging with GNSS data. In (**b**), the GNSS stations used are displayed with black–white circles and the fault lines are displayed using a white dashed line.

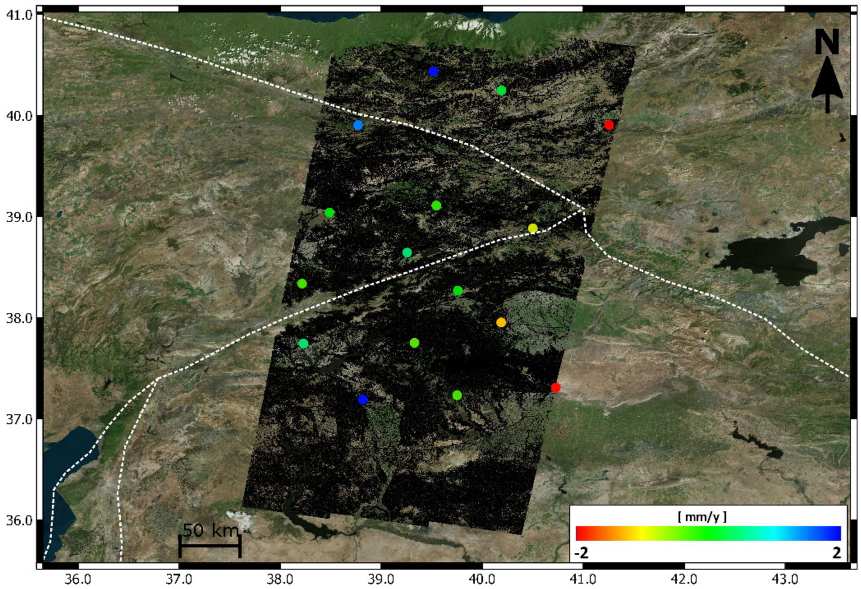

(**a**)

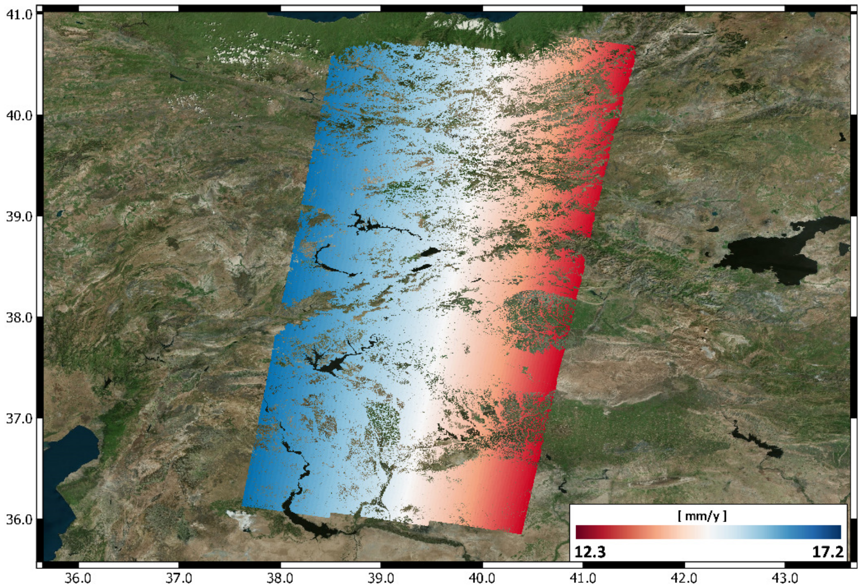

(**b**)

Figure 11. Results for the North Anatolian Fault, showing (**a**) the measured and color-coded Δ_0 and (**b**) the removed continental drift screen.

4.2. North Anatolian Fault Dataset

Applications related to the measurement of tectonic movements are the most challenging for InSAR. The requirement of an accuracy of 1 mm/y at more that 100 km (<10 nstrain) pushes the technique to its limits [5]. Notwithstanding, it has been demonstrated that, since actual SAR missions are characterized by very stable oscillators [31] and very good orbit knowledge [32,33], such numbers can be considered achievable. The major limitation is atmospheric effects. If the interferometric time series is not long enough, integration with other data would be necessary in order to fulfill the requirements at very large distances. Moreover, the possibility of referencing the measurements to standard reference systems (e.g., Eurasian Plate, etc.) would extend the usability of the final results.

The technique must then also be demonstrated on an appropriate example for tectonics. The North Anatolian Fault was chosen, as it is a typical case study investigated by many geo-scientists using SAR interferometry [34,35]. The area of interest is covered by a Sentinel-1A/B stripe extending for more than 600 km in the along-track direction, see Table 2. In order to make the processing feasible, the stripe was divided into three frames. The three frames were processed independently using the PSInSAR technique. The area is very tectonically active and it is very important to preserve all scales of the measured deformation signal. Figure 10 displays the results together with a mapping of the main path of the North and East Anatolian Fault (dashed white line).

Table 2. North Anatolian Fault Dataset.

Track	Orbit	Acquisitions	Time [years]	GNSS Stations
123/2	DESCE	134	3.3	5
123/3	DESCE	134	3.3	9
123/4	DESCE	134	3.3	4

5. Conclusions

The results show how the technique is able to both remove dependence on the reference point and mitigate residual atmospheric errors present in the final InSAR results. The described methodology works under some straightforward assumptions on the input data that have to be considered:

- The GNSS/InSAR time series must overlapped in space and time,
- the 3D GNSS velocities and their variances are known, and
- the motion of the GNSS station should be representative of the motion of the area.

The method was studied on both simulated and real data. Simulations show that even with a reduced set of GNSS stations it is possible to retrieve the absolute motion with good accuracy. On the other hand, the capability of the approach to mitigate residual atmospheric errors depends both on the GNSS station density and the spatial correlation of the errors. In order to provide some numbers, the error was modeled as an $AR(1)$ process with a correlation length of 60 km and variable overall variance. Such numbers were used because they match with the experiments. Two real test cases were then processed to demonstrate the approach by trying to address applications that should benefit from the technique. The results are promising and open the door to an accurate cross-validation between GNSS/InSAR. The extension of the approach to time series would also be interesting, merging InSAR phases with continuous GNSS measurements. The approach could be conceptually equivalent, since the deformation rates are just a scaling of the single-phase measurements, but the spatial covariance of each interferogram would be needed.

For the sake of precision, it is noted that estimation of $\widehat{v}_{ref}$ is also generally possible using only InSAR data. The key parameter to be considered here is indeed the length of the time series T_{obs}. Theoretically speaking, with a long time series, it is possible to robustly estimate the motion of the reference point by comparing the interferometric deformation rates with the rates estimated from group delays, using co-registration shifts or the PS positions [36,37]. Moreover, if T_{obs} is large enough, the residual atmospheric effects are also sufficiently small to fulfill even the strict requirements [8] set by applications aimed at measuring tectonic movements [5]. Notwithstanding, if T_{obs} is not large enough to fulfill the accuracy requirements at large distances, then merging with GNSS is necessary.

In general, it is possible to conclude that the developed method helps to increase, when necessary, the accuracy of InSAR over large distances [8]. The final product has the spatial coverage of InSAR, and is an optimal combination of InSAR and GNSS information based on the knowledge of the error statistics. This preserves all scales of the deformation signal and also allows characterization of the final product error.

Author Contributions: Conceptualization, A.P., F.R.G. and R.B.; Methodology, A.P.; Software, A.P. and F.R.G.; Investigation, A.P.; Writing–Original Draft Preparation, A.P.; Writing–Review and Editing, A.P. and R.B. All authors have read and agreed to the published version of the manuscript.

Funding: This research received no external funding.

Acknowledgments: The authors would like to thank Ekaterina Tymofyeyeva for the suggestions that helped improving the manuscript.

Conflicts of Interest: The authors declare no conflict of interest.

Abbreviations

The following abbreviations are used in this manuscript:

SAR	Synthetic Aperture Radar
InSAR	Synthetic Aperture Radar Interferometry
PS	Persistent Scatterer
PSI	Persistent Scatterers Interferometry
LoS	Line of Sight
GNSS	Global Navigation Satellite System
ECMWF	European Centre for Medium-Range Weather Forecasts
ERA	ECMWF Re-Analysis

References

1. Rosen, P.; Hensley, S.; Joughin, I.; K.Li, F.; Madsen, S.; Rodriguez, E.; Goldstein, R.M. Synthetic aperture radar interferometry. *Proc. IEEE* **2000**, *88*, 333–382. [CrossRef]
2. Rosen, P.A.; Hensley, S.; Zebker, H.A.; Webb, F.H.; Fielding, E.J. Surface deformation and coherence measurements of Kilauea Volcano, Hawaii, from SIR-C radar interferometry. *J. Geophys. Res. Planets* **1996**, *101*, 23109–23125. [CrossRef]
3. Gray, A.L.; Mattar, K.E.; Sofko, G. Influence of ionospheric electron density fluctuations on satellite radar interferometry. *Geophys. Res. Lett.* **2000**, *27*, 1451–1454. [CrossRef]
4. Hanssen, R. *Radar Interferometry: Data Interpretation and Error Analysis*; Springer: Dordrecht, The Netherlands, 2001.
5. Wright, T.J. The earthquake deformation cycle. *Astron. Geophys.* **2016**, *57*, 4.20–4.26. atw148. [CrossRef]
6. Torres, R.; Snoeij, P.; Geudtner, D.; Bibby, D.; Davidson, M.; Attema, E.; Potin, P.; Rommen, B.; Floury, N.; Brown, M.; et al. GMES Sentinel-1 mission. *Remote Sens. Environ.* **2012**, *120*, 9–24. [CrossRef]
7. Moreira, A.; Krieger, G.; Hajnsek, I.; Papathanassiou, K.; Younis, M.; Lopez-Dekker, P.; Huber, S.; Villano, M.; Pardini, M.; Eineder, M.; et al. Tandem-L: A Highly Innovative Bistatic SAR Mission for Global Observation of Dynamic Processes on the Earth's Surface. *IEEE Geosci. Remote Sens. Mag.* **2015**, *3*, 8–23. [CrossRef]
8. Gonzalez, F.R.; Parizzi, A.; Brcic, R. Evaluating the impact of geodetic corrections on interferometric deformation measurements. In Proceedings of the EUSAR 2018: 12th European Conference on Synthetic Aperture Radar, Aachen, Germany, 4–7 June 2018; pp. 1–5.
9. Gudmundsson, S.; Carstensen, J.M.; Sigmundsson, F. Unwrapping ground displacement signals in satellite radar interferograms with aid of GPS data and MRF regularization. *IEEE Trans. Geosci. Remote Sens.* **2002**, *40*, 1743–1754. [CrossRef]
10. Shanker, A.P.; Zebker, H. Edgelist phase unwrapping algorithm for time series InSAR analysis. *JOSA A* **2010**, *27*, 605–612. [CrossRef]
11. Wei, M.; Sandwell, D.; Smith-Konter, B. Optimal combination of InSAR and GPS for measuring interseismic crustal deformation. *Adv. Space Res.* **2010**, *46*, 236–249. [CrossRef]
12. Tong, X.; Sandwell, D.; Smith-Konter, B. High-resolution interseismic velocity data along the San Andreas fault from GPS and InSAR. *J. Geophys. Res. Solid Earth* **2013**, *118*, 369–389. [CrossRef]

13. Farolfi, G.; Bianchini, S.; Casagli, N. Integration of GNSS and Satellite InSAR Data: Derivation of Fine-Scale Vertical Surface Motion Maps of Po Plain, Northern Apennines, and Southern Alps, Italy. *IEEE Trans. Geosci. Remote Sens.* **2019**, *57*, 319–328. [CrossRef]
14. Wang, H.; Wright, T. Satellite geodetic imaging reveals internal deformation of western Tibet. *Geophys. Res. Lett.* **2012**, *39*, doi:10.1029/2012GL051222. [CrossRef]
15. Catalão, J.; Nico, G.; Hanssen, R.; Catita, C. Merging GPS and atmospherically corrected InSAR data to map 3-D terrain displacement velocity. *IEEE Trans. Geosci. Remote Sens.* **2011**, *49*, 2354–2360. [CrossRef]
16. Bekaert, D.; Segall, P.; Wright, T.; Hooper, A. A network inversion filter combining GNSS and InSAR for tectonic slip modeling. *J. Geophys. Res. Solid Earth* **2016**, *121*, 2069–2086. [CrossRef]
17. Mahapatra, P.S.; Samiei-Esfahany, S.; van der Marel, H.; Hanssen, R.F. On the use of transponders as coherent radar targets for SAR interferometry. *IEEE Trans. Geosci. Remote Sens.* **2014**, *52*, 1869–1878. [CrossRef]
18. Mahapatra, P.; van der Marel, H.; van Leijen, F.; Samiei-Esfahany, S.; Klees, R.; Hanssen, R. InSAR datum connection using GNSS-augmented radar transponders. *J. Geod.* **2018**, *92*, 21–32. [CrossRef]
19. Mahapatra, P.S.; Samiei-Esfahany, S.; Hanssen, R.F. Geodetic Network Design for InSAR. *IEEE Trans. Geosci. Remote Sens.* **2015**, *53*, 3669–3680. [CrossRef]
20. Jonsson, S.; Zebker, H.; Segall, P.; Amelung, F. Fault Slip Distribution of the 1999 Mw 7.1 Hector Mine, California, Earthquake, Estimated from Satellite Radar and GPS Measurements. *Bull. Seismol. Soc. Am.* **2002**, *92*, 1377–1389. [CrossRef]
21. Kalia, A.; Frei, M.; Lege, T. A Copernicus downstream-service for the nationwide monitoring of surface displacements in Germany. *Remote Sens. Environ.* **2017**, *202*, 234–249. [CrossRef]
22. Fattahi, H.; Amelung, F. InSAR bias and uncertainty due to the systematic and stochastic tropospheric delay. *J. Geophys. Res. Solid Earth* **2015**, *120*, 8758–8773. [CrossRef]
23. Cong, X.; Balss, U.; Eineder, M.; Fritz, T. Imaging geodesy—Centimeter-level ranging accuracy with TerraSAR-X: An update. *IEEE Geosci. Remote Sens. Lett.* **2012**, *9*, 948–952. [CrossRef]
24. Cong, X. SAR Interferometry for Volcano Monitoring: 3D-PSI Analysis and Mitigation of Atmospheric Refractivity. Ph.D. Thesis, Technische Universität München, München, Germany, 2014.
25. Proakis, J.; Manolakis, D. *Digital Signal Processing*; Prentice Hall: Upper Saddle River, NJ, USA, 2006.
26. Ferretti, A.; Prati, C.; Rocca, F. Permanent scatterers in SAR interferometry. *IEEE Trans. Geosci. Remote Sens.* **2001**, *39*, 8–20. [CrossRef]
27. MIDAS Velocity Fields. Available online: http://geodesy.unr.edu/ (accessed on 1 October 2018).
28. Blewitt, G.; Kreemer, C.; Hammond, W.C.; Gazeaux, J. MIDAS robust trend estimator for accurate GPS station velocities without step detection. *J. Geophys. Res. Solid Earth* **2016**, *121*, 2054–2068. [CrossRef]
29. Rouby, H.; Métivier, L.; Rebischung, P.; Altamimi, Z.; Collilieux, X. ITRF2014 plate motion model. *Geophys. J. Int.* **2017**, *209*, 1906–1912. [CrossRef]
30. Ketelaar, V.G. *Satellite Radar Interferometry: Subsidence Monitoring Techniques*; Springer Science & Business Media: Berlin/Heidelberg, Germany, 2009; Volume 14.
31. Larsen, Y.; Marinkovic, P.; Dehls, J.F.; Perski, Z.; Hooper, A.J.; Wright, T.J. The Sentinel-1 constellation for InSAR applications: Experiences from the InSARAP project. In Proceedings of the 2017 IEEE International Geoscience and Remote Sensing Symposium (IGARSS), Fort Worth, TX, USA, 23–28 July 2017; pp. 5545–5548.
32. Yoon, Y.T.; Eineder, M.; Yague-Martinez, N.; Montenbruck, O. TerraSAR-X Precise Trajectory Estimation and Quality Assessment. *IEEE Trans. Geosci. Remote Sens.* **2009**, *47*, 1859–1868. [CrossRef]
33. Peter, H.; Jäggi, A.; Fernández, J.; Escobar, D.; Ayuga, F.; Arnold, D.; Wermuth, M.; Hackel, S.; Otten, M.; Simons, W.; et al. Sentinel-1A–First precise orbit determination results. *Adv. Space Res.* **2017**, *60*, 879–892. [CrossRef]
34. Cakir, Z.; Ergintav, S.; Akoğlu, A.M.; Çakmak, R.; Tatar, O.; Meghraoui, M. InSAR velocity field across the North Anatolian Fault (eastern Turkey): Implications for the loading and release of interseismic strain accumulation. *J. Geophys. Res. Solid Earth* **2014**, *119*, 7934–7943. [CrossRef]
35. Hussain, E.; Wright, T.J.; Walters, R.J.; Bekaert, D.P.; Lloyd, R.; Hooper, A. Constant strain accumulation rate between major earthquakes on the North Anatolian Fault. *Nat. Commun.* **2018**, *9*, 1392. [CrossRef]

36. Madsen, S.N.; Zebker, H.A.; Martin, J. Topographic mapping using radar interferometry: Processing techniques. *IEEE Trans. Geosci. Remote Sens.* **1993**, *31*, 246–256. [CrossRef]
37. Eineder, M.; Minet, C.; Steigenberger, P.; Cong, X.; Fritz, T. Imaging Geodesy—Toward Centimeter-Level Ranging Accuracy With TerraSAR-X. *IEEE Trans. Geosci. Remote Sens.* **2011**, *49*, 661–671. TGRS.2010.2060264. [CrossRef]

D

Parizzi, A., Brcic R. and De Zan F. (2021). InSAR Performance for Large-Scale Deformation Measurement. IEEE Transactions on Geoscience and Remote Sensing, 59(10):8510-8520

Summary This article deals with the analysis of InSAR performance for large-scale deformation measurement. The study evaluates the use of models, especially numerical weather prediction reanalysis, to mitigate disturbances in SAR interferograms. The impact of such corrections is evaluated by analyzing short-time baseline phase variograms in order to derive a lower bound for the interferometric accuracy, especially at large distances. The variance is then propagated from single interferograms to deformation rates. Finally, using GNSS measurements, the predicted error bars are validated on a large Sentinel-1 data set.

Contributions of the candidate Derivation of the performance model. Practical implementation of the experiments. Writing the paper.

InSAR Performance for Large-Scale Deformation Measurement

Alessandro Parizzi, Ramon Brcic, and Francesco De Zan

Abstract—**This article deals with the analysis of InSAR performance for large-scale deformation measurement. The study evaluates the use of models, especially numerical weather prediction reanalysis, to mitigate disturbances in SAR interferograms. The impact of such corrections is evaluated by analyzing short-time baseline phase variograms in order to derive a lower bound for the interferometric accuracy, especially at large distances. The variance is then propagated from single interferograms to deformation rates. Finally, using GNSS measurements, the predicted error bars are validated on a large Sentinel-1 data set.**

Index Terms—**Deformation, GNSS, InSAR, numerical weather prediction (NWP), performance.**

I. INTRODUCTION

THE Sentinel-1 mission [1] systematically provides SAR data suitable for interferometric applications with a swath width of 250 km. Future SAR satellites will further extend this to even larger swaths [2], [3]. The measurement of tectonic movements particularly benefits from the large-scale deformation measurements that SAR interferometry provides. Nevertheless, since the magnitude of the relative error increases with distance [4]–[6], the performance of relative deformation measurements between very distant points may not achieve the required accuracy for tectonic applications [7]. Typically, interferometry works well for applications such as infrastructure monitoring or urban subsidence since they involve relatively short scales (10–20 km). It is then common practice to remove the low-pass spatial frequencies of the estimated deformation signal by filtering or detrending. This is appropriate if the application is not the measurement of large-scale deformation. However, the rising scientific interest in using InSAR to measure this kind of deformation [8] requires preservation of all the spatial wavelengths of the deformation and proper treatment and knowledge of the error bars at such distances.

The atmosphere has always been recognized as one of the main error sources in interferometric measurements [4]. The main problem stems from its spatial characteristic that prevents complete separation from the deformation signal by spatial filtering. Temporal filtering, even if it improves the time series quality, is also not a general solution. This is due to nonlinear deformation, uncompensated seasonal effects, and irregular sampling due to snow cover. The performance of the estimated deformation rates is still limited by the atmospheric delay. Therefore, external information is necessary to reconstruct and compensate for the unwanted delay in the interferograms [9]. Information from GNSS stations or other remote sensing instruments, such as MODIS or MERIS, are typically used despite the different resolutions [10]–[12]. The correction of tropospheric stratification was successful using both model-based and data-driven approaches [13]–[15]. In the past decade, the use of numerical weather prediction (NWP) became a valuable tool for systematic correction of both SAR group and phase delays, hence improving the performance and capabilities of the techniques [16]–[20].

Starting from this basis, this article first investigates interferometric performance at large distances when ECMWF ERA-5 NWP data were used for the corrections. Then, based on a simple theoretical model, a possible error description is provided and its validity is demonstrated on real data. Before going further, a brief discussion of other error sources affecting the measurements at long distances, and how they were considered, is warranted.

The ionosphere can generate huge errors at low frequency (L-band and P-band) SAR [21]. In C-band, its effect is less severe even though exceptions have been reported [22]. In such cases, compensation using the split spectrum technique can reduce the error to the level of the troposphere so that it is no longer the limiting factor [23]. Here, ionospheric effects have been corrected using CODE models in order to mitigate larger scale ionospheric effects [24]. The effect of solid earth tides (SETs) involves scales much larger than the SAR swath; however, their projection onto the SAR line of sight (LoS) along the swath can generate centimeter-level phase ramps. Therefore, SETs were compensated using the IERS 2010 convention [24], [25]. Finally, SAR missions are characterized by very stable oscillators [26] and very good orbit knowledge [27], [28]. This study does not consider the uncertainties related to the residuals of ionosphere and SET corrections nor the accuracy of the state vectors. Instead, it is implicitly assumed that the residual error of signals related to the ionosphere, SETs, and orbit state vectors is negligible compared with the tropospheric signal that becomes the limiting factor for interferometric performance at large distance, as verified in the Appendix. Violation of this assumption leads to an underestimation of the tropospheric component. Hence, this study is intended to outline the bound for the improvement related to tropospheric corrections.

Manuscript received July 20, 2020; revised October 8, 2020; accepted November 14, 2020. Date of publication December 3, 2020; date of current version September 27, 2021. This work was supported in part by Helmholtz-Gemeinschaft under the Project Tectonics and Volcanoes in South America with InSAR (TecVolSA). *(Corresponding author: Alessandro Parizzi.)*

The authors are with Remote Sensing Technology Institute, German Aerospace Center (DLR), 82234 Wessling, Germany (e-mail: alessandro.parizzi@dlr.de).

Digital Object Identifier 10.1109/TGRS.2020.3039006

II. INTERFEROMETRIC PERFORMANCE MODELING WITH TROPOSPHERIC CORRECTION

The use of NWP for mitigating the tropospheric signal in the interferometric phase is limited both in accuracy, due to the limitations of the model itself, and in resolution. The best sampling available is 9 km in the case of ECMWF products, several orders of magnitude larger than the SAR resolution, even after interferometric multilooking. The accuracy of NWP can be strongly site dependent since it depends on data availability and the fit of the model to actual tropospheric conditions. For the ECMWF products considered here, there is a strong dependence of accuracy on latitude [29]. However, it should be pointed out that since the interferograms are intrinsically relative, the impact of model bias in the simulated interferometric phase is limited. More important is the variance of the error between the real zenith delay z_t and the modeled delay $\widehat{z}_t$ $\epsilon = z_t - \widehat{z}_t$. This can be seen as a Gaussian process in time and space with mean μ_ϵ, variance σ_ϵ^2, and spatial correlation function Λ. The interferometric error between two points A and B for reference acquisition r and secondary acquisition s is

$$\phi_\epsilon = (\epsilon_{r,A} - \epsilon_{s,A})\frac{e^{-\frac{h_A}{H}}}{\cos\theta_A} - (\epsilon_{r,B} - \epsilon_{s,B})\frac{e^{-\frac{h_B}{H}}}{\cos\theta_B} \tag{1}$$

where θ is the local incidence angle. The effect of the altered path delay due to topography is considered using the exponential mapping function as in [30] with h_A and h_B the height of the points with respect to the ellipsoid and H the so-called height of the atmosphere, typically fixed to 7 km. Assuming that the error is first-order stationary, the mean interferometric phase error is $\mathbb{E}[\phi_\epsilon] = 0$ even if the residual error has nonzero mean, $\mu_\epsilon \neq 0$ as visible from (1). Assuming that the atmosphere and the error are temporally uncorrelated, the interferometric phase error power is

$$\mathbb{E}\left[\phi_\epsilon^2\right] = 2\sigma_\epsilon^2\frac{e^{-\frac{2h_B}{H}}\cos^2\theta_A + e^{-\frac{2h_A}{H}}\cos^2\theta_B}{\cos^2\theta_A\cos^2\theta_B} - \frac{4\Lambda(A,B)}{\cos\theta_A\cos\theta_B}e^{-\frac{h_B+h_A}{H}} \tag{2}$$

where Λ is a correlation function that $\Lambda(A \equiv B) = \sigma_\epsilon^2$ and $\Lambda(A, B) \to 0$ at large distance. The residual error in the interferometric phase between points A and B described in (2) is a parameterization of the sample variograms that can be calculated from data. Equation (2) approaches 0 as the distance $d \to 0$ and is $\propto \sigma_\epsilon^2$ as $d \to \infty$. This means that at large distances (≥40–50 km), the interferometric measurements become limited by the accuracy of the models used for the correction, as verified in the Appendix.

In order to study the troposphere-induced error and its mitigation through the use of NWP, short-time interferograms are generated from every acquisition with the next. This approach should prevent bias due to a common reference as well as eventual seasonality present in the tropospheric delay[1] and the impact of deformation. The latter point requires clarification. The fast revisit time of the Sentinel-1 mission allows temporal baselines of 6, 12, or, in worse case, 24 days. Since the residual error, including effects such as tropospheric turbulence, is assessed to be on the order of centimeters, deformation rates of several tens of cm/y would be necessary in order to produce effects comparable to those from the troposphere. Such rates occur due to landslides or in mining areas that are typically restricted in time and space. It follows that variograms computed by averaging over the scene should not be strongly impacted by such rapid deformation types. The projection of tectonic plate motion onto the range varying LoS is a large-scale effect that could seriously bias variogram estimation. Such movements are mainly horizontal and can reach 6 and 7 cm/y. Projection onto the LoS (30° to 45° at near and far range, respectively, for Sentinel-1), combined with the previously mentioned revisit times, shows its impact to be negligible. The eventual presence of seismic events in the time series should be assessed and coseismic interferometric pairs avoided when estimating the variograms.

The tropospheric error is considered temporally uncorrelated. This hypothesis should hold at least for the troposphere corrected phase since all seasonal effects are included in the NWP and are hence compensated. The interferometric phase variogram between acquisitions n and m, $\Gamma_{n,m}$, is then the sum of the two variograms of the errors in acquisition n and m, Γ_n and Γ_m

$$\begin{aligned}\Gamma_{n,m}(d) &= \mathbb{E}[((\phi_n(A) - \phi_n(B)) - (\phi_m(A) - \phi_m(B)))^2] \\ &= \Gamma_n + \Gamma_m\end{aligned} \tag{3}$$

where ϕ is the phase at points A and B and d is the distance between the points.

By averaging the set of short-time baseline variograms $\bar{\Gamma} = \mathbb{E}[\Gamma]$, it is possible to derive the average behavior of the residual interferometric phase error. Performing this experiment before and after the NWP correction allows an analysis of the impact of the corrections at different scales. The interferometric data and NWP models have different resolutions, and hence, different behavior is expected at different scales. Fig. 1 shows an example of variogram behavior before and after correction using a long stripe of mosaicked Sentinel-1 interferograms (see also the Appendix and [24]). Although the spread of the gain is large at all scales, the temporal average of the variograms clearly shows the considerable gain due to the NWP correction that increases at large scales (≥40–50 km). This is particularly important in tectonic strain applications where high relative accuracy is required at large scales.

Assuming that the troposphere is the main source of error at large distances (≥40–50 km), one can now derive its impact on deformation rate measurements. The variogram of the linear deformation rate estimates is obtained by scaling $\bar{\Gamma}$ by the linear regression formula [31]

$$\Gamma_\text{v}(d) = \frac{1}{2}\frac{\lambda^2}{16\pi^2}\frac{\bar{\Gamma}(d)}{M\sigma_t^2} \tag{4}$$

where the factor $1/2$ accounts for the common reference acquisition, M is the number of acquisitions, and σ_t^2 is the spread of the temporal sampling $\sigma_t^2 = \sum_i t_i^2/M - (\sum_i t_i/M)^2$.

---

[1] Seasonality should be removed by the tropospheric models but could be still present in the noncorrected interferograms used to compute the performance gain.

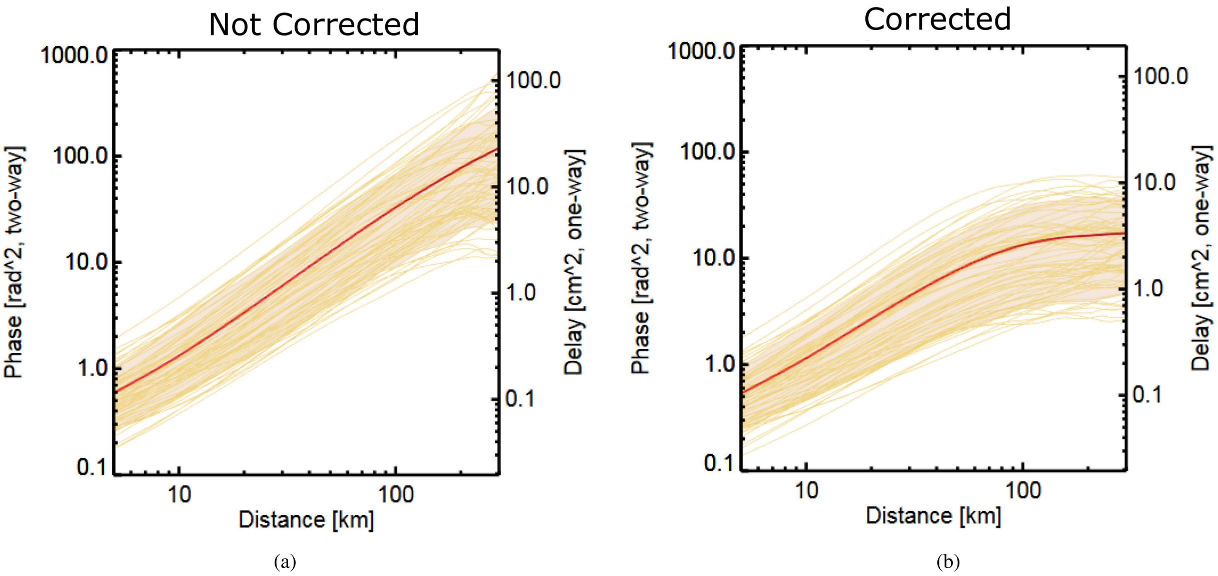

(a) (b)

Fig. 1. Single variograms, $\Gamma_i + \Gamma_{i+1}$ (thin orange lines), and their mean, $\bar{\Gamma}$ (bold red line). (a) Without and (b) with NWP corrections.

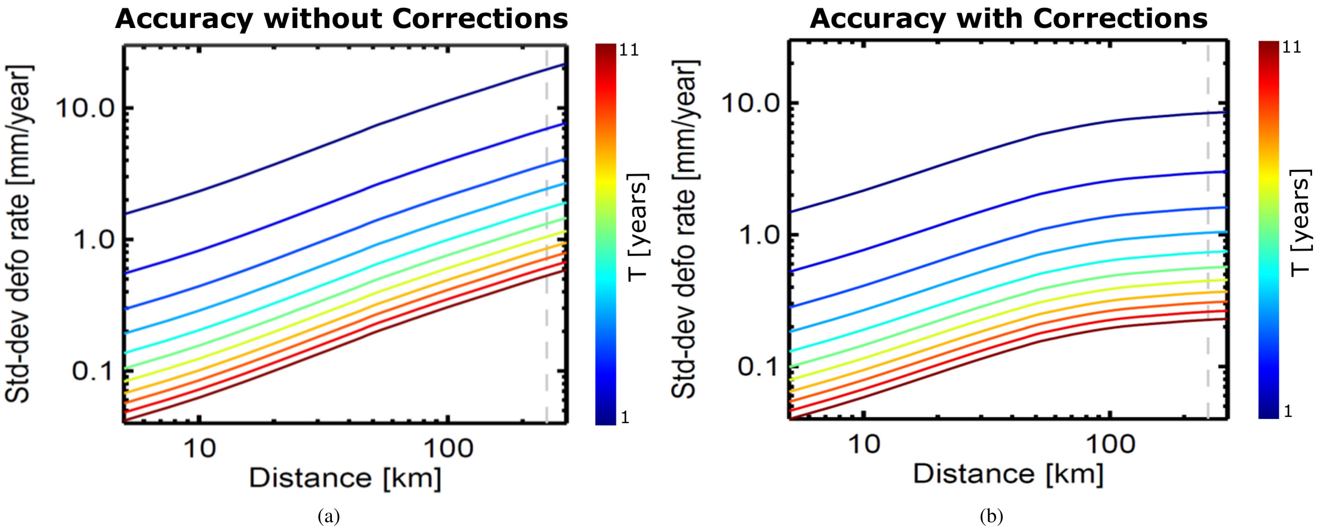

(a) (b)

Fig. 2. Variograms of the deformation rate estimates with the length of the time series color-coded and assuming a 12-day revisit time. (a) Without tropospheric corrections. (b) With tropospheric corrections.

Fig. 2 shows an example of the impact of NWP corrections on the deformation rate estimates at different scales when varying the length of the time series. It is interesting to note how the typical 1-mm/y accuracy requirement is achieved after four years with the corrected data set, while almost eight years are required if no correction is applied. In this section, the rationale of the study has been briefly described accompanied by examples. In Section III, this approach is extended to a larger set of data worldwide to analyze and validate what has just been presented.

III. PERFORMANCE OF THE NWP TROPOSPHERIC CORRECTION

Section II demonstrated how compensation of the tropospheric delay reduced the spatially correlated noise. Variograms are a convenient way to characterize this noise component. By comparing the interferometric phase variograms before and after the correction, it should be possible to observe the gain at different scales. Since the data used for compensation are not provided at the same resolution of the interferograms, a significant reduction of the tropospheric contribution can only be expected at scales larger than the NWP model resolution. Here, ECMWF ERA-5 data are used with a spatial gridding of 30 km. It should be noted that the accuracy of the correction has been demonstrated to vary considerably worldwide [15], [29].

In order to comprehensively evaluate correction performance, 146 Sentinel-1 stacks[2] have been processed over various regions of the world. Each of these stacks spans at least four years and contains up to 200 acquisitions. As described in

---

[2] A "stack" is a set of interferometrically compatible SAR acquisitions coregistered to a common reference.

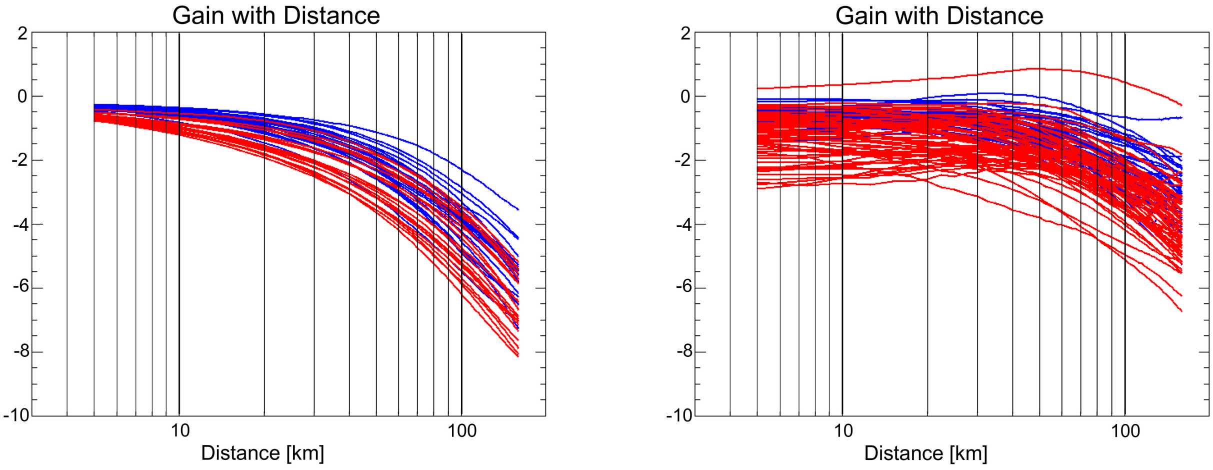

(a) (b)

Fig. 3. Variogram ratios, $G_{\text{dB}}(d)$, for (a) German Ground Motion Service and (b) all other stacks. Every line corresponds to $G_{\text{dB}}(d)$ for a single stack. The ascending stacks are depicted in blue and the descending in red.

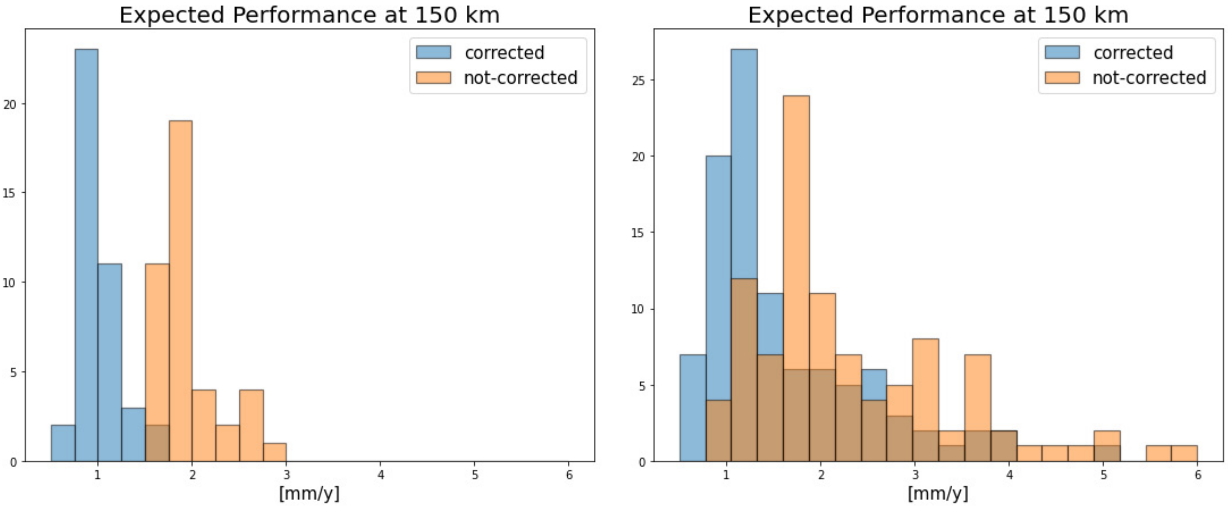

(a) (b)

Fig. 4. Expected performance at 150 km before (red) and after (blue) the tropospheric corrections. (a) German Ground Motion Service only. (b) All other available data sets.

Section II, only short-time baseline interferograms were used to ensure that the troposphere signal dominates. The average variogram $\bar{\Gamma}$ was also calculated at different scales. A measure of the gain provided by the correction is provided by the metric

$$G_{\text{dB}}(d) = 10\log_{10}\left(\frac{\bar{\Gamma}_{\text{corr}}(d)}{\bar{\Gamma}_{\text{raw}}(d)}\right) \tag{5}$$

the ratio, in decibels, of the average variograms with and without the correction.

Fig. 3 shows $G_{\text{dB}}(d)$ for stacks from the German Ground Motion Service separately from all others.

An evaluation of the performance at large distances was also performed. The average variograms before and after corrections were fitted using typical variogram models (exponential, Gaussian, and spherical), hence reducing the variance of the variogram estimate. Using this information together with temporal sampling information and (4), the performance in measuring the deformation rates at 150 km was estimated with and without the tropospheric corrections. Fig. 4 shows the histograms of the accuracies in mm/y with the German Ground Motion Service shown separately from all others.

Mitigation of tropospheric effects and the correct characterization of their spatial characteristics are critical in developing error models for missions that allow [1] or will allow [2], [3] systematic interferometric processing on a global scale.

Figs. 3–5 show that a significant gain is attained when the tropospheric delay is corrected. As already pointed out in [29], the gain is region dependent. A very high gain is achieved where the model accuracy is also very good, such as in Europe or USA. Only one of the 146 stacks, located in Indonesia, was the corrections found to slightly worsen the performance at medium scale and is clearly visible in Fig. 4.

In Fig. 3, a smaller but nonnegligible gain is also observable at short scales ($\leq$10 km). This value can vary from 0 up to

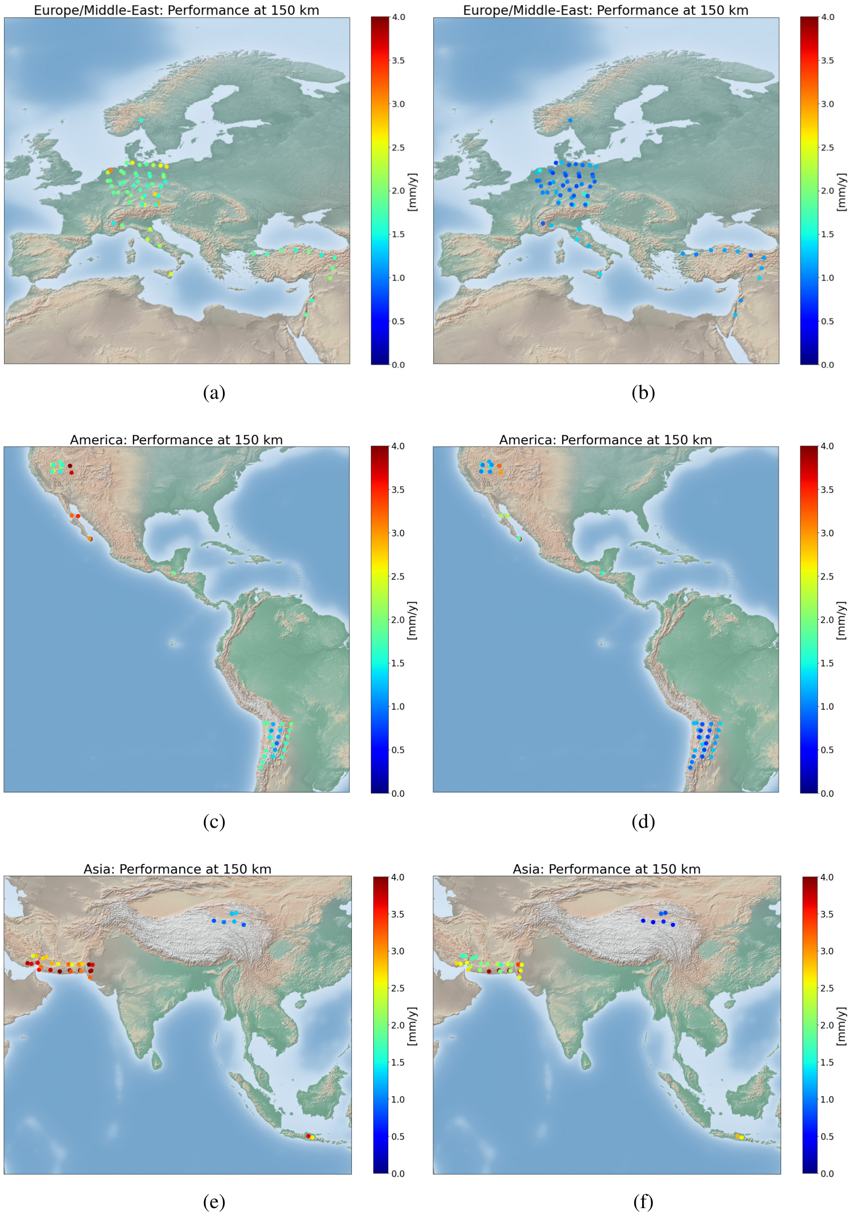

(a) (b)

(c) (d)

(e) (f)

Fig. 5. Performance at 150 km (a), (c), and (e) before and (b), (d), and (f) after the corrections. (Top row) Europe and the Middle East, (Middle row) North and South America, and (Bottom row) Asia.

3–4 dB depending on the test site, as visible in Fig. 6. The tropospheric models can correct stratification effects at scales smaller than the models' resolution since the topography, available at the reference DEM resolution, can be used to project the models to phase errors [15]. Therefore, such a gain can only be attributed to the compensation of tropospheric stratification since the resolution of the correction model is much coarser than the topographic variation.

IV. ACCURACY OF INSAR VELOCITIES AND VALIDATION

Knowledge of displacement rate precision is of central importance in geophysical studies of large-scale tectonic movements where the precision requirements are often very high [7]. In Section II, it has been shown how the residual tropospheric noise can be characterized from short-time baseline interferograms and how this can be translated into displacement rate accuracy. This approach involves assumptions about the residual error, i.e., the short-time baseline interferograms characterize the error, that could be questioned. For the sake of completeness, the behavior of the displacement rate as described in (4) must be verified in practice.

This was achieved by cross validation with GNSS measurements using the rationale developed in [32] for integrating GNSS and InSAR measurements. Consider N locations where two displacement rates v_D (in LoS) and $\underline{v}_G$ (in x, y, z) are obtained from InSAR and GNSS, respectively. With $\underline{s}$ as the LoS vector, the difference between the two velocities at position i, Δ_i, is

$$\Delta_i = v_{D,i} - \underline{v}_{G,i}^T \underline{s} = \delta_i + v_{ref} + n_i \tag{6}$$

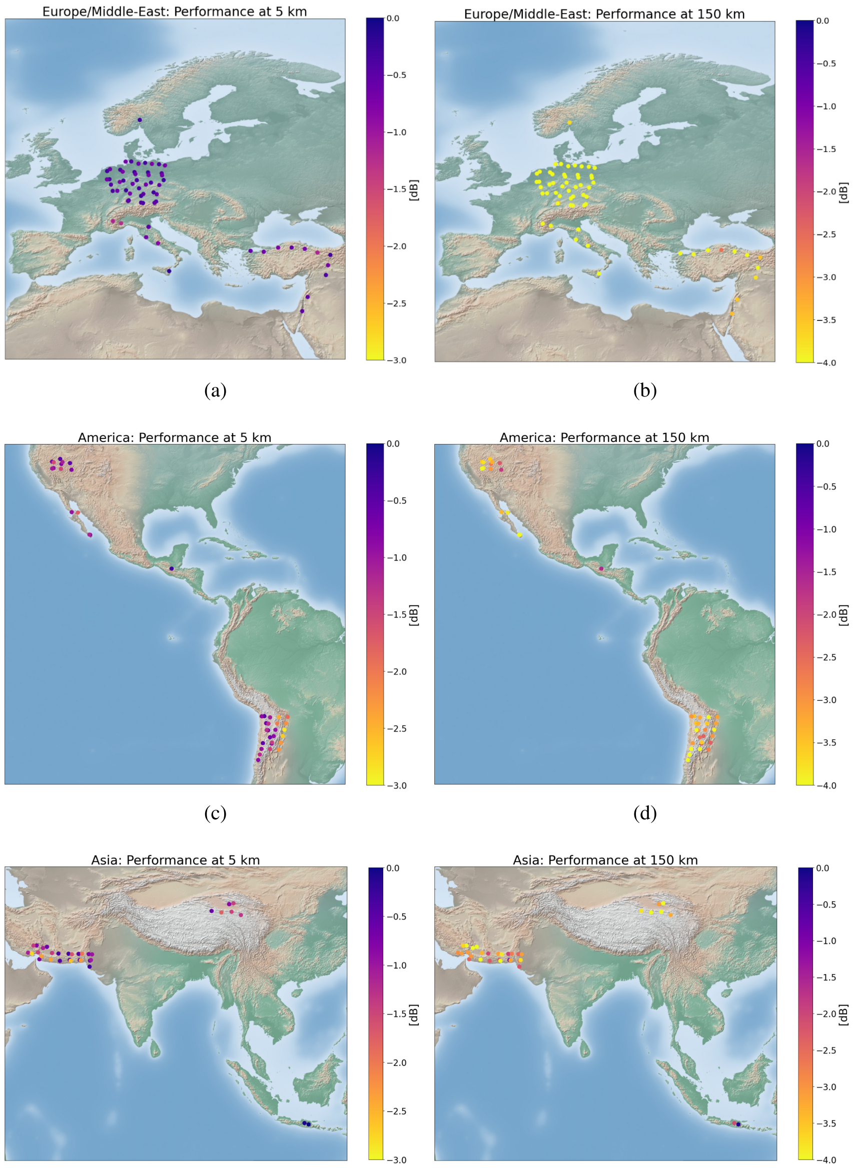

(a) (b)

(c) (d)

(e) (f)

Fig. 6. Correction gain at (a), (c), and (e) 5 and (b), (d), and (f) 150 km. (Top row) Europe and the Middle East, (Middle row) North and South America, and (Bottom row) Asia.

where v_{ref} is the velocity of the reference point used in InSAR processing, δ_i represents spatially varying residual atmospheric zero-mean error from InSAR processing, and n_i is the random error. The quantity Δ_i is obtained in practice by selecting a set of InSAR measurements located within a radius of a few hundred meters around the GNSS stations. In order to reduce the influence of clutter, the interferometric measurements are averaged. In this way, the random noise component n_i can be considered almost completely due to GNSS.

To use ((6)), a statistical description of the vector $\underline{\Delta}$ is required, i.e., the covariance matrix $\mathbf{R}$ of the difference measurements. Three terms can be distinguished: 1) random noise from the GNSS measurements $\sigma^2_{G,i}$ obtained by projecting the variance of the (x, y, z) components of the velocities onto the LoS; 2) random noise from the InSAR measurements $\sigma^2_{D,i}$; and 3) spatially correlated noise due to residual atmospheric effects. The full covariance matrix is

$$\mathbf{R} = \mathrm{diag}\left(\sigma^2_{G,0}, \ldots \sigma^2_{G,N-1}\right) + \mathrm{diag}\left(\sigma^2_{D,0}, \ldots \sigma^2_{D,N-1}\right) + \mathbf{C}_\delta. \tag{7}$$

The first two terms are diagonal matrices since they represent the spatially uncorrelated errors of the independent GNSS and InSAR measurements, respectively. The last term, $\mathbf{C}_\delta$, representing residual atmospheric error, still has to be found [33]. It can be determined from the average variogram $\bar{\Gamma}_{\mathrm{corr}}(d)$ according to (4).

Given a full statistical characterization of the GNSS/InSAR differences and assuming the GNSS accuracies to be correct, we can now verify whether Γ_v actually represents the variogram of the velocity error. First, from the vector $\underline{\Delta}$ of N differences between GNSS and InSAR velocities, we compute

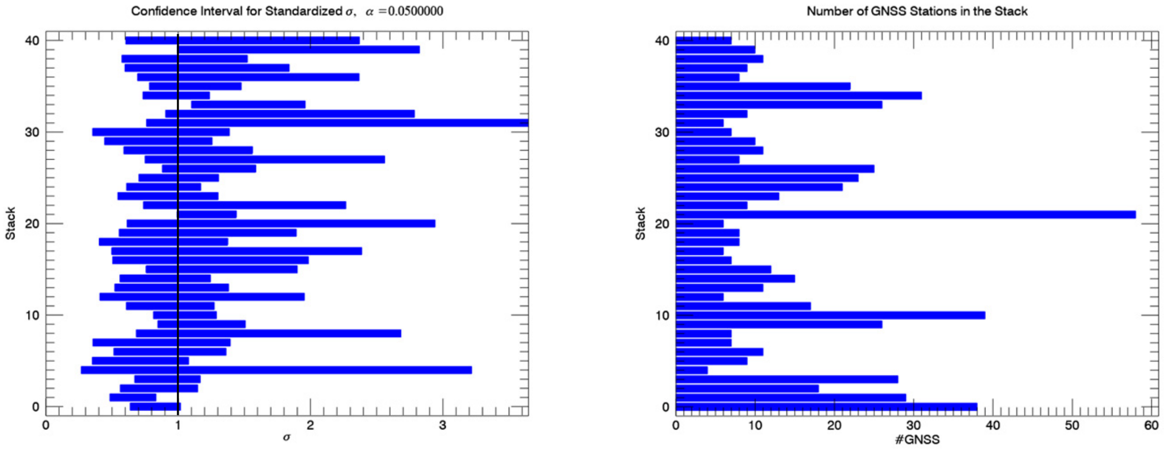

(a)

(b)

Fig. 7. Results of the InSAR/GNSS velocities cross validation. (a) Number of GNSS stations present in each stack. (b) Confidence intervals where the black line denotes $\sigma_T = 1$.

all $(N^2 - N)/2$ unique pairwise differences between the elements. Their mean is expected to be zero according to (6) and their variance is

$$\sigma_\Delta^2(i,j) = \mathbb{E}[(\Delta_i - \Delta_j)^2] = \sigma_{G,i}^2 + \sigma_{G,j}^2 + \Gamma_v(d_{i,j}). \quad (8)$$

The scales at which Γ_v can be verified by this method clearly depend on the spatial distribution of GNSS stations, with the range of scales being set by the smallest and largest distances between the stations.

A statistic defined as the standardized difference

$$T_{i,j} = \frac{\Delta_i - \Delta_j}{\sigma_\Delta(i,j)} \quad (9)$$

should follow a standard normal distribution if the error description is correct. To test the validity of the variance model in (8), a χ^2-test can be performed on $\underline{T}$. The confidence region at significance level α for the true σ_T^2 is

$$\sqrt{\frac{(N-1)\hat{\sigma_T^2}}{\chi^2_{1-\alpha/2,N-1}}} < \sigma_T < \sqrt{\frac{(N-1)\hat{\sigma_T^2}}{\chi^2_{\alpha/2,N-1}}} \quad (10)$$

where the number of degrees of freedom is $N-1$ and $\hat{\sigma_T^2}$ is the sample variance of T. The validation approach will focus on analyzing the distribution of $\underline{T}$ and the confidence interval for σ_T.

A. Cross Validation of the German Ground Deformation Service Data Set Using GNSS Stations

The cross-validation scheme was performed on the German deformation map. The data set includes 41 stacks acquired in both ascending and descending geometries. This region was chosen due to easy and open access to a very dense GNSS network from Nevada Geodetic Laboratories [34], [35] with all stacks containing sufficient GNSS stations.

The confidence intervals for σ_T at 5% significance level are shown in Fig. 7(a). Of course, the dependence on the number of GNSS stations, shown in Fig. 7(b), is strong. However, for almost all stacks, the confidence intervals include $\sigma_T = 1$ indicating acceptance of the null hypothesis $H_0 : \sigma_T = 1$ versus the alternative $H_1 : \sigma_T \neq 1$. Fig. 8 shows the distribution of $\underline{T}$ pooled over all stacks, along with the nominal standard normal distribution under the null. The pooled value of $\hat{\sigma_T}$ is 1.03, showing very good agreement between the model and GNSS data.

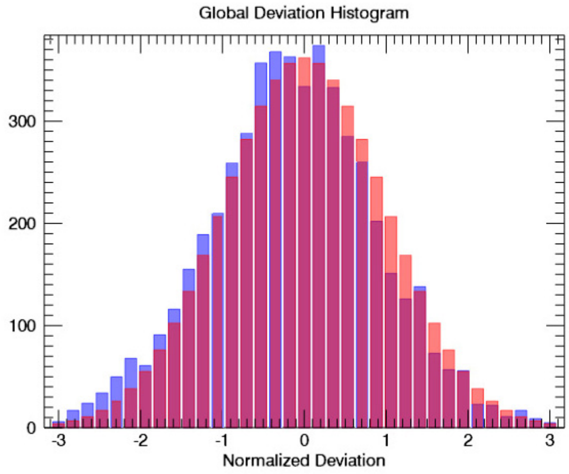

Fig. 8. Histogram of the pooled vectors $\underline{T}$ using NGL GNSS results (blue) compared to the nominal $N(0,1)$ distribution (red).

Fig. 9(a) shows the error variogram from InSAR data compared to all possible pairwise differences $(\Delta_i - \Delta_j)^2$ in order to show the fit of the variogram model at various scales. Since the accuracy of GNSS measurements also plays a role, the GNSS error contribution is included as per (8). The power of the GNSS contribution can be close to that of the InSAR one, especially at smaller scales where GNSS may distort the validation. For this purpose, a special validation was designed.

B. Validation at Local Scales for the German Deformation Map

Given that there is only limited large-scale deformation over German territory, the experiment was repeated using a

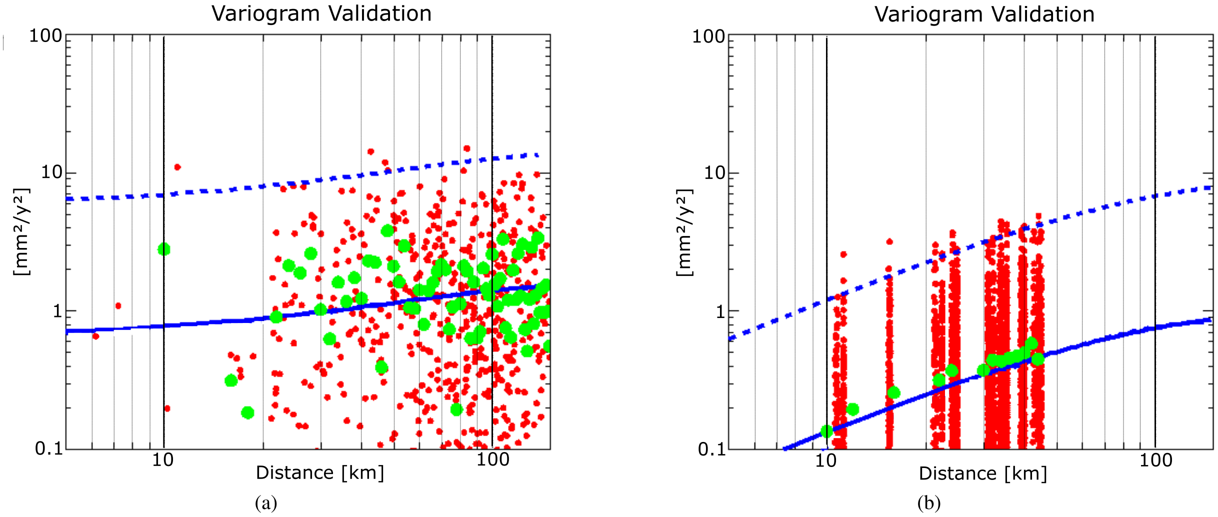

(a)

(b)

Fig. 9. Comparison between variograms (blue line) and all pairwise differences $(\Delta_i - \Delta_j)^2$ (red dots) for an ascending stack of the German Ground Motion Service. In order to highlight the plausible area for the measurements, the blue dashed lines correspond to $(3\sigma)^2$ variograms and the bold one to σ^2. The green dots correspond to the pairwise differences after averaging over 2-km bins, as in (8). The variograms are shown (a), including the GNSS error component as in Section IV-A and (b) using the zero-velocity synthetic network as in Section IV-B.

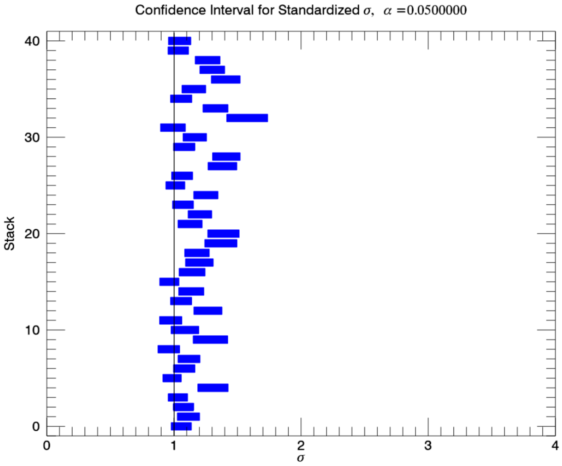

Fig. 10. Confidence intervals for each stack for the experiment of Section IV-B. The black line denotes $\sigma_T = 1$.

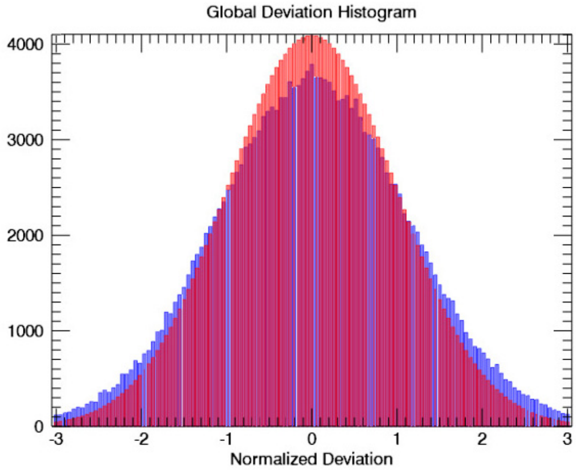

Fig. 11. Histogram of the pooled vectors $\underline{T}$ using synthetic GNSS stations (blue) compared to the nominal $N(0, 1)$ distribution (red).

network of synthetic GNSS having no motion generated on a 0.1° × 0.1° grid. The well-known large-scale deformation due to mining, gas extraction, and so forth were excluded. Since continental drift can generate ramps over range, the motion of the Eurasian plate was also removed from the InSAR velocities [36]. It is noted that since the motion model is constant over the whole plate, residual effects may be present. However, since the analysis is on relatively small scales (≤45 km), it is assumed that such effects are also small.

Confidence intervals for σ_T are shown in Fig. 10 for each stack. The intervals are much smaller than in Fig. 7 since the amount of available data is much larger. In general, the confidence intervals lie close to the null value $\sigma_T = 1$, but the agreement is not as great as previously. This may be related to the hypothesis of zero motion failing or other residual effects. Fig. 11 shows the histogram of $\underline{T}$ pooled over all stacks, the pooled value of $\hat{\sigma_T}$ is 1.15. The variogram of the pairwise differences is also shown for a single stack in Fig. 9, in Fig. 9(a) using real and in Fig. 9(b) synthetic GNSS data.

V. CONCLUSION

This study discussed the potential and the limitations of InSAR for large-scale displacement measurements. The main concluding points are as follows.

1) The measurement of large-scale displacement signals precludes spatial filtering since all displacement components must be preserved in the final product. In order to provide sufficient accuracy at large scales, tropospheric corrections are recommended.
2) Performance may be site dependent, but the target of 1 mm/y at 100 km is achievable in five years given good weather models (in Europe or USA) or in general where

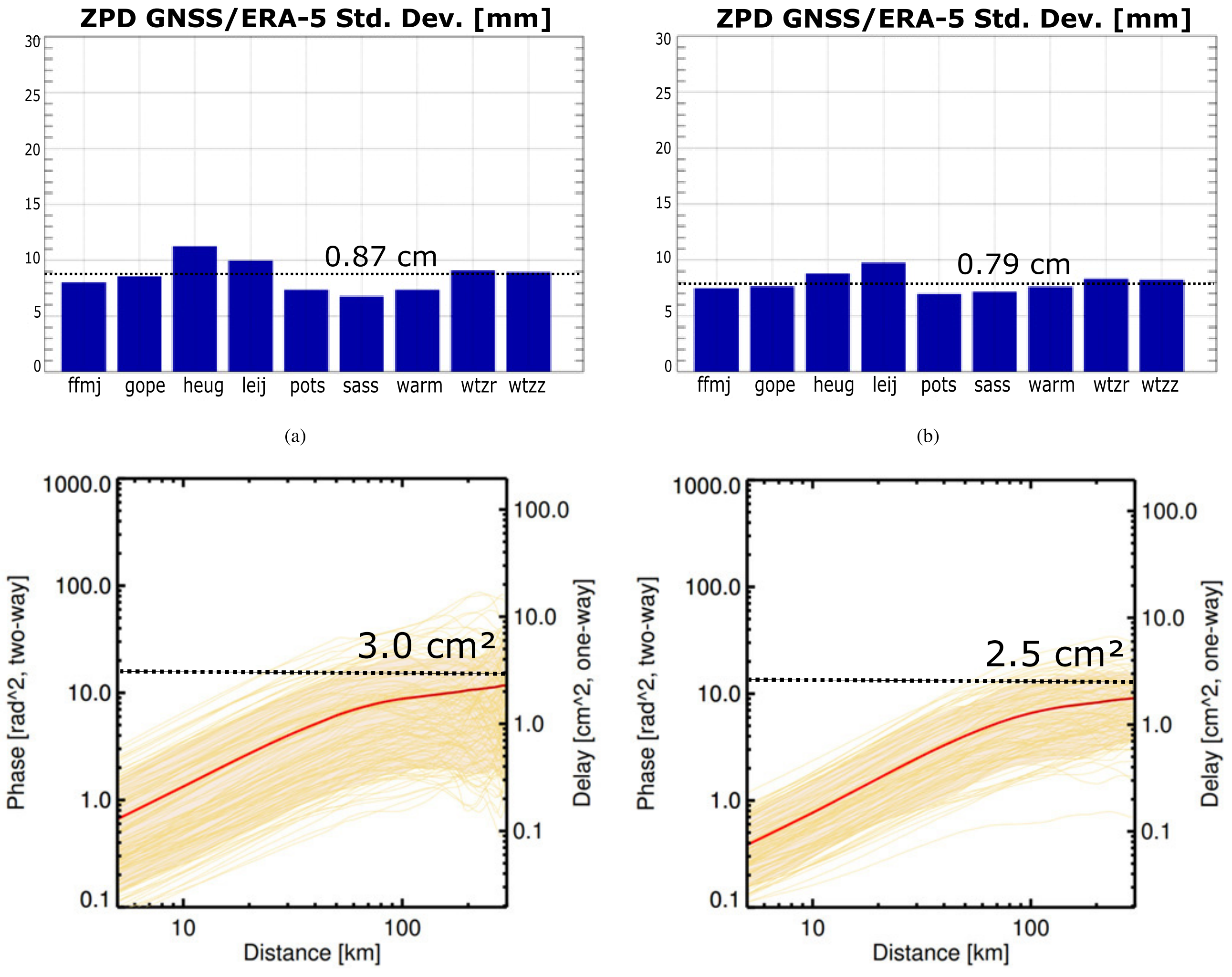

(a) (b) (c) (d)

Fig. 12. Standard deviation of the ECMWF ERA5 and GNSS ZPD differences is shown for each station for (a) ascending (18:00) and (b) descending (06:00) passes, respectively. The estimated variograms saturate at the values expected due to NWP model error for both (c) ascending and (d) descending passes (this corresponds to the variogram in Fig. 1 computed in the zenith direction).

the errors are small due to reduced atmospheric delay, i.e., over the Tibetan Plateau.

3) Short-time baseline variograms allow a reasonable evaluation of displacement rate performance providing valuable error bars to users. Such measurements must be included in the product since residual tropospheric noise is the main limiting factor at large distances.
4) In the Appendix, a lower bound on the interferometric phase accuracy at large distance was outlined and related to the accuracy of the models used for the corrections. Finally, as NWP models are continuously being improved, follow-on effects for InSAR can be expected.

Future work shall address the correction of tropospheric stratification in more detail. In this study, the problem has been only partially discussed since the focus was more on large scales. The designed framework does not allow for a quantitative validation as the one carried out for Germany since a dense network of GNSS installed both on ridges and valleys would be needed. Therefore, a different approach must be implemented.

APPENDIX

VERIFYING THE LOWER BOUND ON CORRECTED PHASE ACCURACY

Equation (1) models the residual tropospheric error in NWP corrected interferograms. The variance of the error is obtained by expanding

$$\mathbb{E}\left[\phi_\epsilon^2\right] = \mathbb{E}\left[\left((\epsilon_{r,A}-\epsilon_{s,A})\frac{e^{-\frac{h_A}{H}}}{\cos\theta_A} - (\epsilon_{r,B}-\epsilon_{s,B})\frac{e^{-\frac{h_B}{H}}}{\cos\theta_B}\right)^2\right]. \tag{11}$$

The temporal correlation of the reference and secondary acquisitions errors can be considered 0 everywhere since they are separated by at least six days $\mathbb{E}[\epsilon_r\epsilon_s] \equiv 0$. On the other hand, a spatial correlation $\mathbb{E}[\epsilon_A\epsilon_B] = \Lambda(A, B)$ exists for both reference and secondary acquisitions, leading to (2).

According to this model, the spatial correlation function at large distances should tend to 0 $\Lambda(\infty) = 0$, and therefore, the error variance in such a regime should only depend on the accuracy of the tropospheric corrections used. Moreover, since this verification experiment is performed on a large area characterized by flat or slightly varying topography, the exponential term can be considered constant and hence absorbed by the measurement error

$$\mathbb{E}\left[\phi_\epsilon^2\right] = \frac{2\sigma_\epsilon^2}{\cos^2\theta_A} + \frac{2\sigma_\epsilon^2}{\cos^2\theta_B}. \tag{12}$$

In order to verify this, a study was carried out using Sentinel-1 interferograms with very long azimuth extension over Germany. The unwrapped phases from multiple slices were mosaicked allowing variograms at scales of up to 300 km. The variogram samples were chosen along (almost) isorange lines in order that the incidence angle not varies and the measurements projected onto the zenith direction. In this way, the effects of incidence angle could be factored out.

Analogously to [29], the zenith path delay predicted by ERA-5 was compared to GNSS-based estimates. Since the NWP model accuracy varies with geographic location, a subset of nine GNSS stations in Germany were used. The difference between the GNSS and ERA-5 ZPDs should approximate the NWP error, given that the GNSS values represent the true delay. This comparison was performed for ascending and descending geometries at the local solar times of 18:00 and 06:00, respectively. Statistics were calculated over one year of data for each geometry.

In an ERA-5 corrected interferogram, the error between two points separated by a distance d should approach the saturation value $\sigma_Z^2 = 4\widehat{\sigma_\epsilon^2}$ in (12) since $\Lambda(d) \rightarrow 0$ for large d and $\theta_A = \theta_B = 0$ at zenith. Hence, it is sufficient to confirm that the variograms saturate on average at the value $4\widehat{\sigma_\epsilon^2}$. The results in Fig. 12 show an estimate of $4\widehat{\sigma_\epsilon^2}$ along with the variograms for ascending and descending geometries. It is interesting to note that the performance of these two geometries is comparable at 300 km. One would expect better performance for the descending pass, made in the morning when the atmosphere contains less energy. This is partially true considering midscales from 50 to 80 km where stronger turbulence due to more atmospheric power for the ascending pass leads to a larger average power and spread around the average. However, once the distance reaches the scale of the NWP model, one is limited by the error of the NWP model independently of the time of day.

An important implication of this is that a global analysis of ERA-5/GNSS deviations could provide a lower bound for the achievable accuracy in measuring large-scale displacement using InSAR.

ACKNOWLEDGMENT

The authors would like to thank the anonymous reviewers for helping improve the manuscript.

REFERENCES

[1] R. Torres *et al.*, "GMES Sentinel-1 mission," *Remote Sens. Environ.*, vol. 120, pp. 9–24, May 2012.

[2] P. A. Rosen, Y. Kim, R. Kumar, T. Misra, R. Bhan, and V. R. Sagi, "Global persistent SAR sampling with the NASA-ISRO SAR (NISAR) mission," in *Proc. IEEE Radar Conf. (RadarConf)*, May 2017, pp. 0410–0414.

[3] A. Moreira *et al.*, "Tandem-L: A highly innovative bistatic SAR mission for global observation of dynamic processes on the Earth's surface," *IEEE Geosci. Remote Sens. Mag.*, vol. 3, no. 2, pp. 8–23, Jun. 2015.

[4] P. A. Rosen, S. Hensley, H. A. Zebker, F. H. Webb, and E. J. Fielding, "Surface deformation and coherence measurements of kilauea volcano, Hawaii, from SIR-C radar interferometry," *J. Geophys. Res. Planets*, vol. 101, no. E10, pp. 23109–23125, 1996. [Online]. Available: http://dx.doi.org/10.1029/96JE01459

[5] A. L. Gray, K. E. Mattar, and G. Sofko, "Influence of ionospheric electron density fluctuations on satellite radar interferometry," *Geophys. Res. Lett.*, vol. 27, no. 10, pp. 1451–1454, May 2000.

[6] R. Hanssen, *Radar Interferometry: Data Interpretation and Error Analysis*, Norwell, MA, USA: Kluwer, 2001.

[7] T. J. Wright, "The earthquake deformation cycle," *Astron. Geophys.*, vol. 57, no. 4, pp. 4.20–4.26, Aug. 2016, doi: 10.1093/astrogeo/atw148.

[8] E. Hussain, T. J. Wright, R. J. Walters, D. P. S. Bekaert, R. Lloyd, and A. Hooper, "Constant strain accumulation rate between major earthquakes on the north anatolian fault," *Nature Commun.*, vol. 9, no. 1, p. 1392, Dec. 2018.

[9] C. Delacourt, P. Briole, and J. A. Achache, "Tropospheric corrections of SAR interferograms with strong topography. Application to ETNA," *Geophys. Res. Lett.*, vol. 25, no. 15, pp. 2849–2852, Aug. 1998.

[10] Z. Li, J.-P. Muller, P. Cross, and E. J. Fielding, "Interferometric synthetic aperture radar (InSAR) atmospheric correction: GPS, moderate resolution imaging spectroradiometer (MODIS), and InSAR integration," *J. Geophys. Res.*, vol. 110, 2005, Art. no. B03410, doi: 10.1029/2004JB003446.

[11] F. Meyer, R. Bamler, R. Leinweber, and J. Fischer, "A comparative analysis of tropospheric water vapor measurements from MERIS and SAR," in *Proc. IEEE Int. Geosci. Remote Sens. Symp. (IGARSS)*, Jul. 2008, pp. IV-228–IV-231.

[12] Z. Li, E. J. Fielding, and P. Cross, "Integration of InSAR time-series analysis and water-vapor correction for mapping postseismic motion after the 2003 Bam (Iran) earthquake," *IEEE Trans. Geosci. Remote Sens.*, vol. 47, no. 9, pp. 3220–3230, Sep. 2009.

[13] M.-P. Doin, C. Lasserre, G. Peltzer, O. Cavalié, and C. Doubre, "Corrections of stratified tropospheric delays in SAR interferometry: Validation with global atmospheric models," *J. Appl. Geophys.*, vol. 69, no. 1, pp. 35–50, Sep. 2009.

[14] T. R. Lauknes, "InSAR tropospheric stratification delays: Correction using a small baseline approach," *IEEE Geosci. Remote Sens. Lett.*, vol. 8, no. 6, pp. 1070–1074, Nov. 2011.

[15] X. Cong, "SAR interferometry for volcano monitoring: 3-D-PSI analysis and mitigation of atmospheric refractivity," Ph.D. dissertation, Dept. Remote Sens. Technol., Technische Univ. München, Munich, Germany, 2014.

[16] R. Jolivet, R. Grandin, C. Lasserre, M.-P. Doin, and G. Peltzer, "Systematic InSAR tropospheric phase delay corrections from global meteorological reanalysis data," *Geophys. Res. Lett.*, vol. 38, 2011, Art. no. L17311, doi: 10.1029/2011GL048757.

[17] M. Eineder, C. Minet, P. Steigenberger, X. Cong, and T. Fritz, "Imaging geodesy—Toward centimeter-level ranging accuracy with TerraSAR-X," *IEEE Trans. Geosci. Remote Sens.*, vol. 49, no. 2, pp. 661–671, Feb. 2011.

[18] R. Jolivet *et al.*, "Improving InSAR geodesy using global atmospheric models," *J. Geophys. Res. Solid Earth*, vol. 119, no. 3, pp. 2324–2341, Mar. 2014.

[19] X. Cong, U. Balss, M. Eineder, and T. Fritz, "Imaging geodesy—centimeter-level ranging accuracy with TerraSAR-X: An update," *IEEE Geosci. Remote Sens. Lett.*, vol. 9, no. 5, pp. 948–952, Sep. 2012.

[20] D. P. S. Bekaert, R. J. Walters, T. J. Wright, A. J. Hooper, and D. J. Parker, "Statistical comparison of InSAR tropospheric correction techniques," *Remote Sens. Environ.*, vol. 170, pp. 40–47, Dec. 2015.

[21] F. Meyer, R. Bamler, N. Jakowski, and T. Fritz, "The potential of low-frequency SAR systems for mapping ionospheric TEC distributions," *IEEE Geosci. Remote Sens. Lett.*, vol. 3, no. 4, pp. 560–564, Oct. 2006.

[22] G. Gomba, F. R. Gonzalez, and F. De Zan, "Ionospheric phase screen compensation for the Sentinel-1 TOPS and ALOS-2 ScanSAR modes," *IEEE Trans. Geosci. Remote Sens.*, vol. 55, no. 1, pp. 223–235, Jan. 2017.

[23] G. Gomba, A. Parizzi, F. De Zan, M. Eineder, and R. Bamler, "Toward operational compensation of ionospheric effects in SAR interferograms: The split-spectrum method," *IEEE Trans. Geosci. Remote Sens.*, vol. 54, no. 3, pp. 1446–1461, Mar. 2016.

[24] F. R. Gonzalez, A. Parizzi, and R. Brcic, "Evaluating the impact of geodetic corrections on interferometric deformation measurements," in *Proc. 12th Eur. Conf. Synth. Aperture Radar*, Jun. 2018, pp. 1–5.

[25] M. Eineder, U. Balss, S. Suchandt, C. Gisinger, X. Cong, and H. Runge, "A definition of next-generation SAR products for geodetic applications," in *Proc. IEEE Int. Geosci. Remote Sens. Symp. (IGARSS)*, Jul. 2015, pp. 1638–1641.

[26] Y. Larsen, P. Marinkovic, J. F. Dehls, Z. Perski, A. J. Hooper, and T. J. Wright, "The Sentinel-1 constellation for InSAR applications: Experiences from the InSARAP project," in *Proc. IEEE Int. Geosci. Remote Sens. Symp. (IGARSS)*, Jul. 2017, pp. 5545–5548.

[27] Y. T. Yoon, M. Eineder, N. Yague-Martinez, and O. Montenbruck, "TerraSAR-X precise trajectory estimation and quality assessment," *IEEE Trans. Geosci. Remote Sens.*, vol. 47, no. 6, pp. 1859–1868, Jun. 2009.

[28] H. Peter *et al.*, "Sentinel-1A–First precise orbit determination results," *Adv. Space Res.*, vol. 60, no. 5, pp. 879–892, Sep. 2017.

[29] X. Cong, U. Balss, F. R. Gonzalez, and M. Eineder, "Mitigation of tropospheric delay in SAR and InSAR using NWP data: Its validation and application examples," *Remote Sens.*, vol. 10, no. 10, p. 1515, Sep. 2018.

[30] H. Breit, T. Fritz, U. Balss, M. Lachaise, A. Niedermeier, and M. Vonavka, "TerraSAR-X SAR processing and products," *IEEE Trans. Geosci. Remote Sens.*, vol. 48, no. 2, pp. 727–740, Feb. 2010.

[31] T. R. Emardson, M. Simons, and F. H. Webb, "Neutral atmospheric delay in interferometric synthetic aperture radar applications: Statistical description and mitigation," *J. Geophys. Res.*, vol. 108, no. B5, p. 2231, 2003, doi: 10.1029/2002JB001781.

[32] A. Parizzi, F. R. Gonzalez, and R. Brcic, "A covariance-based approach to merging InSAR and GNSS displacement rate measurements," *Remote Sens.*, vol. 12, no. 2, p. 300, Jan. 2020.

[33] H. Fattahi and F. Amelung, "InSAR bias and uncertainty due to the systematic and stochastic tropospheric delay," *J. Geophys. Res. Solid Earth*, vol. 120, no. 12, pp. 8758–8773, Dec. 2015.

[34] *MIDAS Velocity Fields*. Accessed: Oct. 1, 2018. [Online]. Available: http://geodesy.unr.edu/

[35] G. Blewitt, C. Kreemer, W. C. Hammond, and J. Gazeaux, "MIDAS robust trend estimator for accurate GPS station velocities without step detection," *J. Geophys. Res. Solid Earth*, vol. 121, no. 3, pp. 2054–2068, Mar. 2016.

[36] Z. Altamimi, L. Métivier, P. Rebischung, H. Rouby, and X. Collilieux, "ITRF2014 plate motion model," *Geophys. J. Int.*, vol. 209, no. 3, pp. 1906–1912, Jun. 2017, doi: 10.1093/gji/ggx136.

Alessandro Parizzi received the master's degree in telecommunications engineering from the Politecnico di Milan, Milan, Italy, in 2004.

From 2004 to 2006, he was with the Department of Electronics, Politecnico di Milan, where he was working in the field of synthetic aperture radar (SAR) interferometry and in the design of artificial radar targets. Since 2006, he has been with the SAR Signal Processing Department, Remote Sensing Technology Institute, German Aerospace Center (DLR), Wessling, Germany, mainly involved in SAR interferometry projects for deformation measurements. His research interest includes the study of interferometric applications and their performance.

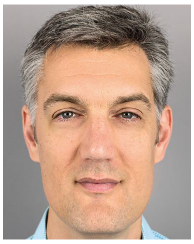

Ramon Brcic received the B.Eng. (Hons. 1) degree in aerospace avionics from the Queensland University of Technology (QUT), Brisbane, QLD, Australia, in 1998, and the Ph.D. degree in electrical engineering from the Curtin University of Technology (CUT), Perth, WA, Australia, in 2003.

From 2003 to 2007, he was a Research Associate with the Signal Processing Group, Technische Universität Darmstadt (TUD), Darmstadt, Germany. Since 2008, he has been with the SAR Signal Processing Department, Remote Sensing Technology Institute, German Aerospace Center (DLR), Wessling, Germany, as a Research Scientist, working on multitemporal interferometric SAR. He had been involved in various projects for ESA and the design and operation of the German ground motion service.

Francesco De Zan studied telecommunications engineering at the Politecnico di Milan, Milan, Italy, from 1998 to 2004, with a focus on signal processing and remote sensing, where he received the Ph.D. degree in synthetic aperture radar (SAR) interferometry with distributed and decorrelating targets in 2008.

During these years, he also contributed to the development of the TOPS acquisition mode (Student Prize at the 2006 EUSAR Conference). In 2007, he visited for two quarters the Stanford Exploration Group, Stanford University, Stanford, CA, USA, which is specialized in the use of seismic waves to image the interior of the Earth. After the conclusion of his Ph.D., he moved to the Munich area (Germany) to join the German Aerospace Center (DLR), Wessling, Germany, first with the Microwave and Radar Institute, then with the Remote Sensing Technology Institute. He has worked on aspects related to acquisition planning, performance models for deformation retrieval with InSAR and SAR tomographic applications, orbit design, and so on. He was also involved in the calibration of the TanDEM-X interferometer, discovering and explaining a number of interferometric effects that were hampering the quality of the DEM products. He has worked on several projects for ESA related to mission design, commissioning, and application development for SAR satellites. He has coauthored few patents in the SAR field. He has given several introductory lessons at the university level on SAR and SAR interferometry and has supervised some master's and Ph.D. theses. His research interests are in the field of SAR include performance of phase and delay estimators, ionospheric propagation estimation, focusing and precise geolocation of targets, vegetation soil moisture effects, and inconsistencies in SAR interferometric phases.

E

Parizzi A.(2020). Potential of an automatic Grounding Zone Characterisation using wrapped InSAR Phase. In 2020 IEEE International Geoscience and Remote Sensing Symposium (IGARSS)

Summary The work deals with the identification and the characterization of the grounding zone area using InSAR data. The idea is to point towards a methodology that minimizes the role of the operator and provides results with performance that can be mathematically described using input parameters. The approach uses the information of the interferometric phase gradient to follow the path of the grounding zone and fit them using a physical model that describes the ice bending. The approach is tested on more than 300 km grounding zone comparing also the results with existing products.

Contributions of the candidate Initiator of this work. Idea and development of the method. Practical implementation and testing with the data sets. Writing the paper.

IGARSS 2020 - 2020 IEEE International Geoscience and Remote Sensing Symposium | 978-1-7281-6374-1/20/$31.00 ©2020 IEEE | DOI: 10.1109/IGARSS39084.2020.9323199

POTENTIAL OF AN AUTOMATIC GROUNDING ZONE CHARACTERIZATION USING WRAPPED INSAR PHASE

Alessandro Parizzi

Remote Sensing Technology Institute German Aerospace Center (DLR)
Münchenerstraße 20 82234 Weßling; alessandro.parizzi@dlr.de

ABSTRACT

The work deals with the identification and the characterization of the grounding zone area using InSAR data. The idea is to point towards a methodology that minimizes the role of the operator and provides results with performance that can be mathematically described using input parameters. The approach uses the information of the interferometric phase gradient to follow the path of the grounding zone and fit them using a physical model that describes the ice bending. The approach is tested on more than 300 km grounding zone comparing also the results with existing products.

Index Terms— InSAR; Deformation Measurements; Cryosphere; Grounding Line

1. INTRODUCTION

The characterization of the transition from floating to grounded ice is a very important information for glaciologists. Its behavior and evolution supports the understanding of the dynamic processes of the ice sheets. A systematic monitoring is therefore necessary to support scientists working in this field.

Since many years researchers deploy instrumentation to derive measurements in order to locate and understand the temporal evolution of the ice-sea boundary[1] [2] . The rise of the remote sensing satellites gave the perspective of a more systematic and global mapping of areas that would be anyway difficult and expensive to survey. The strong sensitivity of InSAR to vertical displacements allows a clear identification of the transition highlighting the ice deformation due to the tidal cycle. In [3] the potential of interferometry for the study of grounding areas has been shown identifying their position and measuring their movements. Over many years the coverage and the systematic of the interferometric measurements has been increased reaching a global maps of the Grounding Lines (GL)[4].

However the interferometric data are typically used to identify the grounding area manually marking the position of the Grounding Line directly on the computed interferograms. This work studies an approach that is able to identify and measure the Grounding Zone (GZ) in a more automatic fashion. Since the wrapped interferometric phase is inherently a measure of the deformation gradient InSAR data can be used analogously to the tiltmeter measurement also avoiding the phase unwrapping that could harm the robustness of the approach. The study relies on the physical model proposed in [5] and applied in [6] but using the phase gradients instead of the absolute phase. The gradient information allows both to follow the geometry of the GZ and to estimate the model parameters.

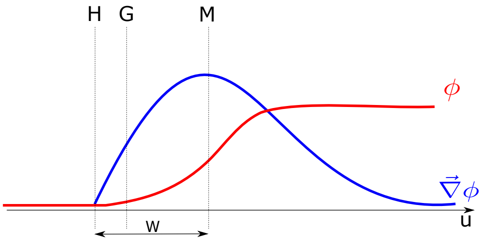

Fig. 1: Schematic of the Grounding Area displaying phase and phase gradient profile. H is the position of the hinge Line, G of the Grounding Line and M is the maximum of the gradient.

2. METHODOLOGY

The model proposed in [5] describes the displacement due to the tide cycle of the floating ice w.r.t the grounded ice. The idea of the proposed algorithm is to be able to spatially follow the grounding zone on the wrapped SAR interferogram and characterize it fitting the physical model in [5]. As previously mentioned in Section 1 the approach is based on the spatial gradients of the interferometric phase $\vec{\nabla}\phi$ that are computed estimating the main fringe frequency window-wise on the complex SAR interferogram. Being (r, a) the range and azimuth coordinates in radar geometry, the interferogram is a complex number $z(r, a)$. Considering the interferometric phase varying by several wavelengths within the scale of the deformation pattern, it is possible to perform a local linear approximation of the deformation phase. Hence in a given point (r_0, a_0) the phase ϕ of the interferogram $z = Ae^{j\phi}$ can be substituted by its first order Taylor approximation:

$$\phi \approx \frac{4\pi}{\lambda}\left(\frac{\partial\delta_s}{\partial r}(r-r_0)+\frac{\partial\delta_s}{\partial a}(a-a_0)\right)+\phi_0 \qquad (1)$$

where A is the product of master and slave reflectivity and $\delta_s = \boldsymbol{\delta}^T\boldsymbol{s}$ is the projection of the displacement vector $\boldsymbol{\delta}$ along the line of sight $\boldsymbol{s}$ (LoS). Equation 1 shows how, under the linear approximation hypothesis, the deformation gradients are basically a scaling of the interferogram fringe frequencies [7]. Therefore the gradient measurements $\vec{\nabla}\delta_s$ can be hence estimated from the single look complex data performing a frequency estimation [8], [9]. Multi-looking and sub-sampling are anyhow implicit in the fringe frequency estimation since the computation is done window-wise. This allows theoretically identifying gradients that would not any more visible at the multi-looked interferogram level due the resolution reduction .

The deformation gradient provides basically two information the amplitude $\Gamma = \left\|\vec{\nabla}\delta_s(u)\right\|$ and the angle $\eta = \angle\vec{\nabla}\delta_s$. η, represents the direction of maximum slope and $\frac{\pi}{2}+\eta$ identifies the local direction of the GZ path. The gradient data can be hence re-sampled along the direction u defined as the direction rotated by η w.r.t. the reference axes. Now exploiting the model in [5] it is possible to model the data as follows:

$$\Gamma = \frac{\partial\delta_v(u)}{\partial u} = \frac{2\beta\Delta}{1+e^{-\pi}} sin(\beta(u-H))e^{-\beta(u-H)} \quad \forall u \geq H \qquad (2)$$

where Δ is tide the displacement, β is a shape factor describing the width of the bending area, H is the hinge line position along the axis u. The inversion of the GZ parameters can be hence performed bypassing the phase unwrapping [1] by fitting in Equation 2 the estimated gradient Γ.

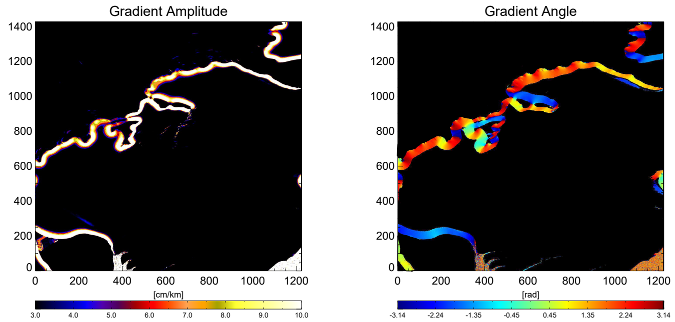

Fig. 2: Estimated Phase gradients displayed in terms of Amplitude and Angle.

The inversion derives first the position of the so called Hinge Line (HL) and β that provide a characterization of the GZ. β is a shape factor that describes the curve determining the width of the GZ. This is visible from the analytic expression of the distance W_{peak} between the HL and the maximum of the deformation gradient that identify the center of the GZ see Figure 1.

$$W_{peak} = \frac{\pi}{4\beta} \qquad (3)$$

Iterating the described steps on the gradient map the fringe belt can be followed estimating the parameters of the GZ as in Figure 3.

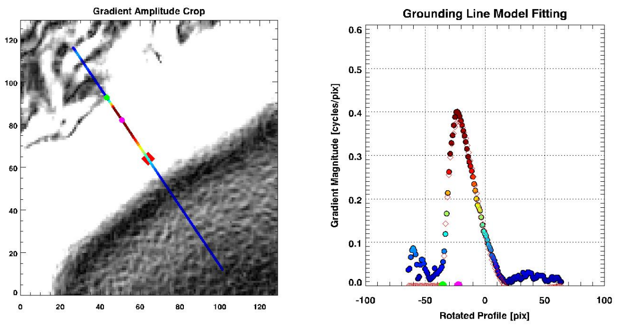

Fig. 3: Model fitting in the gradients map

3. RESULTS

Real data experiments have been carried out in order to test the potential automation of the procedure. Two test sites have been selected testing both qualitatively and quantitatively the accuracy of the estimated positions. Two ERS Tandem pairs (1 day temporal baseline) and one Sentinel one Double Differences [4] over the Antarctica have been processed and the described algorithm have been applied on the computed interferograms. A semi-automatic implementation has been tested in order to verify the described approach. An a-priori has been defined over the interferogram. Starting from that the algorithm finds the gradient direction for each point intersecting the a-priori, interpolates the gradient along such line and fits the model to the gradient amplitude retrieving the estimated position for the HL (black dots). The vector of the "‘raw"’ retrieved positions is finally geocoded.

3.1. Schirmacher Area using ERS-Tandem

In the first test site considered it is possible to notice a quite complex geometry of the grounding line that follows the coastline in all gulfs and peninsulas. Figure 4 shows a the result of the estimation displaying the retrieved positions of the HL and the distance between HL and maximum gradient point color-coded. This information can compactly show

---

[1] For the sake of precision it would be rather to say that the procedure implicitly solve the phase ambiguities supported by the model

a model-based characterization of the GZ since it displays position and dimension of the GZ.

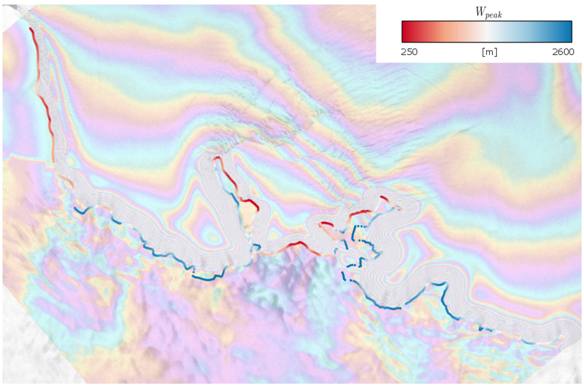

Fig. 4: The overview of the whole processed area showing both the HL positions and the W_{peak} distance color-coded.

3.2. Inter-comparison with MEaSURES data set

However a quantitative comparison of the derived product with existing products is necessary in order to verify the trustworthiness of the estimated positions. Therefore another area of interest in the Princess Raghild Coast has been selected. The same ERS Tandem data used to generate the MEaSUREs product have been processed . The HL position has been then calculated using the same strategy described for the first test site. As already visible from the overview Figure 5 the positions are very similar nonetheless the result has been compared with MEaSUREs computing the local distance of each extracted point from the reference product. The local distance between the two product has been calculated computing for each point of the distance from the slope that fits the three closest points of the other product. Proceeding in this way it was possible to collect a vector of local distances to be used to derive some statistics. The histogram and the statistics of the differences are plotted in Figure 5. The deviation of the position is about 115 m but drops to 82 m if robustly computed using MAD. Such numbers are compatible with accuracies measured in [4]. A not negligible bias ($> 150m$) is however detectable between the different position. Looking more in detail to Figure 5 is visible that the proposed method positions are located systematically more in the inland. This should probably be related to a different definition of the position between the MEaSUREs (GL) product and the model used in this study (HL), see Figure 1.

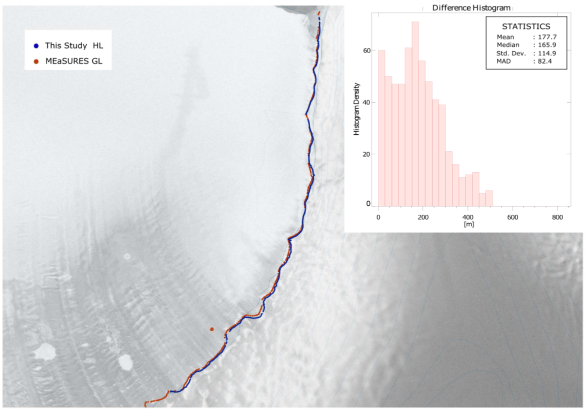

Fig. 5: Result of the comparison on the second test site, extracted products (MEaSUREs in red , this study in blue) and the histogram and the statistics of the local distances.

3.3. Schirmacher Area using Sentinel-1 Double Differences

Nowadays the Sentinel-1 mission is able provide interferometric data on regular basis with a global coverage. Therefore this is the most suitable sensor to address the problem of Grounding Zones monitoring using InSAR. However the 6 days revisit time does not allow to neglect the ice motion specially in proximity of Glaciers. Therefore, in this case, the use of interferometric double differences have to be considered [4]. The approach can be extended to gradients having two interferograms w.r.t a master image temporally located in the middle of the three acquisitions. Given that it would be possible to delete the constant horizontal motion component simply adding the gradients vector retrieved from the tow interferograms.

$$\vec{\nabla}\phi_{dd} = \vec{\nabla}\phi_{-1} + \vec{\nabla}\phi_1 \tag{4}$$

where ϕ_{-1} and ϕ_1 represent the two interferograms. The results of the extracted map are shown in Figure 6, the derived Hinge Line position is shown in Figure 7

4. CONCLUSIONS

The proposed method shows potential in characterizing the GZ using directly wrapped SAR interferograms pointing towards a more automatic approach. The implementation developed in this work starts from a coarse a-priori roughly derived by the gradient map.Starting from that the relations between the physics of the problem and the measurement approach (InSAR) are used to derive a fine mapping of the HL

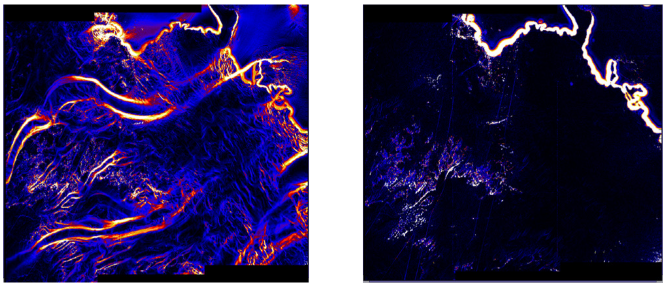

Fig. 6: Interfeograms (left) and double differences (right) phase gradients amplitude

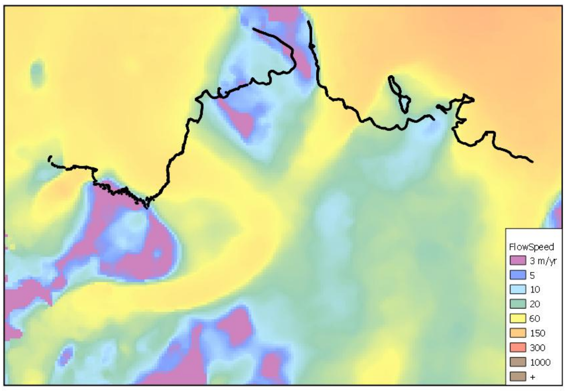

Fig. 7: Hinge Line derived from Sentinel-1 double differences, plotted over the Ice Velocity map [10].

and a measurements of the GZ width. This requires consistently less effort than the typical manual mapping using the fringe belt: for a single interferogram only few benchmarks roughly located in the fringe belt are necessary. This work is focused on the investigation of a general a approach using InSAR data. In order to do that the model in [5] [6] has been used. The choice is mainly related to its easy analytic expression, nonetheless other more sophisticated models can be "‘plugged"’ into this framework [11]. Since most of the problems could derive from the nature of real data also different test sites and data have been considered analyzing the retrieved results. Moreover a quantitative comparison with existing GL products has been also carried out. In the proposed test sites more than 300 km GZ have been processed showing besides a good agreement with the MEaSUREs data set. Finally the method has been applied also to Sentinel-1 data extending it for the use of double differences.

5. REFERENCES

[1] S. N. Stephenson, "Glacier Flexure and the Position of Grounding Lines: Measurements By Tiltmeter on Rutford Ice Stream, Antarctica," *Annals of Glaciology*, vol. 5, pp. 165–169, 1984.

[2] A. M. Smith, "The use of tiltmeters to study the dynamics of antarctic ice-shelf grounding lines," *Journal of Glaciology*, vol. 37, no. 125, pp. 51–58, 1991.

[3] Richard M. Goldstein, Hermann Engelhardt, Barclay Kamb, and Richard M. Frolich, "Satellite Radar Interferometry for Monitoring Ice Sheet Motion: Application to an Antarctic Ice Stream," *Science*, vol. 262, no. 5139, pp. 1525–1530, 1993.

[4] E. Rignot, J. Mouginot, and B. Scheuchl, "Antarctic grounding line mapping from differential satellite radar interferometry," *Geophysical Research Letters*, vol. 38, no. 10, 2011.

[5] G. Holdsworth, "Flexure of a Floating Ice Tongue," *Journal of Glaciology*, vol. 8, no. 54, pp. 385–397, 1969.

[6] Eric Rignot, "Hinge-line migration of Petermann Gletscher, north Greenland, detected using satellite-radar interferometry," *Journal of Glaciology*, vol. 44, no. 148, pp. 469–476, 1998.

[7] A. Parizzi and W. Abdel Jaber, "Estimating Strain and Rotation From Wrapped SAR Interferograms," *IEEE Geoscience and Remote Sensing Letters*, vol. 15, no. 9, pp. 1367–1371, Sept 2018.

[8] S. Kay and R. Nekovei, "An efficient two-dimensional frequency estimator," *Acoustics, Speech and Signal Processing, IEEE Transactions on*, vol. 38, no. 10, pp. 1807–1809, Oct 1990.

[9] A. Monti Guarnieri and S. Tebaldini, "ML-Based Fringe-Frequency Estimation for InSAR," *IEEE Geoscience and Remote Sensing Letters*, vol. 7, no. 1, pp. 136–140, Jan 2010.

[10] J. Mouginot, E. Rignot, and B. Scheuchl, "Continent-Wide, Interferometric SAR Phase, Mapping of Antarctic Ice Velocity," *Geophysical Research Letters*, vol. 46, no. 16, pp. 9710–9718, 2019.

[11] Christian T. Wild, Oliver J. Marsh, and Wolfgang Rack, "Unraveling InSAR Observed Antarctic Ice-Shelf Flexure Using 2-D Elastic and Viscoelastic Modeling," *Frontiers in Earth Science*, vol. 6, pp. 28, 2018.

Bibliography

[1] Adam, N., Kampes, B., Eineder, M., Worawattanamateekul, J., and Kircher, M. (2003). The development of a scientific permanent scatterer system. In *Proceedings of the Joint ISPRS/EARSeL Workshop "High Resolution Mapping from Space 2003"*. ISPRS.

[2] Agram, P. S. and Simons, M. (2015). A noise model for InSAR time series. *Journal of Geophysical Research: Solid Earth*, 120(4):2752–2771.

[3] Ali, S. T. and Feigl, K. L. (2012). A new strategy for estimating geophysical parameters from InSAR data: Application to the Krafla central volcano in Iceland. *Geochemistry, Geophysics and Geosystems*, 16(6).

[4] Ansari, H., De Zan, F., and Bamler, R. (2017). Sequential Estimator: Toward Efficient InSAR Time Series Analysis. *IEEE Transactions on Geoscience and Remote Sensing*, 55(10):5637–5652.

[5] Ansari, H., De Zan, F., and Parizzi, A. (2021). Study of Systematic Bias in Measuring Surface Deformation With SAR Interferometry. *IEEE Transactions on Geoscience and Remote Sensing*, 59(2):1285–1301.

[6] Ansari, H., Zan, F. D., Parizzi, A., Eineder, M., Goel, K., and Adam, N. (2016). Measuring 3-D Surface Motion With Future SAR Systems Based on Reflector Antennae. *IEEE Geoscience and Remote Sensing Letters*, 13(2):272–276.

[7] Banda, F., Dall, J., and Tebaldini, S. (2016). Single and Multipolarimetric P-Band SAR Tomography of Subsurface Ice Structure. *IEEE Transactions on Geoscience and Remote Sensing*, 54(5):2832–2845.

[8] Bekaert, D., Walters, R., Wright, T., Hooper, A., and Parker, D. (2015). Statistical comparison of insar tropospheric correction techniques. *Remote Sensing of Environment*, 170:40 – 47.

[9] Berardino, P., Fornaro, G., Lanari, R., and Sansosti, E. (2002). A new algorithm for surface deformation monitoring based on small baseline differential SAR interferograms. *IEEE Transactions on Geoscience and Remote Sensing*, 40(11):2375–2383.

[10] Blewitt, G., Kreemer, C., Hammond, W. C., and Gazeaux, J. (2016). MIDAS robust trend estimator for accurate GPS station velocities without step detection. *Journal of Geophysical Research: Solid Earth*, 121(3):2054–2068.

[11] Breit, H., Fritz, T., Balss, U., Lachaise, M., Niedermeier, A., and Vonavka, M. (2010). TerraSAR-X SAR Processing and Products. *IEEE Transactions on Geoscience and Remote Sensing*, 48(2):727–740.

[12] Cakir, Z., Chabalier, J.-B. d., Armijo, R., Meyer, B., Barka, A., and Peltzer, G. (2003). Coseismic and early post-seismic slip associated with the 1999 Izmit earthquake (Turkey), from SAR interferometry and tectonic field observations. *Geophysical Journal International*, 155(1):93–110.

[13] Cakir, Z., Ergintav, S., Akoğlu, A. M., Çakmak, R., Tatar, O., and Meghraoui, M. (2014). InSAR velocity field across the North Anatolian Fault (eastern Turkey): Implications for the loading and release of interseismic strain accumulation. *Journal of Geophysical Research: Solid Earth*, 119(10):7934–7943.

[14] Chen, C. and Zebker, H. (2002). Phase unwrapping for large SAR interferograms: statistical segmentation and generalized network models. *IEEE Transactions on Geoscience and Remote Sensing*, 40(8):1709–1719.

[15] Cong, X. (2014). *SAR Interferometry for Volcano Monitoring: 3D-PSI Analysis and Mitigation of Atmospheric Refractivity*. PhD thesis, Technische Universität München, München, Germany.

[16] Cong, X., Balss, U., Eineder, M., and Fritz, T. (2012). Imaging geodesy—Centimeter-level ranging accuracy with TerraSAR-X: An update. *IEEE Geoscience and Remote Sensing Letters*, 9(5):948–952.

[17] Cong, X., Balss, U., Rodriguez Gonzalez, F., and Eineder, M. (2018). Mitigation of Tropospheric Delay in SAR and InSAR Using NWP Data: Its Validation and Application Examples. *Remote Sensing*, 10(10).

[18] Costantini, M. (1998). A novel phase unwrapping method based on network programming. *IEEE Transactions on Geoscience and Remote Sensing*, 36(3):813–821.

[19] Curlander, J. and McDonough, R. (1992). *Synthetic Aperture Radar: Systems and Signal Processing*. Wiley Series in Remote Sensing and Image Processing. Wiley.

[20] De Zan, F. (2008). *Optimizing SAR interferometry for decorrelating scatterers*. PhD thesis, Politecnico di Milano Milano, Italy.

[21] De Zan, F. and Gomba, G. (2018). Vegetation and soil moisture inversion from SAR closure phases: First experiments and results. *Remote sensing of environment*, 217:562–572.

[22] De Zan, F., Parizzi, A., Prats-Iraola, P., and López-Dekker, P. (2014). A SAR Interferometric Model for Soil Moisture. *IEEE Transactions on Geoscience and Remote Sensing*, 52(1):418–425.

[23] De Zan, F., Zonno, M., and López-Dekker, P. (2015). Phase Inconsistencies and Multiple Scattering in SAR Interferometry. *IEEE Transactions on Geoscience and Remote Sensing*, 53(12):6608–6616.

[24] Delacourt, C., Briole, P., and Achache, J. A. (1998). Tropospheric corrections of SAR interferograms with strong topography. Application to Etna. *Geophysical Research Letters*, 25(15):2849–2852.

[25] der Veen, C. J. V. (2013). *Fundamentals of Glacier Dynamics*. CRC Press.

[26] Doin, M.-P., Lasserre, C., Peltzer, G., Cavalié, O., and Doubre, C. (2009). Corrections of stratified tropospheric delays in SAR interferometry: Validation with global atmospheric models. *Journal of Applied Geophysics*, 69(1):35 – 50. Advances in SAR Interferometry from the 2007 Fringe Workshop.

[27] Eineder, M., Balss, U., Suchandt, S., Gisinger, C., Cong, X., and Runge, H. (2015). A definition of next-generation SAR products for geodetic applications. In *2015 IEEE International Geoscience and Remote Sensing Symposium (IGARSS)*, pages 1638–1641.

[28] Eineder, M., Minet, C., Steigenberger, P., Cong, X., and Fritz, T. (2011). Imaging Geodesy—Toward Centimeter-Level Ranging Accuracy With TerraSAR-X. *IEEE Transactions on Geoscience and Remote Sensing*, 49(2):661–671.

[29] Emardson, T. R., Simons, M., and Webb, F. H. (2003). Neutral atmospheric delay in interferometric synthetic aperture radar applications: Statistical description and mitigation. *Journal of Geophysical Research: Solid Earth*, 108(B5).

[30] Facchini, M. and Zanetta, P. (1995). Derivatives of displacement obtained by direct manipulation of phase-shifted interferograms. *Appl. Opt.*, 34(31):7202–7206.

[31] Fattahi, H. and Amelung, F. (2015). InSAR bias and uncertainty due to the systematic and stochastic tropospheric delay. *Journal of Geophysical Research: Solid Earth*, 120(12):8758–8773.

[32] Feigl, K. L. and Thurber, C. H. (2009). A method for modelling radar interferograms without phase unwrapping: Application to the M 5 Fawnskin, California earthquake of 1992 December 4. *Geophys. J. Int*, 176:491–504.

[33] Ferretti, A., Fumagalli, A., Novali, F., Prati, C., Rocca, F., and Rucci, A. (2011). A New Algorithm for Processing Interferometric Data-Stacks: SqueeSAR. *IEEE Transactions on Geoscience and Remote Sensing*, 49(9):3460–3470.

[34] Ferretti, A., Prati, C., and Rocca, F. (2001a). Multibaseline phase unwrapping for InSAR topography estimation. *Il nuovo cimento C*, 24(1):159–176.

[35] Ferretti, A., Prati, C., and Rocca, F. (2001b). Permanent scatterers in sar interferometry. *Geoscience and Remote Sensing, IEEE Transactions on*, 39(1):8–20.

[36] Fornaro, G., Atzori, S., Calo, F., Reale, D., and Salvi, S. (2012). Inversion of Wrapped Differential Interferometric SAR Data for Fault Dislocation Modeling. *Geoscience and Remote Sensing, IEEE Transactions on*, 50(6):2175–2184.

[37] Forster, R. R., Jezek, K. C., Koenig, L., and Deeb, E. (2003). Measurement of glacier geophysical properties from InSAR wrapped phase. *IEEE Transactions on Geoscience and Remote Sensing*, 41(11):2595–2604.

[38] Gatelli, F., Monti Guamieri, A., Parizzi, F., Pasquali, P., Prati, C., and Rocca, F. (1994). The wavenumber shift in SAR interferometry. *Geoscience and Remote Sensing, IEEE Transactions on*, 32(4):855–865.

[39] Ghiglia, D. C. and Romero, L. A. (1994). Robust two-dimensional weighted and unweighted phase unwrapping that uses fast transforms and iterative methods. *J. Opt. Soc. Am. A*, 11(1):107–117.

[40] Goldstein, R. M., Engelhardt, H., Kamb, B., and Frolich, R. M. (1993). Satellite Radar Interferometry for Monitoring Ice Sheet Motion: Application to an Antarctic Ice Stream. *Science*, 262(5139):1525–1530.

[41] Goldstein, R. M., Zebker, H. A., and Werner, C. L. (1988). Satellite radar interferometry: Two-dimensional phase unwrapping. *Radio Science*, 23(4):713–720.

[42] Gomba, G., Parizzi, A., De Zan, F., Eineder, M., and Bamler, R. (2016). Toward Operational Compensation of Ionospheric Effects in SAR Interferograms: The Split-Spectrum Method. *IEEE Transactions on Geoscience and Remote Sensing*, 54(3):1446–1461.

[43] Gomba, G., Rodríguez González, F., and De Zan, F. (2017). Ionospheric Phase Screen Compensation for the Sentinel-1 TOPS and ALOS-2 ScanSAR Modes. *IEEE Transactions on Geoscience and Remote Sensing*, 55(1):223–235.

[44] Gonzalez, F. R., Parizzi, A., and Brcic, R. (2018). Evaluating the impact of geodetic corrections on interferometric deformation measurements. In *EUSAR 2018; 12th European Conference on Synthetic Aperture Radar*, pages 1–5.

[45] Gray, A. L., Mattar, K. E., and Sofko, G. (2000). Influence of ionospheric electron density fluctuations on satellite radar interferometry. *Geophysical Research Letters*, 27(10):1451–1454.

[46] Gray, L. (2011). Using multiple RADARSAT InSAR pairs to estimate a full three-dimensional solution for glacial ice movement. *Geophysical Research Letters*, 38(5):n/a–n/a. L05502.

[47] Guarnieri, A. M. and Tebaldini, S. (2007). Hybrid CramÉr–Rao Bounds for Crustal Displacement Field Estimators in SAR Interferometry. *IEEE Signal Processing Letters*, 14(12):1012–1015.

[48] Guarnieri, A. M. and Tebaldini, S. (2008). On the Exploitation of Target Statistics for SAR Interferometry Applications. *IEEE Transactions on Geoscience and Remote Sensing*, 46(11):3436–3443.

[49] Guarnieri, A. M. and Tebaldini, S. (2010). ML-Based Fringe-Frequency Estimation for InSAR. *IEEE Geoscience and Remote Sensing Letters*, 7(1):136–140.

[50] Hanssen, R. (2001). *Radar Interferometry: Data Interpretation and Error Analysis*. Dordrecht, The Netherlands.

[51] Holdsworth, G. (1969). Flexure of a Floating Ice Tongue. *Journal of Glaciology*, 8(54):385–397.

[52] Hooper, A., Zebker, H., Segall, P., and Kampes, B. (2004). A new method for measuring deformation on volcanoes and other natural terrains using insar persistent scatterers. *Geophysical Research Letters*, 31(23).

[53] Hooper, A. and Zebker, H. A. (2007). Phase unwrapping in three dimensions with application to InSAR time series. *J. Opt. Soc. Am. A*, 24(9):2737–2747.

[54] Hussain, E., Wright, T. J., Walters, R. J., Bekaert, D. P., Lloyd, R., and Hooper, A. (2018). Constant strain accumulation rate between major earthquakes on the North Anatolian Fault. *Nature communications*, 9(1):1392.

[55] Jolivet, R., Agram, P. S., Lin, N. Y., Simons, M., Doin, M.-P., Peltzer, G., and Li, Z. (2014). Improving InSAR geodesy using Global Atmospheric Models. *Journal of Geophysical Research: Solid Earth*, 119(3):2324–2341.

[56] Jolivet, R., Grandin, R., Lasserre, C., Doin, M.-P., and Peltzer, G. (2011). Systematic InSAR tropospheric phase delay corrections from global meteorological reanalysis data. *Geophysical Research Letters*, 38(17).

[57] Jonsson, S., Zebker, H., Segall, P., and Amelung, F. (2002). Fault Slip Distribution of the 1999 Mw 7.1 Hector Mine, California, Earthquake, Estimated from Satellite Radar and GPS Measurements. *Bulletin of the Seismological Society of America*, 92(4):1377–1389.

[58] Joughin, I. R., Kwok, R., and Fahnestock, M. A. (1998). Interferometric estimation of three-dimensional ice-flow using ascending and descending passes. *IEEE Transactions on Geoscience and Remote Sensing*, 36(1):25–37.

[59] Kalia, A., Frei, M., and Lege, T. (2017). A Copernicus downstream-service for the nationwide monitoring of surface displacements in Germany. *Remote Sensing of Environment*, 202:234–249.

[60] Kay, S. and Nekovei, R. (1990). An efficient two-dimensional frequency estimator. *Acoustics, Speech and Signal Processing, IEEE Transactions on*, 38(10):1807–1809.

[61] Ketelaar, V. G. (2009). *Satellite radar interferometry: Subsidence monitoring techniques*, volume 14. Springer Science & Business Media.

[62] Knospe, S. and Jonsson, S. (2010). Covariance Estimation for dInSAR Surface Deformation Measurements in the Presence of Anisotropic Atmospheric Noise. *Geoscience and Remote Sensing, IEEE Transactions on*, 48(4):2057–2065.

[63] Konrad, H., Shepherd, A., Gilbert, L., Hogg, A. E., McMillan, M., Muir, A., and Slater, T. (2018). Net retreat of antarctic glacier grounding lines. *Nature Geoscience*, 11(4):258–262.

[64] Lang, O., Rabus, B. T., and Dech, S. (2004). Velocity map of the Thwaites Glacier catchment, West Antarctica. *Journal of Glaciology*, 50(168):46–56.

[65] Larsen, Y., Marinkovic, P., Dehls, J. F., Perski, Z., Hooper, A. J., and Wright, T. J. (2017). The Sentinel-1 constellation for InSAR applications: Experiences from the InSARAP project. In *2017 IEEE International Geoscience and Remote Sensing Symposium (IGARSS)*, pages 5545–5548. IEEE.

[66] Lauknes, T. R. (2011). nSAR Tropospheric Stratification Delays: Correction Using a Small Baseline Approach. *IEEE Geoscience and Remote Sensing Letters*, 8(6):1070–1074.

[67] Li, Z., Fielding, E. J., and Cross, P. (2009). Integration of InSAR Time-Series Analysis and Water-Vapor Correction for Mapping Postseismic Motion After the 2003 Bam (Iran) Earthquake. *IEEE Transactions on Geoscience and Remote Sensing*, 47(9):3220–3230.

[68] Li, Z., Muller, J.-P., Cross, P., and Fielding, E. J. (2005). Interferometric synthetic aperture radar (InSAR) atmospheric correction: GPS, Moderate Resolution Imaging Spectroradiometer (MODIS), and InSAR integration. *Journal of Geophysical Research: Solid Earth*, 110(B3).

[69] López-Dekker, P., Prats, P., Zan, F. D., Schulze, D., Krieger, G., and Moreira, A. (2011). TanDEM-X First DEM Acquisition: A Crossing Orbit Experiment. *IEEE Geoscience and Remote Sensing Letters*, 8:943–947.

[70] Marinkovic, P. and Larsen, Y. (2013). Consequences of long-term ASAR local oscillator frequency decay—An empirical study of 10 years of data. In *Living planet symposium*. European Space Agency Edinburgh, Frascati.

[71] Meyer, F., Bamler, R., Jakowski, N., and Fritz, T. (2006). The Potential of Low-Frequency SAR Systems for Mapping Ionospheric TEC Distributions. *IEEE Geoscience and Remote Sensing Letters*, 3(4):560–564.

[72] Meyer, F., Bamler, R., Leinweber, R., and Fischer, J. (2008). A Comparative Analysis of Tropospheric Water Vapor Measurements from MERIS and SAR. In *IGARSS 2008 - 2008 IEEE International Geoscience and Remote Sensing Symposium*, volume 4, pages IV – 228–IV – 231.

[Michel and Rignot] Michel, R. and Rignot, E. Flow of Glaciar Moreno, Argentina, from repeat-pass Shuttle Imaging Radar images: comparison of the phase correlation method with radar interferometry. *Journal of Glaciology*, 45(149):93–100.

[74] Milillo, P., Rignot, E., Mouginot, J., Scheuchl, B., Morlighem, M., Li, X., and Salzer, J. T. (2017). On the Short-term Grounding Zone Dynamics of Pine Island Glacier, West Antarctica, Observed With COSMO-SkyMed Interferometric Data. *Geophysical Research Letters*, 44(20):10,436–10,444.

[75] Mora, O., Mallorqui, J., and Duro, J. (2002). Generation of deformation maps at low resolution using differential interferometric SAR data. In *IEEE International Geoscience and Remote Sensing Symposium*, volume 5, pages 2696–2698 vol.5.

[76] Moreira, A., Krieger, G., Hajnsek, I., Papathanassiou, K., Younis, M., Lopez-Dekker, P., Huber, S., Villano, M., Pardini, M., Eineder, M., Zan, F. D., and Parizzi, A. (2015). Tandem-L: A Highly Innovative Bistatic SAR Mission for Global Observation of Dynamic Processes on the Earth's Surface. *IEEE Geoscience and Remote Sensing Magazine*, 3(2):8–23.

[77] NGL (2018). MIDAS Velocity Fields. Available online: http://geodesy.unr.edu/ (accessed on 1 October 2018).

[78] Okada, Y. (1985). Surface deformation due to shear and tensile faults in a half-space. *Bull. Seismol. Soc. Am.*, 75:1135–1154.

[79] Parizzi, A. and Brcic, R. (2011). Adaptive insar stack multilooking exploiting amplitude statistics: A comparison between different techniques and practical results. *Geoscience and Remote Sensing Letters, IEEE*, 8(3):441–445.

[80] Parizzi, A., Cong, X. Y., and Eineder, M. (2010). First Results from Multifrequency Interferometry. A Comparison of Different Decorrelation Time Constants at L, C and X Band. In Lacoste, H., editor, *ESA Special Publication*, volume 677 of *ESA Special Publication*, page 5.

[81] Pepe, A., Yang, Y., Manzo, M., and Lanari, R. (2015). Improved EMCF-SBAS Processing Chain Based on Advanced Techniques for the Noise-Filtering and Selection of Small Baseline Multi-Look DInSAR Interferograms. *IEEE Transactions on Geoscience and Remote Sensing*, 53(8):4394–4417.

[82] Perissin, D. and Ferretti, A. (2007). Urban-target recognition by means of repeated spaceborne sar images. *IEEE Transactions on Geoscience and Remote Sensing*, 45(12):4043–4058.

[83] Peter, H., Jäggi, A., Fernández, J., Escobar, D., Ayuga, F., Arnold, D., Wermuth, M., Hackel, S., Otten, M., Simons, W., et al. (2017). Sentinel-1A–First precise orbit determination results. *Advances in space research*, 60(5):879–892.

[84] Pintori, F., Serpelloni, E., and Gualandi, A. (2021). Common mode signals and vertical velocities in the great alpine area from gnss data. *Solid Earth Discussions*, 2021:1–37.

[85] Proakis, J. and Manolakis, D. (2006). *Digital Signal Processing*. Prentice Hall.

[86] Rignot, E. (1996). Tidal motion, ice velocity and melt rate of Petermann Gletscher, Greenland, measured from radar interferometry. *Journal of Glaciology*, 42(142):476–485.

[87] Rignot, E. (1998). Hinge-line migration of Petermann Gletscher, north Greenland, detected using satellite-radar interferometry. *Journal of Glaciology*, 44(148):469–476.

[88] Rignot, E., Mouginot, J., Morlighem, M., Seroussi, H., and Scheuchl, B. (2014). Widespread, rapid grounding line retreat of Pine Island, Thwaites, Smith, and Kohler glaciers, West Antarctica, from 1992 to 2011. *Geophysical Research Letters*, 41(10):3502–3509.

[89] Rignot, E., Mouginot, J., and Scheuchl, B. (2011). Antarctic grounding line mapping from differential satellite radar interferometry. *Geophysical Research Letters*, 38(10).

[90] Rosen, P., Hensley, S., Joughin, I., K.Li, F., Madsen, S., Rodriguez, E., and Goldstein, R. M. (2000). Synthetic aperture radar interferometry. *Proceedings of the IEEE*, 88(3):333–382.

[91] Rosen, P. A., Hensley, S., Zebker, H. A., Webb, F. H., and Fielding, E. J. (1996). Surface deformation and coherence measurements of Kilauea Volcano, Hawaii, from SIR-C radar interferometry. *Journal of Geophysical Research: Planets*, 101(E10):23109–23125.

[92] Rosen, P. A., Kim, Y., Kumar, R., Misra, T., Bhan, R., and Sagi, V. R. (2017). Global persistent SAR sampling with the NASA-ISRO SAR (NISAR) mission. In *2017 IEEE Radar Conference (RadarConf)*, pages 0410–0414. IEEE.

[93] Rouby, H., Métivier, L., Rebischung, P., Altamimi, Z., and Collilieux, X. (2017). ITRF2014 plate motion model. *Geophysical Journal International*, 209(3):1906–1912.

[94] Sandwell, D. and Price, E. (1998). Phase gradient approach to stacking interferograms. *Journal of Geophysical Research*, 103:30,183–30,204.

[95] Scherneck, H.-G. (1991). A parametrized solid earth tide model and ocean tide loading effects for global geodetic baseline measurements. *Geophysical Journal International*, 106(3):677–694.

[96] Segall, P. (2010). *Earthquake and Volcano Deformation*. Princeton University Press.

[97] Sharov, A. (2003). Gradient Approach to InSAR modelling of glacial dynamics and morphology. *Proc. 22nd EARSeL Symp.*, Millpress, Rotterdam:373–381.

[98] Smith, A. M. (1991). The use of tiltmeters to study the dynamics of antarctic ice-shelf grounding lines. *Journal of Glaciology*, 37(125):51–58.

[99] Stephenson, S. N. (1984). Glacier Flexure and the Position of Grounding Lines: Measurements By Tiltmeter on Rutford Ice Stream, Antarctica. *Annals of Glaciology*, 5:165–169.

[100] Torres, R., Snoeij, P., Geudtner, D., Bibby, D., Davidson, M., Attema, E., Potin, P., Rommen, B., Floury, N., Brown, M., et al. (2012). GMES Sentinel-1 mission. *Remote Sensing of Environment*, 120:9–24.

[101] Werner, C., Wegmuller, U., Strozzi, T., and Wiesmann, A. (2003). Interferometric point target analysis for deformation mapping. In *IGARSS 2003. 2003 IEEE International Geoscience and Remote Sensing Symposium. Proceedings (IEEE Cat. No.03CH37477)*, volume 7, pages 4362–4364 vol.7.

[102] Wiener, N. (1964). *Extrapolation, Interpolation, and Smoothing of Stationary Time Series*. The MIT Press.

[103] Wright, T., Fielding, E., and Parsons, B. (2001). Triggered slip: observations of the 17 august 1999 izmit (turkey) earthquake using radar interferometry. *Geophysical Research Letters*, 28(6):1079–1082.

[104] Wright, T. J. (2016). The earthquake deformation cycle. *Astronomy & Geophysics*, 57(4):4.20–4.26.

[105] Wright, T. J., Parsons, B. E., and Lu, Z. (2004). Toward mapping surface deformation in three dimensions using InSAR. *Geophysical Research Letters*, 31.

[106] Xu, X. and Sandwell, D. T. (2020). Toward Absolute Phase Change Recovery With InSAR: Correcting for Earth Tides and Phase Unwrapping Ambiguities. *IEEE Transactions on Geoscience and Remote Sensing*, 58(1):726–733.

[107] Yoon, Y. T., Eineder, M., Yague-Martinez, N., and Montenbruck, O. (2009). TerraSAR-X Precise Trajectory Estimation and Quality Assessment. *IEEE Transactions on Geoscience and Remote Sensing*, 47(6):1859–1868.

[108] Zebker, H. and Villasenor, J. (1992). Decorrelation in interferometric radar echoes. *Geoscience and Remote Sensing, IEEE Transactions on*, 30(5):950–959.

[109] Zwieback, S., Hensley, S., and Hajnsek, I. (2015). Assessment of soil moisture effects on L-band radar interferometry. *Remote Sensing of Environment*, 164:77–89.